

Some surface expressions of mantle convective instabilities

Maëlis Arnould

▶ **To cite this version:**

Maëlis Arnould. Some surface expressions of mantle convective instabilities. Earth Sciences. Université de Lyon; University of Sydney, 2018. English. ⟨NNT : 2018LYSEN036⟩. ⟨tel-01974445⟩

HAL Id: tel-01974445

https://theses.hal.science/tel-01974445v1

Submitted on 8 Jan 2019

HAL is a multi-disciplinary open access archive for the deposit and dissemination of scientific research documents, whether they are published or not. The documents may come from teaching and research institutions in France or abroad, or from public or private research centers.

L'archive ouverte pluridisciplinaire **HAL**, est destinée au dépôt et à la diffusion de documents scientifiques de niveau recherche, publiés ou non, émanant des établissements d'enseignement et de recherche français ou étrangers, des laboratoires publics ou privés.



HAL Authorization





Numéro National de Thèse : **2018LYSEN036**

THESE de DOCTORAT DE L'UNIVERSITE DE LYON

opérée par
l'Ecole Normale Supérieure de Lyon
en cotutelle avec
The University of Sydney

Ecole Doctorale N°52
Ecole Doctorale Physique et Astrophysique de Lyon

Discipline de doctorat : Sciences de la Terre et de l'Univers

Soutenue publiquement le 26/09/2018, par :

Maëlis ARNOULD

Some surface expressions of mantle convective instabilities

Étude de l'expression de surface d'instabilités convectives mantelliques

---

Devant le jury composé de :

Greff-Lefftz Marianne	Professeure, Institut de Physique du Globe de Paris	Rapporteure
Conrad Clinton	Professor, University of Oslo	Rapporteur
Rouby Delphine	Chargée de recherche, CNRS (GET)	Examinatrice
Davaille Anne	Directrice de Recherche, CNRS (FAST)	Examinatrice
Labrosse Stéphane	Professeur, École Normale Supérieure de Lyon	Examinateur
Coltice Nicolas	Professeur, École Normale Supérieure de Paris	Directeur de thèse
Müller R. Dietmar	Professor, University of Sydney	Co-tuteur de thèse
Flament Nicolas	Lecturer, University of Wollongong	Co-encadrant de thèse

Remerciements

Ça y est, c'est bientôt la fin (ou le début pour toi, brave lecteur)! Vient donc le moment traditionnel de faire un bref retour sur cette formidable aventure humaine qu'a été cette thèse et de remercier tous ceux qui m'ont accompagné dans l'exploration des profondeurs de la Terre.

Tout d'abord, je souhaiterais remercier tous les membres de mon jury, qui ont gentiment accepté d'évaluer ce travail de 3 années. La diversité de vos champs d'expertise ont rendu l'exercice de l'écriture de ce manuscrit intense, mais aussi intéressante je l'espère.

Cette thèse n'aurait sûrement pas été ce qu'elle est si mes 2 Nicos n'avaient été particulièrement à l'écoute, malgré les déménagements et les bébés ;) Je ne vais pas être longue, mais merci pour cette liberté que vous m'avez laissée pour mener du mieux possible mes projets, pour vos conseils (que je n'ai malheureusement pas toujours suivis, trop souvent à mes dépends!) et pour vos "cheer up" sessions dès les premiers signes de coups de mou! Merci à mes 2 coauteurs de la dernière heure, Valentin et Jérôme, pour votre disponibilité, votre bonne humeur et pour avoir chacun à votre façon contribué à diversifier les méthodes d'étude développées dans cette thèse (maths et pétro), voire à la sauver carrément :)

À Lyon, j'ai eu la chance d'évoluer au sein du projet AUGURY dont j'ai pu voir et vivre toutes les transitions, du départ de Léa à celui de Martina, Marie, Claire puis Mélanie. Merci les filles pour tous les moments passés dans l'open-space ou au R6, et votre soutien de dernière heure dans la relecture de ma thèse, ou psychologique à Valflaunès! Tout au long de ma thèse, je n'ai pas réussi à m'ennuyer grâce à vous! Récemment, l'arrivée de Mike et Susanne m'auront aussi beaucoup aidé à garder le moral au retour d'Australie! Par ailleurs, deux années et demi passées au coeur de la Ouad auront été riches en surprises, fou-rires, vidéos un peu compromettantes, sorties au Condorcet, et repas animés le midi ; et ce grâce aux thésards (passés, présents ou futurs) du labo: Mary, Maxime, les 2 Manus, Alex, Ulysse, Jean, Victor, Chloé, Rémi, Florian, Alice, les martiens Sylvain, Lucia et Cédric et les biogéochimistes Arnauld, David et Ivan. Merci aussi aux autres thésards du labo, Fanny, Céline, Théo, Chouch' et Adrien pour ces soirées occasionnelles, à tous les autres membres du LGL pour votre accueil et aux potes de promo partis vers d'autres horizons pour les bons moments de retrouvailles partagés pendant cette thèse. Par ailleurs, ces remerciements lyonnais ne seraient rien sans une pensée pour mes colocs Jean et Lauren, ou plus récemment Catherine, Richard, Faustine et Minette pour avoir supporté mes sautes d'humeur au quotidien, ainsi qu'une pensée pour la Brâba, qui m'a permis de m'évader de la

thèse en poésie et théâtralement...

I switch to english to acknowledge all the nice people that I met during my one-year journey to the other side of Earth. My greatest thoughts are of course for my two new best friends in Australia: Xuesong and John! John, it was a huge pleasure for me to meet you, share your place in Bronte with you, Katherine, the fish and the pigs, have lengthy conversations about politics or geography, your life in Papua-New-Guinea, your adventures in Vanuatu or in more remote Pacific Islands, learn about soccer or cricket, drink Australian or French wine, have Indian food for dinner, and listen to your old audiotapes coming from all over the world. Xuesong, my dear friend, I miss so much our hiking sessions in the Blue Mountains or in the Royal National Park, I've been sooo happy to invite you to Mauritius to share with you a part of my cultural heritage and childhood and be a tourist guide for you in Lyon :) I can't wait to meet you again somewhere, let it be in China, Australia, London or Paris :)... Jia you for the end of your PhD! Of course, thank you Dietmar and all the EarthByters for your warm welcome in Sydney, Gilles, Wenchao, Ruken, Eline, Kirsten, Rhiannon, Omer, Sabin, Mandi, Andrew and Nick for occasional or frequent lunch or crepe and nutella sharing, and Patrice and Tristan, for your kindness and your french accent, Simon and Shan for your mood and the hot pot in Sutherland :) I also want to address special thanks to Daniel and Hansen, thank you for all those shared moments and hope to see you again! I had the chance to live three months and a half in Wollongong, away from Sydney endless activity and crowds! There, it was so nice to live in your place, Lili, with Wanchese and Rosa, close to the beach and the bush!

Je continue mon tour du monde, pour faire un clin d'oeil aux Réunionnais, aux Mauriciens, aux Vosgiens et à Josiane, qui n'ont toujours pas compris que ça y est, j'ai (presque) fini mes études et n'ont eu de cesse de me réclamer à leurs côtés. Sabine, je n'aurais certainement pas fait de thèse si tu n'avais pas été là dès le début de mon aventure en Métropole! Merci aussi à ma famille Cassoulet à moi, pour votre soutien inconditionnel et nos sessions Skype interminables! Et puis à Jeanjean, bien sûr, toi qui m'a accompagnée, comprise et rassurée tellement souvent au cours de cette thèse, malgré la distance que je nous ai imposée et qui a été tellement dure à supporter...

Et enfin, je clos ces remerciements avec une pensée pour papi Roger et Martine, à qui ces travaux et mon éloignement m'auront malheureusement empêchée de dire au-revoir...

Abstract

Earth's lithosphere, which is the upper boundary layer of mantle convection, represents the interface between the external and internal envelopes of our Planet. The multiple interactions between the mantle and lithosphere generate lateral (plate tectonics) and vertical (dynamic topography) deformations of Earth's surface. Understanding the influence of the dynamics of mantle convective instabilities on the surface is fundamental to improve our interpretations of a large range of surface observations, such as the formation of sedimentary basins, continental motions, the location of hotspots, the presence of gravity anomalies or sea-level variations.

This thesis aims at developing numerical models of whole-mantle convection self-generating plate-like tectonics in order to study the impacts of the development and the dynamics of mantle convective instabilities (such as slabs or mantle plumes) on the continuous reshaping of the surface.

First, I focus on the influence of the coupling between mantle convective motions and plate tectonics on the development of dynamic topography (*i.e.* surface vertical deformations induced by mantle convection) at different spatial and temporal scales. The results suggest that Earth's surface can deform over large spatial scales ($> \ 10^4$ km) induced by whole-mantle convection to small-scales ($< \ 500$ km) arising from small-scale sub-lithospheric convection. The temporal variations of dynamic topography range between five and several hundreds of millions of years depending on the convective instabilities from which they originate. In particular, subduction initiation and slab break-off events control the existence of intermediate scales of dynamic topography (between 500 and 10^4 km). This reflects that the interplay between mantle convection and lithosphere dynamics generates complex spatial and temporal patterns of dynamic topography consistent with constraints for Earth.

A second aim of this thesis is to understand the dynamics of mantle plumes and their interactions with surface. I first characterize in detail the behaviour of mantle plumes arising in models of whole-mantle convection self-generating plate-like tectonics, in light of surface observations. Then, I study how the interactions between surface plate tectonics and mantle convection affect plume motions. Finally, I use observations of the thermal signature of plume/ridge interactions to propose a reconstruction of the relative motions between the Azores mantle plume and the Mid-Atlantic Ridge.

Résumé détaillé

Constituant la couche limite supérieure de la convection mantellique, la lithosphère terrestre est à l'interface entre les enveloppes externes et internes de notre Planète. Les interactions multiples entre celle-ci et le manteau sont à l'origine de déformations latérales (tectonique des plaques) et verticales (topographie dynamique) de la surface terrestre. Comprendre comment la formation et l'évolution d'instabilités convectives mantelliques renouvellent sans-cesse la surface est donc primordial pour améliorer nos interprétations d'un grand nombre d'observations de surface, telles que la formation de bassins sédimentaires, le mouvement des continents, la localisation des points chauds, la formation d'anomalies gravimétriques ou encore les variations du niveau marin.

Cette thèse propose de développer des modèles numériques de convection mantellique générant de façon auto-organisée de la tectonique des plaques en surface afin d'étudier la façon dont le développement et la dynamique d'instabilités convectives telles que les panneaux de subduction ou les panaches mantelliques modifient la surface, dans un contexte de tectonique de surface approchant le régime terrestre.

Le Chapitre 1 propose un historique de l'évolution de l'état de nos connaissances concernant l'influence de la convection mantellique terrestre sur la dynamique de surface. Ce Chapitre s'ouvre sur les explications mythologiques d'abord invoquées pour expliquer séismes et volcanisme aux quatre coins du monde, avant de poser les bases de la physique de la convection ainsi que les différentes découvertes ayant mené à la théorie de la tectonique des plaques. Puis, les principales interactions entre dynamique du manteau et de la lithosphère sont énoncés, en séparant l'effet des zones de subduction et celui des panaches mantelliques, puis en précisant les multiples rétroactions complexes existant entre la surface et le manteau, en considérant l'exemple de l'influence des mouvements des continents sur les réorganisations globales de la convection. Enfin, ce Chapitre s'ouvre sur le développement de la problématique de ce manuscrit, en énonçant préalablement les diffrentes grandes questions qu'il existe actuellement au sein de la communauté scientifique.

Le Chapitre 2 débute par la description des différentes équations physiques et approximations couramment utilisées pour décrire la convection mantellique d'origine thermique avant d'aborder les spécificités de la convection thermo-chimique ainsi que les simplifications réalisées pour modéliser la rhéologie du manteau terrestre. Puis, les méthodes permettant de modéliser la rhéologie de la lithosphère, la dynamique de la tectonique des plaques et les spécificités de la lithosphére continentale sont envisagées. Enfin, ce Chapitre s'ouvre rapidement sur les détails techniques des méthodes de modélisation numérique utilisées tout au long de cette thèse.

Après une rapide introduction, le Chapitre 3 décrit les premiers résultats de cette thèse concernant l'influence du couplage des mouvements de convection mantellique et de tectonique des plaques sur le développement de topographie dynamique (*i.e.* les mouvements verticaux de la lithosphère induits par la convection mantellique) à différentes échelles spatio-temporelles. Mes résultats suggèrent que la surface terrestre peut se déformer à toutes les échelles spatiales, du fait de mouvements convectifs de grande ampleur faisant intervenir le manteau entier ($> \ 10^4$ km) ou encore de convection à petite échelle sub-lithosphérique ($<$ 500 km). Les variations temporelles de topographie dynamique s'étendent de cinq à plusieurs centaines de millions d'années selon la nature des processus convectifs dont elles dérivent. En particulier, la dynamique d'initiation ou d'arrêt des zones de subduction contrôle l'existence d'échelles intermédiaires de topographie dynamique (longueurs d'onde variant entre 500 et 10^4 km). Ces résultats montrent donc que les interactions entre la dynamique de la lithosphère et la convection mantellique génèrent des motifs spatio-temporels de topographie dynamique complexes et cohérents par rapport aux observations terrestres.

Le Chapitre 4 se focalise sur la dynamique des panaches mantelliques, et leurs interactions avec la surface. Je caractérise d'abord précisément le comportement des panaches générés dans nos modèles de convection à la lumière d'observations de surface. Puis, j'étudie la façon dont leurs interactions avec la tectonique de surface et les différentes échelles convectives modifient leurs mouvements latéraux. Enfin, la compréhension de la signature thermique des interactions entre panaches et rides océaniques me permet de proposer une reconstitution des mouvements relatifs entre le panache des Açores et la ride médio-Atlantique.

Enfin, le Chapitre 5 récapitule les principaux résultats de cette thèse, avant de montrer comment ce travail s'intègre au projet Augury vient à reconstruire la convection mantellique à partir d'observations de surface. Enfin, quelques axes de perspectives à ce travail sont ouverts, avec quelques pistes d'améliorations techniques aux modèles numériques, des idées d'études à effectuer pour mieux comprendre les rétroactions entre manteau et lithosphère, tout cela dans le but de participer à plus long terme à l'amélioration de la qualité des reconstructions tectoniques, pour qu'elles prennent en compte plus de contraintes géodynamiques.

Contents

1 Introduction **1**

1.1 First evidence of surface expressions of mantle dynamics 2

1.1.1 Mythology, fascination and fantasy about the surface expressions of internal Earth dynamics 2

1.1.2 Impact of mantle convective instabilities on global tectonics 6

1.2 The multiple interactions between mantle instabilities and the surface 21

1.2.1 Subduction zones: cold anomalies sinking in the mantle 21

1.2.2 Mantle plumes: hot rising anomalies predicted by the physics of mantle convection 32

1.2.3 Convective cells and plate tectonics : mutual feedbacks? 44

1.3 Towards an integrative approach of mantle and lithosphere interactions? 47

1.3.1 Current challenges and perspectives 47

1.3.2 Problem statement 49

1.3.3 Outline of this thesis 49

2 Numerical modeling of the influence of whole-mantle convection on a plate-like lithosphere **51**

2.1 Numerical modeling of mantle dynamics 52

2.1.1 Thermal convection approximations and limitations 52

2.1.2 Modeling thermo-chemical convection 62

2.1.3 Modeling mantle rheology 63

2.2 Numerical modeling of lithosphere dynamics 68

2.2.1 Numerical models of mantle convection with plate-like tectonics 68

2.2.2 Modeling oceanic and continental lithosphere 75

2.3 Computation 76

2.3.1 Numerical approximation, discretization and geometry 77

2.3.2 Solving conservation equations 79

2.3.3 Initial and boundary conditions 81

2.3.4 Scaling or dimensionalization 83

3 On the scales of dynamic topography in whole-mantle convection models with plate-like tectonics 84

3.1 Introduction . . . 85

3.2 Modeling surface topography . . . 88

3.3 On the scales of dynamic topography in whole-mantle convection models . . . 90

3.3.1 Introduction . . . 91

3.3.2 Methods . . . 93

3.3.3 Results . . . 104

3.3.4 Discussion . . . 111

3.3.5 Conclusions . . . 117

3.4 Conclusions and perspectives . . . 120

4 Some surface expressions of mantle plume dynamics 122

4.1 Introduction . . . 123

4.2 Sources of hotspot relative motions in whole-mantle convection models . . . 124

4.2.1 Introduction . . . 125

4.2.2 Modeling mantle plumes in 3D-whole mantle convection models . . . 128

4.2.3 Mantle plume phenomenology . . . 134

4.2.4 Analysis of the motion of mantle plumes . . . 147

4.2.5 Discussion . . . 160

4.2.6 Conclusion . . . 162

4.3 Northward drift of the Azores plume in the Earth's mantle . . . 164

4.3.1 Abstract . . . 164

4.3.2 Introduction . . . 164

4.3.3 Results . . . 167

4.3.4 Method . . . 173

4.4 Conclusion and perspectives . . . 175

4.4.1 Conclusion . . . 175

4.4.2 Perspectives . . . 176

5 Conclusion and Perspectives 184

Bibliography 192

A Comparison of a 1D discrete signal with a 2D signal defined on the sphere $\mathbb{S}^2$ 233

A.1 Notations 233

A.2 Approximation of a function on a sphere by longitudinal functions 234

B Supplementary Information for: Northward drift of the Azores plume in the Earth's mantle 240

B.1 Petrological analysis of along-axis MAR basalts 240

B.2 Analysis of the thermal imprint of modelled plumes 250

B.2.1 Numerical set up 250

B.2.2 Characteristics of modelled plumes 252

B.3 Kinematic analysis of South and Central Atlantic hotspot tracks 255

Chapter 1

Introduction

Contents

1.1 First evidence of surface expressions of mantle dynamics 2

1.1.1 Mythology, fascination and fantasy about the surface expressions of internal Earth dynamics 2

1.1.2 Impact of mantle convective instabilities on global tectonics 6

1.1.2.1 The physics of convection 6

1.1.2.2 First evidence of mantle convection 9

1.2 The multiple interactions between mantle instabilities and the surface 21

1.2.1 Subduction zones: cold anomalies sinking in the mantle 21

1.2.1.1 Characteristics of subduction zones 21

1.2.1.2 The initiation of subduction zones 23

1.2.1.3 Subduction driving forces 27

1.2.1.4 Topography and gravity in the vicinity of subduction zones 29

1.2.2 Mantle plumes: hot rising anomalies predicted by the physics of mantle convection 32

1.2.2.1 Characteristics of mantle plumes 33

1.2.2.2 The initiation of plumes 35

1.2.2.3 The stability of plumes 40

1.2.2.4 The activity of plumes: from birth to death 41

1.2.3 Convective cells and plate tectonics : mutual feedbacks? 44

1.3 Towards an integrative approach of mantle and lithosphere interactions? . . . 47

1.3.1 Current challenges and perspectives 47

1.3.2 Problem statement 49

1.3.3 Outline of this thesis 49

Human beings have always been fascinated by natural processes which constantly reshape the environment in which different civilizations took turns. Natural hazards were first justified by religious beliefs. Then, the development of complex engineering instruments or physical, experimental, numerical and mathematical explanations made it possible to measure natural phenomena precisely and successively contributed to the understanding that Earth is an active planet. The goal of Chapter 1 is to show the current understanding about how Earth's surface dynamics (plate tectonics, hotspots, dynamic topography, geoid...) reflects different aspects of mantle internal motions.

In the subsequent sections, I review some of the major historical evolutions of our knowledge which led to the understanding that Earth's surface dynamics is intimately linked with the physics of mantle convection (section 1.1). In section 1.2, I review the major interactions between surface lithospheric deformations and the dynamics of mantle convective instabilities, therefore highlighting the specificities and the complexity of Earth's mantle convection. Nowadays, Earth's surface/interior coupling is still far from being entirely understood. Therefore, I finally point out some current areas of work to which this thesis aims at contributing (section 1.3).

1.1 First evidence of surface expressions of mantle dynamics

1.1.1 Mythology, fascination and fantasy about the surface expressions of internal Earth dynamics

Since Antiquity and the early days of writing, mythology has recorded how much Humans are fascinated by natural hazards linked to internal Earth activity, such as earthquakes and volcanoes. Invoking the action of various divinities was a way to "explain" those intriguing and feared phenomena capable of profoundly modifying the landscape, and that Humans could not predict nor control.

For instance, the Ancient Greek and Roman civilizations were built on an active Earth region, submitted to various earthquakes and volcanic eruptions. In the Greek mythology, Poseidon, husband of Gê, goddess of Earth, was the god responsible for shaking Earth, whenever he was upset by Human behaviors. The Gigante Enceladus, prisoner from Athena below Mount Etna, was responsible for its eruptions, whenever he wanted to escape (Fig. 1.1).



Figure 1.1: Renaissance engraving representing Enceladus trapped below Mount Etna and trying to escape, provoking an eruption (Picart, 1733).

In the Japanese mythology, a giant catfish, the *Namazu*, was supposed to be responsible for earthquakes and tsunamis in this active tectonic region, whenever it escaped from the care of the god Kashima (Fig. 1.2). In the Norse mythology of Vikings, a dragon located in the *Hel world* (one of the nine worlds of the Tree of worlds *Yggdrasill*) was responsible for volcanic eruptions and earthquakes on Iceland, while the goddess Pele would intermittently wake the Hawaiian volcanoes. Finally, in the Maori imaginary, volcanic eruptions of the Taranakis were caused by jealousy and rivalry between three personified mountains. Despite their geographic distance, most myths shared the faith that internal activity inside Earth is responsible for surface tectonic and volcanic activity.

In parallel to the development of mythologic beliefs about Earth's interior, philosophers and scientists such as Aristotle, Thales or Erathostenes tried to bring a more scientific vision of such events, by describing them precisely and invoking meteorological processes occuring inside Earth, already believed to be spherical, such as underground storms and winds. Internal Earth was therefore seen as *"cavernous and passive, crossed by fluids and active substances, causing Earth to shake"* (Bernard,



Figure 1.2: Namazu motif earthquake art. The giant catfish is being blamed for an earthquake by people living in Shin Yoshiwara and threatening to cause aftershocks (Anonymous, Edo era - 1855).

2003). Various theories were soon developed to try to predict and measure Earth's seismic and volcanic activity (Fig. 1.3), as well as to attempt to understand the composition and dynamics of Earth's interior.



Figure 1.3: Engraving by the *Houfeng Didong Yi*, a Chinese sismoscope invented by Zhang Heng of China's Han dynasty (-206-220) (Heng, 132).

From being composed of water in Antiquity, Renaissance naturalists and philosophers believed that Earth's interior was composed of fire or molten rocks (Fig. 1.4), thanks to observations emanating from scientific expeditions during Vesuvius and Etna volcanic eruptions. The development of modern physics and the improvements of engineering during the XIXth century allowed the invention of new and more performant measuring instruments. This led to the understanding of the composition and dynamics of Earth's interior and attempts to link Earth's internal activity to surface phenomena. This

active search for internal causes of surface processes started to excite and fascinate people, as recorded by the emergence of fiction books mixing scientific discoveries, expeditions inside Earth, engineering and adventures (*e.g.* Fig. 1.5, Verne (1864)).

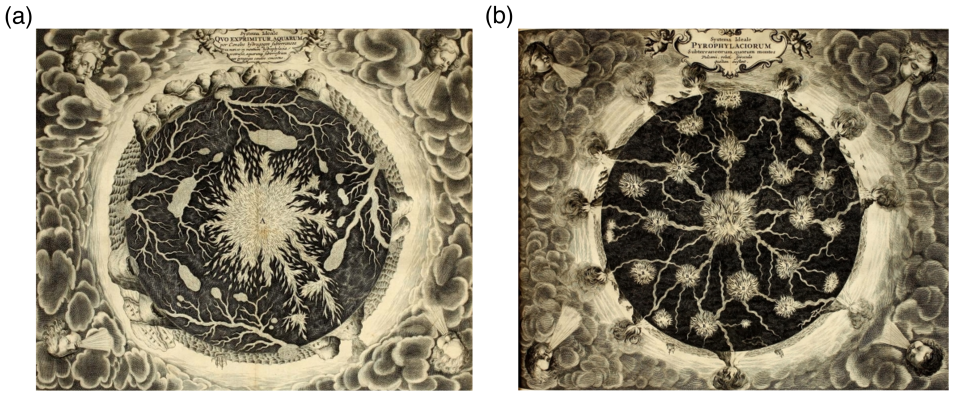


Figure 1.4: Engraving of the Jesuit Athanasius Kircher, illustrating his theory of interconnection between the water network (a) and underground fire network (b) causing volcanic eruptions (Kircher, 1665).



Figure 1.5: *"Descends dans le cratère du Yocul de Sneffels que l'ombre du Scartaris vient caresser dans les calendes de juillet, voyageur audacieux, et tu parviendras au centre de la Terre. Ce que j'ai fait. Signé Arne Saknussemm"* (Descend into the crater of Yocul of Sneffels, which the shade of Scartaris caresses, before the kalends of July, audacious traveler, and you will reach the centre of Earth. I did it. Signed: Arne Saknussemm, Verne (1864)).

After this small preamble of human intuitions at all times about the activity of Earth's interior, I now review the major milestones which led to the understanding that Earth's mantle is convecting and that lithospheric dynamics is coupled to mantle internal motions.

1.1.2 Impact of mantle convective instabilities on global tectonics

The first reference to mantle convection as the main driver for surface motions was from W. Hopkins (1793-1866), who tried to explain mountain ranges building by internal convergent motions between two mantle convective cells at the start of Earth's history. In the following, I review the historical milestones in the understanding of the process of convection and how it has been applied to Earth's mantle and surface.

1.1.2.1 The physics of convection

Convection is one of the 3 ways for a material to transport heat (together with *conduction*, which represents a heat transfer by microscopic vibrations of matter, and *radiation*, which represents a heat transfer by photons). Convection corresponds to the macroscopic transport of heat due to density variations inside a material. In 1900, Bénard was the first to make quantitative experiments on heated-from-below honey or spermaceti and describe the process of convection (Bénard, 1900, 1901). His observations were then formalized by Boussinesq (Boussinesq, 1901) and Lord J. Rayleigh (Rayleigh, 1916), although it was then found that the structures described by Bénard are characteristic of the thermal Marangoni effect (Pearson, 1958). They showed that the Archimedes force is the driving mechanism leading to convection, by transporting areas of low density upwards and regions of large density downwards, which results in both material and heat transport. Moreover, J. Rayleigh showed that the onset of convection is controled by the balance between the buoyancy force and the dissipation forces (viscous forces and effect of thermal diffusion) acting against fluid motions. This is measured by the dimensionless Rayleigh number Ra. In the case of a fluid heated from below, Ra is defined as follows:

$$\mathrm{Ra} = \frac{\alpha g \Delta T \rho D^3}{\eta \kappa} \tag{1.1}$$

with α the surface thermal expansivity, g the gravitational acceleration, ρ the reference density, η the reference viscosity, ΔT the temperature difference within the domain, D the domain thickness and κ the thermal diffusivity. J. Rayleigh found that convective instabilities only start once a critical Rayleigh

number (Ra_c) is reached thanks to linear stability analysis, which is a way to study the steadiness of a static system (artificially maintained in an gravitationally unstable state) by initiating infinitely small perturbations inside the linearized equations of convection. If the fluid's Rayleigh number is higher than this value, it is able to convect. In the case of thermal convection (also called Rayleigh-Bénard convection), density gradients are caused by thermal anomalies: once the critical Rayleigh number is reached, basal buoyant hot instabilities start rising while top cold areas sink because of their density excess. If the Rayleigh number of the considered fluid is close to its Ra_c, convective patterns form stationary rolls. For intermediate Rayleigh numbers, convection develops episodic patterns. Finally, if the Rayleigh number is several orders of magnitude greater than Ra_c, convection becomes chaotic and therefore unpredictable and highly time-dependent (Fig. 1.6).

Convection can be formalized into equations of conservation of mass, momentum, energy and composition in the framework of continuum mechanics (*i.e.* all quantities of the considered fluid represent an average, independent from molecular fluctuations) (*e.g.* Batchelor, Landau and Lifchitz, 1980, Jarvis and McKenzie, 1980, Ricard, 2015). Depending on the viscosity of the fluid and its thermal and chemical properties, different approximations can be chosen. The application of those equations for Earth's interior and the corresponding approximations are developed at-length in section 2.1.

In a fluid, the convective behaviour is associated with a specific thermal state: its interfaces are called thermal boundary layers (TBLs) and characterized by steep temperature gradients. At the TBLs, heat is exchanged via conduction with the environment and heat outflows are preferentially located in upwelling areas. The thickness of TBLs depends on the Rayleigh number as seen on Fig. 1.6. Inside the fluid, the material is well-mixed and, depending on the approximations used, the interior of each cell is isothermal (in the case of an incompressible fluid) or adiabatic (if compressibility is considered, when a parcel of fluid is moved upwards and undergoes decompression, it cools down, while it would heat up if moved downwards).

The initiation of thermal instabilities (also called Rayleigh-Taylor instabilities) from the TBLs in chaotic convective fluids can be formalized into the TBL instability theory (Howard, 1966). The onset time and growth rate of Rayleigh-Taylor instabilities are controled by the local Rayleigh number Ra_δ:

$$Ra_\delta = \frac{\alpha g \Delta T \rho \delta^3}{\eta \kappa} \tag{1.2}$$

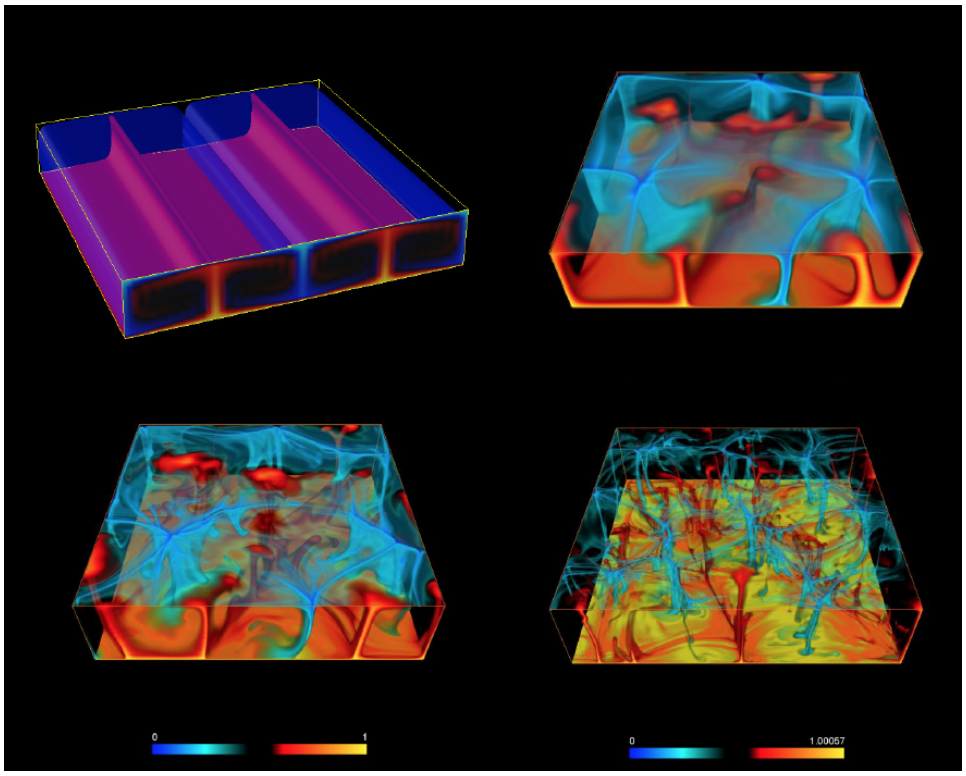


Figure 1.6: Convection patterns inside a fluid heated from below at Rayleigh number 10^5, 10^6, 10^7 and 10^8. The Ra_c of the considered system is of the order of 10^3. The temperature colorbars range from 0 (top boundary) to 1 (bottom boundary). The Boussinesq approximation is used. The increase in Rayleigh number corresponds to a decrease of the boundary layer thicknesses and width of the plumes. Only in the case of the lowest Rayleigh number (top left) is the convection stationary, with cells of aspect ratio $\approx \sqrt{2}$, as predicted by marginal stability. For higher Rayleigh numbers, the patterns are highly time-dependent (Ricard, 2015).

where δ is the thermal boundary layer's thickness. The generation of transient thermal instabilities follows a cycle of growth by diffusion, instability after reaching a critical thickness δ_c, and finally disconnection from the TBL to form a plume. The timescale t_c of this cycle is:

$$t_c = \frac{D^2}{\pi\kappa}\left(\frac{\mathrm{Ra}_{\delta,c}}{\mathrm{Ra}_\delta}\right)^{2/3} \tag{1.3}$$

with $\mathrm{Ra}_{\delta,c}$, the local critical Rayleigh number. Various experimental (*e.g.* Sparrow et al., 1970, Davaille and Jaupart, 1993, Manga et al., 2001) and numerical studies (*e.g.* Tackley, 1998, Houseman, 1990, Parmentier and Sotin, 2000) confirmed this relationship and showed that the spacing between plumes is controled by their critical thickness δ_c, that they are connected by ridges, and that their diameter decreases as the Rayleigh number increases (Fig. 1.6).

In conclusion, the Rayleigh-Bénard convective regime corresponds to:

- **a density-driven flow, which vigor depends on its Rayleigh number,**
- **a distinctive thermal structure, with thermal boundary layers and a well-mixed interior,**
- **efficient heat exchange with its environment.**

In the following section, I demonstrate that Earth's mantle is convecting, and show that its dynamics is intrinsically linked with Earth's surface behaviour, by following the chronological order of the major breakthroughs.

1.1.2.2 First evidence of mantle convection

Earth's outer shell deforms elastically

Based on observations that Earth rotates around the Sun and that the Moon rotates around the Earth, Isaac Newton (Newton, 1687) theorized the idea of the gravitational attraction by the Moon and the Sun as the driving mechanism for tides. Using the difference between the theoretical effect of long-period marine tides with observations on Earth, Lord Kelvin (Kelvin, 1863) concluded that the Earth deforms at least partially elastically and has the rigidity of steel, since it dissipates the the marine tide to about 0.68 of it's theorerical value if the Earth was fully rigid.

Earth's mantle is solid and viscous: it can flow

One of the first modern evidence of the nature of Earth's interior was the recording of a teleseismic earthquake occuring in Tokyo by a seismometer based in Postdam in April 1889 (Fig. 1.7, Von Rebeur-Paschwitz (1889)). Based on the properties of wave propagation, scientists soon understood that Earth's interior was composed of a material at least partly solid and capable of transmitting seismic waves tens of thousands of kilometers away from their epicenter.

The development of seismology boomed in early XXth century, with the deployment of more and more sophisticated seismometers worldwide, which contributed to the understanding of Earth's internal structure and composition (e.g. Mohorovicic (1992), Oldham (1906), Lehmann (1936)). By



Figure 1.7: First ever recorded seismogram. The magnitude 5.8 earthquake was located in Japan and recorded in Postdam thanks to a photographical recording horizontal pendulum (Von Rebeur-Paschwitz, 1889).

the mid-XXth century, it was thus known that Earth's interior is composed of 4 major concentric layers (Bullen, 1956): a highly viscous and elastic lithosphere of two kinds (oceanic and continental lithosphere), a solid mantle, a liquid external core (Jeffreys, 1926) and a solid internal core of high density (Lehmann, 1936).

Earth's mantle and lithosphere were therefore first considered as elastic layers, capable of transmitting seismic waves on timescales of a few seconds, and tides on timescales of a few hours. However, the ellipsoidal shape of Earth caused by its rotation favored a viscous behaviour. Gravity and topographic studies on the Scandinavian craton showed that Earth's surface readjusts isostatically over scales of at least tens of thousands of years (Airy, 1955, Pratt, 1959). Viscous deformations of the mantle were thus invoked to compensate vertical motions of Earth's elastic lithosphere. Upper mantle viscosity was estimated to be 3×10^{21} Pa·s by Haskell (1935). Therefore, the mantle was now considered to be capable of flowing on timescales of ten thousands of years, even if the opponents to mantle convection such as H. Jeffreys, had invoked the fact that a plastic yielding had to be reached in the asthenosphere before mantle convection could take place. Moreover, because of the high viscosity of the mantle, its Rayleigh number Ra is very large ($> 10^7$): heat transport by material motions is more efficient than transport by thermal diffusion. Depending on the timescales of perturbations, Earth's mantle is therefore capable of deforming elastically or viscously. The critical timescale controlling its behaviour

is called the Maxwell time (τ_M) which is defined as follows:

$$\tau_M = \frac{\eta}{\mu} \tag{1.4}$$

where μ is the shear modulus and η the viscosity. In the upper mantle conditions, τ_M is of the order of a few hundred to a few thousand years, explaining intuitively contradicting observations.

Plate tectonics revolution: lateral motions of Earth's surface are linked to mantle convection

In parallel to this increasing interest of physicists for explaining Earth's mantle structure and dynamics, the rapidly expanding field of geology during the XIXth century required explanations that would eventually lead to the theory of plate tectonics in the mid-XXth century.

The theory of continental drift

While the fit of continental coastlines' geometry had been uncovered since the XVIth century by the Flemish geographer A. Orthelius (1527-1598), who had invoked earthquakes and floods as the mechanism causing continental drift, our modern vision of plate tectonics, as being driven by mantle convective motions, only developed in the 1960's.

During the start of the XXth century, modern geology started to grow, with more and more scientists interested in understanding the formation of sedimentary basins or mountain ranges. Isostasy was discovered from gravimetry studies in mountain ranges and provided a first-order explanation for the continents/oceans topography dichotomy (Airy, 1955, Pratt, 1959). Fossil records on different continents, geomorphological and structural geology observations of stratigraphic sequences and thrust nappes all pointed to large-scale lateral and vertical motions of Earth's surface (e.g. Bertrand (1900)). Indeed, from records of sea-level variations, the occurrence of *Glossopteris* fern fossils in India, Africa and South-America, E. Suess (1831-1914) built the idea that those lands once formed a supercontinent, called Gondwanaland, which underwent whole-Earth thermal contractions due to the cooling of its interior, leading to ocean transgressions and regressions (Suess, 1904-1924).

From 1912, the meteorologist A. Wegener (1880-1930) started to build his theory of continental drift, which is considered as a cornerstone for modern geology. From paleontological, geometrical (correspondence between Africa and South-America coastlines) and geomorphological and paleo-climatic (glacial deposits) pieces of evidence, he successfully reconstructed the paleo-position of continents (composed of *sial*), believed to float and freely drift over the plastic phase *sima* composing Earth's oceanic sections and upper mantle (Fig. 1.8, Wegener (1924)). However, his theory was first rejected by the scientific community. Indeed, he had invoked tidal forces as the mechanism leading to the lateral motion of continents, although this force is 10^{14} times too small than required to move landmasses (Jeffreys, 1923). Subsequent potential causes for continental drift involved precession of the equinoxes, attraction between continents, departure from isostatic equilibrium or from hydrostatic pressure in the crust, attraction towards the equator, condensation due to readjustments of material inside Earth, thermal contractions and expansions, and convection (Holmes, 1931).

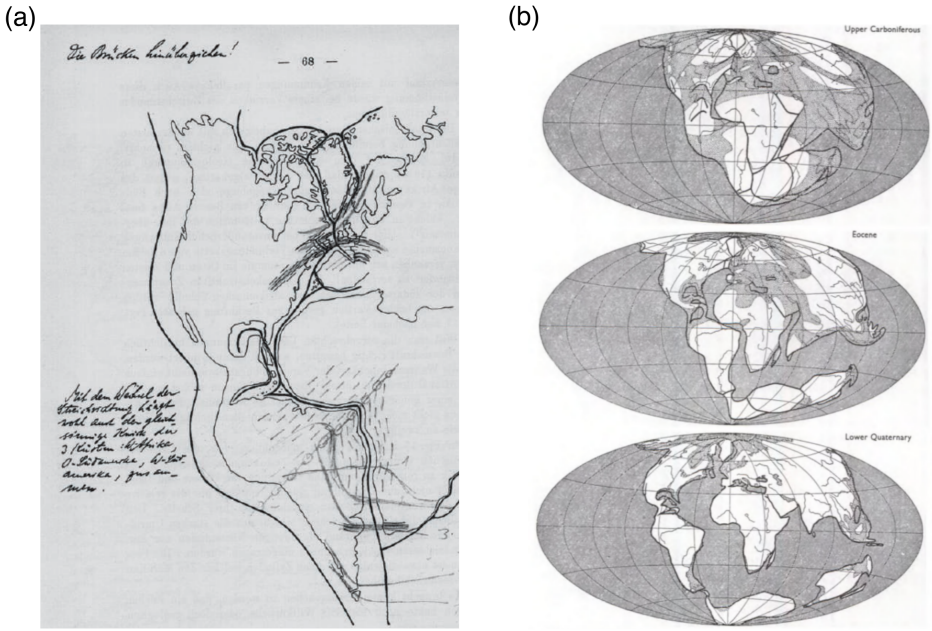


Figure 1.8: (a) Reproduction of Wegener's own copy of the 1915 monograph, showing the merging between Africa and South-Africa (Romano and Cifelli, 2015). At the top, Wegener writes *'Pull over the bridges!"*, a reference to earlier suggestions of sunken intercontinental bridges (Suess, 1904-1924). (b) Reconstruction of the paleo-position of continents, as thought by Wegener (1924). Dark grey areas represent oceans, light grey areas denote shallow seas, emerged areas are in white. Black lines outline present-day coastlines, and are present for identification purposes.

The development of paleomagnetism and structural geology in the 1950's nevertheless advocated for the mobility of continents. It was only in the mid-sixties, that Wegener's theory was definitely

accepted, notably thanks to accumulating evidence of continental motions and the works of A. Holmes and E. Argand, who advocated for mantle convection as the driver for lateral motions of continents (Fig. 1.9, *e.g.* Holmes (1931)). Dewey and Bird (1970) contributed to demonstrate that continental drift provides a powerful and unifying explanation for a diversity of geological observations, such as mountain ranges.

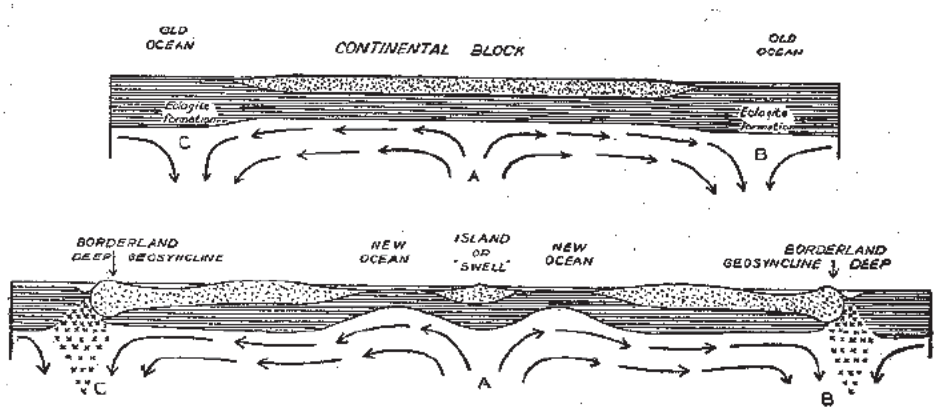


Figure 1.9: Sketch showing how mantle convection leads to surface/mantle coupling leading to supercontinent breakup: (top) mantle upwellings are localized below continental crust (dotted areas) whereas downwellings are at continental margins. The dashed area represents the "intermediate layer" composed of diorite, gabbros, amphibolites and granulites. (bottom) Ultimately, the supercontinent breaks apart and a new ocean is formed above the upwelling region. On the old margins of continents, downwellings occur in areas of eclogite formation (crosses) (Holmes, 1931).

Towards the theory of plate tectonics

One of the major observations leading to the acceptance of the plate tectonics theory by the scientific community came from submarine campaigns of seafloor mapping thanks to sonar, developed during World War II. In 1950, H. Hess proposed that continents are not drifting over the *sima*, but are passively entrained by the expansion of the seafloor from mid-ocean ridges, based on observations that the seafloor is not smooth, but full of seamounts, canyons and trenches (Fig. 1.10(a), Hess, 1962). This explanation was further explored by F. Vine and D. Matthews who observed that the magnetic profile of the seafloor is symmetric about mid-ocean ridges axes (Vine and Matthews, 1963). Earthquakes at subduction zones following Wadatchi-Benioff planes in the mantle were soon interpreted as evidence for lithosphere returning to the mantle in those regions by Isacks et al. (1968) (Fig. 1.10(b)).

In 1967, J. Morgan synthesized paleomagnetic, topographic and seismologic arguments into the plate tectonics theory (Fig. 1.11(a), Morgan, 1968). Plates were therefore considered as lithospheric

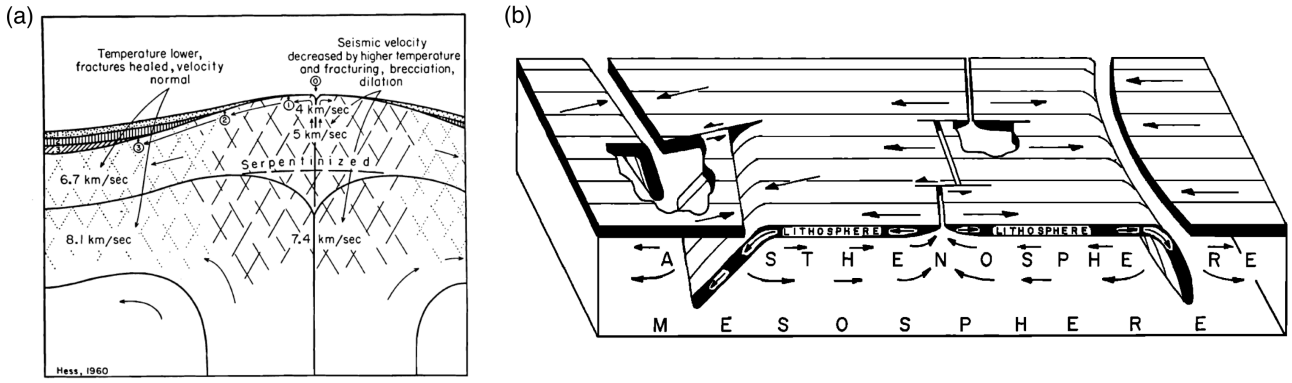


Figure 1.10: (a) Diagram representing (1) apparent progressive overlap of ocean sediments on a mid-ocean ridge which would actually be the effect of the mantle moving laterally away from ridge crest, and (2) the postulated fracturing where convective flow changes direction from vertical to horizontal (Hess, 1962).(b) Diagram showing the key role of high-strengh lithosphere on the motions of mantle and plates (Isacks et al., 1968). In this model, asthenospheric flow represents the compensation flow in response to downward motions of negatively buoyant slabs.

rigid blocks with deformations occurring only at their boundaries, and moving relatively to each other due to Euler rotations. Plate boundaries and velocities have been constantly refined since then, notably by incorporating new seismic data and GPS measurements of plate velocities. From the initial classification of plate boundaries into three types (convergent, divergent and transform boundaries), new models of present-day plate tectonics now incorporate more complexity, such as areas of diffuse deformation (Fig. 1.11(b), Gordon (1998), Zatman et al. (2005)). It is now a kinematic theory explaining various surface observations, but it does not account for the causes of such motions, although there is a consensus in the community that plate tectonic motions are linked to mantle convection.

Towards the building of plate tectonic reconstructions

In the 1960's, using the reasoning that Earth has always had a dipolar magnetic field and that the magnetic poles have always been close to Earth's rotation poles, K. Runcorn measured apparent polar wanders recorded from continental rocks and used them as a tool to reconstruct the paleo-position of continents (Runcorn, 1959). After observations of aligned Hawaiian seamounts by Hess (1946), and the proposal of Wilson (1963) that they are linked to fixed mantle plumes, Morgan (1971) proposed to use them as a reference frame to reconstruct past plate tectonic motions. From the geometry of oceanic fracture zones, seafloor magnetic anomalies, apparent polar wander, or hotspot tracks,

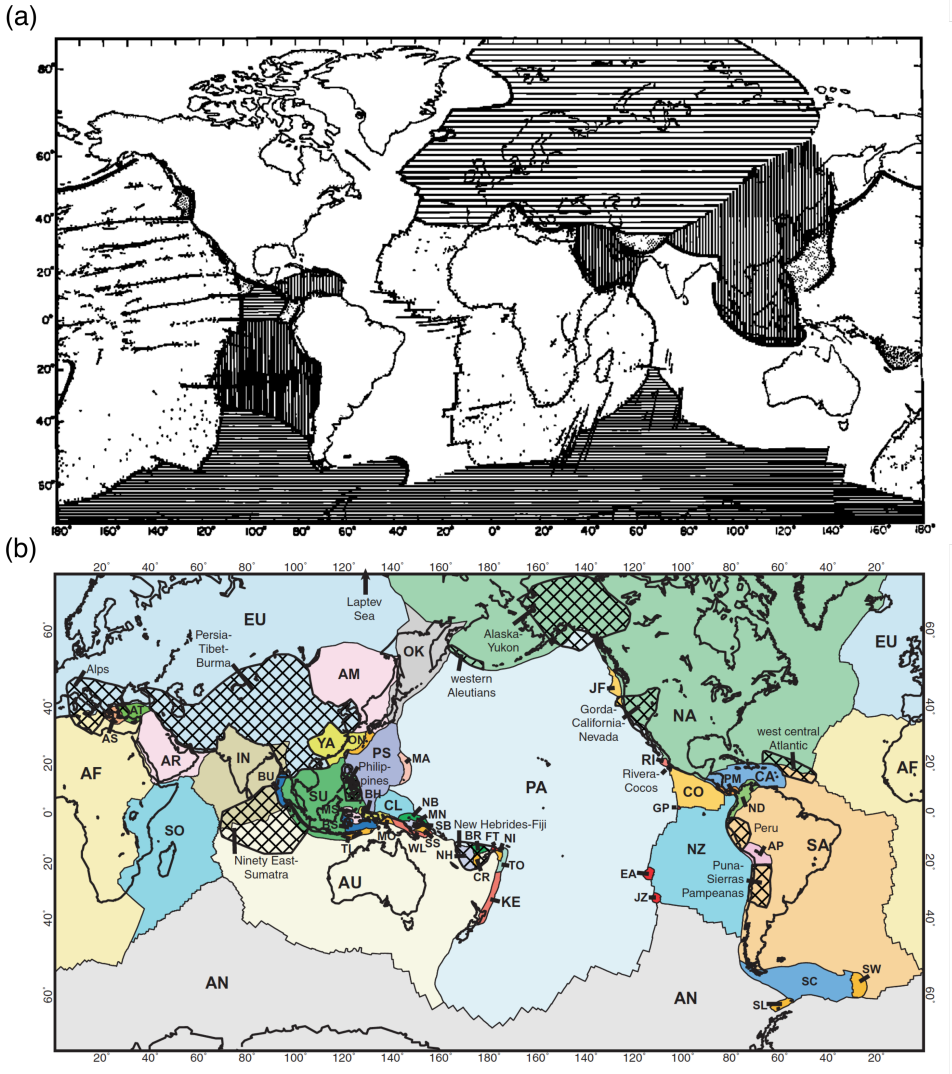


Figure 1.11: (a) Tectonic "blocks" in 1968 (Morgan, 1968). (b) 52 tectonic plates in 2003 (Bird, 2003). Dashed areas represent diffuse boundaries.

scenarios for kinematically constrained plate reconstructions were refined (*e.g.* Dewey and Bird, 1970) and compared with paleo-geographic considerations (*e.g.* Parish et al., 1982).

Even if the plate tectonics theory had been first developed independently from the physical forces which cause plates to move, it soon appeared necessary to understand the dynamics of mantle convection in order to properly interpret surface observations and reconstruct their past motions. Moreover, the question of the driving forces has motivated research on both lithosphere and mantle motions in order to understand which of these two layers exerts the strongest control on the observed dynamics. I now show how scientists progressively considered the surface dynamics as an integrated part of mantle convection.

First models of mantle-lithosphere interactions

From the 1930's, the necessity of combining observations and numerical or experimental models to understand the physics of mantle/surface dynamics kept increasing. In 1935, C. Pekeris was the first to develop an analytical model of mantle convection in order to study the effects of mantle convective scales on stresses and topography at the surface (Pekeris, 1935). He predicted that Earth's lithosphere can be substantially deflected by rising and sinking anomalies, which was later confirmed by geological observations (*e.g.* Mitrovica et al., 1989). In 1939, D. Griggs experimentally modeled convective cells in the asthenosphere to show the potential role of mantle convection on the building of mountain ranges (Fig. 1.12, (Griggs, 1939)).

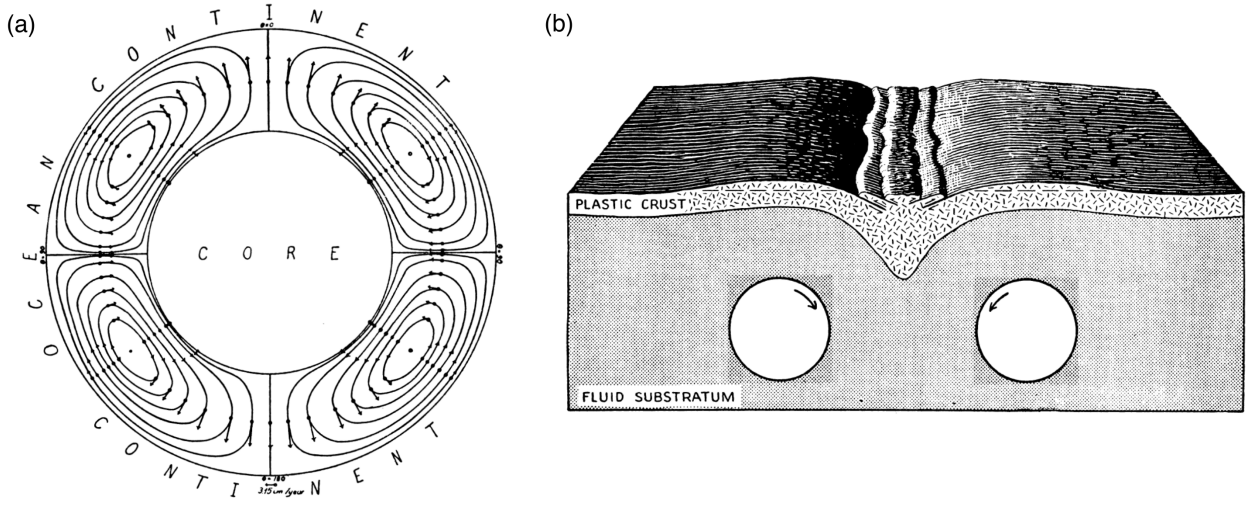


Figure 1.12: (a) Analytical model of mantle convection of Pekeris (1935) and (b) analogical model for the building of mountains of Griggs (1939)

The thermal state of Earth's mantle, indicative of convection

In parallel to the development of those models, the quantitative study of the thermal state of the mantle and its sources of energy contributed to the further characterization of mantle convection and led to appreciate plate tectonics as the upper thermal boundary layer of mantle convection.

Internal heating by radioactivity

After the discovery of radioactive elements inside the continental crust and the mantle, scientists questioned the calculations of Lord Kelvin who had found that Earth's age was 40-200 Ma, based on the

idea that Earth had cooled entirely by conduction. However, the presence of radioactivity inside rocks was first considered as an obstacle to the idea of mantle convection since radioactivity was believed as more concentrated near the surface, therefore heating the top of the mantle and creating stable thermal and density contrasts. Holmes (1931) nevertheless rehabilitated the idea of mantle convection by stating that such a process was necessary to efficiently evacuate heat produced by internal heating due to radioactive elements in the mantle. He therefore proposed a model of convective cells causing continental drift at a rate of about 5 cm·yr $^{-1}$ and capable of explaining petrological and topographic observations (Fig. 1.13 and 1.9). It is now known that internal radioactive heating can lead to different modes of convection (Weinstein and Olson, 1990). Indeed, while fluids heated from below generate both active upwellings and downwellings in an equal proportion (also called Rayleigh-Taylor instabilities), mixed heating generates active downwellings while upwellings are more infrequent and rather passive (Weinstein and Olson, 1990, McKenzie et al., 1974).

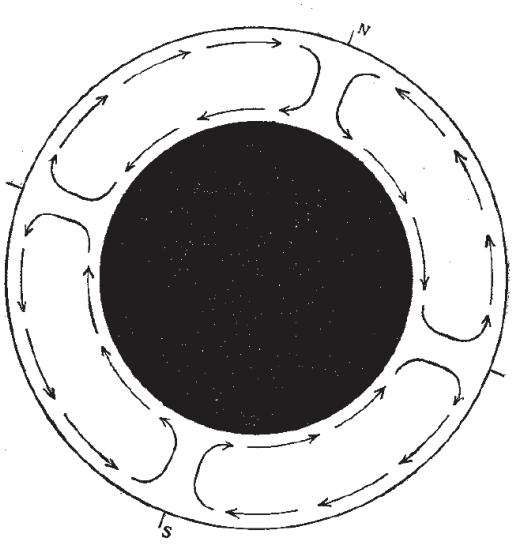


Figure 1.13: Schematic view of mantle convective cells, as presented by Holmes (1931). Upwellings were supposed to occur at the equator since the mantle is thicker there (because of Earth's viscous bulge caused by its rotation) and more radioactive elements are present.

Surface heat flow

A critical surface observation of mantle convection is the outgoing heat flux from the mantle. Measuring the spatial distribution of heat flow at the surface of Earth can indeed give insight on the source of mantle motions and the modality of convection. On continents, heat flow was first estimated from the temperature inside drilling holes. Then, conductometers were developed and led

to maps of heat flow distribution at the surface of Earth (Pollack et al. (1993) and Davies and Davies (2010), Fig. 1.14).

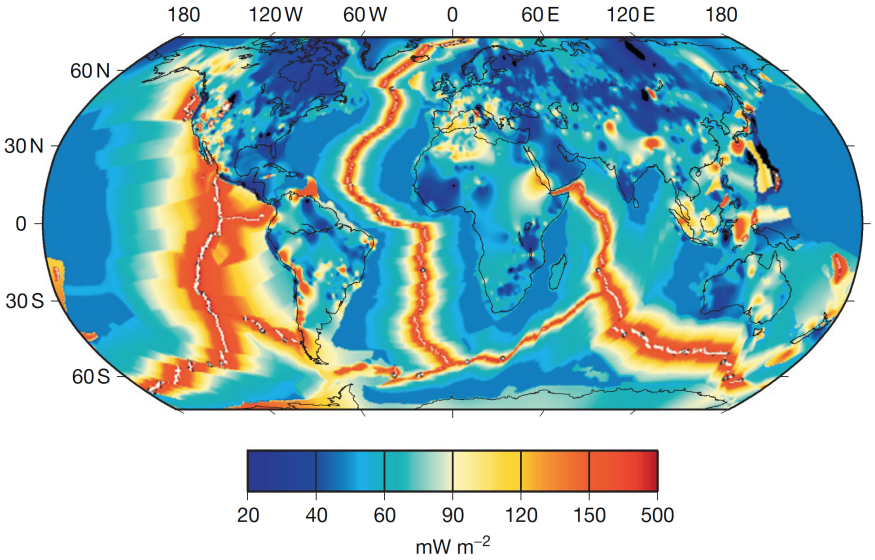


Figure 1.14: Global heat flow of Earth, combining heat flux measurements on land and on continental margins with a thermal model for the cooling of the oceanic lithosphere (Jaupart and Mareschal, 2015)

In oceans, a simple thermal model of boundary conductive cooling (the half-space cooling model) can account for the observed reduced heat flow corresponding to ageing oceanic lithosphere (Fig. 1.11, 1.14, *e.g.* Sclater et al., 1980). In this model, it is assumed that the plate moves as a unit, that the surface thermal condition is 0°C while the base of the lithosphere corresponds to the isotherm $T_M = 1,300$°C, and that heat is transported by conduction. The time-dependent temperature profile is obtained by solving the instant cooling problem: material at the temperature T_M is brought instantaneously to the surface (Turcotte and Oxburgh, 1967). Therefore, temperature depends on the age of lithosphere as follows:

$$T(z,\tau) = T_M \mathrm{erf}\left(\frac{z}{2\sqrt{\kappa\tau}}\right) = \frac{2T_M}{\sqrt{\pi}} \int_0^{z/2\sqrt{\kappa\tau}} \exp(-z'^2)\mathrm{d}z' \tag{1.5}$$

with T the temperature, z the depth, τ the age of the lithosphere, T_M the axial ridge temperature and erf the error function (Jaupart and Mareschal, 2015). The surface heat flux also varies with the age of the lithosphere as:

$$q(0,\tau) = \frac{kT_M}{\sqrt{\pi\kappa\tau}} = C_Q \tau^{-1/2} \tag{1.6}$$

where C_Q is a constant, and k the thermal conductivity. This model proves to be in broad agreement with measurements of heat flow at oceanic seafloor for ages comprised between $\sim$ 1 Ma and 100 Ma

(Fig. 1.15(a)). Another model, the plate-cooling model (McKenzie, 1967), considers the cooling of a layer with finite thickness, instead of defining the base of the lithosphere by an isotherm. Reasons for the oceanic heat flow to deviate from prediction for younger and older ages are detailed in section 1.2.1.2.

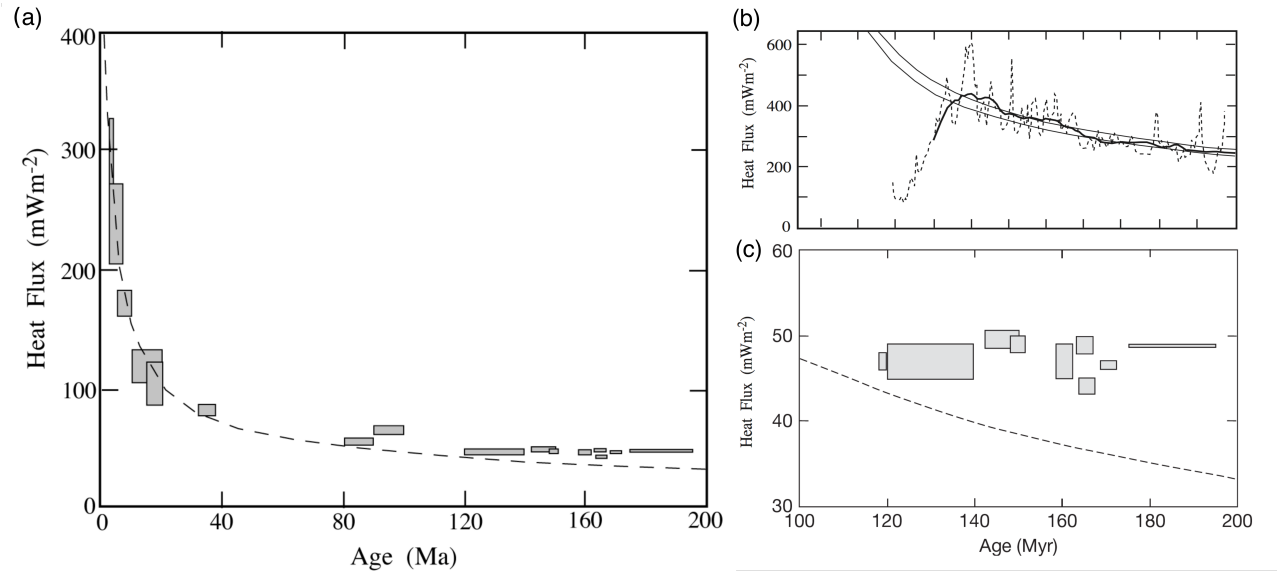


Figure 1.15: (a) Ocean-averaged seafloor heat flux data measurements as a function of the age of lithosphere. The dashed line corresponds to a half-space cooling model (Jaupart and Mareschal, 2015). (b) High-resolution heat flux profile near Juan de Fuca Ridge. The two dashed lines correspond to predictions of the half-space cooling model with different C_Q (Davies, 2001). (c) Heat flux data and prediction of the half-space cooling model for ages larger than 100 Ma (Lister et al., 1990).

On first order, oceanic lithosphere evacuates heat by conduction and would therefore represent the upper mantle thermal boundary layer of convection (TBL). Mantle plumes and subduction zones can thus be considered as TBL instabilities.

However, on continents, the pattern of surface heat flow is more complex than in oceans (Fig. 1.14). The heat flow is about 40 mW·m^{-2} and mainly results from continental crust radioactivity (only 15 mW·m^{-2} result from mantle flow). Therefore, continents are considered as insulators (Jaupart et al., 1998). As a consequence, mantle convection is likely to be disturbed since lateral complex flow can develop below continents (*e.g.* Rossby, 1965, Elder, 1967, Whitehead, 1972, Whitehead Jr, 1976, Guillou and Jaupart, 1995). The size and distribution of continents at the surface of Earth strongly modify mantle convection planform (*e.g.* Coltice et al., 2007, Zhong et al., 2007). Upwellings would preferentially take place below continents while subduction zones would tend to distribute on their

sides.

Mantle geotherm

Temperature measurements from drillings and studies of metamorphic gradients further showed that Earth's lithosphere corresponds to the upper thermal boundary layer of mantle convection, having a steep average gradient of 30 K·km^{-1}. The thermal base of the lithosphere is represented by the 1,600 K isotherm, which corresponds to both the inflection of the geotherm and mechanical changes in the deformation regime of rocks.

In the mantle, constraints on the temperature of material come from combined seismology and mineralogy studies which allowed to define temperature anchorage points. Geothermobarometry is used to constrain the pressure and temperature of origin of a large number of olivine-rich peridotite xenoliths brought to the surface by kimberlite of hotspot volcanoes. For example, this allows to constrain sub-continental temperature to about 700 K at 70 km depth. Moreover, the existence of seismic discontinuities in the mantle (such as in the transition zone, 410-670 km depth) is explained by the presence of phase transitions. High-pressure/high-temperature experiments carried out on olivine showed the transition from olivine-α to wadsleyite (olivine-β) at 410 km depth, ringwoodite (olivine-γ) at 520 km depth, and bridgmanite (or perovskite) at 660 km, which correspond to sharp seismic discontinuities at those depths. From these experiments, the temperature at the transition zone is about 1,900 K. Finally, the temperature at the base of the mantle can be constrained by the perovskite-post-perovskite phase transition (Hernlund et al., 2005) or extrapolations of external core temperatures (which is constrained by estimates of iron crystallization at the internal-external core boundary). In addition to those anchorage points, considerations on the thermal profile of convective cells made it possible to define the temperature gradient in the mantle as adiabatic and being $\sim$0.3 K·km^{-1} (Schubert et al., 2001). However, several numerical models have suggested that the presence of internal heating leads to sub-adiabaticity in Earth's mantle, by promoting a slower increase of temperature with depth (*e.g.* McKenzie et al., 1974, Sotin and Labrosse, 1999, Bunge et al., 2001, Bunge, 2005, Zhong, 2006), although they disagree on the slope of the sub-adiabatic gradient. The existence of sub-adiabaticity in Earth's mantle can affect our interpretations of compositional anomalies (Mattern et al., 2005), our estimates of core heat flow (Bunge, 2005) and of Earth's energy budget (Davies, 2007).

Thanks to joint efforts in both physics and geology, we can now view Earth's surface oceanic lithosphere as the upper thermal boundary layer of complex mantle convection from a physics perspective. By its nature, Earth's surface tectonics is therefore entirely coupled with mantle's dynamics. For example, conclusions about Earth's topography, the formation or the breakup of continents or reconstructions based on hotspot tracks highly depend on our knowledge of mantle scales of convection and mantle plume and subduction zones' behaviour. Since plumes and subduction zones are the most prominent features of mantle convection, I now focus on their influence on lithosphere dynamics and I show which surface observations can witness mantle dynamics specificities.

1.2 The multiple interactions between mantle instabilities and the surface

In this section, I review the major actions of mantle convective instabilities on surface dynamics, with an emphasis on the specificities of Earth's internal dynamics compared to more simple convective systems.

1.2.1 Subduction zones: cold anomalies sinking in the mantle

Subduction zones are one of the major components of Earth plate tectonics and mantle convection, since, as seen in section 1.2.1.3, they are one of the main contributions to plate motion. They also represent the most available source of observations of the dynamics of Earth's mantle instabilities. Therefore, in this section, I review some of these observations, and show how our current knowledge of the dynamics of subduction zones draws a much more complex image of those instabilities than classical Rayleigh-Taylor instabilities.

1.2.1.1 Characteristics of subduction zones

Subduction zones correspond to areas of intra-oceanic (*e.g.* the Philippines arc) or oceanic-continental (the Andine subduction zone) plate convergence. Their total length is approximately 51,000 km (Bird, 2003). The prominent surface characteristic of subduction zones is their asymmetric topography. The subducting plate consists of a viscous fore-bulge caused by the bending of the plate in the mantle and it connects to the overriding plate through a deep trench that can reach 11 km depth (the Marianas

trench). Intra-oceanic subduction zones are characterized by an island-arc (*e.g.* the Marianas arc) with an intense seismic and volcanic activity and a back-arc basin corresponding to extensive stresses due to subduction trench retreat and to the viscous coupling of the overriding plate with sinking mantle material entrained with the slab (Fig. 1.16, *e.g* Zhong and Gurnis (1994)). In the case of an oceanic-continental subduction, the overriding plate is characterized by a high mountain range built due to compressive stresses, with a high volcanic and seismic activity (*e.g.* the Andes). Extensive stresses can nevertheless be present in the arc, (*e.g.* the southwestern Mexico mountain range which results from flat-slab subduction (Gérault et al., 2015)).

The sinking material is responsible for a large amount of seismic activity, caused by lock-release stress cycles along the top of the subducting plate and down to the transition zone, therefore defining the Benioff plane (Isacks et al., 1968), which can be used to define a subduction dip-angle. The volcanic activity corresponds to the melting of the mantle wedge due to the dehydration of the subducted crust at about 100 km depth. Island-arc volcanic products geochemically define the calco-alcaline series, corresponding to highly crust-contaminated magmas which underwent metasomatism. The shape of the subducting material can be classically imaged through seismic tomography (which consists in the mapping of anomalous seismic velocities relatively to a radial seismic profile of reference like PREM or IASP91). More recently, the use of gravitational gradients measured from the GOCE satellite mission allowed the detection of slab geometries down to mid-mantle depths, and complemented seismic tomographic studies (Panet et al., 2014). The geometry of subduction zones is complex: dip-angles vary from near-zero (for flat-slabs, such as in some areas below the Andes), to nearly 90° in the Marianas trench, some of them stagnate at the mantle transition zone (*e.g.* the Aleutian slab), or in the lower mantle (*e.g.* the Tonga of the Java slab), or descend throughout the mantle without being affected by mantle phase transitions (*e.g.* the Marianas slab or the Cocos slab, Goes et al., 2017). Slab sinking rate is thought to be several centimeters per year, the same order as surface plate velocities. A simple calculation of the gravitational effect of negative buoyancy on the sinking rate of the material leads to values of about 10 cm·yr^{-1} in the upper mantle (Turcotte and Oxburgh, 1967, Forsyth and Uyeda, 1975, King, 2007a). Ricard et al. (1993) required a factor 3-4 velocity decrease at the transition zone to account for predictions of mantle's viscosity jump and to reproduce surface plate velocities while Van Der Meer et al. (2010) required an average lower-mantle vertical sinking rate of 1.2 ± 0.3 cm·yr^{-1} in order to explain the positions and depths of subduction zones during

the last 300 Ma (using tomography and tectonic reconstructions), consistent with estimates of slab sinking rates derived from plate reconstructions (Butterworth et al., 2014). Some authors also propose temporal variations of slab sinking rates, due to the alternation of slab stagnation and accumulation at the transition zone followed by avalanche events in the lower mantle (*e.g.* Tackley et al., 1993, Solheim and Peltier, 1994, Honda et al., 1993, Schellart and Spakman, 2012).

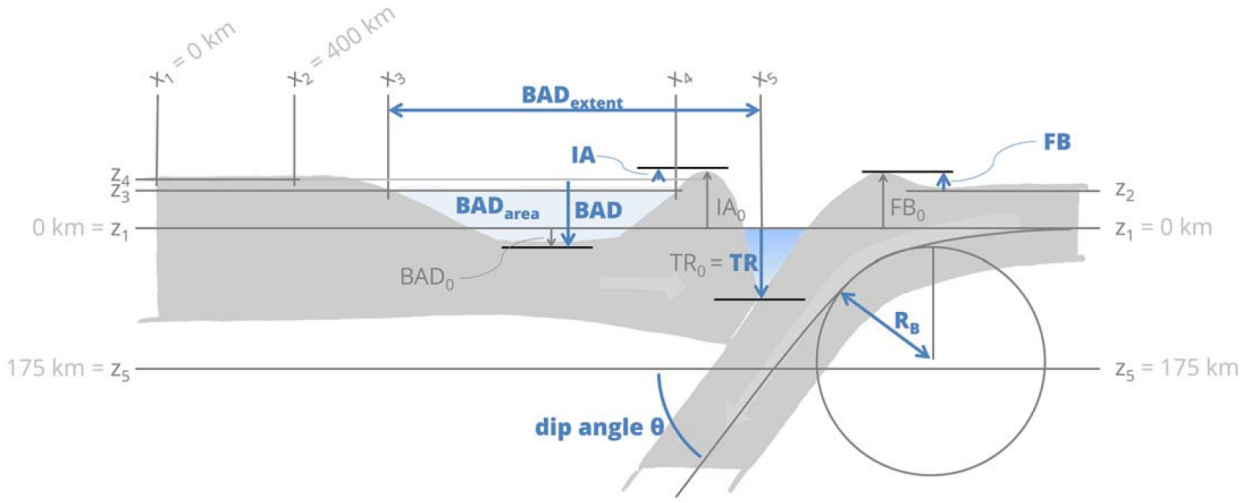


Figure 1.16: Topographic characteristics of an intra-oceanic subduction zone (Crameri et al., 2017). The subducting plate topography (right) is characterized by a viscous fore-bulge (FB) and a subduction trench (TR). The overriding plate topography is composed of an island-arc (IA) and a back-arc depression (BAD). The subducting lithosphere is characterized by a dip-angle θ and a plate bending radius (R_B).

1.2.1.2 The initiation of subduction zones

Since the 1970's and the discovery of subduction zones (Isacks et al., 1968), the problem of their initiation has remained controversial, although there is a consensus about the negatively buoyant nature of those sinking mantle instabilities (Stern and Gerya, 2017). As shown by the correspondance between oceanic heat flow and the plate-cooling model for intermediate oceanic plate ages (Fig. 1.15(a)), Earth's lithosphere can be considered as the upper TBL of mantle convection, and subductions should correspond to Rayleigh-Taylor instabilities tweaked by the specific rheology of lithosphere. However, for young oceanic lithosphere ages, significant hydrothermal convection in the oceanic crust leads to more efficient cooling than predicted by the half-space cooling model (Fig. 1.15(b)). According to this model, when the oceanic lithosphere ages, it cools down as a function of the age and becomes thicker. When the lithosphere thickness ($\rho_{lith_m} = 3.3\ 10^3$ kg·m^{-3}) reaches about 9 times the crust

thickness (ρ_{lith_c} = 2.9 10^3 kg·m^{-3}), plate density becomes higher than the asthenospheric mantle (ρ_{asth} = 3.2 10^3 kg·m^{-3}) and starts to sink. For a typical oceanic crust of 7 km, this would imply that subduction always starts at about 100 Ma. Although the elastic behaviour of lithospheric plates (McKenzie, 1977) and the compressive stress field (Mueller and Phillips, 1991) tend to prevent them from sinking, metamorphic phase transitions of the subducting material (eclogitization) increase their negative buoyancy and maintain active subductions.

Measurements of oceanic seafloor ages indicate that subduction exists at all lithospheric ages (*e.g.* Müller et al., 1997, Sclater et al., 1980), in contradiction with the idea of the sinking of only negatively buoyant seafloor (*see* section 1.1.2.2). Indeed, the seafloor age-area distribution follows a linear relationship (with a so-called triangular shape, Fig. 1.17) (Sclater et al., 1980, Rowley, 2002, Cogné and Humler, 2004):

$$\frac{\mathrm{d}A}{\mathrm{d}\tau} = C_A(1 - \tau/\tau_m) \tag{1.7}$$

where $A(\tau)$ represents the proportion of seafloor younger than age τ, C_A is the rate of production of new seafloor (about 3 km^2 yr^{-1} for present-day), and τ_m is the maximal age of the seafloor (180 Ma). This area-age relationship may have varied through time (*e.g.* Becker et al., 2009), as a consequence of variations in seafloor spreading rates.

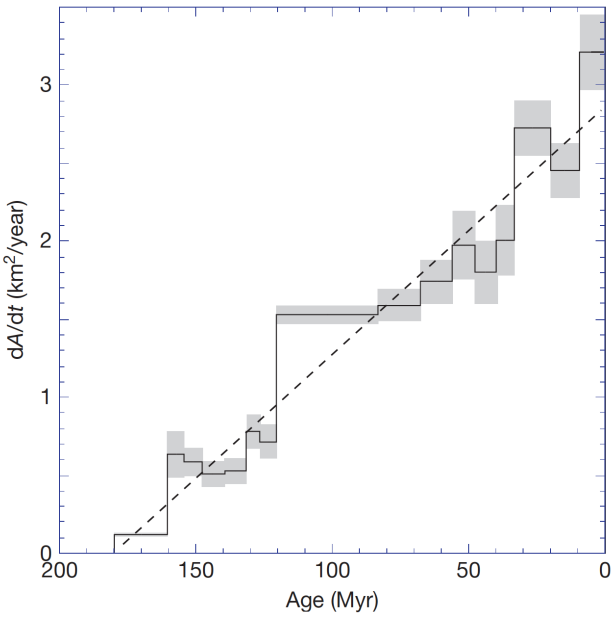


Figure 1.17: Distribution of seafloor ages. The dashed line is the best-fit linear function (Cogné and Humler, 2004).

The fact that oceanic lithosphere older than 100 Ma can still be present at the surface of Earth (*e.g.* in the western Pacific) is compatible with the departure of oceanic heat-flux measurements from the half-space cooling model (Fig. 1.15(c)). For such ages, oceanic lithosphere does not thicken anymore, and remains buoyant enough to be stable. Reasons invoked for a sustained heat flux at old oceanic lithospheres are the presence of small-scale convection (*e.g.* Parsons and McKenzie, 1978, Stein and Stein, 1992, McKenzie, 1967, Solomatov, 2004), thermal rejuvenation of oceanic seafloor by mantle plumes (*e.g.* Smith and Sandwell, 1997, Korenaga and Korenaga, 2008, Davies, 1988a,b), or radioactive heat production in the mantle (Jarvis and Peltier, 1982). Lithospheric rheology also plays an important role in initiating subduction zones, since its visco-elastic properties act as a resisting force against subduction. Numerical models have shown that ridge-push forces can drive slab initiation in the case of preexistence of weak zones (Toth and Gurnis, 1998, Doin and Henry, 2001). After the slab reaches a length of 150 km, subduction becomes self-sustained (Gurnis et al., 2004).

Subduction of young seafloor (*e.g.* the Nazca ridge, subducting below the South-American plate) appears contradictory with the positive buoyancy of young oceanic lithosphere in those regions. Negative buoyancy is therefore not the only source for subduction initiation. Various concepts have thus been developed to explain initiation of subduction zones in the context of modern plate-tectonics (Gurnis et al., 2004) or to initiate plate tectonics on early-Earth (Rey et al., 2014). Those mechanisms can be classified into *induced* and *spontaneous* initiations of subductions (Stern, 2004, Stern and Gerya, 2017). *Spontaneous* subduction initiations correspond to forces originating at the initation location and comprise passive margin collapse, transform collapse and plume head margin collapse, while *induced* initiations correspond to transference or polarity reversals (Fig. 1.18).

Other mechanisms imply the effect of the presence of continents, whose formation can be responsible for kick-starting the plate tectonics regime (Rey et al., 2014), and whose configuration is likely to affect the area-age distribution of the seafloor (Coltice et al., 2012). Mantle flow reorganizations are also likely to quickly generate new plates (Mallard et al., 2016). Rheological heterogeneities in the lithosphere can also cause the plates to weaken enough to start to sink. However, if the weak zone is too large, double-sided subduction takes place (Gerya et al., 2008). The presence of narrow weak zones can be explained by hydrothermal circulation through preexisting fractures (Gerya et al., 2008, Dymkova and Gerya, 2013), shear heating (Thielmann and Kaus, 2012), grainsize reduction (Bercovici,

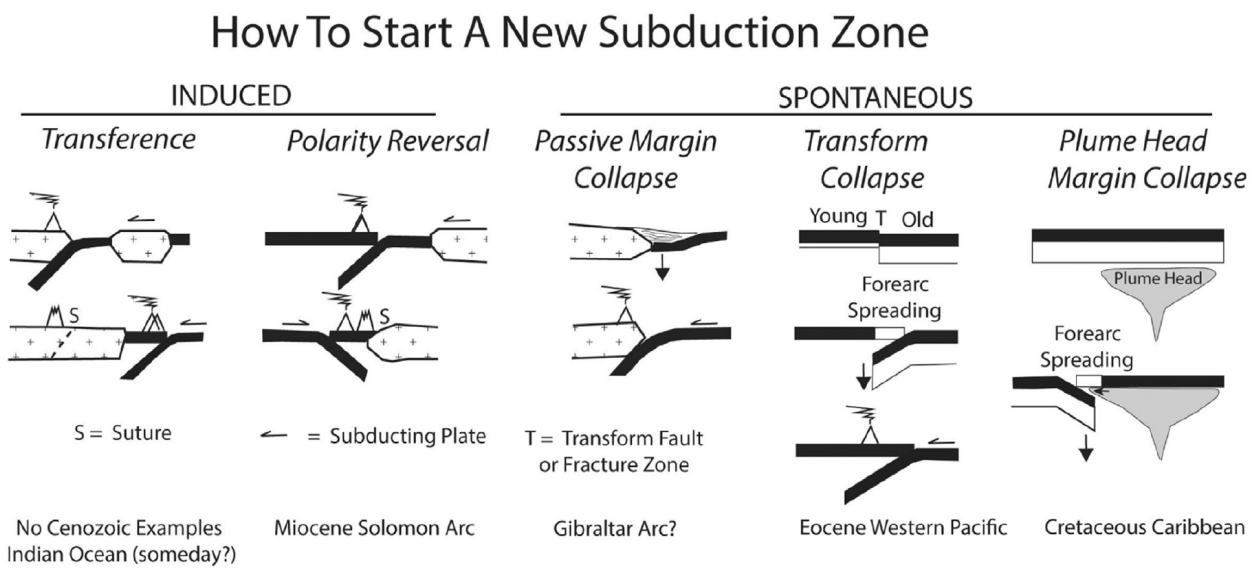


Figure 1.18: Classification and examples of initiation mechanisms of subduction zones (Stern and Gerya, 2017).

2003) or seismic weakening (Van Dinther et al., 2013). As a consequence, understanding the ambient stress field, force balance and distribution of lithospheric rheological weaknesses is needed to better understand the initiation of new subduction zones.

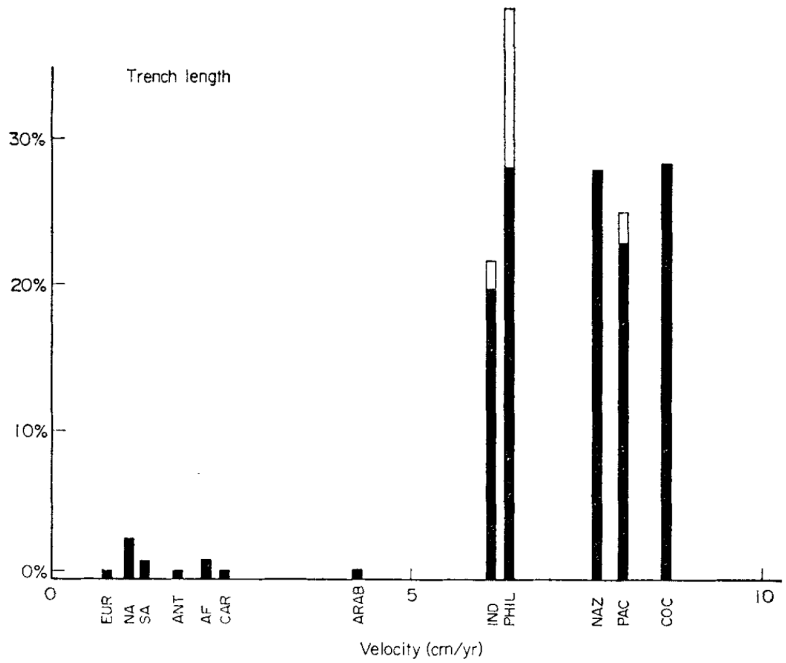


Figure 1.19: Percentage of circumference of plate connected to downgoing slabs. Open bars are total length, filled bars correspond to effective length, which is defined as the length of the boundary capable of exerting a net driving or resisting force (Forsyth and Uyeda, 1975).

1.2.1.3 Subduction driving forces

Subduction zones are necessary to sustain the plate tectonics regime. In this section, I show how those sinking mantle instabilities exert control on the surface plate behaviour.

Since the development of plate tectonics, the active role of subduction zones has been invoked as the main driver for lateral motions of the surface (*e.g.* Isacks et al., 1968). A striking observation of this coupling is the remarkable relationship between plate velocities and corresponding subduction length (Fig. 1.19). However, the respective roles of sinking lithospheric stress transmission to the surface (*slab pull*, Elsasser, 1969) and stress induced by viscously entrained mantle (*slab suction*, Turcotte and Oxburgh, 1967) on plate tectonic motions have long been debated (*e.g.* Conrad and Lithgow-Bertelloni, 2002). The slab pull force depends on its dip-angle, its length, its relative excess density relative to the ambient mantle (related to its age) and its rate of subduction (McKenzie, 1969). It corresponds to the energy transmitted to the plate by the sinking slab, and can be written:

$$F_{SP} = M_e g \tag{1.8}$$

where M_e is the excess mass of the slab. Forsyth and Uyeda (1975) considered it as the main driving force of plate tectonics, whereas other authors state that the viscous drag force opposing slab sinking almost compensates entirely its negative buoyancy (Sandiford et al., 1995). It can be of the order of 1.9×10^{21} N in total for all upper-mantle slabs, while slab-suction force which depends on the viscosity structure of the mantle can be of the order of 1.6×10^{21} N (Conrad and Lithgow-Bertelloni, 2002) for all upper and lower mantle slabs, and therefore comparable to the slab-pull force. By computing separately the effect of slab pull and slab suction on present-day plate velocities, Conrad and Lithgow-Bertelloni (2002) showed that slab-pull alone creates realistic subducting plate velocities but causes the overriding plates to systematically move away from subduction trenches while slab suction would cause unrealistic equally convergent velocities on each side of subduction zones (Fig. 1.20). Conrad and Lithgow-Bertelloni (2004) found that slab-pull accounts for 60 % of the driving force of slabs while slab-suction contributes to 40 % of it. The combination of slab-pull and slab suction in the upper mantle leads to better reproduction of surface velocities. Because viscosity increases by a factor of 30-100 times between the upper and the lower mantle according to geoid studies (*e.g.* Hager, 1984), the pull effect of slabs in the lower mantle is negligible. These conclusions also apply for reconstructions

back to the Mesozoic (Conrad and Lithgow-Bertelloni, 2004).

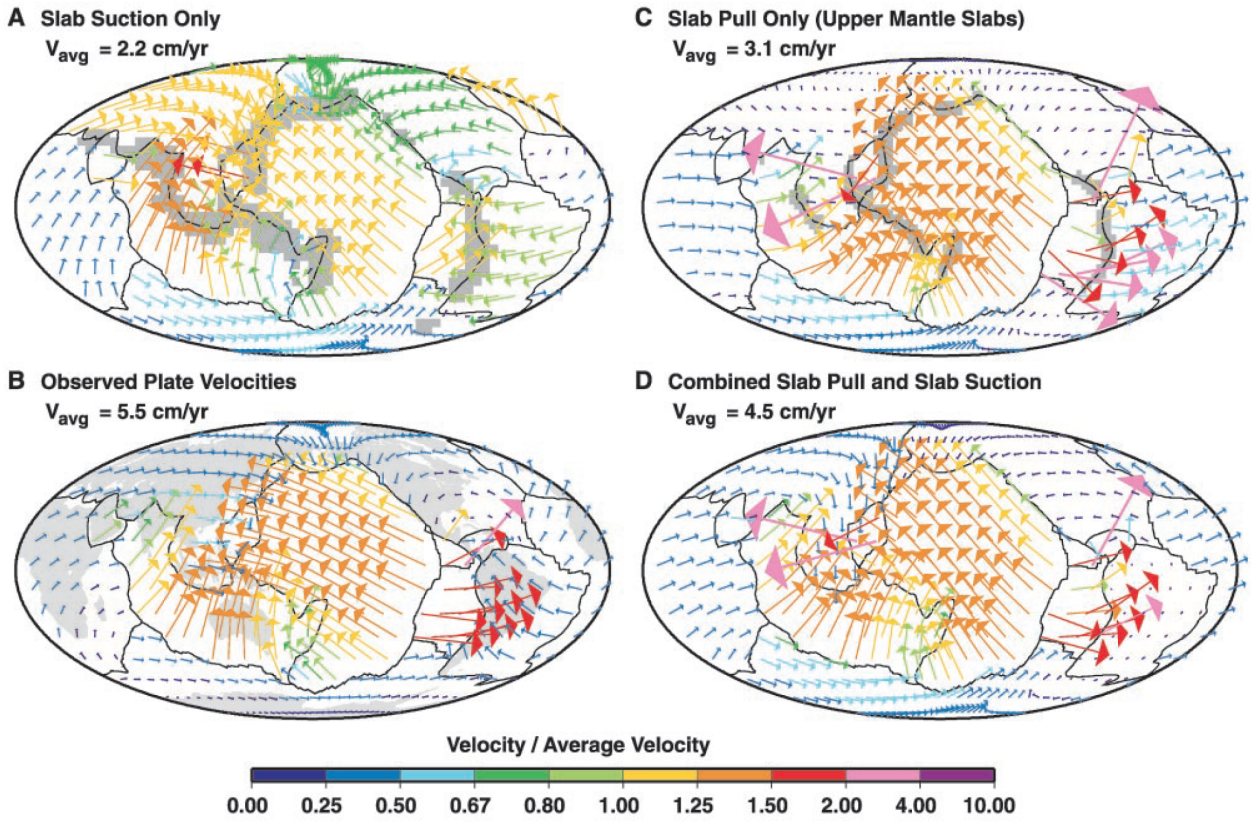


Figure 1.20: Modeled plate velocity fields in the case of applied **(A)** only slab-suction **(C)** only slab-pull and **(D)** slab-pull and slab-suction. **(B)** corresponds to present-day surface plate velocities (Conrad and Lithgow-Bertelloni, 2002).

Therefore, lithospheric slabs are able to generate a non-negligible mantle flow, which can be decomposed into a poloidal (vertical mass transport) and a toroidal (lateral mass transport) flow (O'Connell et al., 1991). This toroidal flow is responsible for trench curvature and migration (Kneller and Van Keken, 2007, Becker et al., 2009), which also depends on the slab width (Royden and Husson, 2006) and strength (Funiciello et al., 2008). The force applied on sinking slab is more likely to generate trench retreat than trench advance, which corresponds to present-day observations and reconstructions (Spence, 1977, Schellart et al., 2008, Williams et al., 2015). This has an impact on large-scale convection, the formation of back-arc basins, island-arc volcanism and seismic anisotropy. More generally, dense sinking material is capable of entraining the mantle by viscous coupling, which can deform the surface, as predicted by Pekeris (1935).

1.2.1.4 Topography and gravity in the vicinity of subduction zones

As mentioned earlier, sinking slabs are responsible for deflecting the surface (Davies, 1981), producing one of the most striking topographic features at the surface of Earth (Fig. 1.21). Understanding topography at subduction zones therefore gives some insight on the dynamics of internal Earth. For example, subduction trench depth is proven to scale with the age of the subducting lithosphere (*e.g.* Zhong and Gurnis, 1992) and the upper plate strain (*e.g.* Lallemand et al., 2005). A low-viscosity mantle wedge is also necessary for producing a shallow back-arc basin (Billen and Gurnis, 2001). The viscous fore-bulge height depends primarily on the dip-angle, the rheology of the subducting plate and its slab-pull force which is responsible for its bending (Crameri et al., 2017).

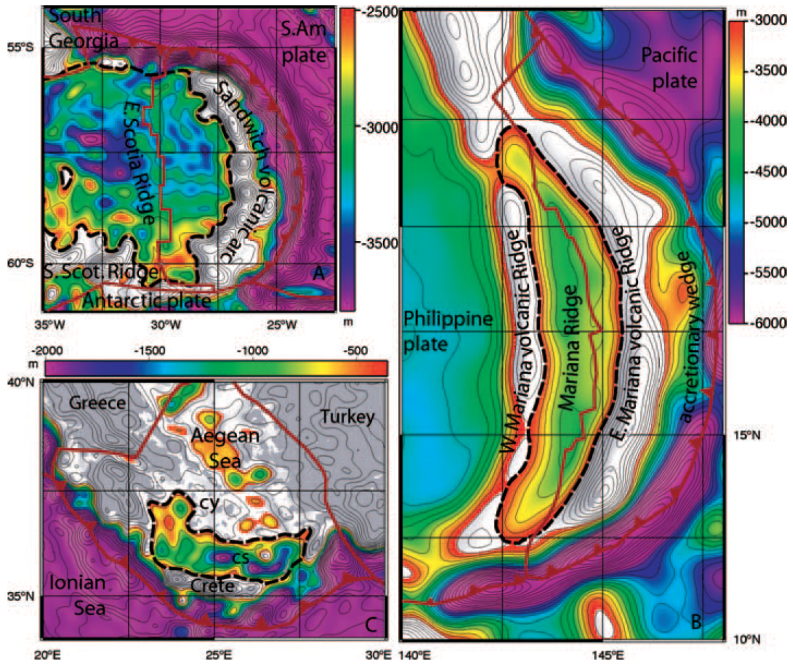


Figure 1.21: Topography of (A) East Scotia, (B) Marianas and (C) Aegean seas (wavelengths > 50 km only), Deflection of topography towards center of basins are contoured with dashed lines. Isocontours are every 350 m (Husson, 2006).

The long-wavelength geoid of Earth (spherical harmonic degrees 4-9) represents its surface of constant gravitational potential corresponding to the mean sea-level. It is positive in most of the convergent regions, such as in the Andes (*e.g.* Runcorn, 1967, Hager, 1984, Hager and Richards, 1989). As seen on Fig. 1.22, the combined effect of the depth and geometry of dense anomalies, their dynamic effect on surface topography (which causes a self-gravitational effect) and the viscosity structure of the mantle result in diverse geoid anomalies in subduction zones areas (Richards and Hager, 1984,

Ricard et al., 1984). Since the resulting geoid anomaly is positive at most downwelling locations, it suggests that Earth's mantle is layered in viscosity (Hager, 1984), and that it increases by a factor of 30-100 between the upper and the lower mantle. This value is consistent with post-glacial studies (Mitrovica, 1996, Mitrovica and Forte, 1997, Lambeck, 1990) and plate velocities study (Ricard and Vigny, 1989, Lithgow-Bertelloni and Richards, 1995). Shorter-wavelength geoid anomalies (spherical harmonic degrees higher than 9) reveal narrow regions ($\sim$ 200 km) of negative anomalies of -20 m coinciding with subduction trenches, while local maxima correlate with back-arc basins (King, 2002). The lateral variations of small-scale gravitational potential around subduction zones are therefore intimately related to their geometry and surface topography.

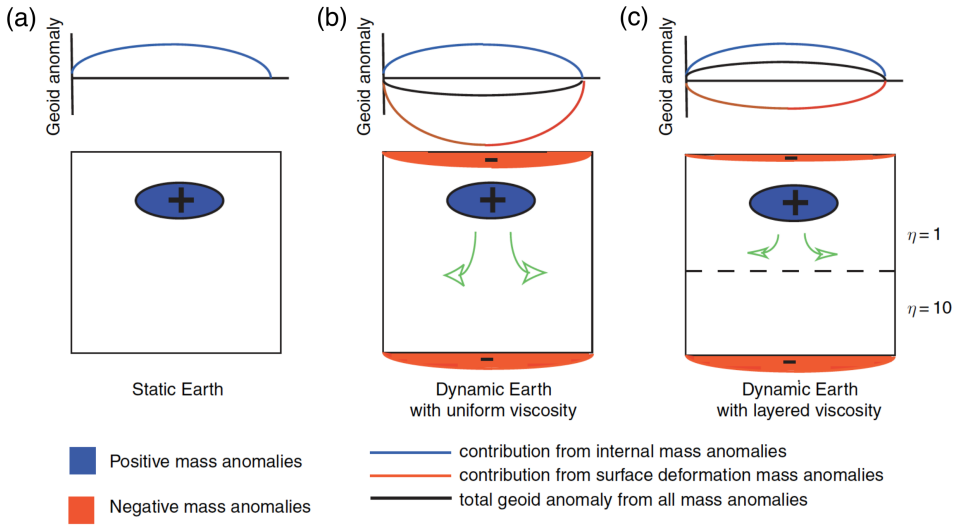


Figure 1.22: Schematic representation of geoid anomalies over a positive mass anomaly in (a) a static mantle, (b) an isoviscous mantle and (c) a layered viscosity mantle. The blue line represents the component of the anomaly due to the internal mass, while the red line is the component of the anomaly due to the surface deformation. The black line is the sum of the components (King, 2007a).

Modeling subduction-induced topography has therefore been one of the major goals of internal geodynamics. By numerically modeling slablets in the mantle, Hager et al. (1985) and Ricard et al. (1993) showed that they could reproduce Earth's geoid lows fairly reasonably, therefore demonstrating the important role of subductions on deflecting Earth's surface. Mitrovica et al. (1989) used this property of sinking slabs in order to explain the presence of the migrating sedimentary depocenter of the Cretaceous Interior Basin of North-America, first described by Weimer (1970) by invoking the eastward deflection of the Farallon slab below the North-American plate, able to tilt and flood the continent. Gurnis (1993b) generalized this behaviour by finding that continents are anomalously

depressed. This effect of moving density anomalies inside the mantle is called dynamic topography (*e.g.* Pekeris, 1935, Hager, 1984, Ricard et al., 1993, Gurnis, 1990, Forte et al., 1993, Flament et al., 2013). Observations of such slab-induced surface deflections of a few hundreds of meters were made by Cazenave et al. (1989) and Davies and Pribac (1993), who calculated the oceanic residual topography after the removal of the sedimentary loading and sea-floor subsidence resulting from plate-cooling from the observed topography signal in oceans. This was compared to present-day dynamic topography by computing instantaneous-flow models of mantle convection from seismic tomography models (*e.g.* Conrad and Gurnis, 2003, Spasojevic and Gurnis, 2012, Steinberger, 2007). From the 1990's, different authors attempted to reconstruct the past locations of large-scale basins induced by sinking anomalies in the mantle (Fig. 1.23). They used plate tectonic reconstructions to constrain the past location of slabs (Ricard et al., 1993, Lithgow-Bertelloni and Silver, 1998, Flament et al., 2013) or backward advected seismic tomographic models (Moucha et al., 2008), in order to relate the resulting large-scale dynamic topography patterns to geological records of past sea-level changes and sedimentation rates on continents.

Nevertheless, the wavelengths and amplitudes of the surface deflection induced by mantle flow linked with sinking slabs are still debated, since dynamic topography is calculated from different models of mantle convection (see Fig. 1.23), the definitions of dynamic topography vary amongst authors and methods of extraction of dynamic topography from models also differ (Flament et al., 2013). In particular, at wavelengths smaller than 1,000 km, the respective roles of lithosphere elastic flexure and dynamic support by mantle convection are still discussed (McKenzie, 2010, Husson, 2006). Moreover, the amplitude of modeled long-wavelength dynamic topography resulting from sinking slabs varies between a few hundred meters (*e.g.* Le Stunff and Ricard, 1995, Ribe and Christensen, 1994, Kaban et al., 2004, Braun, 2010, Hoggard et al., 2016) and more than 1 km (*e.g.* Forte et al., 1993, Liu and Gurnis, 2010, Flament et al., 2014, Husson et al., 2014). Since the understanding of the potential effect of subducting slabs on negative topographic anomalies at all spatial scales can help to interpret the onset of sedimentary basins formation, temporal variations in sedimentation rates, the timing of sea-level changes and the tilting and flooding of continents, it is crucial to model dynamic topography as precisely as possible and to quantify their temporal and spatial influence on Earth's gravity and surface topography (*see* Chapter 3).

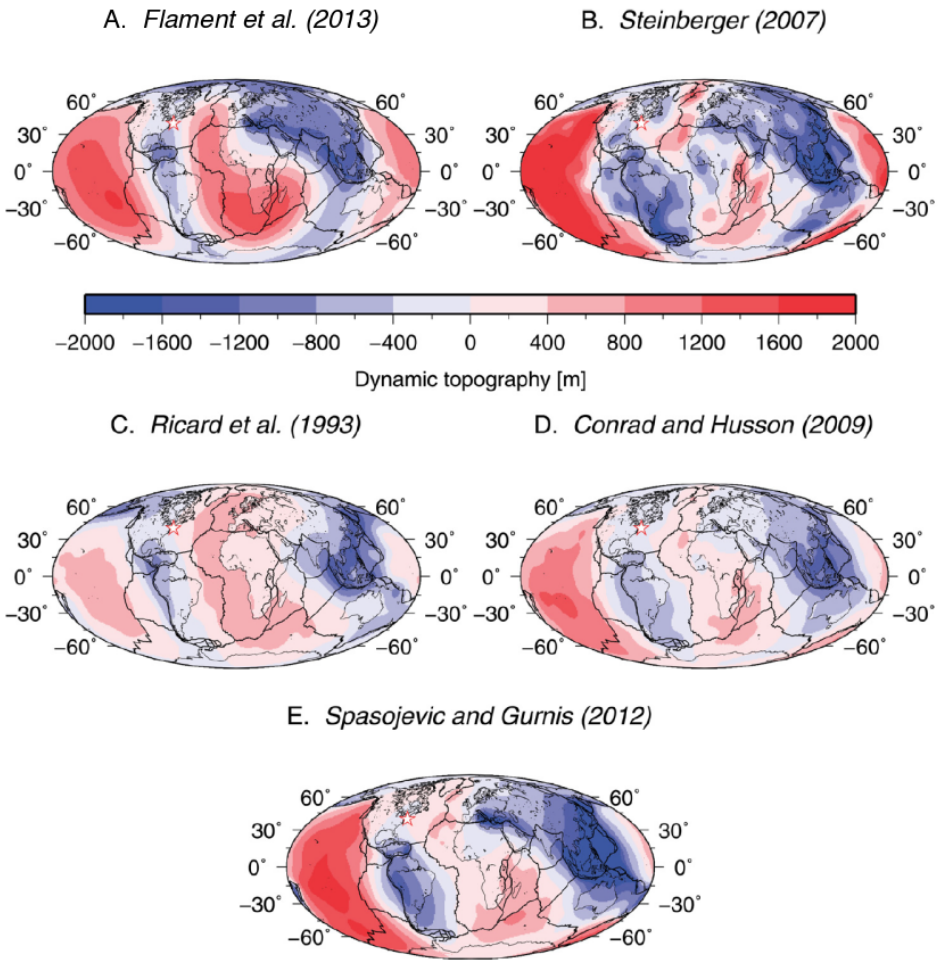


Figure 1.23: Present-day dynamic topography predicted by five models. A and C show the dynamic topography fields predicted by numerical and analytical mantle flow models respectively. B D and E show the dynamic topography field predicted by present-day instantaneous mantle flow models using a density structure based on Earth's mantle seismic tomographic models (Flament et al., 2013).

1.2.2 Mantle plumes: hot rising anomalies predicted by the physics of mantle convection

The second kind of mantle instabilities predicted by mantle convection physics is mantle plumes. As stated in section 1.1.2.2, the existence of mantle internal heating is a potential obstacle to the development of active upwellings in the mantle. However, since some heat originates from the core (at least 9 TW, Jaupart and Mareschal (2015), 5-15 TW according to Labrosse (2007), or even 30 TW (Gomi and Hirose, 2015), depending on the thermal conductivity of the core), deeply-rooted mantle plumes can develop (Morgan, 1971), although this is still questioned (*e.g. www.mantleplumes.org,* Foulger and Natland, 2003, Anderson, 2013). In this section, I review the major observations which led to the characterization of mantle plumes.

1.2.2.1 Characteristics of mantle plumes

Mantle plumes were first invoked by Wilson (1963), in order to explain observed intraplate alignments of volcanoes and seamounts often displaying an age progression in oceanic domain, such as the Hawaiian chain (Fig. 1.24). In his study, T. Wilson anchored stationary "hotspots" at 200 km depth. Later, Morgan (1971, 1972) advocated for a deep origin of mantle plumes, which he described as being anchored at the core-mantle boundary, being 150 km in diameter and rising at a rate of 2 $m \cdot yr^{-1}$. He counted 20 hotspots, both in the continental and the oceanic domain. He proposed them as a source for the motion of tectonic plates and continental breakup, based on observations and age measurements of continental large igneous provinces (LIPs) seeming to precede the opening of a new ocean (*e.g.* the Parana-Etendeka trapps and the opening of the South-Atlantic). Moreover, he considered mantle plumes as being fixed in the mantle based on Pacific hotspot tracks, therefore providing a fixed reference frame for the reconstruction of plate tectonics. Minster et al. (1974) then suggested that mantle plumes must be rooted at the CMB, and are therefore not affected by lithospheric motions.

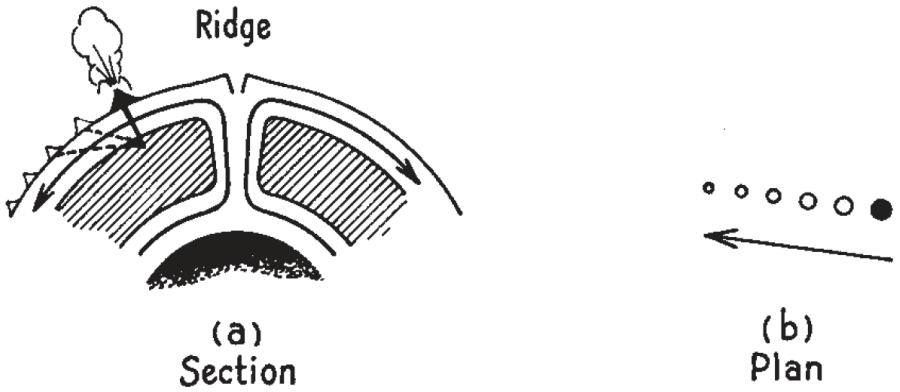


Figure 1.24: Schematic representation for the possible origin of the Hawaii by Wilson (1963).

Among the criteria for attributing a surface volcanic activity to the existence of a mantle plume in a specific location, are the followings (Courtillot et al., 2003):

- the presence of an age-progressive volcanic chain, lasting between $\sim$ 20 Ma (*e.g.* the Society and Marquesas) to more than 120 Ma (*e.g.* the Tristan da Cunha hotspot track), often located far from any plate boundary or near a spreading ridge, and initiating with a LIP, which sometimes led to biodiversity crises (*e.g.* the Siberian trapps and the Permian-Triassic crisis, Renne et al., 1995)

- the geochemistry of the volcanic rocks erupted, which should at least partly follow the alcaline series (Ocean Island Basalts, OIBs), denoting a primordial and deep origin, as opposed to Mid-Oceanic Ridge Basalts (MORBs), which are more depleted. The corresponding melting rates are often of the order of a few percents (resulting from decompression melting below the lithosphere), contrary to the MORBs and their 20 % of melting. Most of them have also a high He^4/He^3 ratio, suggesting a primitive origin (Farley and Neroda, 1998), although this conclusion is still debated (*e.g.* Hilton et al., 1995, Coltice and Ricard, 1999).

- the presence of a topographic swell of at least $\sim$ 1,000 km wide (*e.g.* Crough, 1983, McNutt, 1998) and positive gravity anomalies (*e.g.* Crough, 1978, Crosby and McKenzie, 2009). The size of the topographic swells seems to depend on the age of lithosphere (Cazenave et al., 1988), and their existence would be caused by either the dynamic support from rising buoyant material below the lithosphere (Olson, 1990), thermal erosion of the lithosphere (Detrick and Crough, 1978), or compositional buoyancy (Jordan, 1979, Phipps Morgan et al., 1995).

- low seismic anomalies below the considered hotspot, indicating hot and/or denser material.

Depending on the strictness of those criteria, the number of hotspots deriving from mantle plumes described in the literature has varied through time, from 7 (Courtillot et al., 2003) to 117 (Vogt, 1981), showing the lack of consensus on their existence and characteristics. Indeed, many hotspot chains do not display clear age progression (*e.g.* the *'Cameroon Hot Line"*) or alignments (*e.g.* the Cape Verde, McNutt (1988)), and the link between LIPs and hotspot tracks is not straightforward in all cases (*e.g.* the Central Atlantic Magmatic Province (CAMP) does not link to any hotspot chain, the Hawaiian and Cobbs hotspot tracks end at subduction zones, which erased any potential remnant of LIP). Since mantle plumes are thought to be narrow conduits, the resolution of seismic tomography was long considered as too poor to image them properly. However, recent progress in the imaging of mantle seismic anomalies led to the conclusion that a non-negligible number of hotspots are located above a low seismic anomaly, sometimes extending down to the CMB (*e.g.* Montelli et al., 2004, French and Romanowicz, 2015, Boschi et al., 2007). In the tomography model of French and Romanowicz (2015), mantle plumes are seen as broad and rather vertical conduits, up to 600 km wide in the lower mantle, and thinning and being deflected in the upper mantle only.

1.2.2.2 The initiation of plumes

Since the studies of Yuen and Peltier (1980) who demonstrated the unstable nature of the D" layer, and the results of Loper and Stacey (1983), who stated that *"Not only are plumes a necessary consequence of a thermal boundary layer, but their existence is impossible without that layer"*, the rise of mantle plumes is thought to be coherent with the TBL instability theory (Davaille and Vatteville, 2005). Nevertheless, the lifetime, spatial distribution and properties of plumes strongly depend on the fraction of core heating (which varies from 5-30 TW depending on uncertainties on the presence of radioactive elements in the core, the energy sources considered and the values of thermal conductivity of Earth's core, Labrosse, 2007, Gomi and Hirose, 2015), the presence of a compositionally different layer at the TBL (Farnetani and Samuel, 2005, Jellinek and Manga, 2002), and the influence of large-scale convection and distribution of subduction zones (Sleep, 1992).

A critical parameter to understand the dynamics of rising plumes is their temperature. Mantle plumes are indeed considered as hot thermal or thermo-chemical anomalies rising throughout the mantle. Geochemical evidence of their near-surface temperature excess (which corresponds to the temperature difference between mantle plume conduits and the average ambient mantle at a considered depth) can be inferred from estimates of melting rates and depths (McKenzie, 1984, Ribe and Christensen, 1999), olivine phenocrysts (Putirka, 2005) or the chemical composition of basalts (Herzberg et al., 2007). Petrological values favor plume temperature excesses of 100-200 K while models based on melt production rates predict excess temperature of 200-300 K. Adiabatic extrapolation of those upper mantle temperature excesses to the CMB lead to excesses greater than 1,000 K (Boehler, 2000). Mechanisms invoked for decreasing the plume temperature excess throughout the mantle are the action of subadiabacity and decompression (Zhong, 2006) and the rooting of plumes at a basal thermo-chemical layer (Farnetani, 1997).

Morphology of thermal plumes

According to the TBL instability theory, the initiation of a plume starts with the formation of a large diapir, called the plume head. Rising instabilities can take between 10-100 Myr to form at lower mantle conditions (Olson et al., 1987, Davaille and Vatteville, 2005), following Equation 1.3. Rising heads are followed by a narrower tail connected to the lower thermal boundary layer (Campbell and Griffiths,

1990). This shape results from the large viscosity contrast between the plume and the ambient mantle material, which is strongly dependent on temperature (see Chapter 2). This characteristic shape has been associated to the fact that observed hotspot tracks are often linked to continental or oceanic LIPs, which correspond to intense production of basaltic lava (which generally cover areas of $1-4\times10^6$ km^2) during a short period of time (< 5 Myr) (Fig. 1.25, *e.g.* Courtillot and Renne, 2003).

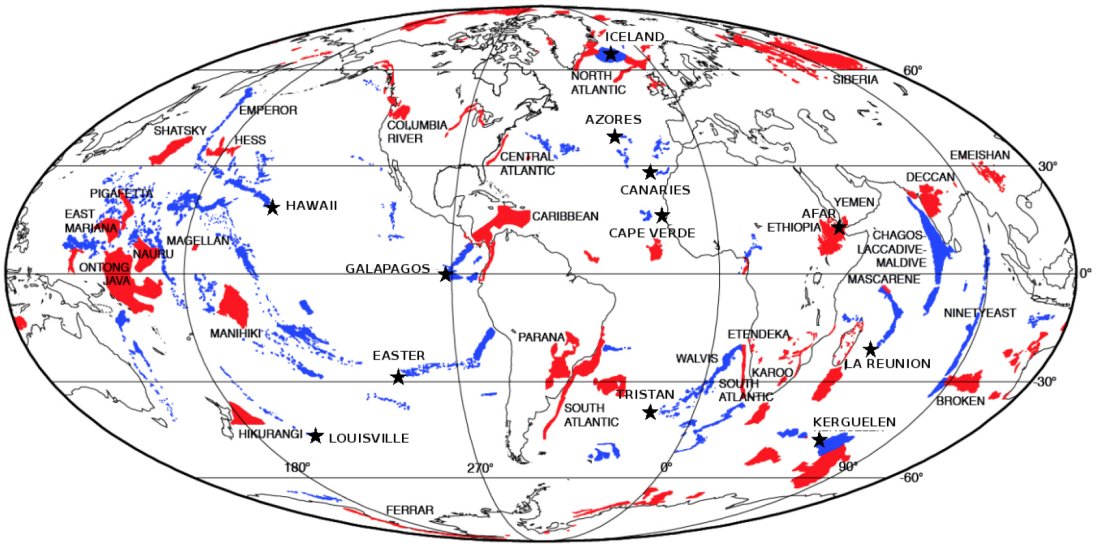


Figure 1.25: Distribution of hotspots (stars) and Phanerozoic LIPs. In red: LIPs of portions of LIPs generated by a transient "plume head". In blue, hotspots tracks generated by a persistent "plume tail" (Farnetani and Hofmann, 2011).

LLSVPs and thermo-chemical plumes

Since the middle of the 1980's, the improvement of seismic data coverage and the development of global tomographic methods for imaging Earth's deep mantle led to produce the first global images of internal lateral seismic velocity heterogeneities (*e.g.* Su et al., 1994, Li and Romanowicz, 1996). Amongst those heterogeneities, two large-scale low-shear velocity provinces (LLSVPs) were identified in the lowermost mantle, one lying below the African continent and the other below the Pacific. In 2012, Lekic et al. (2012) showed the robustness of those two heterogeneities, which also coincide with large-scale geoid highs and anomalously elevated large-scale topography regions also called superswells (McNutt, 1987, 1998, Nyblade and Robinson, 1994), thanks to a cluster analysis of different tomography models. However, the origin (cooling of a primordial basal magma ocean (Labrosse, 2007) or subduction material segregation and accumulation (Christensen and Hofmann, 1994)) and nature of such anomalies are still debated. Sidorin and Gurnis (1998), Wen et al. (2001), He et al. (2006) and

Frost and Rost (2014) concluded that the boundaries of both LLSVPs are sharp, which would indicate a distinct composition from the ambient mantle, although it is still questioned (Davies et al., 2012).

Linear stability analyses of two compositionally different fluids, initially chemically stratified (Sotin and Parmentier, 1989), and analogue experiments conducted by *e.g.* Richter and McKenzie (1981), Christensen (1984b), Olson et al. (1984), Davaille (1999), Davaille et al. (2002), Le Bars and Davaille (2004), Jellinek and Manga (2002) led to the building of regime diagrams of the two layers behaviours depending on their relative density ($\Delta\rho$), their relative thickness, the Rayleigh number of the system and their viscosity ratio. The buoyancy ratio B was defined as a dimensionless parameter measuring the relative stability of the chemical anomaly:

$$B = \frac{\Delta\rho}{\rho\alpha\Delta T} \tag{1.9}$$

From those analyses, different regimes were observed, from the thermal destabilization of the compositionally stratified medium into 3D-domes, doming-ridges, passive ridges, piles, or anchored thermo-chemical plumes. When the viscosity contrast is large, secondary plumes can form above domes. This situation would be analogue to a compositionally different fluid extending throughout the lower mantle depth, and originating plumes in the upper mantle, where the viscosity contrast is higher. When the buoyancy ratio is greater than a critical number (which depends on viscosity), the chemical stratification does not deform and a TBL forms at the interface between the two fluids, from which rising plumes originate. They are nevertheless weaker than in the case of thermal convection since their temperature contrast is lower (*e.g.* Farnetani, 1997, Christensen, 1984b, Tackley, 1998), they do not have a head, and they lead to very small viscous entrainment of the denser layer, which is deformed into cusps. Other regimes imply for example, the formation of falling domes, especially if thermo-chemical plumes are particularly enriched in silicium (Samuel and Bercovici, 2006).

As a consequence, several types of mantle plumes/hotspots have been proposed, to account for the diversity of shapes and signatures of Earth's hotspots (Fig. 1.26), based on their origin.

Seismic analyses of Earth's normal modes (*e.g.* Koelemeijer et al., 2017) and numerical models (*e.g.* Mulyukova et al., 2015) further explored the viability of the previously described regimes in Earth's lower mantle conditions, and showed that LLSVPs can correspond to large-scale mantle upwellings,

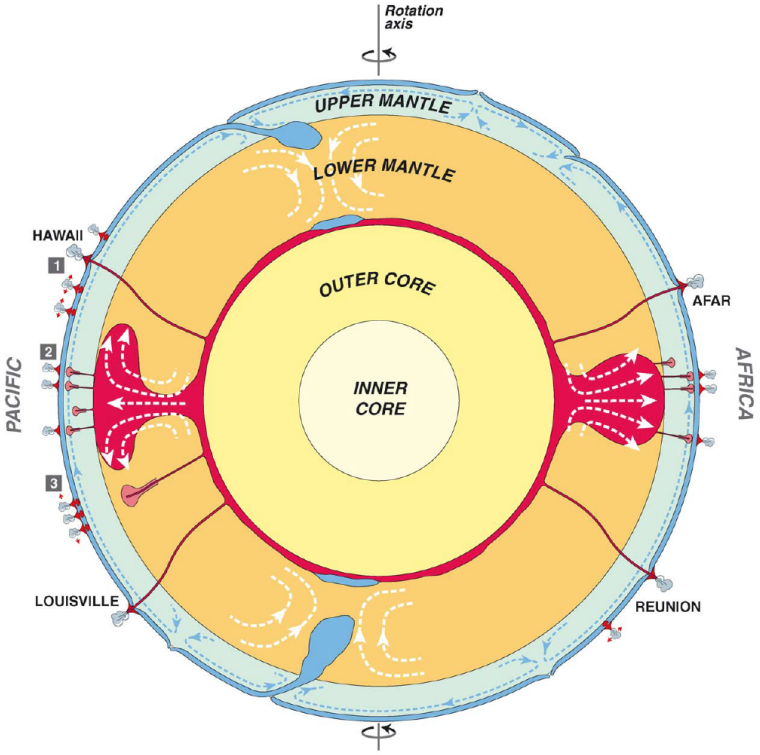


Figure 1.26: Schematic longitudinal cross-section of the dynamic Earth outlining three types of mantle plumes/hotspots: the "primary" plumes would come from the CMB, the "secondary" plumes possibly come from the top of domes near the depth of the transition zone, the "tertiary" hotspots may have a superficial origin linked to tensile stresses in the lithosphere and decompression melting (Courtillot et al., 2003).

possibly compositionally different from the ambient mantle. Burke et al. (2008) compared the spatial distribution of mantle plumes and LLSVPs to suggest that deep mantle plumes originate from Plume Generation Zones (PGZs) located at the boundaries of LLSVPs. Although these conclusions were questioned by Austermann et al. (2014), Torsvik et al. (2010) further stated that LLSVPs have remained stationary over the last 200 Ma (Fig. 1.27) from the reconstructed location of erupted kimberlites.

The relative stability of LLSVPs over hundreds of millions of years is nevertheless questioned by the fact that large-scale convection likely deforms deep-seated thermochemical heterogeneities, therefore modifying their topography (Steinberger and Torsvik, 2012, Li and Zhong, 2017). In particular, slabs reaching the lowermost mantle can trigger the birth of hotspots of various shapes, depending on the strength and angle of the impingement.

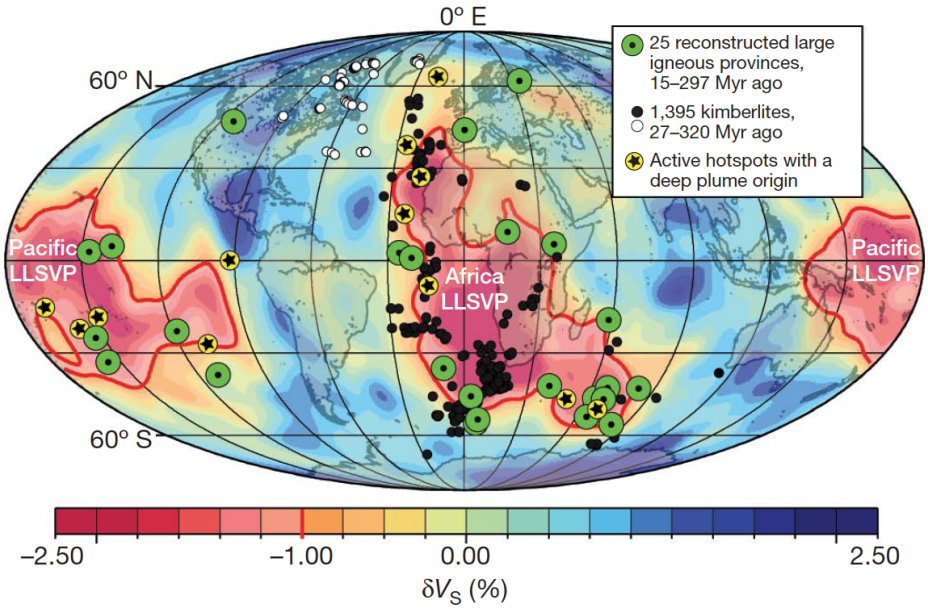


Figure 1.27: Reconstructed large igneous provinces and kimberlites for the past 320 Ma with respect to shear-wave anomalies at the base of the mantle from Becker and Boschi (2002) (Torsvik et al., 2010).

In order to reconcile all those observations, Li and Zhong (2017) proposed a systematic study of the sources of mantle plumes thanks to numerical models of mantle convection. They showed that the thermal expansivity and thermal diffusivity of the lower mantle decrease combined with a viscosity increase lead to an increasing number of mantle plumes originating from basal thermo-chemical layers, and mainly on their edges. Thermal plumes can still originate far from thermo-chemical basal layers and in this case, they originate from TBL instabilities, as described previously.

Alternatives to mantle plumes

It is also important to remember that intraplate volcanism can also be explained by other mechanisms, presented as possible alternatives to the existence of mantle plumes. For example, a large number of aligned Pacific islands and seamounts do not show clear age-progression. As a consequence, Ballmer et al. (2007, 2009) invoked the influence of melting induced by old oceanic sub-lithospheric small-scale convection in the formation of those topographic anomalies. Some authors also suggest the influence of localized rheological heterogeneities in the lithosphere, such as cracks (Forsyth et al., 2006). Conrad and Behn (2010) and Conrad et al. (2011) showed a spatial correlation between intraplate volcanism and areas of the asthenosphere experiencing fast shearing. They therefore propose

a major control of the shear flow of asthenosphere in the generation of hotspots that are not fed by a mantle plume. In the case of the Cameroon Hot Line or the Eastern Australia volcanism, the rheological and thickness differences between continental and oceanic lithosphere can be responsible for edge-driven convection, leading to areas of intraplate volcanism (King and Ritsema, 2000, King, 2007b, Burke, 2001, Milelli et al., 2012, Davies and Rawlinson, 2014). Finally, Foulger and Natland (2003), Anderson (2001) proposed that hotspot volcanism is not the surface expression of mantle plumes, but the by-product of plate tectonics. Plate tectonics would cause areas of the shallow mantle to melt due to the reactivation of old suture zones localizing intense deformation and be responsible for upper-mantle compositional heterogeneities or continental delamination processes. Nevertheless, Husson et al. (2012) highlighted the existence of a correlation $> 77\%$ between some hotspots (the "primary" hotspots of Courtillot et al. (2003) and the "deep" and "potentially deep" plumes imaged by Montelli et al. (2006)) and lower-mantle upwelling regions. This correlation is still 65% if considering Anderson's catalogue of hotspots (*www.mantleplumes.org*). The alternative mechanisms described above would therefore be preferentially considered in regions where secondary hotspots do not correspond to mantle upwellings.

1.2.2.3 The stability of plumes

When Morgan proposed that hotspots derive from mantle plumes anchored in the lower mantle, he assumed their fixity relatively to the moving lithosphere (Morgan, 1971), which is in contradiction with the idea of chaotic mantle convection. Precise geochronological and paleomagnetic measurements at hotspot tracks have since then been conducted, with contrasting conclusions about the fixity of mantle plumes (*e.g.* Minster et al., 1974, Burke et al., 1973, Molnar and Stock, 1987, McElhinny, 1973, DiVenere and Kent, 1999, Tarduno and Cottrell, 1997). For example, the use of different sets of paleomagnetic and geochronological data by McElhinny (1973), DiVenere and Kent (1999), Raymond et al. (2000), Besse and Courtillot (2002), Tarduno and Cottrell (1997), Tarduno et al. (2003, 2009), Wright et al. (2015) and Konrad et al. (2018) confirmed that at least the Hawaiian hotspot moved southwards by up to 5 cm·yr^{-1} between 81 and 47 Ma, in contradiction with the explanation of the Hawaiian-Emperor bend by a true polar wander event (Koivisto et al., 2014) or a change in the Pacific plate motion (Torsvik et al., 2017). Koppers et al. (2004) observed a non-linear age progression of the Louisville hotspot, indicating non-negligible eastward motion of this mantle plume as well.

Although the fixity of mantle plumes is debated, a large number of plate tectonic reconstructions used fixed hotspots as a reference frame for reconstructing past plate tectonics (*e.g.* Morgan, 1971, Duncan, 1981, Müller et al., 1993). More recently, because of growing evidence of hotspot motions, attempts to account for moving hotspots in reconstructing plate tectonics arose (Steinberger and O'Connell, 2000, O'Neill et al., 2005, Doubrovine et al., 2012). Torsvik et al. (2010) proposed that mantle plumes originate from PGZs attached to the boundaries of stable LLSVPs, and suggests using this property as a constraint for future reconstructions. Indeed, the organization of large-scale convection into stable cells can be accounted for the stability of large-scale upwellings location during the past 250 Ma according to Conrad et al. (2013). Nevertheless, the stability of LLSVPs is debated (*e.g.* Müller et al., 2016, Flament et al., 2017).

It is not clear to what extent mantle plumes can and do move. Reconstructing plate tectonics from the position of hotspots therefore still requires an understanding of how plumes interact with different scales of mantle convection and lithospheric motions in a self-organized system, in order to estimate the range of possible hotspot rates of motion.

1.2.2.4 The activity of plumes: from birth to death

As previously described, the best evidence used to understand the origin and dynamics of thermal anomalies generating hotspots, is their topographic swell. Crough (1983) calculated a *depth anomaly* (residual topography) of oceanic seafloor by removing the effect of age-dependent crustal thickness (Fig. 1.28). This revealed anomalously shallow and often asymmetric elongated regions, which coincide with the location of most hotspots (with the exception of Madeira and the Canaries). Those topographic swells of about 1 km high are also often elongated in the same direction as hotspot chains and plate motions and progressively vanish below the oldest seamounts, which provides further support for an action of mantle thermal anomalies in generating surface topographic highs. Potential causes for these topographic swells comprised the accumulation of sediments, flexure, a thicker crust, thermally-eroded lithosphere or anomalously hot asthenosphere. The relative action of the last three processes are still discussed, since contradictory seismic observations of lithospheric thinning or normal thicknesses and crustal thickening exist (*e.g.* Li et al., 2004, Stein and Stein, 1993, White and McKenzie, 1995, Rychert et al., 2018).

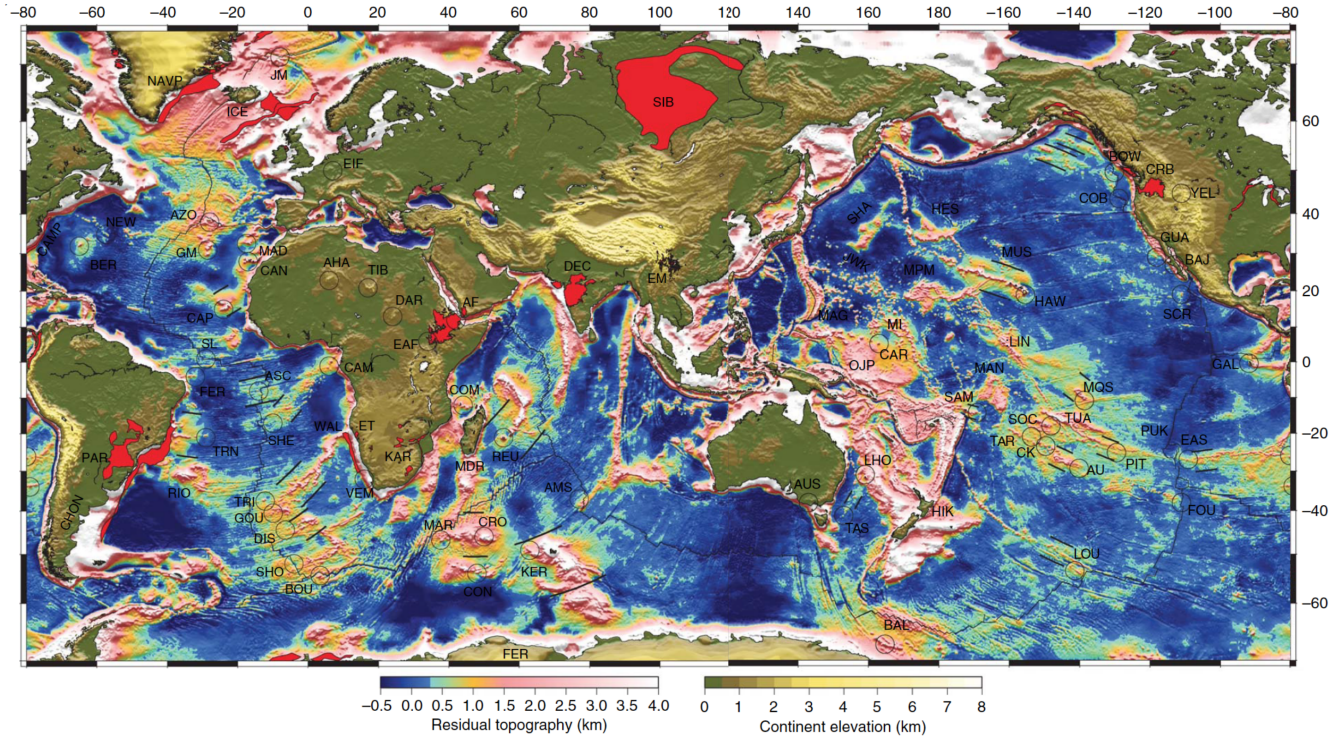


Figure 1.28: Elevation of the continents and residual topography in the oceans, evaluated from the predicted bathymetry of Smith and Sandwell (1997) corrected from sediment loading and thicknesses (Laske and Masters, 1997), and for seafloor subsidence with age (Stein and Stein, 1992), using seafloor ages from Müller et al. (1993). Color change from blue to turquoise is at 300 m and delineates the approximate boundaries of anomalously shallow seafloor. Circles mark estimated locations of most recent hotspot volcanism. Pairs of lines are used to measure widths of some of the hotspot swells. Flood basalt provinces on continents and continental margins are red. (Figure adapted from Ito and van Keken, 2007).

From the analysis of hotspot swells, it is possible to infer the activity of hotspots, by calculating their buoyancy flux B_P from the estimate of volumetric rate of swell creation (Davies, 1988a, Sleep, 1990, Schilling, 1991, Crosby and McKenzie, 2009), and the amount of heat that they carry q_P (*e.g.* Sleep, 1990). From the careful analysis of Earth's hotspots activity, it has been possible to state that it can vary through time, since any variation in plume buoyancy is likely to feed through to surface topography, gravity anomalies, crustal thickness, volcanic activity and heat flux (*e.g.* Poore et al., 2009), although the precise quantification of plume activity from surface observations sometimes differs dramatically between different authors. For example, the Iceland buoyancy flux from topographic swells is on the order of 1.4 Mg·s^{-1} while estimates vary between 17-47 Mg·s^{-1} (Poore et al., 2009) to more than $>$ 70 Mg·s^{-1} (Parnell-Turner et al., 2014) from the study of V-shaped ridges.

Another crucial observation indicative of mantle plumes dynamics is their present-day relative proximity to mid-ocean ridges (Weinstein and Olson, 1989). Whittaker et al. (2015) extended this observation to the last 180 Ma at least. In fact, a non-negligible number of plumes directly interact with ridges (*e.g.* Ito et al., 2003), which results in anomalously shallow ridge axis depths (e.g. Vogt, 1976, Schilling, 1991), thick crust (as seen by seismic and gravity studies, *e.g.* White and McKenzie, 1995, Canales et al., 2002) and geochemical anomalies (such as high $^{87}Sr/^{86}Sr$ (Hart et al., 1973), high La/Sm (Ito et al., 2003) or high $^{4}He/^{3}He$ (Graham, 2002)). Analytical and numerical models of plume interacting with stable or migrating ridges conducted in the 1990's (Ribe et al., 1995, Ribe, 1996, Albers and Christensen, 2001, Ito et al., 2003) generally conform with observations and show that the interaction width between plumes and ridges (also called *waist*) increases with plume buoyancy flux and decreases with plate spreading rate, plume viscosity and plume-ridge separation. However, the actual geometry of along-axis channels (*e.g.* the V-shaped ridges of Iceland or the Azores) and hotspot-to-ridge channels (*e.g.* the connection Reunion-Rodrigues-central Indian ridge or the Easter-Sala Y Gomez seamount chain-Easter microplate rifts) is still discussed, some advocating for wide-spread hotspot material below the lithosphere (*e.g.* Ribe, 1996) and others favoring narrow plume channels (70 km wide) (e.g. Kingsley and Schilling, 1998). The amount of water in plume material and the topographic and deformation setting of the lithosphere seem to play a non-negligible influence on the lateral spreading of mantle plumes, but this needs further investigation (Wallace, 1998).

The relative proximity between hotspots and mid-ocean ridges has also raised questions about their possible role in the generation of divergent plate boundaries (*e.g.* Morgan, 1971, Storey, 1995, Courtillot et al., 1999). Morgan (1971) was the first to propose an active role of mantle plumes in doming and fracturing supercontinents, in contrast with models advocating for a passive subcontinental heat generation, continental breakup being initiated by far-field stresses (McKenzie, 1978, White, 1989) and/or hot subcontinental asthenosphere (Anderson, 1982).

Mantle plumes can also cause temporal reorganisation of ridges, by propagating new long-lived/short-lived segments (*e.g.* near the Galapagos, Cobb, the Ascension and St Helena hotspots, Hey, 1977, Wilson and Hey, 1995), or by causing ridge-jumps towards hotspots (*e.g.* near Iceland or Amsterdam-St Paul, Hardarson et al., 1997, Conder et al., 2000). Mantle plumes would therefore be responsible for ridge reorganizations in order for the ridge axis to stay in the vicinity of the hotspot (Dyment,

1998), and this behaviour has been proposed as a cause for long-lived asymmetric spreading (Müller et al., 1993).

In contrast with their proposed link with divergent boundary creation, mantle plumes have been recently invoked as the cause of subduction initiations (Ueda et al., 2008), due to their weakening and thinning effect on the lithosphere. Gerya et al. (2015) suggested the initiation of plate tectonics was due to plume-induced subduction of strong and negatively buoyant lithosphere. Others see a role of plumes in the generation of the south margin of the Caribbean (Whattam and Stern, 2015), or even in the production of some of Venus' topographic characteristics (Sandwell and Schubert, 1992, Davaille et al., 2017). Finally, some authors see a role of plumes in speeding of slowing down surface plates. For example, Cande and Stegman (2011) proposed that the Reunion plume provided a plume-push force contributing to India acceleration between 68 and $\sim$ 50 Ma.

1.2.3 Convective cells and plate tectonics : mutual feedbacks?

As raised in sections 1.2.1 and 1.2.2, mantle convection exerts a definite control on surface dynamics. For example, subduction zones, via their slab-pull force, entrain lateral motions of plate tectonics, and via their slab-suction force and the induced toroidal flow, also participate in subduction topography and geometry (Conrad and Lithgow-Bertelloni, 2002, Funiciello et al., 2008). On the other hand, lithospheric rheology also controls slabs geometry and dynamics: depending on the ability of a surface plate to bend, single or double-sided subductions will initiate (Crameri et al., 2012a); slab initiation also depends on lithospheric thickness, density and strength (section 1.2.1.2).

In many ways, surface plate rheology controls plate tectonics layout and the multiple scales of convection, although the fine-scale understanding of those processes is far from being reached. Indeed, lithospheric rheology plays an undeniable role in the initiation and the continuation of plate boundaries (*e.g.* Toth and Gurnis, 1998, Corti et al., 2007). For example, Mallard et al. (2016) showed that the strength of lithosphere controls the number and size of plates, as well as the dominant mantle convective cells. To draw these conclusions, they analyzed numerical models of mantle convection self-generating plate-like tectonics by using a simplified rheology of oceanic lithosphere involving different yield stresses. Moreover, in that study, the authors showed that the geometry and location of subduction zones control plates fragmentation. They therefore propose a dynamic feedback between

mantle and lithosphere dynamics, where the dominant scales of convection control the largest plates size and subduction curvature contributes to the formation of smaller plates size.

However, the presence of finite-size continents is likely to perturb these conclusions. Indeed, we can consider continents as high-strength rafts, which cannot undergo complete subduction, and are difficult to break apart. On Earth, their relatively large size is also likely to regulate dominant plate sizes and convective scales. Moreover, several supercontinent cycles have been recorded throughout geological timescales (*e.g.* Wilson et al., 1966, Worsley et al., 1982, Kerr, 1985), as recorded by geological remnants of ocean openings and closures. Those involve the formation and the disaggregation of supercontinents on timescales of several hundred million years (also called *Wilson cycles*), therefore potentially modifying both surface plate-size distribution and mantle convective scales. Gurnis (1988) was the first to deduce from 2D numerical models that supercontinent cycles correspond to a feedback between continental motions and mantle convection. He proposed that continental plates aggregate over large-scale downwelling regions. By inhibiting the formation of new subduction zones, the parts of mantle located below the supercontinent would reheat and cause its disaggregation. The reasons for reheating the mantle below a supercontinent are still discussed. Some advocate for the action of active upwelling in the form of mantle plumes, which would impinge the base of supercontinents and cause their break-up (Morgan, 1971, Sobolev et al., 2011, Cande and Stegman, 2011). The presence of LIPs contemporaneous with rifting events and linked to hotspot tracks would be one of the best proofs of such process. Others favor a more passive process, where the insulating properties of continental lithosphere would play a major role (Armitage et al., 2010, Fromm et al., 2015, Ryberg et al., 2015). Indeed, by inhibiting heat evacuation from the underneath mantle, the presence of supercontinents would lead to the heating of the uppermost mantle, which would in turn weaken continental lithosphere. The action of far-field stresses, such as subduction in the super-ocean, would also participate to break supercontinents. This scenario was first proposed by Anderson (1982), and later confirmed by Coltice et al. (2007) and Zhong et al. (2007). Zhong et al. (2007) also proposed that supercontinent cycles can highly perturb whole-mantle convection by generating alternating degree-1/degree-2 dominant scales of convection, by redistributing areas of large-scale upwellings and downwellings (Fig. 1.29). As a consequence, feedbacks between mantle convection and lithospheric dynamics control large-scale reorganizations.

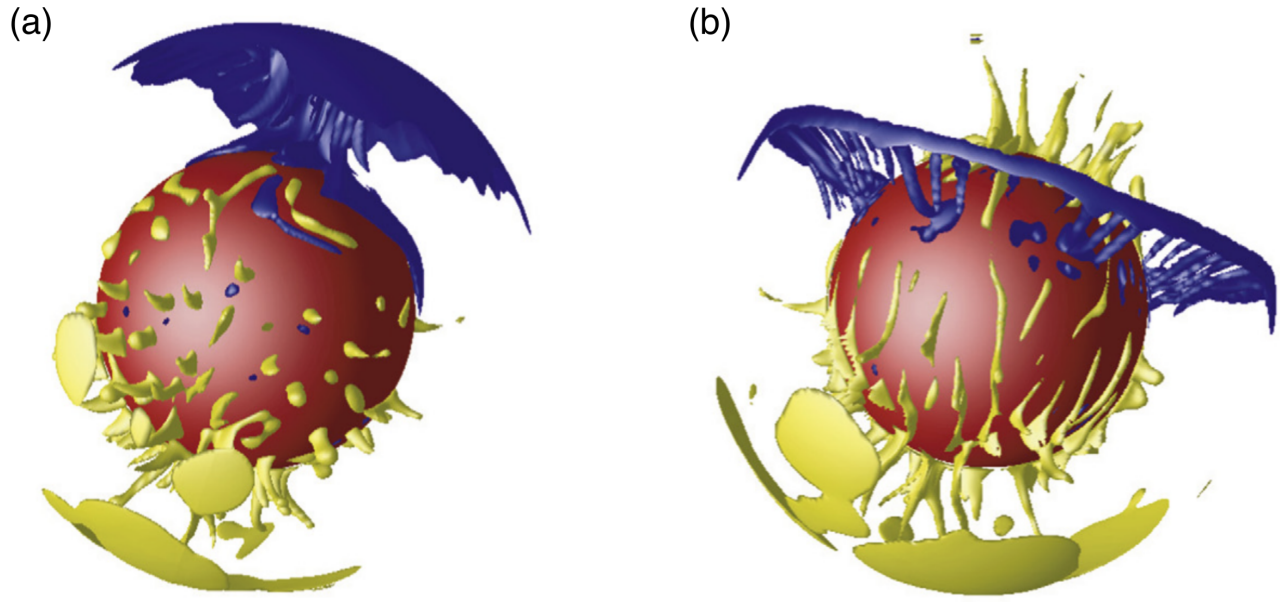


Figure 1.29: Convective structures from a 3D-fully dynamic models of mantle convection (a) with oceanic highly viscous lithosphere (degree-1 convection) and (b) with a supercontinent at the North Pole (degree-2 convection) (Zhong et al., 2007).

Moreover, vigorous upper-mantle convection is believed to take place, both because of a low-viscosity asthenosphere (as confirmed by seismic analyses and by geodynamic studies based on geoid and post-glacial results (Hager and Richards, 1989, Thoraval and Richards, 1997) and high viscosity contrasts between asthenosphere and lithosphere, which are likely to promote small-scale convection (Moresi and Solomatov, 1995). However, the dominant wavelengths in the asthenosphere, and their potential ability to generate long-wavelength plate-tectonics are still not fully understood, as well as the amount and variability of asthenospheric/lithospheric coupling (Van Summeren et al., 2012). Indeed, depending on the flow regime in the asthenosphere, different driving forces can arise and potentially lead to a different surface response. Indeed, the *Couette flow* consists of shear-driven flow by plate tectonic motions: plate velocities are greater than the mantle and are therefore responsible for its lateral motion. On the contrary, the *Poiseuille flow* consists of a flow channelization in the asthenosphere, leading to asthenospheric velocities higher than surface plate velocities, and therefore providing a mantle-drag force for plate motions. Höink and Lenardic (2010) showed that the dominant flow regime depends on the relative strength of the lithosphere, with potential effects on upper mantle seismic anisotropy, the amplitude of surface dynamic topography and heat flux over convective cells. Lateral variations in the strength of lithosphere and changes in global surface plate velocities can lead to a lateral and temporal diversity of asthenospheric regimes, with different impacts on surface deformation and

driving forces. A better understanding of such surface observations will therefore ultimately help interpret the feedbacks between lithospheric properties and mantle modes of convection from which they originate.

I have now described some of the studies that use the surface expressions of sinking slabs and rising plumes in the mantle in order to infer some of the properties of those convective instabilities and the above lithosphere. From all the examples described above, it is clear that plate tectonic and mantle dynamics are intimately and physically coupled processes. In an effort to link geodynamically the physics of mantle convective processes and surface tectonics, I discuss current challenges related to our understanding of their intricate relationships in the next section.

1.3 Towards an integrative approach of mantle and lithosphere interactions?

1.3.1 Current challenges and perspectives

From the problems and uncertainties raised in the previous sections, some challenges remain:

- The **role of lithospheric and mantle rheology** in the deformations and motions of those two layers is still far from being understood. This needs further connections between micro-scale mineralogical and petrological studies of lithospheric and mantle rocks behaviour, and geodynamical experimental and numerical modeling. Ultimately, rheological laws will be used to self-consistently model the structural behaviour of the lithosphere, but until then, alternative and simplified laws are used. They are discussed in section 2.2.1.

- The **mechanisms responsible for initiating and driving plate tectonics** are unclear. Unravelling these mechanisms will eventually help to bridge the gap between the kinematic theory of plate tectonics and the physics of mantle convection, by finding physical explanations for the lateral motions of surface plate tectonics. Moreover, in the perspective of improving our current knowledge about the past motions of plates, understanding the physics of the stability of mantle plumes, and the relative motions between the mantle and the lithosphere will help to define a solid reference frame for plate reconstructions.

- The **relative contribution of mantle and lithosphere on surface topography** is also ambiguous. The spatial and temporal scales of variation of topography seem to be controled by the source of deformation: lithospheric isostasy and lithospheric elastic flexure are thought to act on relatively short spatial scales, while dynamic topography (caused by mantle moving density anomalies) is classically believed to dominate on wavelengths longer than 1,000 km (McKenzie, 2010). However, this has been questioned by Petersen et al. (2010), who showed that surface deformations over timescales of 1-2 Myr and spatial scales of several hundreds of kilometers can result from small-scale convection beneath the lithosphere. Moreover, there is a discrepancy on the amplitudes of dynamic topography generated by mantle convection at different spatial scales. Observation-derived residual topography proposes a small contribution of mantle convection (amplitudes smaller than 300 km) at spatial scales longer than 5,000 km while predicted dynamic topography from mantle convection models advocate for amplitudes larger than 1 km at the considered wavelengths (Hoggard et al., 2016).

- The precise **characterization of mantle plumes-lithosphere relationships** (hotspot topographic swells, interaction with ridges, implication in supercontinental breakup) will help to refine our understanding of both the dynamics of the mantle (such as the source(s) of mantle plumes fixity, the amount of heat driven from the core to the surface, their interaction with large- and small-scale convection, the rheology and composition of mantle slow seismic velocity anomalies), and the dynamics of the surface (such as the spatial and temporal scales of plume-driven uplifts, the use of hotspot tracks as a reference frame for plate reconstructions, their potential implication in generating new plate boundaries and driving some of the plate tectonic motions).

- The **temporal evolution of Earth's internal and lithospheric dynamics** will finally give some clues about the long-term retroactions between mantle and lithosphere. As described in section 1.2.3, supercontinent cycles regulate and are regulated by the spatial distribution of divergent and convergent zones, the surface heat flow and mantle large-scale convection. Understanding the physics of supercontinent cycles is important for constraining plate tectonics reconstructions, and interpreting geological processes such as long-term sea-level changes caused by seafloor depth variations.

1.3.2 Problem statement

In the previous section, I have listed some open questions regarding the surface expressions of mantle convective instabilities, based on the developments of the previous sections. Those questions can be summarized into:

- **What do surface observations reveal about the properties and behaviour of Earth's mantle?**
- **How does mantle convection interact with Earth's lithosphere to produce these observations?**

As stated throughout this introduction, the answers to those questions are certainly diverse and require multidisciplinary approaches, to account for the complexity of surface observations of lithospheric deformations and its interactions with the multiple scales of convection. Our way to approach this problem is to use numerical models of mantle generating self-consistent mantle instabilities and surface plate tectonics with Earth-like properties in order to derive synthetic observations, that could be compared with Earth observations. The misfit between modeled and observed surface characteristics will ultimately help to refine our models and understand the physics underlying surface observations.

More specifically, this thesis aims at using complex numerical models of mantle self-generating plate-like tectonics in order to:

- **Understand surface vertical motions related to the presence of moving mantle density anomalies.** This implies to study the spatial and temporal evolution of the topography in our numerical models.
- **Characterize the behaviour of mantle upwellings**, and study their interactions with the lithosphere and mantle different convective scales.

1.3.3 Outline of this thesis

One way to tackle those questions is to use a direct approach, which consists in computing forward models of mantle convection self-generating plate-like tectonics with Earth-like surface characteristics. Contrary to other methods which use surface plate reconstructions as a boundary condition for the temporal evolution of mantle circulation or the inversion of mantle seismic tomography field back

in time, the one used in this thesis is fully-dynamic and enables to study the physical relationships between plate tectonics and mantle flow without introducing uncertainties on the mantle temperature field and excessive stresses and forces between the surface and the mantle.

The contribution of this thesis to those questions is structured as follows. Chapter 2 first presents the computational methods used to numerically model the complex interactions between plate-like surface tectonics and mantle convection, after a brief description of mantle convection equations and approximations used in this thesis. Chapter 3 then presents results regarding the interplay between spatial and temporal scales of dynamic topography emerging from 2D-whole-mantle convection models with plate-like tectonics. I focus on the role of subduction zones in reorganising intermediate scales of mantle flow on timescales of tens to hundreds of millions of years, therefore generating intermediate scales of dynamic topography. Chapter 4 presents a detailed study of the characteristics of mantle plumes in 3D models of mantle convection with self-consistent plate-like tectonics. This Chapter shows that model plumes present Earth-like characteristics, which allows further comparisons with Earth's hotspots. I then study their interactions with mantle convective scales and lithospheric motions, in order to quantify their potential lateral motions. I finally apply our approach to the study of the interactions between the Mid-Atlantic Ridge and the Azores. Finally, Chapter 5 sums up the main conclusions of this work and proposes guidance for future studies.

Chapter 2

Numerical modeling of the influence of whole-mantle convection on a plate-like lithosphere

Contents

2.1 Numerical modeling of mantle dynamics 52

2.1.1 Thermal convection approximations and limitations 52

2.1.1.1 Continuum mechanics approximation 52

2.1.1.2 General equations and reference state 52

2.1.1.3 Useful approximations in the case of mantle convection 57

2.1.2 Modeling thermo-chemical convection 62

2.1.3 Modeling mantle rheology 63

2.2 Numerical modeling of lithosphere dynamics 68

2.2.1 Numerical models of mantle convection with plate-like tectonics 68

2.2.1.1 Rheology of Earth's lithosphere 68

2.2.1.2 Modeling plate-like tectonics 70

2.2.2 Modeling oceanic and continental lithosphere 75

2.3 Computation 76

2.3.1 Numerical approximation, discretization and geometry 77

2.3.2 Solving conservation equations 79

2.3.3 Initial and boundary conditions 81

2.3.4 Scaling or dimensionalization 83

In this Chapter, I detail the physics and approximations of mantle convection before reviewing the different methods used to numerically model mantle convection and plate-like tectonics. I also present the methods used in this thesis to self-consistently generate whole-mantle convection with plate-like tectonics. Finding a set of parameters leading to an Earth-like regime has been the first step of the presented work. The main characteristics of those models is that they allow us to study time-dependent mantle dynamics at very high-resolution, which is fundamental to study the interaction between plate tectonics and mantle dynamics on temporal and spatial scales that have not been possible previously.

2.1 Numerical modeling of mantle dynamics

2.1.1 Thermal convection approximations and limitations

Extensive descriptions of the physics of mantle convection can be found in Schubert et al. (2001), Turcotte and Schubert (2014), Ricard (2015) and Yoshida (2017). In this section, I propose a small description of the possible approximations used to model mantle convection.

2.1.1.1 Continuum mechanics approximation

I use laws derived from the physics of continuum mechanics in order to describe mantle convection. This choice is relevant since mantle convective deformations have some effects on large scales (also called mesoscopic - macroscopic scales). Therefore, the macroscopic laws of continuum physics can be applied, even if motions are dependent of intra-crystalline deformations. Moreover, building constitutive laws from atomic/molecular/crystalline properties of mantle material is a difficult task. Some researchers are currently trying to develop such constitutive laws for olivine at mantle pressure and temperature conditions (*e.g.* Boioli et al., 2017, Davaille et al., 2018), using a combination of numerical, analytical and experimental methods to formalize the state of olivine across scales.

2.1.1.2 General equations and reference state

In this section, I only focus on thermal convection, while large-scale compositional heterogeneities are considered in section 2.1.2.

General equations

Conservation equations can be used to describe the physics of a continuum. They provide a formal way to characterize the temporal evolution of some quantities in a closed system potentially subject to influxes and outfluxes. Three main quantities are conserved : mass, momentum and energy.

Mass conservation corresponds to the balance between the variation of density ρ in a parcel of fluid with a volume Ω and the flow across its boundaries Σ. The equation of mass conservation (continuity equation) is therefore defined by:

$$\frac{\mathrm{D}\rho}{\mathrm{D}t} + \rho \boldsymbol{\nabla}.\boldsymbol{v} = 0 \tag{2.1}$$

with $\frac{\mathrm{D}}{\mathrm{D}t} = \frac{\partial}{\partial t} + \boldsymbol{v}.\boldsymbol{\nabla}$ corresponding to the Lagrangian time derivative, t the time and $\mathbf{v}$ the velocity.

The total **momentum** of the volume Ω of a parcel of fluid corresponds to $\int_\Omega \rho \mathbf{v} \mathrm{d}V$. Its variations result from the advective transport of momentum across the surface Σ of the system, forces acting on Σ and internal body forces. The equation of momentum conservation corresponds to Newton's second law and is defined by:

$$\rho \frac{\mathrm{D}\mathbf{v}}{\mathrm{D}t} = -\boldsymbol{\nabla}.\boldsymbol{\sigma} + \mathbf{f} \tag{2.2}$$

with $\boldsymbol{\sigma} = -P\mathbf{I} + \boldsymbol{\tau}$ the stress tensor, representing the surface force applied on the parcel of fluid, which decomposes into an isotropic fluid pressure P and a deviatoric stress $\boldsymbol{\tau}$, and $\mathbf{f}$ the body forces. $\boldsymbol{I}$ is the identity tensor. Body forces potentially include: the gravitational body force ($\rho\mathbf{g}$ with $\mathbf{g}$ the gravitational acceleration), the Coriolis force (which results from Earth's rotation), a pressure-driven buoyancy force representing the compressibility of the fluid, self-gravitation effects which correspond to perturbations in the gravity field due to convective motions, and electromagnetic and electrostatic forces. The left term in Eq. 2.2 represents the inertial force.

In Earth's mantle, the effect of the Coriolis force and electromagnetic and electrostatic effects are negligible. In the case of a Newtonian fluid and if the only applied body force is the gravitational potential, the equation of momentum conservation is defined as follows:

$$\rho \frac{\mathrm{D}\mathbf{v}}{\mathrm{D}t} = -\boldsymbol{\nabla} P + \boldsymbol{\nabla}.\left\{\eta\left[\boldsymbol{\nabla}\mathbf{v} + (\boldsymbol{\nabla}\mathbf{v})^T - \frac{2}{3}(\boldsymbol{\nabla}.\mathbf{v})\boldsymbol{I}\right]\right\} + \rho\mathbf{g} \tag{2.3}$$

with η the dynamic viscosity. This equation is called the Navier-Stokes equation.

Energy conservation corresponds to the application of the first and second principles of thermodynamics. Any change in the internal energy of a parcel of fluid corresponds to the advection of energy across its surface Σ by a macroscopic flow, a transfer of energy through Σ via diffusion or conduction, the work of body and surface forces and volumetrically distributed internal heating. The second principle of thermodynamics states that entropy cannot decrease in an isolated system. From the thermal energy equation describing the temporal evolution of entropy S of a parcel of fluid $\rho T \frac{\mathrm{D}S}{\mathrm{D}t} = \boldsymbol{\tau} : \boldsymbol{\nabla v} + k\boldsymbol{\nabla}^2 T + \rho H$, the thermodynamic decomposition $\frac{\mathrm{D}S}{\mathrm{D}t} = \left(\frac{\partial S}{\partial T}\right)_P \frac{\mathrm{D}T}{\mathrm{D}t} + \left(\frac{\partial S}{\partial P}\right)_T \frac{\mathrm{D}P}{\mathrm{D}t}$ and the thermodynamic identities $\left(\frac{\partial S}{\partial T}\right)_P = \frac{c_p}{T}$ and $\left(\frac{\partial S}{\partial P}\right)_T = -\frac{\alpha}{\rho}$, the equation of energy conservation is:

$$\frac{c_p}{T}\frac{\mathrm{D}T}{\mathrm{D}t} - \frac{\alpha}{\rho}\frac{\mathrm{D}P}{\mathrm{D}t} = \boldsymbol{\tau} : \boldsymbol{\nabla v} + k\boldsymbol{\nabla}^2 T + \rho H \tag{2.4}$$

with c_p the specific heat at constant pressure, α the thermal expansivity, k the thermal conductivity, T the temperature and H the rate of internal heat production. $\boldsymbol{\tau} : \boldsymbol{\nabla v}$ represents the viscous dissipation, $k\nabla^2 T$ represents diffusion of heat by conduction (Fourier's law), with k the thermal diffusivity constant and ρH is the term of internal heat production. The term on the left hand side is the rate of change of temperature due to adiabatic compression or expansion. From this term and the hydrostatic relation:

$$\boldsymbol{\nabla} P = \rho \boldsymbol{g}, \tag{2.5}$$

the adiabatic gradient can be defined:

$$\left(\frac{\partial T}{\partial z}\right)_S = \frac{\alpha T \boldsymbol{g}}{c_p} \tag{2.6}$$

with z the depth.

Complementary to these equations of conservation, **Poisson's equation** describes the links between gravitational potential Ψ and density ρ and corresponds to:

$$\boldsymbol{\nabla}^2 \boldsymbol{\Psi} = -4\pi G \rho \tag{2.7}$$

with G the gravitational constant, ∇^2 the Laplacian operator and $\mathbf{g} = \boldsymbol{\nabla \Psi}$.

Reference state

Before solving the equations of conservation 2.1, 2.2 and 2.4, a reference state $\bar{X}$ is defined for the variables P, T, ρ and $\boldsymbol{g}$. The *prime* superscript represents perturbations from this reference state. The reference state is a mathematical tool which facilitates the consideration of basic equations. In general, the reference state represents a motionless and steady fluid and varies with only one spatial variable (depth z). When defining the reference state, the thermodynamic variables α (thermal expansivity), c_p (specific heat capacity), k (thermal conductivity) and χ_T (isothermal compressibility) must be defined in a thermodynamically consistent way.

A large approximation resides in the definition of $\bar{\rho}$, which represents the equation of state of mantle rocks $\rho(P,T)$. Most mantle density changes are due to hydrostatic compression (pressure causes a 65 % increase of density throughout the mantle) while density variations caused by convective motions are relatively small. Therefore, the equation of state can be linearized:

$$\begin{aligned}\rho = \bar{\rho}(\bar{P},\bar{T}) + \rho' &= \bar{\rho}(\bar{P},\bar{T}) + \left(\frac{\overline{\partial\rho}}{\partial P}\right)_T P' + \left(\frac{\overline{\partial\rho}}{\partial T}\right)_P T' \\ &= \bar{\rho}(\bar{P},\bar{T}) + \bar{\rho}\bar{\chi_T}P' - \bar{\alpha}\bar{\rho}T'\end{aligned} \tag{2.8}$$

where $\bar{\rho}(\bar{P},\bar{T})$ represents the reference state for ρ and $\rho' = \bar{\rho}\bar{\chi_T}P' - \bar{\alpha}\bar{\rho}T'$ is the departure from this reference state.

The gravitational acceleration is defined as $\boldsymbol{g} = \bar{\boldsymbol{g}} + \boldsymbol{g'}$, with $\bar{\boldsymbol{g}} = \boldsymbol{\nabla}\bar{\boldsymbol{\Psi}}$ and $\boldsymbol{g'}$ the perturbed gravitational acceleration. The reference state $\bar{P}$ for pressure is obtained from the integration of the hydrostatic relation 2.5. Reference temperature $\bar{T}$ is deduced from the adiabatic gradient 2.6.

Non-dimensionalization

All variables of the studied system are usually non-dimensionalized prior to evaluating their values and evolution. All variables can be scaled using representative constant scaling factors, denoted by the subscript "0". Different reference parameters can be used to dimensionalize the different equations of convection (e.g. Schubert et al. (2001), Ricard (2015), Yoshida (2017)). Typical reference values used in the following chapters are detailed in table 2.1.

Table 2.1: Non-dimensional and dimensional reference parameters

Parameter	Non-dim. value	Dim. value
Reference length parameter (mantle depth, D_0)	1	2,890 km
Reference gravity parameter (gravitational acceleration, g_0)	1	9.81 $\mathrm{m{\cdot}s^{-2}}$
Reference thermal conductivity (k_0)	1	3.15 $\mathrm{W{\cdot}m^{-1}{\cdot}K^{-1}}$
Reference specific heat capacity (c_{p_0})	1	1250 $\mathrm{J\ kg^{-1}{\cdot}K^{-1}}$
Reference thermal diffusivity coefficient ($\kappa_0 = \frac{k_0}{\rho_0 c_{p_0}}$)	1	10^{-6} $\mathrm{m^2{\cdot}s^{-1}}$
Reference time scale (thermal diffusion time, $t_0 = \frac{D_0^2}{\kappa_0^*}$)	1	8.35 10^{18} s,
Reference surface thermal expansivity (α_0)	1	3 10^{-5} $\mathrm{K^{-1}}$
Reference viscosity parameter (η_0)	1	1 10^{22} Pa·s
Reference surface density (ρ_0)	1	3,300 $\mathrm{kg{\cdot}m^{-3}}$
Reference isothermal compressibility (χ_{T_0})	1	1 10^{-11} $\mathrm{Pa^{-1}}$
Reference temperature parameter (non-adiabatic temperature difference throughout the mantle, ΔT_0)	1	2500 K

* as defined in our models. See section 3.3 for details.

From a combination of those reference parameters, any dimensionless quantity can be obtained. Dimensionless variables are denoted by the superscript "*" and correspond to:

- $z^{*'} = \frac{z'}{D_0}$
- $P^{*'} = P' \frac{D_0^2 \rho_0 c_{p_0}}{\eta_0 k_0}$
- $\bar{\alpha}^* = \frac{\bar{\alpha}}{\alpha_0}$
- $t^{*'} = t' \frac{\kappa_0}{D_0^2}$
- $T^{*'} = \frac{T'}{\Delta T_0}$
- $\bar{\chi}_T^* = \frac{\bar{\chi}_T}{\chi_{T_0}}$
- $\boldsymbol{v^{*'}} = \boldsymbol{v'} \frac{D_0 \rho_0 c_{p_0}}{k_0}$
- $\rho^{*'} = \frac{\rho'}{\rho_0}$
- $\boldsymbol{g^{*'}} = \boldsymbol{\nabla \Psi^{*'}}$

In Equation 2.2, the perturbed state for the gravitational body force consists of two terms: $\rho^{*'}\bar{\boldsymbol{g}}^* + \bar{\rho}^*\boldsymbol{g^{*'}} = \rho^{*'}\bar{\boldsymbol{g}}^* + \bar{\rho}^*\boldsymbol{\nabla \Psi^{*'}}$. This second term $\bar{\rho}^*\boldsymbol{\nabla \Psi^{*'}}$ is called self-gravitation and accounts for gravitational perturbations induced by mantle convection. Therefore, when solving for both convection and gravitational potential, Equation 2.7 has to be solved and this term has to be added to the momentum equation 2.2. For clarity, since all the following equations refer to perturbations of the reference state, the prime notation is omitted.

The non-dimensionalization step makes it possible to compare the properties and dynamics of systems differing by their size, composition, thermodynamic properties, through the direct comparison of dimensionless numbers that arise naturally from the non-dimensionalization of Equations 2.8, 2.1, 2.2 and 2.4. For example, the non-dimensionalization of the equation of state 2.8 gives:

$$\frac{\rho^*}{\bar{\rho}} = 1 + \overline{\chi_T^*} P^* \mathrm{M}^2 \,\mathrm{Pr} - \bar{\alpha}^* T^* \nu \tag{2.9}$$

with:

- the Mach number, M, representing the ratio thermal diffusive velocity to the sound speed.

$M \approx 10^{-9}$ for the mantle.

- the Prandtl number, $\mathrm{Pr} = \frac{\eta_0}{\rho_0 \kappa_0} \approx 10^{26}$ for the mantle, representing the ratio momentum diffusion to heat diffusion.

- and the fractional density change of mantle rocks due to non-adiabatic temperature variations $\nu = \alpha_0 \Delta T_0 \approx 10^{-2}$ for the mantle.

From the non-dimensionalization of Equations 2.1, 2.2 and 2.4, we can also define:

- the Grüneisen parameter, $\mathrm{Gr} = \frac{\alpha_0 K_{a0}}{\rho_0 c_{p0}} \approx 1$ for the mantle, with K_{a0} the mantle reference bulk modulus

- the Dissipation number, $\mathrm{Di} = \frac{\alpha_0 g_0, D_0}{c_{p0}}$. $\mathrm{Di} \approx 0.5$ for the mantle,

- the Compressibility number, $\mathrm{Co} = \frac{\mathrm{Di}}{\mathrm{Gr}} \approx 0.5$ for the mantle,

- and the Rayleigh number, $\mathrm{Ra} = \frac{\alpha_0 \rho_0 g_0 D_0^3 \Delta T_0}{\eta_0 \kappa_0} > 10^7$ for the mantle.

From the values of those dimensionless numbers, Equations 2.8, 2.1, 2.2 and 2.4 can be further simplified in order to solve them for the problem of mantle convection. All the following equations are non-dimensionalized. For simplicity, the * notation is dropped.

2.1.1.3 Useful approximations in the case of mantle convection

Anelastic Liquid Approximation (ALA)

In the case of the terrestrial mantle, the Prandtl number is of the order of 10^{26}, meaning that inertia is negligible in the equation of momentum conservation 2.2. This means that if the internal distribution of density anomalies is known, the flow can be computed independently from the temperature equation (*instantaneous models*, *e.g.* Hager and O'Connell (1979), Becker and Faccenna (2011)). The Mach number is of the order of 10^{-9}, meaning that short wavelength phenomena induced by sound wave do not affect density (Ogura and Phillips, 1962). The **Anelastic Liquid Approximation** (ALA) can therefore be used to model mantle convection by assuming $\mathrm{M}^2\mathrm{Pr} \longrightarrow 0$ (Jarvis and McKenzie, 1980, McKenzie et al., 1974, Schmeling, 1989, Schubert et al., 2001). Under this approximation, the

equation of state 2.9 is assumed to be independent of time (Ogura and Phillips, 1962):

$$\frac{1}{\bar{\rho}}\frac{\partial \rho}{\partial t} = \overline{\chi_T}\mathrm{M}^2\mathrm{Pr}\left(\frac{\partial P}{\partial t}\right) - \bar{\alpha}\nu\left(\frac{\partial T}{\partial t}\right) = 0 \tag{2.10}$$

This definition implies that the fraction of density change due to thermal expansion $\nu \longrightarrow 0$ (Yoshida, 2017).

Reference state: From the reference equation of state for density 2.9, the following equation of state can be defined:

$$\rho = \bar{\rho}(1 - \bar{\alpha}T\nu) \tag{2.11}$$

In the ALA approximation, the reference state can be defined in two ways:

- By considering $\bar{\alpha}$, $\bar{c_P}$, $\bar{\boldsymbol{g}}$ and $\bar{\mathrm{Gr}}$ as constant and the adiabatic reference state, the following Adams-Williamson reference state (Yoshida, 2017) can be defined:

$$\begin{aligned} \bar{P}(z) &= \bar{P}_0 + \frac{\mathrm{Co}}{\mathrm{M}^2\,\mathrm{Pr}}\bar{\rho_a}\bar{g}(D_0 - z) \\ \bar{T}(z) &= \bar{T}_0 \times \exp(\mathrm{Di}\frac{\bar{\alpha}\bar{g}}{\bar{c_p}}(D_0 - z)) \\ \bar{\rho}(z) &= \bar{\rho}_0 \times \exp(\mathrm{Co}(D_0 - z)) \end{aligned} \tag{2.12}$$

  However, a careful interpretation of mantle convection models using this reference state is needed since the exponential increase of the reference mantle temperature gradient with depth is likely to stabilize the lower mantle reference state against convection (Schubert et al., 2001).

- In the other reference state (*e.g.* Glatzmaier, 1988), $\bar{\mathrm{Gr}}$ is constant and the state of reference is considered as adiabatic, polytropic (the bulk modulus is a linear function of pressure, which correspond to the Murnaghan state, Murnaghan (1951)) and hydrostatic. This makes it possible to define $\bar{P}$, $\bar{\alpha}$ and $\bar{T}$ self-consistently as a function of $\bar{\rho}$ from laboratory experiments (*e.g.* Chopelas and Boehler, 1992).

Conservation equations In the ALA approximation, conservation equations simplify as:

$$
\begin{aligned}
\boldsymbol{\nabla}.(\bar{\rho}\mathbf{v}) =& 0 \\
0 =& -\boldsymbol{\nabla}P + \boldsymbol{\nabla}.\boldsymbol{\tau} && \textit{(surface stresses)} \\
& -\bar{\rho}\bar{g}\bar{\chi_T}P\mathrm{Co}\frac{c_{p0}}{c_{v0}}\boldsymbol{e_r} && \textit{(pressure-driven buoyancy term)} \\
& +\bar{\rho}\bar{g}\bar{\alpha}T\mathrm{Ra}\boldsymbol{e_r} && \textit{(gravitational body force)} \\
& +\bar{\rho}\boldsymbol{\nabla}\Psi && \textit{(self-gravitation)} \\
\bar{\rho}\bar{c_p}\frac{\mathrm{D}T}{\mathrm{D}t} =& \bar{k}\boldsymbol{\nabla}^2 T && \textit{(heat diffusion)} \\
& +\bar{\alpha}T\bar{\rho}v_r\bar{\boldsymbol{g}}\mathrm{Di} && \textit{(adiabatic compression)} \\
& +\frac{\mathrm{Di}}{Ra}\boldsymbol{\tau}:\boldsymbol{\nabla}\boldsymbol{v} && \textit{(viscous dissipation)} \\
& +\bar{\rho}H_n && \textit{(radioactive production)}
\end{aligned}
\tag{2.13}
$$

with $\mathbf{e_r}$ the radial unit vector, v_r the radial component of velocity, Ψ the gravitational potential, c_{v0} the reference heat capacity at constant volume and H_n the internal heating number corresponding to $H_n = \frac{HD_0^2}{\kappa_0 c_{p0}\Delta T}$. Zhong et al. (2008) demonstrated that the self-gravitation term is important to calculate the geoid, but does not influence the flow. Therefore, in the following, this term is neglected.

Truncated Anelastic Liquid Approximation (TALA)

The use of the **Truncated Anelastic Liquid Approximation** (TALA) is motivated by the fact that the decrease of the pressure-driven buoyancy term from the energy equation simplifies the numerical simulation and improves the computational efficiency (Ita and King, 1994, Jarvis and McKenzie, 1980, Steinbach et al., 1989). The averaged surface heat flux, the averaged surface velocity, the Nusselt number, the viscous dissipation and the work differ by a few percents among the ALA and the TALA. Yoshida (2017) unified ALA and TALA by explaining that when $M^2 Pr \longrightarrow 0$, then $\nu \longrightarrow 0$ automatically. However, the Use of the TALA approximation results in an imbalance between the total viscous heating and the total adiabatic heating (Leng and Zhong, 2008).

The ALA and TALA are used in the mantle to account for mantle compressibility, which corresponds to a change of density with pressure. According to these approximations, thermal instabilities are driven by the departure of the fluid temperature from an adiabatic gradient. Indeed, if the fluid is

superadiabatic (the geotherm gradient is steeper than the adiabatic gradient of about 0.03 $K \cdot km^{-1}$), instabilities will occur while it will remain stable if subadiabatic (the geotherm gradient is lower than the adiabatic one). In mantle convective cells, adiabaticity is dominant and sustained by large-scale vigorous convective motions while superadiabaticity is confined to the TBLs. Since the ALA and TALA are only valid for fluids in conditions staying close to adiabatic, those approximations seem to be a good assumption. However, they have been questioned by Jeanloz and Morris (1987), Bunge et al. (2001) and Alboussière and Ricard (2017) in the case of mantle convection. Indeed, the presence of TBLs, radioactive heating, dissipation and diffusion lead to dramatic deviations of the mantle's geotherm from adiabatic conditions (up to a few hundred degrees of difference). Therefore, the ALA and TALA approximations may not be fully applicable to the mantle.

However, those approximations have been used in numerical models in order to study the effect of compressibility on convective planforms (Glatzmaier, 1988), on mantle plumes (Zhang and Yuen, 1996), or the dynamics of deep-mantle (Deschamps and Tackley, 2008). In this thesis, I do not model compressible convection since it requires extra computational time because of the pressure-driven buoyancy term in the energy equation, and because of the dependence of the onset of mantle convective instabilities on assumptions related to the shape of the reference geotherm.

Extended Boussinesq Approximation (EBA)

The **Extended Boussinesq Approximation** (EBA) was detailed at length in Oxburgh and Turcotte (1978), Jarvis and McKenzie (1980) and Christensen and Yuen (1985). In this approximation, the fluid is treated as incompressible, including across phase changes, except for the driving force by the buoyancy term as for the Boussinesq approximation (BA). The pressure-induced buoyancy term in the momentum equation is ignored wheareas the energy equation is the same as ALA and TALA. Contrary to the BA, the EBA accounts for the adiabatic gradient across the mantle and shear heating in the energy equation. The EBA can be obtained from the ALA or the TALA by setting the Gr to infinity to get $Co \longrightarrow 0$.

Boussinesq Approximation (BA)

Under the **Boussinesq Approximation** (BA), the compressibility number and the dissipation number are equal to zero. The system is approximated by an incompressible fluid behaviour, and is therefore more efficient in terms of computation since no variation of the material properties are assumed through depth and no adiabatic temperature difference across the mantle is considered. This approximation is valid only if $\mathrm{Co} = \frac{\mathrm{Di}}{\mathrm{Gr}} \ll 1$, which is not the case for Earth's mantle ($\mathrm{Di} \approx 0.5$ and $\mathrm{Gr} \approx 1$). Although considered as a significant approximation, mantle convection still occurs, driven by density variations resulting from the non-adiabatic temperature difference across the mantle.

Reference state In the BA, no depth-dependance of thermal expansivity, thermal conductivity and density is classically considered. The reference pressure is the hydrostatic pressure, the reference temperature corresponds to a constant temperature and the equation of state for density 2.9 reduces to:

$$\rho = \rho_0(1 - \bar{\alpha}T) \tag{2.14}$$

Conservation equations In the BA approximation, the conservation equations reduce to:

$$\begin{aligned} \boldsymbol{\nabla}.\mathbf{v} &= 0 \\ 0 &= -\boldsymbol{\nabla}P + \boldsymbol{\nabla}.\left\{\eta\left[\boldsymbol{\nabla}\mathbf{v} + (\boldsymbol{\nabla}\mathbf{v})^T - \frac{2}{3}(\boldsymbol{\nabla}.\mathbf{v})\boldsymbol{I}\right]\right\} + \bar{\rho}\bar{g}\bar{\alpha}T\mathrm{Ra}\boldsymbol{e_r} \\ \bar{\rho}\bar{c}_p\frac{\mathrm{D}T}{\mathrm{D}t} &= \bar{k}\boldsymbol{\nabla}^2T + \bar{\rho}H_n \end{aligned} \tag{2.15}$$

In the following sections, I use the Boussinesq approximation. Although simplifications are quite significant, this approximation has been widely used to model mantle convection, with results comparing favorably with Earth's geoid (Hager, 1984) or seismic tomography models (Becker and Boschi, 2002).

All the approximations formulated above are independent from the viscosity structure of the mantle and the presence of phase changes. I review the specifics of Earth's mantle rheology in section 2.1.3.

2.1.2 Modeling thermo-chemical convection

In Earth's mantle, density variations are not only due to thermal anomalies. As described in Chapter 1, many chemical and phase changes have to be taken into account when modeling mantle convection, which requires modifications and additions to the equations formulated in section 2.1.1.3. For example, the water content of mantle rocks (which is thought to be non-uniform) is likely to change the viscosity and rheological properties of mantle material. The presence of magma pockets in the uppermost mantle or at the CMB (called Ultra Low Velocity Zones (ULVZ, Garnero et al., 1998)) are likely to have a different composition than the surrounding solid material and can also potentially affect locally density gradients and therefore participate in modifying the planform of convection. Fractionation and differentiation mechanisms are also responsible for changing the composition of the solid mantle material surrounding such pockets of liquid. Phase changes present throughout the mantle and the viscosity increase near the transition zone also affect the way mantle material convects. Finally, two large-scale heterogeneities with a potentially different composition are located at the base of the mantle and are likely to interact with large-scale mantle convection (*e.g.* McNamara and Zhong, 2005).

Phase changes and compositional differences lead to a modification of the equation of state 2.8 in order to maintain the Gibbs energy to its minimum:

$$\rho = \bar{\rho}(1 - \bar{\alpha}T\nu + \sum_{i=1}^{N_p} \Delta\rho_i \Gamma_i + \sum_{j=1}^{N_c} \Delta\rho_j C_j) \tag{2.16}$$

with Γ_i, the equation describing the mineralogical phase transitions, usually defined by a step function (Christensen and Yuen, 1985), N_p, the number of phases in the system, C_j, the chemical components, and N_c, the number of chemical changes. As a consequence, this impacts the equations of momentum conservation (by adding extra contributions to the gravitational force, with the intervention of phase Rayleigh and compositional Rayleigh numbers) and energy conservation (by adding an extra term of latent heat) in the anelastic liquid approximation. However, in the Boussinesq approximation, these effects are usually neglected. The buoyancy ratio (see Equation 1.9) can be used to add mantle chemical variations, such as continents or those potentially present in the seismically imaged LLSVPs.

In addition to those changes in the equations of mass, momentum and energy conservation, the presence of compositional heterogeneities requires the conservation of those compositional contrasts by adding the following law for the advection of chemically different particles:

$$\frac{\mathrm{D}C}{\mathrm{D}t} = \frac{1}{\mathrm{Le}}\boldsymbol{\nabla}^2 C \tag{2.17}$$

with C the compositional field an Le is the Lewis number, which is the ratio of thermal diffusivity to chemical diffusivity. In the models, chemical diffusion is neglected and $\frac{\mathrm{D}C}{\mathrm{D}t} = 0$. As a consequence, the momentum equation 2.15 has to be transformed in order to account for chemical buoyancy (Van Keken et al., 1997, Tackley, 1998, Tackley and King, 2003):

$$0 = -\nabla P + \boldsymbol{\nabla}.\boldsymbol{\tau} + \bar{\rho}\bar{g}(\bar{\alpha}T - BC)\mathrm{Ra}\mathbf{e_r} \tag{2.18}$$

with B the buoyancy number defined in Equation 1.9.

In some of the models presented in this thesis, a basal thermo-chemical layer is considered. Its initial uniform thickness is set to 200-300 km depending on the models, and its density excess is about 3 % compared with the ambient mantle, in agreement with estimates for Earth (*e.g.* Kellogg et al., 1999). Therefore, as mantle convection deforms the modeled basal chemical layers, they remain stable during time periods exceeding 10^9 yr and reach a maximal thickness which does not exceed 1,000 km, as predicted by seismic tomography models (Garnero et al., 2016). Model parameters used to represent continents are detailed in section 2.2.2.

2.1.3 Modeling mantle rheology

As mentioned in section 1.1.2.2, Earth's mantle is solid and reacts differently to stresses of different timescales. As shown on Fig. 2.1, it deforms elastically, plastically or viscously depending on the timescales of the deformation processes. Since I am interested in modeling mantle convection, I will approximate Earth's mantle rheology by a viscous fluid.

An important unknown regarding the modeling of Earth's mantle convective planform is its viscosity structure. First attempts to infer mantle viscosity structure from surface observations relied on the understanding of plate surface velocities, post-glacial rebound timescales, lithospheric stress field,

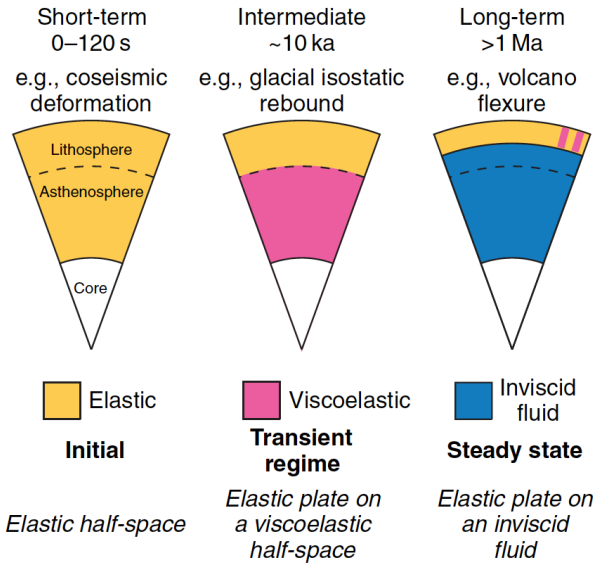


Figure 2.1: Schematic diagram showing how Earth's mantle and lithosphere respond to loads of different timescales. The bold text corresponds to the deformation regime corresponding to each load duration. The italic text indicates the most commonly used deformation models at each timescale (Watts and Schubert, 2007).

geoid and topographic anomalies (Hager and O'Connell, 1981, Bai et al., 1992, Hager et al., 1985, Ricard et al., 1984, Ricard and Wuming, 1991, Ricard et al., 1993). Mineralogical studies supported observations and tended to demonstrate that upper mantle's viscosity is comprised between 3×10^{20} and 3×10^{21} Pa·s (Hirth and Kohlstedt, 2003). As mentioned in section 2.1.1.1, the mantle's macroscopic motions hinge on microscopic plastic deformations, which depend on both mineral properties (grain-size, water content, composition) and thermodynamic conditions (temperature, pressure, stress). As a consequence, mantle viscosity can be described thanks to the following law:

$$\eta = A J_2^{-n} d^m \exp\left(\frac{E_a + PV_a}{RT}\right) \tag{2.19}$$

with E_a and V_a the activation energy and volume, P and T the temperature and pressure, A a multiplicative factor depending on the composition, the melt proportion and the water content of the considered material, J_2 the second stress invariant, d the grain-size, m and n the grain-size and the stress exponents (Weertman and Weertman, 1975). Depending on the mechanism of deformation (dislocation creep, diffusion creep, climbing, grain boundary diffusion), those parameters and exponents are likely to change.

As written in Equation 2.19, mantle viscosity is strongly thermally activated. Depending on the deformation mechanism, E_a varies between 300 and 600 kJ·mol^{-1} (Hirth and Kohlstedt, 2003), which means that an increase of 100 K corresponds to a ten times decrease in viscosity. This strong thermal dependence of mantle viscosity on temperature is above all important for modeling lithosphere/mantle viscosity contrasts (see details in section 2.2).

Besides the strong temperature dependence of mantle's viscosity, it also depends on depth, through the parameter V_a, which should be of the order of 10 cm^3·mol^{-1}. Viscosity increase with depth leads to increased stability of hotspots (Steinberger and O'Connell, 1998) and the existence of larger-scale lower mantle convection (Bunge and Richards, 1996). Thanks to the forward modeling of instantaneous flow and its impact on surface observables or the inversion of those surface observations, many authors also concluded that Earth's mantle viscosity has to increase by a factor of 30-100 between the upper and the lower mantle in order to fit both post-glacial rebound observations and geoid anomalies (*e.g.* Nakiboglu and Lambeck, 1980, Ricard and Wuming, 1991). Seismic topographic models (Van der Hilst et al., 1997) have contributed to validate such an increase of mantle viscosity at the transition zone from the observation of the thickening of slabs in the lower mantle by a factor 3-5 and their ponding near the transition zone. Other studies propose the existence of a viscosity increase at about 1,000 km depth, based on the reevaluation of the non-hydrostatic geoid (Rudolph et al., 2015), on the ponding of numerous slabs at this depth (Ballmer et al., 2015, Goes et al., 2017) or the compositional layering of basalt-enriched material at this depth (as described by King et al., 2015, for the transition zone).

Mineralogical experiments have shown that low stress, fine-grained rocks and temperature favor dislocation creep while high stress, coarse-grained rocks and temperature favor diffusion creep (Karato et al., 1993). Therefore, at Earth's mantle conditions, the decrease of deviatoric stresses with increasing depth tend to favor the diffusive regime, which depends primarily on temperature and grain-size. This law is Newtonian. In contrast, dislocation creep can be formalized by a non Newtonian power law depending on dislocation climb or grain boundary sliding. Mantle convection models usually use dislocation creep in order to describe upper-mantle behaviour. Indeed, observed upper-mantle anisotropy is controlled by dislocations (Nishimura and Forsyth, 1989, Mainprice et al., 2005), slab initiations seem to be governed by a non-Newtonian rheology (Billen and Hirth, 2005) and experiments on dunite

at high pressure and temperature suggest that deformations occur primarily on the dislocation regime (Hirth and Kohlstedt, 2003). In the models of whole-mantle convection, I nevertheless use the diffusive regime to model mantle rheology. As detailed in section 2.2.1.2, only the parts of lithosphere undergoing large stresses will act as a non Newtonian fluid. Moreover, Christensen (1984c) showed that a non Newtonian behaviour can be imitated by using a Newtonian law with a reduced value of activation enthalpy $H_a = E_a + PV_a$.

In the models, I use the following Arrhenius viscosity law, which depends exponentially on both pressure and temperature:

$$\eta(z,T) = \eta_0(z) \times \exp\left(A + \frac{E_a + \Pi(z)V_a}{RT}\right) \tag{2.20}$$

with A chosen so that $\eta = \eta_0$ for $T = 1300$ K (the *a priori* temperature at the base of the lithosphere), E_a the activation energy taken equal to 142 kJ·mol^{-1}, $\Pi(z)$ is the static pressure, V_a is the activation volume, R is the gas constant and T is the temperature. A viscosity jump by a factor 30 is also included at the transition zone d_0 (660 km depth):

$$\eta_0(z) = \eta_{ref} \exp\left(\log(30)\left[1 - 0.5\left(1 - \tanh\left(\frac{d_0 - z}{d_{jump}}\right)\right)\right]\right) \tag{2.21}$$

with η_{ref} being the reference non-dimensionalized viscosity value producing an average value of 1 for $\eta_0(z)$ and $2d_{jump} = 100$ km the thickness of the factor-30 viscosity jump.

Another way to create variations of mantle properties with depth is to model compressibility, to add compositional heterogeneities or to account for depth-dependent thermal conductivity or thermal expansivity. The first ways have already been described above. Thermal conductivity should increase with phase transitions (Badro et al., 2004) and with depth by a factor 2-3 throughout the mantle (Hofmeister, 1999). Even if the effect of thermal conductivity on the planform of convection is potentially important for modeling slabs (Dubuffet et al., 2000), I neglect it. Thermal expansivity is thought to decrease throughout the mantle by a factor between 3 and 5 (Chopelas and Boehler, 1992), as a result of density and temperature increase with depth (see Equation 2.14). As a consequence, convection in the lower mantle is less vigorous, thermal anomalies are wider and buoyancy forces are decreased (Hansen et al., 1993). In the following studies, I consider a thermal expansivity decrease

with depth, from 3×10^{-5} K^{-1} at the surface to 1×10^{-5} K^{-1} at the CMB (Fig. 2.2). Even if it is contradictory with the BA stating that mantle thermodynamic variables are independent on depth, it makes it possible to account for an extra source of buoyancy in the momentum equation, without the need of adding compressibility, viscous dissipation and pressure-driven buoyancy force.

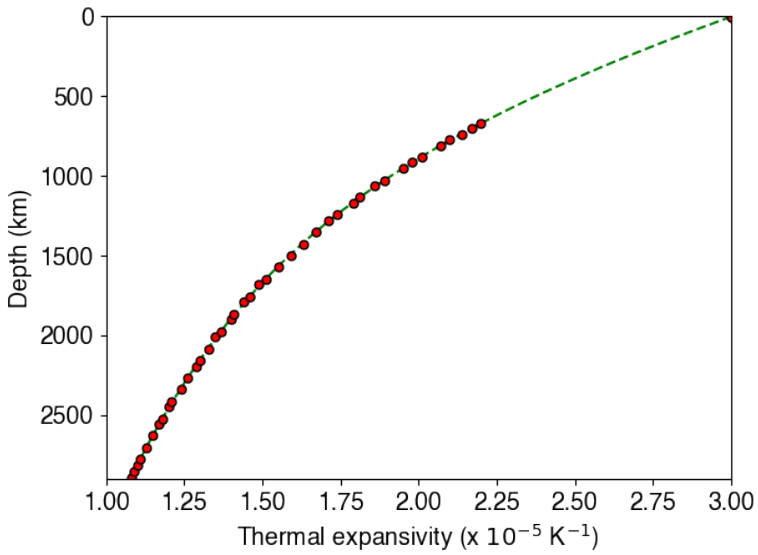


Figure 2.2: Red dots show the thermal expansivity dependence on depth deduced from Raman frequency shifts measurements of $MgSiO_3$-perovskite at high pressure (Gillet et al., 2000). The green dashed line represents the fit of those experimental data used in the following chapters.

Finally, lateral variations of viscosity are also likely to be present throughout the mantle, since lateral variations of temperature are present. They are sometimes neglected in numerical models of mantle convection using only a radial profile of viscosity that are in relatively good agreement with geoid observations (*e.g.* Hager and Richards, 1989). However, they are particularly important in time-dependent models and for the generation of plate-like tectonics. Moreover, they play a potentially important role in the spatial distribution of topography and geoid anomalies (Zhang and Christensen, 1993, Cadek and Fleitout, 2003) and provide a driving mechanism for net rotation between lithosphere and mantle (Ricard et al., 1991). Therefore, in the models, I account for strong lateral viscosity variations.

2.2 Numerical modeling of lithosphere dynamics

2.2.1 Numerical models of mantle convection with plate-like tectonics

2.2.1.1 Rheology of Earth's lithosphere

As mentioned in section 1.1.2.2 and on Fig. 2.1, Earth's surface behaviour differs according to the timescales of the processes contributing to its deformation. Evidence for an elastic behaviour comprises mechanisms of seismic waves propagation, lithospheric flexure due to volcanic loading, sedimentary basins or the bending of subducting plates for which the Maxwell time is of the order of 1-10 Myr. In the extreme case of a lithosphere viscosity of 10^{27} Pa·s, it can reach 450 Myr at most (Patocka et al., 2017), meaning that over the timescales studied in the models, elasticity can play a substantial role.

Non-elastic deformation in the lithosphere can take different forms (faults, folds at all spatial scales), depending on temperature, pressure, the material composition, its water content and the rate of deformation. To study the rheological behaviour of lithospheric material submitted to stresses, scientists have developed high pressure and temperature experiments to build empiric laws describing different deformation regimes.

The most famous one is the Byerlee law (Byerlee, 1978), describing the brittle failure of rocks as a function of pressure.

$$\tau = C_0 + \tan(\phi)\sigma_n \tag{2.22}$$

where τ is the shear stress, σ_n is the normal stress, $\tan(\phi)$ is the friction coefficient, ϕ is the friction angle, and C_0 is the cohesive strength (< 20 MPa). This law shows that the brittle behaviour of lithospheric material is rather independent of the rock type, but depends on the water content and the stress field, and describes the geometry of faults in specific stress fields (friction angles of about 30° for most rocks, according to the Coulomb-Navier failure criterion which corresponds to $\tau = 0.85\ \sigma_n$ if $\sigma_n \leq 200$ MPa, or $\tau = 50$ MPa $+0.6\ \sigma_n$ if 200 MPa $< \sigma_n <$ 1700 MPa).

In contrast, ductile deformation such as folding of rocks depends highly on the rock type (Kirby and Kronenberg, 1987, Brace and Kohlstedt, 1980), pressure and temperature, and grain-size. It can be described by:

$$\dot{\varepsilon} = A f_W d^m \Delta\sigma^{-n} \exp\left(\frac{E_a + PV_a}{RT}\right) \tag{2.23}$$

with $\dot{\varepsilon}$ the shear strain-rate, $\Delta\sigma = \sigma_1 - \sigma_3$ the deviatoric stress (in the case of uni-axial deformation, otherwise, $\Delta\sigma$ is replaced by the second invariant of stress, J_2), A a multiplicative factor depending on the material, f_W the water fugacity factor, d the grain-size, m a diffusion constant and n the power law constant (Burov, 2007). Results from experimental studies in the ductile regime highly depend on the rate of deformation, and require extrapolations in order to be compared with tectonic strain-rates (Goetze and Evans, 1979).

When stresses reach a threshold, lithosphere starts to deform permanently, and continues to do so even if stress does not increase. This behaviour is called the plastic regime.

Earth's lithosphere behaves elasto-visco-plastically. The transition from the brittle to the viscous regime (brittle-ductile behaviour) is very broad (several tens of kilometers), complex and not well understood (Kohlstedt et al., 1995). However, different mechanical layers can still be defined based on their main deformation mechanism: a brittle upper crust, a ductile lower crust and a ductile upper mantle with a potential brittle component depending on strain rate and temperature (Burov et al., 2006). By combining the elastic, the brittle, the plastic and the ductile rheological laws and extrapolating them to geological spatial and temporal scales, Goetze and Evans (1979) defined a *Yield-Strength Envelope* (YSE) for the lithosphere corresponding to a differential stress contour $\Delta\sigma_{\max}(z)$ defined as:

$$\Delta\sigma_{\max}(z) = \text{sign}(\varepsilon)\,\min(|\sigma^b|, |\sigma^d|) \tag{2.24}$$

with $\text{sign}(\varepsilon) = 1$ for extension and -1 for compression, and σ^b and σ^d the maximal brittle and ductile yield stresses. They combine with the elastic stress for a given strain $\sigma(\varepsilon)^e$ to define a differential stress $\Delta\sigma(\varepsilon)$ varying with depth and spatial strength variations:

$$\Delta\sigma(\varepsilon) = \text{sign}(\varepsilon)\,\min(|\Delta\sigma_{\max}(z)|, |\sigma(\varepsilon)^e|) \tag{2.25}$$

From these equations, the YSE of the lithosphere depends on the long-term equivalent elastic thickness T_e of lithosphere which represents its apparent strength. Therefore, constraints of Earth's T_e from flexural processes provide estimates for the integrative strength of lithosphere (Burov and Diament, 1995, 1996, Watts, 2001). This concept of YSE applies well to oceanic lithosphere (Watts, 2001), but it remains problematic on continents and continental margins because of contradicting seismic

observations and elastic thickness estimates (*e.g.* Burov and Diament, 1995, Burov, 2010, 2011).

2.2.1.2 Modeling plate-like tectonics

Numerical modeling of the complexity of the rheology of the lithosphere requires to account for the whole diversity of rheological behaviours described above. If such a complexity is necessary for modeling seismic cycles (which correspond to short-term deformations by earthquakes interrupted by long periods of seismic loading due to locking processes at faults, and therefore require specific numerical methods to deal with a large range of timescales and lengthscales of deformation Lapusta et al. (*e.g.* adaptative timestepping, 2000)), only long-term deformation (corresponding to timescales longer than 1 Myr) is considered here. As shown on Fig. 2.1, Earth's lithosphere elasticity is likely to play a role at these timescales. However, the numerical modeling of the elastic behaviour of Earth's lithosphere requires to implement a Maxwell or a Kelvin-Voigt viscoelastic flow solver (which represent two viscoelastic descriptions of the behaviour of lithosphere) and an increased computational time. Those rheologies are already available in regional codes such as SLIM3D (Popov and Sobolev, 2008). However, until recently, the visco-elastic behaviour of the lithosphere had been neglected in global models of mantle convection with plate tectonics. Zhong (2002) considered the viscoelastic response of lithosphere to static internal loadings in order to calculate the surface geoid and topography. More recently, Golle et al. (2012) connected a viscous mantle flow with a viscoelastic shell representing the lithosphere of solid planets by using normal stresses from the convection model as a boundary layer for lithospheric deformations. Thielmann et al. (2015) suggested that accounting of both lithospheric viscoelasticity and a free-surface produce a significant effect on lithosphere distribution of stresses. Finally, Patocka et al. (2017) developed a fully viscoelastic treatment of mantle convection and lithosphere, in order to allow lateral variations of the thickness of the lithosphere and potential feedbacks between the mantle and the lithosphere viscoelastic layers. They also combined this method with a sticky-air layer domain in order to compute topography directly and showed the importance of both phenomena in the distribution of stresses in Earth's lithosphere while mantle convection is not substantially affected. However, such a code is computationally expensive and has only made it possible to model stagnant-lid planets so far, not Earth. Therefore, in the following Chapters, I neglect the effect of elasticity and approximate Earth's lithosphere by a viscoplastic layer.

In order to characterize the plate-like behaviour of numerical models, different diagnostics have been developed. The first characteristic of Earth's lithosphere is the fact that deformation is generally confined to narrow areas at plate boundaries. In order to quantify how surface deformation is distributed in numerical models, Weinstein and Olson (1992) defined *plateness* as a parameter describing the spatial distribution of surface velocities. According to the definition of Tackley (2000), plateness P is defined as :

$$P = 1 - \frac{f_{80}}{f_{80,const}} \tag{2.26}$$

where f_{80} is the proportion of the surface localizing 80 % of deformation and $f_{80,const}$ corresponds roughly to the proportion of the surface localising 80 % of deformation for an isoviscous model ($f_{80,const} = 0.6$ for a numerical model with internal heating and $\mathrm{Ra} = 10^6$). The plateness of Earth is not known but Kreemer et al. (2014) estimate that at least 14 % of Earth's surface is deforming. By assuming that this surface proportion represents 80 % of the total surface deformation, the plateness is 0.77, which is a lower bound for Earth. Another diagnostic is the mobility of the surface, calculated from the ratio between the RMS velocity of the surface and the RMS velocity of the whole-mantle (Tackley, 2000). Earth surface mobility is not known and difficult to characterize but it should be at least close to 1. Finally, other diagnostics are based on the comparison between the ratio of surface toroidal/poloidal motion between Earth and numerical models. On Earth, the ratio of toroidal to poloidal potential varies between 0.25 and 0.5 over the last 120 Myr (Lithgow-Bertelloni et al., 1993), as a result of the coupling between plate tectonics and mantle buoyancy sources (Gable et al., 1991). This leads to a ratio of surface toroidal/poloidal velocities close to 1 for Earth, and results in the generation of transform (strike-slip) boundaries. Moreover, an optimal plate-like tectonic regime should self-generate single-sided subductions and "passive" and shallow upwelling below ridges.

From studies of lithospheric patterns of deformation (Walcott, 1970), estimates of the viscosity of the lithosphere are at least of the order of 10^{24} Pa·s (for oceanic lithosphere), which is at least 4 orders of magnitude greater than estimates for the asthenosphere. According to Equations 2.19 and 2.23, the viscosity of the lithosphere strongly depends on temperature. Extrapolating a mantle Arrhenius law to the surface leads to a dramatic increase of viscosity (Fig. 2.3) and to stagnant-lid convection, which corresponds to the absence of surface motions (Christensen, 1984c, Solomatov and Moresi, 1996). Therefore, plate-like tectonics cannot be described by simple fluid behaviour and an extra mechanism is needed in order to honour the observations of multiple plates and subduction zones.

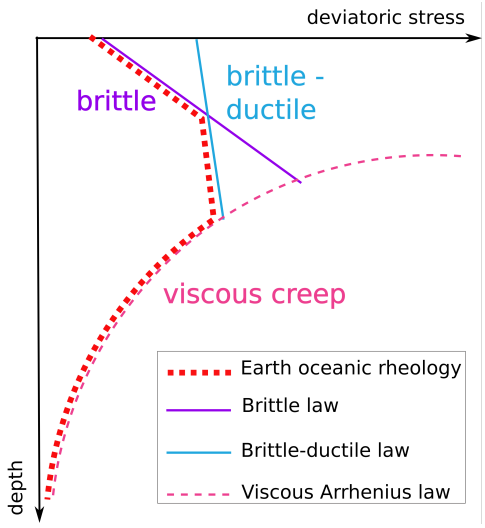


Figure 2.3: Schematic diagram showing Earth's oceanic lithosphere rheology (red dotted line, Kohlstedt et al. (1995)) in comparison to the rheological viscous law corresponding to Equation 2.23 (pink dashed line) and to two pseudo-plastic laws, one fitting the Byerlee law corresponding to a brittle behaviour (purple line) and the other fitting a combined brittle-ductile behaviour (cyan line). Not to scale.

Different ways to numerically model plate-like behaviour have therefore been developed. First attempts involved the imposition of surface plate velocities derived from tectonic reconstructions (*e.g.* Bunge et al., 2002, Spasojevic and Gurnis, 2012, Flament et al., 2013, Moucha et al., 2008) and slab geometry (Bower et al., 2015) in order to force the generation of plate boundaries and model time-dependent models of mantle/lithosphere. However, such a method does not account for the internal density field and may result in plate velocities inconsistent with mantle buoyancy forces. Therefore, Gable et al. (1991), Ricard and Vigny (1989), Monnereau and Quéré (2001) and Lowman et al. (2001) imposed plate boundaries but defined self-consistent surface velocities in a way that the average horizontal velocity and traction vanish at the surface. This is called the *force-balance* method. Another way is to impose weak zones in areas corresponding to plate boundaries (*e.g.* Gurnis, 1988). Deformation is therefore focussed at "fault-like structures" (shear localization). However, those methods do not generate self-consistent plate-like tectonics and are thus not helpful for understanding how Earth's surface lithosphere and mantle deformations interact.

The self-generation of evolving plate-like narrow boundaries concentrating deformation can be achieved by invoking "exotic" non-Newtonian rheologies in order to mimic the characteristics of Earth's plate tectonics, starting with the approximation of a viscous fluid. Indeed, depending on the different coefficients used in Equation 2.23, different behaviours can arise at the surface of mantle convection

models and therefore potentially generate plate-like tectonics (Fig. 2.4, Bercovici (2003)). The use of a Newtonian rheology ($n = 1$) cannot self-generate rigid plates separated by narrow zones of deformation. Non-Newtonian rheologies arise when $n > 1$. The stick-slip and pseudo-stick slip rheologies correspond to the weakening of lithosphere for increasing strain-rates. They generate a strong plate-like behaviour (Bercovici, 1993) characterized by a high strike-slip component (Tackley, 1998) but are non-linear and therefore difficult to implement in mantle convection codes. The Bingham plastic and viscoplastic rheologies describe discontinuous stress/strain-rate relationships. In the viscoplatic rheology, lithosphere deforms like a highly viscous material until stresses exceed a yield-stress. Past this threshold, material deforms at constant stress. This rheology does not produce a strong plate-like behaviour unless combined with reduced mantle viscosity due to melt generation below the lithosphere (Tackley, 2000) or a low viscosity asthenosphere (Richards et al., 2001).

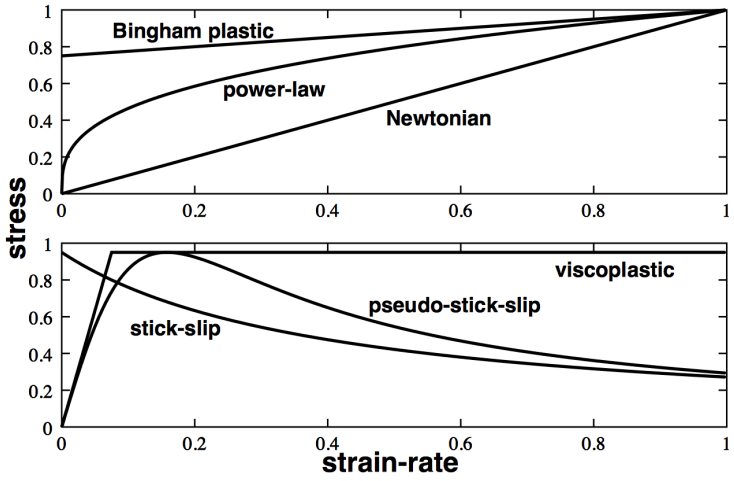


Figure 2.4: Stress versus strain-rate curves for various rheologies (Bercovici, 2003)

In the following chapters, the pseudo-plastic approximation is used. It is relatively easy to implement in numerical models of mantle convection and produces a plate-like behaviour characterized by rigid plates surrounded by narrow boundaries localizing deformation (*e.g.* Tackley, 2000, Richards et al., 2001, Foley and Becker, 2009, Van Heck and Tackley, 2008). Pseudo-plastic materials behave as Newtonian materials at low stresses until they reach a yield-stress σ_Y defined as follows:

$$\sigma_Y = \sigma_{Y_0} + z \times \mathrm{d}\sigma_Y \tag{2.27}$$

where σ_{Y_0} is the surface yield-stress which varies for different materials and $\mathrm{d}\sigma_Y$ is the yield-stress depth derivative (Fig. 2.3). When the yield stress is reached, the modeled lithosphere experiences a dramatic viscosity drop corresponding to:

$$\eta_Y = \frac{\sigma_Y}{2\dot{\varepsilon}_{\mathrm{II}}} \tag{2.28}$$

with $\dot{\varepsilon}_{\mathrm{II}} = \sqrt{0.5\dot{\varepsilon}_{ij}\dot{\varepsilon}_{ij}}$ the second invariant of the strain-rate tensor. Depending on the yield stress, different lithospheric and convective regimes can arise, as shown on Fig. 2.5. Models displaying a plate-like behaviour have a plateness close to one while it decreases rapidly for models in mobile-lid not plate-like regime and stagnant-lid models. Models in stagnant-lid regime have a mobility < 0.5 while this parameter is >1 for models with a low yield stress characterized by mobile-lid not plate like convection. The visco-plastic rheology makes it possible to generate important toroidal flow when combined to a low-viscosity asthenosphere (Tackley, 2000). Moreover, this rheology results in Earth-like plate-size distribution (Mallard et al., 2016) and seafloor age-area relationship (Coltice et al., 2012).

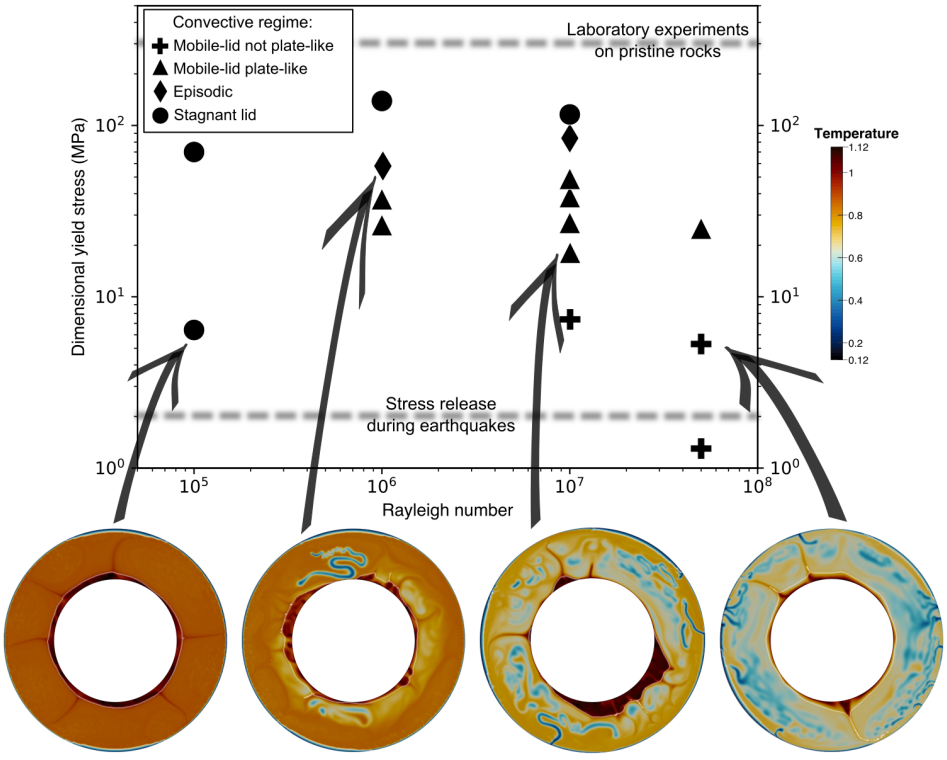


Figure 2.5: Convective regime diagram for a Rayleigh number-yield stress domain. Four regimes can be identified from the convective planform, heat flow and plateness predicted by models.

However, the visco-plastic rheology is still far from reproducing all the complexities of Earth's surface. For example, in such models, double-sided subductions occur instead of asymmetric and single-sided ones (Gerya et al., 2008). Asymmetric subductions can arise from the modeling of a weak layer at the surface of models, leading to a decoupling of the subducting and the overriding plate. The modeling of a free-surface or at least a sticky-air layer (which allows the surface of models to deform) leads to single-sided subductions (Crameri and Tackley, 2014). Moreover, the modeled yield stresses which are supposed to represent Earth's lithospheric strength (about 250 MPa for models at Ra = 10^6, Coltice and Shephard (2018), or 27 MPa for models at Ra = 10^7, Fig. 2.5) are far from the ones deduced from experiments (600 and 1100 MPa at most for pristine quartz and olivine resp., Brace and Kohlstedt (1980)). At least part of this discrepancy is likely to result from the fact that laboratory measurements of rock deformations do not correspond to the timescales of deformation processes at Earth conditions. Future developments are focused on the need to account for the grain-size effect on strain-localization (Bercovici and Ricard, 2014), and memory effects in order to improve the self-generation of plate-like tectonics. An alternative method is to start from microscopic scales in order to produce a macroscopic law able to represent multi-scale deformations of Earth's mantle and lithosphere (Boioli et al., 2015).

2.2.2 Modeling oceanic and continental lithosphere

When modeling Earth-like tectonic features, it is important to account for the main lithospheric rheological heterogeneity, corresponding to oceanic and continental rheological differences. As mentioned in section 1.2.3, continental lithosphere, which composes approximately 40% of Earth's surface, has thermal and rheological properties which can potentially affect large-scale convection and the plate tectonic layout. The analysis of continental rocks and Earth's hypsometric curve (distribution of surface topography) reflects that continental lithosphere is thicker than oceanic lithosphere (continental cratons can reach depths of more than 200 km (*e.g.* Peltier, 1984, Masters et al., 1996) while oceanic lithospheric thickness is about 100 km at most (McKenzie et al., 2005)) and less dense (ρ_c = 3.1 kg·m^{-3} for continental lithosphere whereas ρ_o = 3.25 kg·m^{-3} for an oceanic lithosphere of 100 km (Watts and Schubert, 2007)). Moreover, continental lithosphere is generally less deformable than oceanic lithosphere (except for its crustal part), since it is colder (see section 1.1.2.2).

In the numerical models presented in this thesis, buoyant tracers are used in order to represent continental lithospheric rafts and follow the evolution of their position through time. The modeled continental lithosphere has also an increased viscosity in order to remain stable over long time periods (Lenardic and Moresi, 1999). The total area of continental lithosphere is set to 30-40 % of the total Earth's surface. The continental lithosphere is composed of at least two parts with different rheologies in the models. The center of continents, representing cratonic lithosphere, have an initial thickness of 200 km (Peltier, 1984, Masters et al., 1996), a viscosity at least 100 times more important than oceanic lithosphere, a density contrast of about 225 g·m^{-3} and a surface yield stress at least 100 times more important than oceanic lithosphere, depending on the models presented in the next Chapters. The continental belts are defined as areas of 125 km (Conrad and Lithgow-Bertelloni, 2006), with a viscosity 50 times more important than oceanic lithosphere, a density contrast of about 275 g·m^{-3} and a surface yield stress at least 10 times higher than oceanic lithosphere.

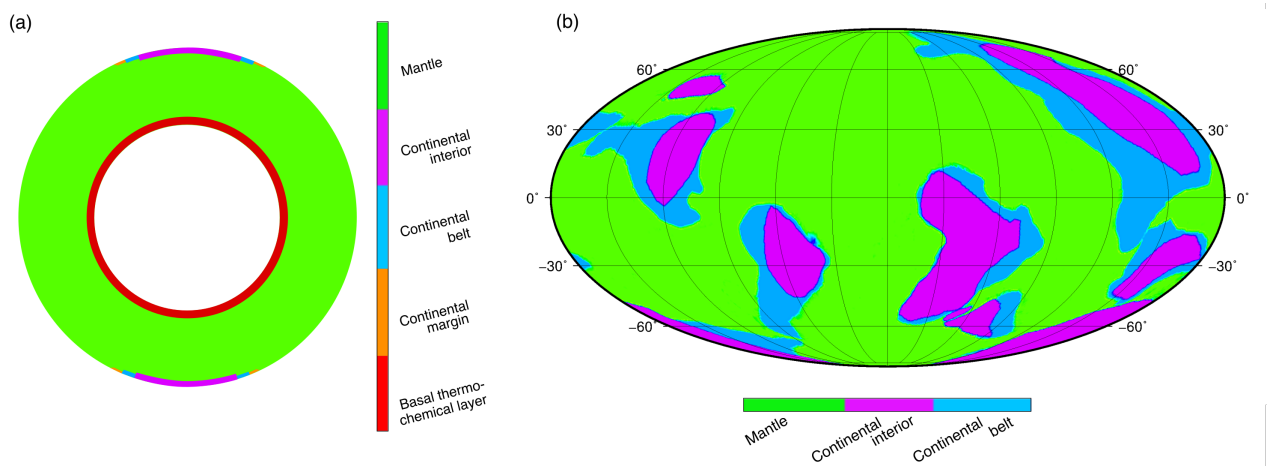


Figure 2.6: Initial compositional field (a) in a 2D-spherical annulus model with continents and basal thermochemical heterogeneities and (b) at the surface of a 3D-spherical model with continents in the same configuration as Earth's continents 80 Myr ago. Continents are composed of three parts differing by their thickness, viscosity and yield stress in 2D models, and two parts in 3D spherical models.

2.3 Computation

Numerical modeling of whole-mantle convection self-generating plate-like tectonics is a technical challenge, given the size of the domain (reaching a numerical resolution of 2 km^3 would require 123×10^9 grid cells), the need for large viscosity contrasts in order to represent Earth-like rheology, the diversity and non-linearity of Earth's mantle and lithosphere rheology and the multiplicity of

spatial and temporal scales of the tectonic and mantle deformation processes. Analytical methods for studying complex mantle and lithosphere deformation processes are thus limited, and numerical methods are needed to account for non-linearity in the advection of temperature (Equation 2.15) or in constitutive laws and for solving lateral variations of viscosity. Therefore, the continuous improvement of numerical methods and computational power have seen the development of alternative and complementary methods for numerically modeling mantle convection with self-consistent plate-like generation.

2.3.1 Numerical approximation, discretization and geometry

Different numerical approximations exist to decompose various fields (such as the pressure, temperature or the stress field) within the whole domain and to solve the four primary unknowns present in the Boussinesq approximation (pressure, temperature, composition and velocity, see Equations 2.15). The first numerical method that has arisen is the *finite-difference method* (Torrance and Turcotte, 1971, Turcotte et al., 1973, McKenzie et al., 1974, Parmentier et al., 1975, Jarvis and McKenzie, 1980). It is based on the differentiation of the conservation equations using Taylor series. This method allows to solve problems with variable viscosity (Christensen, 1984a) and high-Rayleigh number convective vigour (Malevsky and Yuen, 1993). However, it requires a structured grid. Another method consists of calculating the *spectral function* of each field, by decomposing them into spherical harmonic (if spherical domain) or into Fourier (if cartesian geometry) coefficients. It has been successfully used by Hager and O'Connell (1979, 1981), Steinberger and O'Connell (1998) in order to solve Stokes flow problems (which consist in solving only the mass and momentum conservation equations) and to study the effect of internal density anomalies on surface topography, geoid and stress field. However, even if this technique is computationally fast, it does not resolve variations of physical properties such as lateral variations of viscosity larger than 10^5 Pa·s (Schmalholz et al., 2001). The *finite-volume technique* is similar to the finite difference method, except that equations are integrated over the volume of grid cells (Patankar, 1980, Ogawa et al., 1991, Tackley et al., 1994). In the next Chapters, I use the finite-difference/finite-volume numerical code StagYY developed by P. Tackley (Tackley, 2008). This code is coupled with a staggered grid method in order to solve pressure (at the center of grid cells) and velocity (at boundaries of grid cells) at different locations and avoid checkerboard pressure solutions (Fig. 2.7). Finally, other codes, such as ASPECT, use the *finite-element method* to account for complicated geometry and material properties (Christensen, 1984a, King et al., 1990, Bunge et al.,

1997, Zhong et al., 2000, Stadler et al., 2010). Conservation equations are transformed into integrals over the domain, which allows easier manipulation.

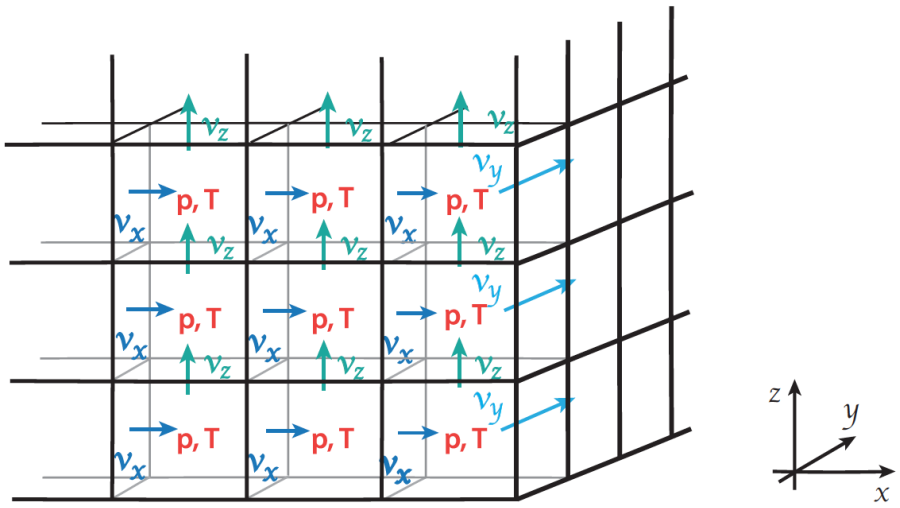


Figure 2.7: Staggered grid used to solve the equations of convection. P and T are defined at grid cell centers while velocity vectors are defined at grid cell boundaries (Bello, 2015)

Two geometries are used in the following Chapters. In Chapter 3, 2D-whole-mantle convection models are computed using a spherical-annulus geometry (Hernlund and Tackley, 2008), which would correspond to an "equatorial" 2D-slice of a spherical shell. Contrary to the 2D-Cartesian geometry, it accounts for the ∼4-times angular distance difference between the surface and the CMB, which implies a thicker basal TBL and therefore, upwellings stronger than downwellings (Ricard, 2007). The effect of sphericity on the temperature field is therefore opposite to the effect of internal heating and temperature-dependent viscosity. Moreover, compared to a cylindrical geometry, the spherical annulus geometry accounts for the curvature of the surface in all directions. Indeed, the Jacobian factor (which measures the variation in a differential element of volume for the coordinate system) is kept equal to the square of the radius, as it would be in spherical geometry (while it would be equal to the radius in cylindrical models). Computation is more efficient than in 3D-spherical geometry and convection arising from 2D-spherical annulus models compares better to 3D-spherical models than other 2D-geometries. Nevertheless, mantle flow is still confined to a plane, and toroidal flow cannot develop for example. Therefore, in Chapter 4, a 3D spherical Yin-Yang geometry (Tackley, 2008) is used in order to study the lateral motion of mantle plumes. This grid geometry (Kageyama and Sato, 2004) is composed of two identical components combining via a simple rotation into a spherical shell.

In this geometry, grid-cells are almost all equivalent in size which avoids cartesian pole singularities, and the domain is relatively easy to parallelize.

The 2D models of mantle convection presented in this thesis have a lateral resolution of about 25 km at the surface and a radial resolution varying between 13 and 26 km, due to a mesh refinement near both the surface and the CMB. In our 3D models of mantle convection, the lateral resolution is 50 km at the surface (about 35 km in average) and the radial resolution varies between 8 and 40 km, which corresponds to a decrease in the lateral resolution by a factor of two compared to 2D models. The spatial resolution of our 3D models is not increased for computational reasons. Moreover, the computation of 2D models with a surface spatial resolution of 50 km result in local uncertainties in the dynamic topography of about 350 m compared to a model with a spatial resolution of 25 km (Fig. 2.8). Since surface dynamic topography is sensitive to the spatial distribution of density anomalies, artifacts caused by numerical convergence problems would have resulted in higher uncertainties.

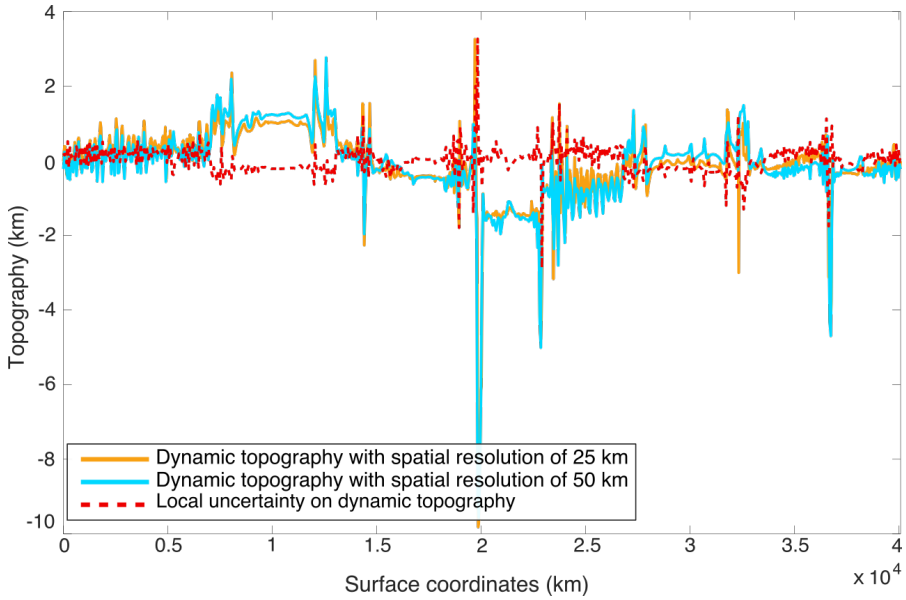


Figure 2.8: Dimensionalized dynamic topography along the surface of two 2D models of mantle convection with two different spatial resolutions. The local uncertainty on dynamic topography corresponds to the difference between the two curves with a different spatial resolution.

2.3.2 Solving conservation equations

In StagYY, solving mantle convection equations is carried out in 2 steps, preceded by the initialization of the temperature field (see section 2.3.3):

- The first step consists of solving for pressure and velocity by accounting for Equations 2.1 and 2.2 (Stokes problem). A classical method starts with an initial guess for pressure and velocity and iteratively improve it until reaching the correct numerical solution by minimizing the error (or residue). Nevertheless, the convergence time of this method depends on the resolution of the domain. Solving for highly variable viscosity contrasts and non-Newtonian rheologies in 3D-models of mantle convection thus requires more efficient iterative methods instead of using direct solvers which requires a lot of memory. The multigrid iterative method has therefore been developed to increase computational efficiency in large problems (Brandt, 1982, Wesseling and Oosterlee, 2001): it consists of accelerating the convergence by solving the problem on coarser grids. In this thesis, the V-cycle scheme (composed of the iteration of several v-cycles at different grid resolutions) is used. In each V-cycle, iterations are first carried on a fine grid to find a first guess solution before the resulting error is restricted to a coarser grid where an approximate solution is found thanks to a few iterations before the coarse error is back-propagated to the fine-grid where additional iterations refine the solution. With this method, the convergence rate becomes independent from the grid size, but slow convergence or even divergence can appear if large viscosity contrasts are present (such as the ones needed to model mantle convection with plate-like tectonics). To overcome this problem, I use the pressure interpolation scheme developed by Tackley (2008) in which errors are normalized by the local viscosity.

- The second step calculates the temperature field one time-step after having solved for pressure and velocity. The temporal advection-diffusion of temperature is solved by accounting for the equation of energy conservation 2.4. To avoid unstable (numerical oscillations) or smeared solutions of temperature anomalies (Kowalik and Murty, 1993), an upwind scheme has been developed (Parmentier and Sotin, 2000), and parallelized through the MPDATA scheme (Multi Positive Definite Advection Transport Algorithm, Smolarkiewicz and Margolin (1998)). Other advection schemes consist in correcting numerical diffusion by following tracers advection (Gerya and Yuen, 2003).

Solving for complex non-linear rheologies (such as the visco-plastic rheology) requires a specific step of iteration at each time-step of the model integration: first, viscosity is calculated from the temperature, pressure and stress field. Then, the velocity field is calculated, which updates the stress field. As a consequence, the required consistency between the new stress field and the viscosity field

potentially leads to supplementary iterations.

Finally, in the case of thermo-chemical convection, the equation of advection of chemical fields 2.17 needs to be solved. This is done using the advection of Lagrangian tracers of different composition, usually thanks to a "marker-in-cell" or a "particle-in-cell" method (*e.g.* Tackley and King, 2003, Van Keken et al., 1997). In StagYY, I use the particle-in-cell method coupled with the ratio-method (Tackley and King, 2003), which requires fewer tracers than in the absolute-method and therefore, less memory. The actual advection of particles is updated using the 2^{nd} order Runge-Kutta method. In our 2D and our 3D models of mantle convection, I use 1.6×10^7 and 8×10^8 tracers respectively.

The StagYY code has been continuously developed since 1992 (Tackley et al., 1993) to incorporate more efficient numerical methods. It includes a new pressure interpolation scheme (Tackley, 2008), the spherical annulus geometry (Hernlund and Tackley, 2008), the tracers-ratio method (Tackley and King, 2003)...) and geophysical complexities (plate-like tectonics self-generation (Tackley, 2000), visco-elasticity (Patocka et al., 2017), free-surface topography (Crameri et al., 2012a), crustal production thanks to melting (Lourenco et al., 2016, Rozel et al., 2017) and compressibility (Tackley, 2008). Thanks to those implementations, it is able to resolve large lateral and radial viscosity variations. Several benchmarks have shown its capabilities (*e.g.* Van Keken et al., 1997, Crameri et al., 2012b, Patocka et al., 2017). It has been parallelized using the MPI standard and shows good scalability (Tackley, 2008). To compute our models, I use between 64 and 128 cores. The total computational time required to model 2D mantle convection during 1×10^9 yr is about 45,000 CPU-hours.

2.3.3 Initial and boundary conditions

As mentioned in section 2.3.2, the numerical solutions of the convective equations depend on the definition of an initial temperature field (and compositional field for thermo-chemical models). The most common way to initialize the mantle temperature field imposes an unstable radial profile of temperature and initiate random perturbations in order for the model to convect. A statistically stationary state is reached when the average temperature of the mantle is near constant, and the core and surface heat flow are stabilized (quasi-statistic equilibrium, Fig 2.9). However, such equilibrated state is slow to establish if the initial condition is far from it, especially for numerical models of whole-mantle convection in the plate-like regime with large viscosity contrasts and a high Rayleigh

number. Therefore, in our case, this initialization step is carried out once for each model geometry and initial compositional field. When changing convective and rheological parameters, I start from a previously equilibrated state and wait for it to reach a new quasi-statistic equilibrium before carrying our analyses.

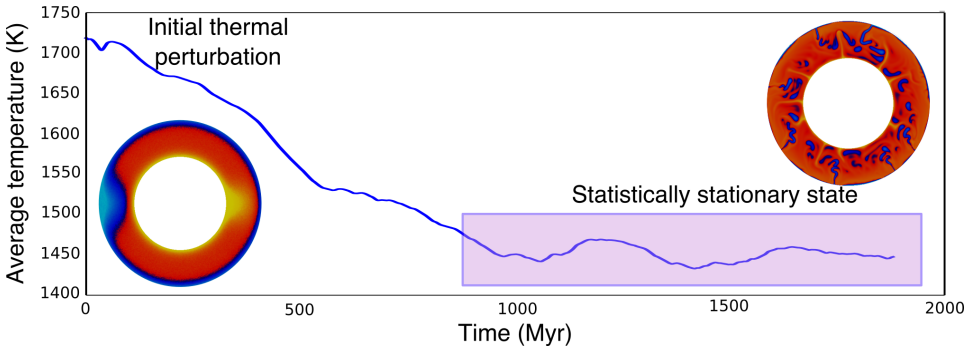


Figure 2.9: Temporal evolution of the average temperature of a 2D-spherical annulus model of mantle convection evolving from the perturbation of a laterally homogeneous temperature field to a statistically stationary state of convection.

In the case of the initialization of compositional fields (continents and/or basal thermo-chemical heterogeneities), the initial geometry of those chemical fields is set and tracers advection is prevented during the equilibration phase. Depending on the density, viscosity and rheological properties of those chemical fields, extra equilibration can be required while tracers are allowed to be advected. This makes it possible to start our analysis while the initially homogeneous basal chemical layer is already deformed by the ambient flow, and while extra-heat trapped below non-moving insulating continents has started to vanish.

The free-slip is used as a boundary condition for both the surface and the CMB in the models. This surface condition does not allow the surface to deform freely contrary to modeling a free-surface (Stadler et al., 2010) or using a sticky-air layer (Crameri et al., 2012a). The use of a free-slip boundary condition can potentially alter the geometry of sinking slabs in the mantle. Indeed, this surface boundary condition favors double-sided subductions (Crameri et al., 2012b). Although our boundary condition leads to faster computations, it necessitates a specific method to extract surface topography, contrary to the two other boundary conditions where topography naturally arises, as detailed in section 3.2. Boundary conditions for temperature at both interfaces are isothermal. Surface non-dimensional temperature is 0.12 (which corresponds to a dimensional temperature of 255 K, corresponding to

Earth's average surface temperature without greenhouse effect) and CMB non-dimensional temperature is 1.12.

For numerical convergence reasons, the possible viscosity variations are also limited throughout the entire domain to seven orders of magnitude at most, by imposing a maximum viscosity cut-off.

2.3.4 Scaling or dimensionalization

We have seen in section 2.1.1.3 that the equations of convection are non-dimensionalized before being numerically solved. As a consequence, all the results are non-dimensionalized. In oder to compare our results with Earth's observations, we have two possibilities:

- We can **dimensionalize** our results by using the relations mentioned in section 2.1.1.3. For example, dimensional time t will be obtained from the diffusion time: $t = \frac{D_0^2}{\kappa_0} t'$ (with D_0 the mantle depth, and κ_0 the thermal diffusivity) (Zhang et al., 2010, Davies et al., 2012). Direct comparison with Earth's observations requires the same surface heat fluxes, surface topography and lateral velocities.

- In the case of modeling conditions far from Earth's dynamics, another possibility is to **scale** our results, in order to account for the differences arising from the convective vigor (*e.g.* Rolf et al., 2014). For example, in numerical models of mantle convection at $\mathrm{Ra} = 10^6$, the thickness of the upper boundary layer (oceanic lithospheric thickness) is at least 200 km, which is twice as thick as the thickest estimates of Earth's oceanic lithosphere thickness. Therefore, in order to compare lengths, one needs to account for this factor 2 of difference. Another example is the scaling of timescales. While dimensionalized $t = \frac{D_0^2}{\kappa_0} t'$, scaled $t_s = \tau_{transit} \times t'$ with $\tau_{transit} = \frac{D_0}{\mathbf{v}_{RMS,surf}}$ the time-averaged transit time corresponding to timescale of slab sinking throughout the mantle at a characteristic speed, often taken as plate tectonics average velocity (Gurnis and Davies, 1986), which is approximately 75 Myr (Bello et al., 2015).

Since the parameters of our models do not correspond exactly to Earth's dynamics, most of our results will be scaled. However, since the modeled Ra is 10^7 the size of convective and lithospheric structures are close to Earth estimates. Therefore, modeled surface topography is simply dimensionalized. Moreover, all the characteristics of the model described in section 4.3 will be dimensionalized, to directly compare with observations for Earth.

Chapter 3

On the scales of dynamic topography in whole-mantle convection models with plate-like tectonics

Contents

3.1 Introduction . . . 85

3.2 Modeling surface topography . . . 88

3.3 On the scales of dynamic topography in whole-mantle convection models . . 90

3.3.1 Introduction . . . 91

3.3.2 Methods . . . 93

3.3.2.1 Two-dimensional convection models with self-consistent plate generation 93

3.3.2.2 Computing dynamic topography . . . 101

3.3.3 Results . . . 104

3.3.3.1 Spatial distribution of dynamic topography . . . 104

3.3.3.2 Spectral decomposition of dynamic topography . . . 106

3.3.3.3 Temporal evolution of dynamic topography . . . 110

3.3.4 Discussion . . . 111

3.3.4.1 Model limitations . . . 111

3.3.4.2 Spatial and temporal influence of dynamic topography on surface processes 114

3.3.5 Conclusions . . . 117

3.4 Conclusions and perspectives . . . 120

3.1 Introduction

As stated in Chapter 1, one of the main observations providing insight on the dynamics of Earth's surface and interior is its topography. Earth's topography corresponds to the deviation of its surface elevation from the mean sea-level (or geoid). Unlike its terrestrial neighbours in the Solar System, Earth's surface topography is not easy to reveal and understand, due to its important interactions with external envelopes (hydrosphere, biosphere and atmosphere). Indeed, the fact that two thirds of Earth's surface is covered with oceans has prevented the study of seafloor topography until the 1960's and the advent of oceanic radar campaigns of seafloor imaging (see section 1.1.2.2).

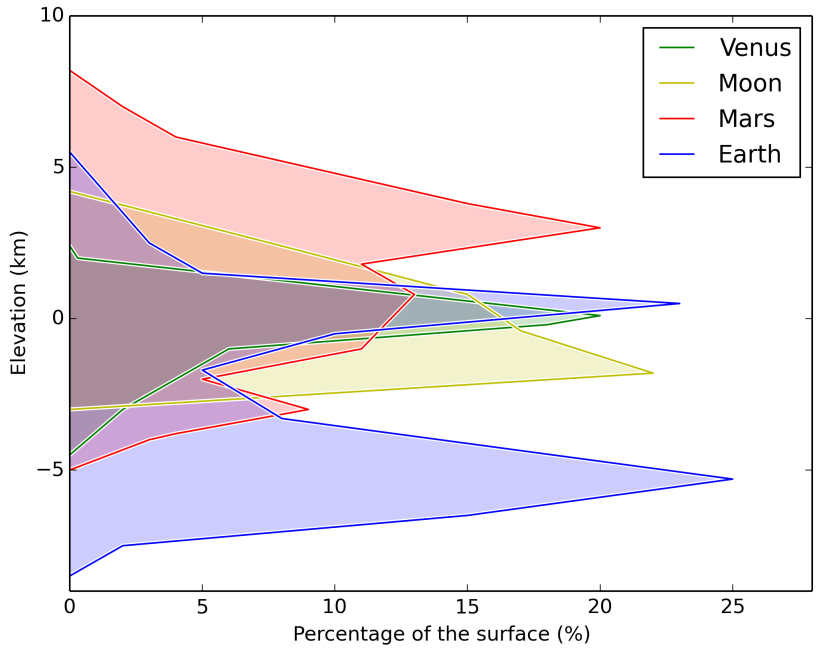


Figure 3.1: Comparative hypsometric curve of Earth, Venus, the Moon and Mars. While Venus, the moon and Mars have unimodal hypsometric distributions, Earth has a distinctive bimodal hypsometric distribution.

A first-order analysis of Earth's surface topography shows a striking bimodal distribution of its elevations, as opposed to the unimodal hypsometry of the Moon, Mars or Venus (Fig. 3.1). It evidences the role of isostasy, a theory stating that most of Earth's outermost layers tend to be in hydrostatic equilibrium (Bowie, 1927). The bimodal distribution of Earth's surface topography results from the first-order large difference between oceanic and continental lithosphere thicknesses and densities. Indeed, continental lithosphere can reach more than 200 km (the average continental

crustal thickness is 40 km) and has an average crustal density of 2.7 kg·m^{-3} while oceanic lithosphere is denser (oceanic crust has a density of 2.9 kg·m^{-3} in average), and has an average thickness < 100 km (with an average oceanic crustal thickness of 6 km).

Different isostatic models have been developed to explain the concept of isostasy. The Airy model (Airy, 1955) considers that surface loads are compensated by variations in the thickness of layers with uniform density while the Pratt model (Pratt, 1959) proposes that lateral density heterogeneities compensate surface loads. The Airy model is particularly adapted to the problem of continental/oceanic lithosphere topography difference, while the Pratt model explains fairly well oceanic topography variations. Therefore, to first order, the Earth appears to be approximately in isostatic equilibrium. This is revealed by the study of free-air gravity anomalies. Indeed, any mass heterogeneity in the lithosphere causes a gravity anomaly, which is compensated by surface deformation. Free-air gravity anomalies measure the departure of the observed gravity field from the predicted one (if accounting for isostatic compensation). Free-air gravity anomalies are generally small (Fig. 3.2). However, in a non-negligible number of regions, free-air gravity anomalies are large and positive or negative (mountain ranges, seamount chains, subduction trenches...), which suggests that processes different from isostasy perturb the gravity field and thus impact surface topography.

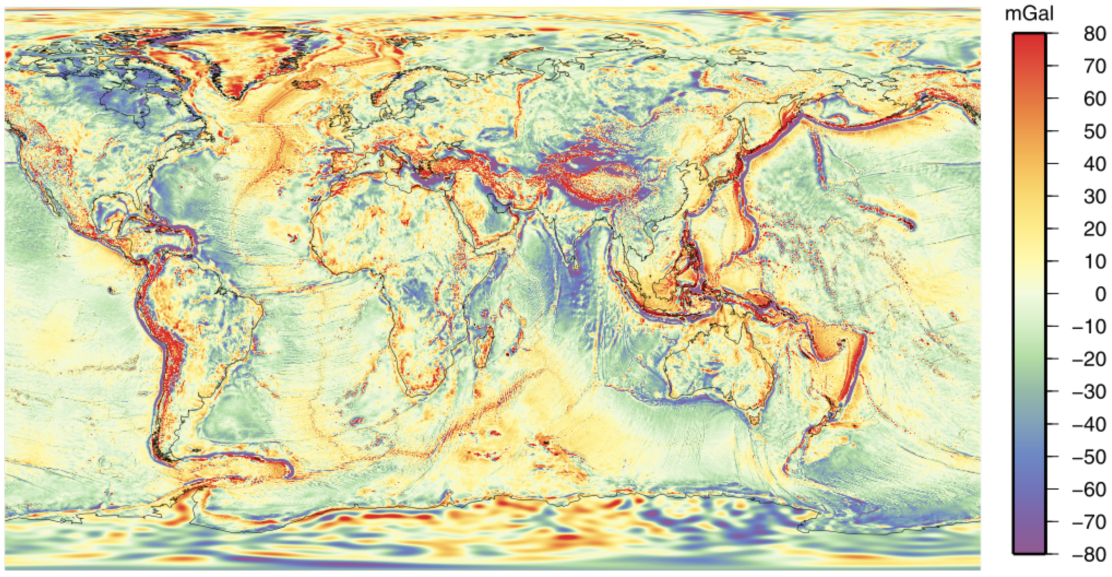


Figure 3.2: World free-air gravity anomalies from the model EGM2008 (Pavlis et al., 2012). Note that, on first order, free-air gravity anomalies are close to zero in many regions.

Small-scale departures from Pratt or Airy isostasy (such as volcanic seamount loadings on surface lithosphere) generally result from flexural isostasy. Flexure was first accounted by Vening-Meinesz (1941) who proposed that load compensation by the surface was a regional process instead of a local phenomenon, due to the elastic nature of Earth's lithosphere. Other gravity anomalies result from ongoing tectonic processes, combined with mantle or surface dynamics, since Earth's lithosphere is the interface between internal and external envelopes. For example, continuous erosion and sedimentation are likely to promote local or regional uplifts or subsidence, in order for the lithosphere to approach isostatic equilibrium. Plate tectonic features such as subduction zones or collision zones generate topographic and gravimetric anomalies that usually take several tens of millions of years to relax and approach a new state of equilibrium. Finally, the action of mantle convection as the instigator of vertical stresses applied on the upper thermal boundary layer contributes to the dynamics of surface topography. This effect is called dynamic topography, and is still poorly constrained.

Attempts to observe the dynamic support of the mantle to surface topography have been carried out by using different methods. The most popular method consists in the evaluation of residual topography (which would correspond to present-day dynamic topography) by measuring the isostatic support of Earth's crust thanks to seismic refraction profiles (*e.g.* Winterbourne et al., 2014, Hoggard et al., 2016). However, if this technique is straightforward at point locations in the oceanic domain along continental margins, where sediments and oceanic lithosphere densities are rather constrained, the heterogeneous nature of continental lithosphere makes it more difficult to interpret seismic profiles in terms of density anomalies. As an alternative, scientists have sometimes used continental free-air gravity anomalies as a proxy for crustal density anomalies on continents (Hoggard et al., 2016). Indeed, the apparent close relation between free-air gravity anomalies and surface topography led McKenzie (1977) to propose the existence of a constant ratio of gravity anomalies to topography anomalies (called admittance), regardless of the wavelength and the viscosity of the fluid. Dynamically supported topography would exist whenever the admittance is equal to 30 mGal·km^{-1} for oceans or 50 mGal·km^{-1} for continents. Although this rule of thumb has been verified in some regions (Winterbourne et al., 2014), it is still heavily debated (*e.g.* Molnar et al., 2015). Colli et al. (2016) recently demonstrated that admittance depends on the wavelength of the considered density anomaly. Other methods have been proposed to characterize Earth's dynamic topography. They include the analysis of V-shaped ridges near mantle plumes (Jones et al., 2002, Cannat et al., 1999), the interpretation of river drainage patterns in

terms of continental margin uplift or subsidence (Pritchard et al., 2009, Roberts et al., 2012, Barnett-Moore et al., 2014), continental inundation events (Mitrovica et al., 1989), the analysis of sequence stratigraphy (Hartley et al., 2011), of carbonate platforms (Czarnota et al., 2013) or of long-wavelength surface deformation such as doming of planation surfaces (Guillocheau et al., 2018) possibly induced by mantle convective processes. Nevertheless, this diversity of observations gives contrasting views of the role of mantle convection on the spatial wavelengths and amplitudes of dynamic topography.

In this Chapter, we will first review the different techniques used to numerically model surface topography (section 3.2). We will then analyze the spatial scales of dynamic topography arising from 2D whole-mantle convection models in order to compare those with other numerical models of whole-mantle convection and observation-based studies, before investigating the temporal dependance of surface dynamic topography on the onset of convective instabilities (section 3.3).

3.2 Modeling surface topography

Predicting the surface topography arising from both lithospheric and mantle properties and dynamics has been attempted using numerical models (*e.g.* McKenzie et al., 1974) since the analytical predictions of Pekeris (1935). Since the majority of numerical models use a free-slip boundary condition, their surface cannot deform, and topography h has to be extracted from the expected effect of normal stresses σ_{zz} applied on the outermost boundary of the models:

$$h = \frac{\sigma_{zz}}{\rho g} \tag{3.1}$$

where ρ is the density and g the gravitational acceleration. Thanks to the development of new numerical methods (see section 2.3), the direct computation of surface topography in numerical models of mantle convection is possible by adding a sticky-air layer of low viscosity above the surface of the models (*e.g.* Crameri et al., 2012a) or by modeling the free-surface conditions (using deforming Lagrangian grids (*e.g.* Melosh and Raefsky, 1980), the Arbitrary Lagrangian-Eulerian method (Fullsack, 1995), or level set functions (Braun et al., 2008)). The use of those techniques results in the accounting for lithospheric surface relaxation which can lead to more realistic topography compared to the use of a free-slip boundary condition which assumes static topography. For example, the use of a sticky-air layer allows to model single-sided subductions with realistic topography (Crameri et al., 2012a).

However, this method is computationally expensive since it requires to solve for the strong viscosity contrasts between the modeled lithosphere and the sticky-air layer, preventing the 3D-modeling of whole-mantle convection. Moreover, the correct modeling of surface topography requires to account for the viscoelastic properties of Earth's lithosphere, which can strongly impact on the relaxation time, as mentioned in section 2.2.1.2 (Patocka et al., 2017). In the following, I will use free-slip boundary conditions, and therefore extract topography from normal stresses (Equation 3.1) for computational reasons.

As mentioned in section 3.1, the understanding of Earth's surface topography is intimately linked to the apprehension of the various causes of surface vertical deformations (surface processes, such as erosion and sedimentation, and internal processes such as tectonic forces, isostasy and dynamic topography). In this thesis, I focus on the effect of internal processes on surface topography. A classical approach differentiates isostatic and dynamic effects (*e.g.* Guerri et al., 2016). Isostatic topography is therefore first defined by accounting for lateral and vertical density anomalies in the outermost layer of the model, from its surface to a compensation depth defined rather arbitrarily (Lachenbruch and Morgan, 1990). Dynamic topography then results from the subtraction of the isostatic component from total topography (Forte et al., 1993, Boschi et al., 2010, Guerri et al., 2016), and should be comparable to observation-derived residual topography (Hoggard et al., 2016). However, several ways of separating the isostatic and the dynamic contribution of Earth's internal dynamics exist, making it difficult to interpret and compare different models (Flament et al., 2013). Indeed, some authors consider the upper thermal boundary layer as part of convection and include it in the dynamic component (*e.g.* Forte et al., 1993). With this definition, only crustal density heterogeneities are considered as isostatic. This definition would require continents to be depressed by several kilometers, which is questioned by Gurnis (1993a). On the contrary, other authors only consider the mantle contribution to topography as resulting from convective motions below the lithosphere and calculate dynamic topography at a considered depth (*e.g.* Le Stunff and Ricard, 1995). An alternative is to compute dynamic topography using Equation 3.1, applied to normal stresses at the surface and ignoring sources of buoyancy located between the surface and an arbitrary depth (Flament et al., 2013). This technique allows the interpretion of the effect of mantle convection on the generation of normal stresses, notably in kinematically-driven models of whole-mantle convection (Flament et al., 2014) with slab-assimilations (Bower et al., 2015), where the uppermost mantle flow is subjected to unphysical

stresses and flow. However, this method only accounts for large-scale deep-mantle convection, while it has been shown that surface topography is more sensitive to upper mantle convection from the analysis of surface deformation kernels (Hager and Richards, 1989). Moreover, these last two definitions cause to neglect lithospheric-scale processes contributing to dynamic topography.

In the following section, I use 2D-models of mantle convection self-generating surface plate tectonics in order to investigate the spatial and temporal evolution of dynamic topography arising from self-consistently moving density heterogeneities.

3.3 On the scales of dynamic topography in whole-mantle convection models

The following section is published as:

Arnould, M., Coltice, C., Flament, N., Seigneur, V, Müller R.D., 2018, On the scales of dynamic topography in whole-mantle convection models with plate-like tectonics, *Geochemistry, Geophysics, Geosystems*, 19. https://doi.org/10.1029/2018GC007516

Abstract

Mantle convection shapes Earth's surface by generating dynamic topography. Observational constraints and regional convection models suggest that surface topography could be sensitive to mantle flow for wavelengths as short as 1,000 km and 250 km, respectively. At these spatial scales, surface processes including sedimentation and relative sea-level change occur on million year timescales. However, time-dependent global mantle flow models do not predict small-scale dynamic topography yet. Here, we present 2D-spherical annulus numerical models of mantle convection with large radial and lateral viscosity contrasts. We first identify the range of Rayleigh number, internal heat production rate and yield stress for which models generate plate-like behaviour, surface heat flow, surface velocities and topography distribution comparable to Earth's. These models produce both whole-mantle convection and small-scale convection in the upper mantle, which results in small- (< 500 km) to large-scale ($> 10^4$ km) dynamic topography, with a spectral power for intermediate scales (500 to 10^4 km) comparable to estimates of present-day residual topography. Timescales of convection and

the associated dynamic topography vary from five to several hundreds of millions of years. For a Rayleigh number of 10^7, we investigate how lithosphere yield stress variations (10-50 MPa) and the presence of deep thermo-chemical heterogeneities favour small-scale (200-500 km) and intermediate scale (500-10^4 km) dynamic topography by controlling the formation of small-scale convection and the number and distribution of subduction zones, respectively. The interplay between mantle convection and lithosphere dynamics generates a complex spatial and temporal pattern of dynamic topography consistent with constraints for Earth.

3.3.1 Introduction

Surface elevations result from both external and internal processes that continuously shape the Earth over a wide range of rhythms and scales. Mantle flow, by transporting temperature and density anomalies and deforming the surface, generates dynamic topography, a mechanism first proposed by Pekeris (1935).

Global models of mantle flow and density can be used to predict Earth's dynamic topography. Instantaneous mantle flow models usually include density anomalies deduced from seismic tomography models (*e.g.* Conrad and Husson, 2009, Hager et al., 1985, Steinberger, 2007), and these density anomalies can be backward advected back to $\sim$ 75 Myr (Conrad and Gurnis, 2003). Some flow models use reconstructed surface plate velocities as a top boundary condition together with a 'slab assimilation' technique in forward models (Bower et al., 2015), or adjoint methods to constrain both mantle flow and surface observables (Liu and Gurnis, 2008). Despite the different methods used, these studies attribute large-scale topography anomalies (wavelengths longer than 10^4 km) to whole-mantle convection (Hager and Richards (1989), Ricard et al. (1993)). For example, Lithgow-Bertelloni and Silver (1998) invoked large-scale whole-mantle upwelling flow to explain large topography anomalies such as the African superswell, and Mitrovica et al. (1989) showed that slabs sinking into the mantle could explain the formation of intra-continental sedimentary basins such as the Western Interior Seaway in North-America. Large-scale dynamic topography in such settings is predicted to evolve at rates between less than 1 m·Myr^{-1} and 80 m·Myr^{-1} (*e.g.* Flament et al., 2014).

Observational constraints require the existence of transient ($<$ 10 Myr) and localised ($<$ 3,000 km) dynamic topography. Pulses of mantle plume activity or upper mantle vigorous convection at a maximal rate of $\sim$ 100 m Myr^{-1} could explain seismic and stratigraphic observations (Hartley et al., 2011, Al-Hajri et al., 2009). Interpretations of river drainage patterns in terms of continental margin

uplift or subsidence (Pritchard et al., 2009, Roberts et al., 2012), or analyses of carbonate platforms (Czarnota et al., 2013) suggest surface uplift at rates between 75 m Myr^{-1} and 400 m Myr^{-1}. Rowley et al. (2013) also suggested that dynamic topography changes at rates of up to 60 m/yr over areas covering hundreds of kilometers could have been responsible for the uplift of the South-Eastern coast of the United States over the last 3 Ma. Regional models of dynamic topography and relative sea-level change associated with small-scale convection (Petersen et al., 2010) predict that surface topography is sensitive to mantle flow for wavelengths as short as 250 km and for timescales of the order of 2-20 Myr. Petersen et al. (2010) showed that small-scale convection could deflect the surface with an amplitude of about ± 300 m and induce high-frequency (period 2-20 Myr) stratigraphic sequences of about 200 km wavelength. Moreover, analytical global models (Hager and Richards, 1989) suggest that dynamic topography should be particularly sensitive to upper-mantle density heterogeneities at short to intermediate wavelengths. A recent global model of present-day residual topography derived from seismic data collected worldwide, mainly at passive margins (Hoggard et al., 2016), confirms that the amplitude of residual topography is significant for wavelengths as short as $\sim$ 1,000 km.

However, most global mantle convection models do not predict significant dynamic topography for wavelengths smaller than 5,000 km (Hoggard et al., 2016). Indeed, instantaneous flow models based on present-day tomography do not contain much density heterogeneity in the upper mantle due to the resolution of seismic tomography. In addition, the spatial variability of the seismic velocity to density conversion factor necessary to predict the mantle flow is uncertain and chemical effects are generally ignored in the uppermost mantle. Moreover, the effect of the uppermost mantle is often removed when calculating dynamic topography from global flow models to exclude lithospheric density anomalies that do not constitute dynamic topography (Flament et al., 2013, Lithgow-Bertelloni and Silver, 1998, Steinberger, 2007). Recently, Steinberger et al. (2017) showed that considering uppermost mantle density heterogeneities from a high-resolution near-surface tomography model, in combination with a global S-wave model, produces intermediate scales of dynamic topography (500 km to 10^4 km).

Here we use time-dependent models to explore the relationship between the spatio-temporal distribution of dynamic topography and the geodynamic processes from which it arises. We present 2D spherical annulus models with large radial and lateral viscosity contrasts that generate both large-scale and small-scale convection and a plate-like behaviour. We first vary the Rayleigh number, yield stress, and internal heat production rate to identify a range of models that generate plate-like behaviour (Tackley, 2000) and produce surface heat flow, surface velocities and topography distribution

comparable to Earth's. In the selected models, the predicted dynamic topography, which we compute by subtracting the model isostatic topography from the total model topography, occurs both at small (< 500 km) and large ($> 10^4$ km) scales . This allows us to investigate the role of small-scale convection, subduction zones, large-scale mantle flow and deep-seated thermo-chemical heterogeneities in controlling the patterns and timescales of dynamic topography evolution.

3.3.2 Methods

3.3.2.1 Two-dimensional convection models with self-consistent plate generation

Governing equations. We solved the following non-dimensionalised equations (3.2) of mass, momentum, energy and composition conservation in 2D-spherical annulus geometry, under the Boussinesq approximation for incompressible mantle flow (*e.g.* Ricard, 2015):

$$\begin{aligned} \nabla \cdot \mathbf{v} &= 0 \\ \nabla p - \nabla \cdot \left[\eta(\underline{\nabla \mathbf{v}} + (\underline{\nabla \mathbf{v}})^T)\right] &= \mathrm{Ra}(\alpha(z)T + BC)\mathbf{e_r} \\ \frac{\mathrm{D}T}{\mathrm{D}t} &= -\nabla \cdot (\nabla T) + H \\ \frac{\mathrm{D}C}{\mathrm{D}t} &= 0 \end{aligned} \tag{3.2}$$

where $\mathbf{v}$ is the velocity vector, p the dynamic pressure, η the viscosity, T the temperature, C the composition (to represent continents and deep thermo-chemical piles), $\alpha(z)$ is the depth-dependent thermal expansivity, H the uniform heat production rate, B the chemical buoyancy ratio and $\mathbf{e_r}$ is the radial unit vector. $\mathrm{D}/\mathrm{D}t = \partial/\partial t + (\mathbf{v} \cdot \nabla)$ is the Lagrangian time derivative. Ra is the Rayleigh number, defined as:

$$\mathrm{Ra} = \frac{\alpha_0 g \Delta T \rho_0 h^3}{\eta_0 \kappa_0} \tag{3.3}$$

with α_0 the surface thermal expansivity, g the gravitational acceleration, ΔT the temperature drop across the mantle, ρ_0 the reference density, η_0 the reference viscosity, h the thickness of the mantle and κ_0 the reference thermal diffusivity. Using a Rayleigh number larger than 10^7 generates an Earth-like mantle vigour with an oceanic lithosphere of 150 km at most.

We used a depth-dependent thermal expansivity law obtained from Raman mode frequency shifts of Mg-SiO_3-perovskite in diamond-anvil-cell experiments and extrapolated to lower-mantle pressure and temperature range (Gillet et al., 2000). The resulting decrease in thermal expansivity by a factor

of three with pressure (Chopelas and Boehler, 1992) broadens thermal anomalies in the deep mantle, stabilises thermo-chemical heterogeneities (Hansen et al., 1993), and favours slab stagnation and hotter mantle plumes (Tosi et al., 2013). Even if depth-dependent thermal expansivity is inconsistent with the Boussinesq approximation which states that mantle thermodynamic variables are independent on depth, it makes it possible to account for an extra source of buoyancy in the momentum equation, without the need of adding compressibility, viscous dissipation and pressure-driven buoyancy force.

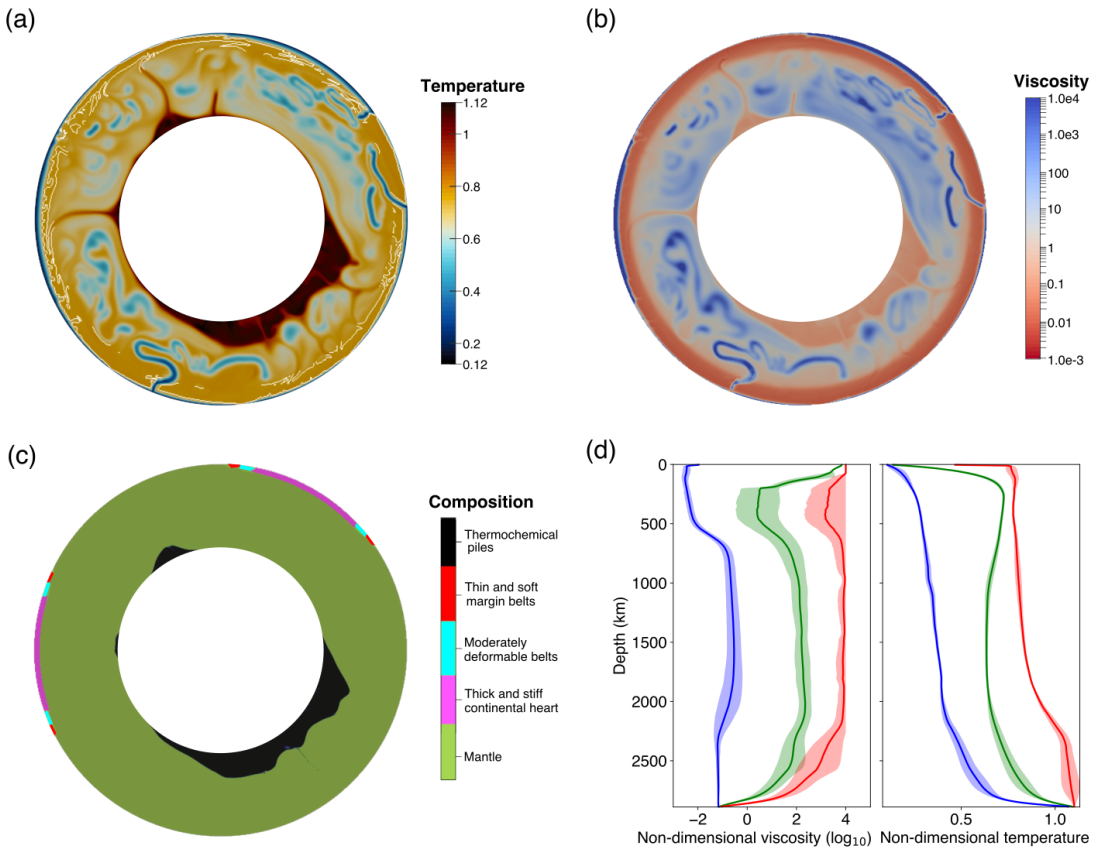


Figure 3.3: Snapshot of the non-dimensional (a) temperature field with the non-dimensional 0.75 isotherm (corresponding to 1600K) contoured in white in the upper mantle, (b) viscosity field and (c) composition field for Model 1 with thermo-chemical continental rafts and deep piles. (d) Non-dimensional minimum (blue), mean (green), maximum (red) viscosity and temperature profiles. Envelopes indicate temporal variations in viscosity and temperature. Note the maximum viscosity cut-off at 10^4.

Viscosity depends exponentially on pressure and temperature following:

$$\eta(z,T) = \eta_0(z) \times \exp\left(A + \frac{E_a + \Pi(z)V_a}{RT}\right) \tag{3.4}$$

where A is chosen so that $\eta = \eta_0$ for $T = 0.64$ (which is the *a priori* temperature at the base of the

lithosphere with dimensional value 1,600 K), E_a is the activation energy taken equal to 142 kJ·mol^{-1}, which is the closest value to available constraints for Earth's activation energy (ranging between 300-600 kJ·mol^{-1}, (Hirth and Kohlstedt, 2003)) that could be resolved numerically , $\Pi(z)$ is the static pressure, V_a is the activation volume, R is the gas constant and T is the temperature. $\eta_0(z)$ is defined in order to ensure a viscosity jump by a factor of 30 at 660 km (d_0) over a depth $2d_{jump}$ of 100 km:

$$\eta_0(z) = \eta_{ref} \exp\left(\log(30)\left[1 - 0.5\left(1 - \tanh\left(\frac{d_0 - z}{d_{jump}}\right)\right)\right]\right) \tag{3.5}$$

where η_{ref} is the reference non-dimensionalised viscosity value producing an average value of 1 for $\eta_0(z)$. The viscosity jump is suggested by geoid and postglacial rebound studies (Nakiboglu and Lambeck (1980), Ricard et al. (1993)). For computational reasons, we applied a maximum viscosity cut-off to limit the resulting viscosity variations to seven orders of magnitude throughout the mantle domain (Fig. 3.3). This is consistent with the study of King (2009), which showed that such a high value of the cut-off would produce topography errors $< 5\%$.

We used a pseudo-plastic rheological law enabling strain localisation (Tackley, 2000) based on the following yield stress threshold:

$$\sigma_Y = \sigma_Y + z \times d\sigma_Y \tag{3.6}$$

where the value of the yield stress at the surface σ_Y is different for different materials, and $d\sigma_Y$ is the yield stress depth derivative. When the yield stress σ_Y is reached, the viscosity η_Y drops markedly following:

$$\eta_Y = \frac{\sigma_Y}{2\dot{\varepsilon}_{\mathrm{II}}} \tag{3.7}$$

where $\dot{\varepsilon}_{\mathrm{II}} = \sqrt{0.5\dot{\varepsilon}_{ij}\dot{\varepsilon}_{ij}}$, the second invariant of the strain rate tensor. This enables the localisation of deformation (Eq. 3.7) in order to mimic the dynamics of plate boundaries (*e.g.* Tackley, 2000) and seafloor area-age distribution (Coltice et al., 2012) at Earth's surface.

The range of values for parameters common to all presented models are listed in Table 3.1.

Model set up. We computed a series of models (Fig. 3.3) with the convection code StagYY (Tackley, 2000). The 2D-spherical annulus geometry makes it possible to compute mantle flow models that are comparable to 3D spherical models without being computationally as expensive (Hernlund and Tackley, 2008). Free-slip conditions are used at both the core-mantle boundary and the surface.

The lateral resolution is about 25 km at the surface and the radial resolution varies between 26 km and 13 km due to a mesh refinement at boundaries.

Table 3.1: Non-dimensional and dimensional parameters

Parameter	**Non-dim. value**	**Dim. value**
Surface temperature (T_{top})	0.12	255 K
Basal temperature (T_{bot})	1.12	2390 K
Mantle domain thickness (h)	1	2890 km
Gravitational acceleration (**g**)	1	9.81 m·s^{-2}
Reference thermal expansivity (α)	1	3×10^{-5} K^{-1}
Reference density (ρ_0)	1	4400 kg·m^{-3}
Reference diffusivity (κ)	1	1×10^{-6} m^2·s^{-1}
Reference conductivity (k_0)	1	3.15 W·m^{-1}·K^{-1}
Viscosity constant (A)	-12.5	-88.75
Activation energy (E_a)	8	142 kJ·mol^{-1}
Activation volume (V_a)	3	13.8 cm^3·mol^{-1}
Maximum viscosity cut-off	10^4	10^{26} Pa·s
Viscosity increase at 660 km	30	
Yield stress gradient for all materials ($d\sigma_Y$)	2.34×10^6	1088 Pa·m^{-1}
Yield stress at the surface - continental interior ($\sigma_{Y_{cont}}$)	1×10^6	$312 - 1.2 \times 10^5$ MPa
Viscosity increase - continental interior	1000	
Buoyancy number - continental interior (B_{cont})	-0.41	-190 kg·m^{-3}
Thickness - continental interior	0.0692	200 km
Yield stress at the surface - continental intermediate belt ($\sigma_{Y_{inter}}$)	4×10^5	$125 - 5.1 \times 10^4$ MPa
Viscosity increase - continental intermediate belt	100	
Buoyancy number - continental intermediate belt (B_{inter})	-0.5	-235 kg·m^{-3}
Thickness - continental intermediate belt	0.0432	125 km
Yield stress at the surface - continental margin belt ($\sigma_{Y_{marg}}$)	2×10^5	$62.4 - 2.6 \times 10^4$ MPa
Viscosity increase - continental margin belt	10	
Buoyancy number - continental margin belt (B_{marg})	-0.6	-280 kg·m^{-3}
Thickness - continental margin belt	0.0256	75 km
Buoyancy number - deep-seated thermo-chemical layer (B_{llsvp})	0.25	117 kg·m^{-3}
Initial thickness - deep-seated thermo-chemical layer	0.1038	300 km

We used 1.6×10^7 tracers and the tracer-ratio method (Tackley and King, 2003) to evaluate compositional fields. We set the initial thickness and excess density of the thermo-chemical layer (when considered) in order to obtain stable thermo-chemical piles through time following geodynamic laboratory (Davaille et al., 2003) and numerical (Deschamps and Tackley, 2009) studies. Although the thermal or thermo-chemical nature of Large-Low Shear Velocity Provinces (LLSVPs) is still debated (Garnero et al., 2016), we chose a maximum height of about 1,000 km above the core-mantle boundary for the volume of the basal layer, which is here considered chemically distinct, having a density excess of 3% compared to the ambient mantle. We considered two continental lithospheric rafts that are stiffer than oceanic lithosphere to remain stable throughout the time of integration (Lenardic and

Moresi, 1999). They cover 30% of the surface area and are divided into three parts (Fig. 3.3): cratons at the center, surrounded by proterozoic belts and mobile belts, in order of decreasing viscosity and density (see Table 3.1). We set decreasing density contrasts from continental interior to boundaries to compensate the effect of their decreasing thickness from interior to boundaries. This ensures that continents remain above the sea-level throughout the time integration despite progressive dynamic erosion of their base. We first obtained an initial condition from the last step of a long equilibration phase in which all tracers are not advected (continents do not move and the basal thermo-chemical heterogeneity is a uniform layer). The initial state resulting from this equilibration phase is in statistical steady-state for average mantle temperature and basal and surface heat flux. However, the fixity of continents during the equilibration phase leads to the presence of a transient initial hot area below continents, favoured by their insulating effect (see Gurnis, 1993b). This provides sub-continental positive buoyancy leading to elevated topography that decreases as continents start moving. Moreover, the existence of a basal chemical layer with a constant thickness promotes an initial uniform distribution of mantle plumes similar to models without basal thermo-chemical heterogeneities. Therefore, the self-consistent and progressive deformation of this basal layer leads to a progressive reorganisation of mantle plumes into clusters over a period of about 200 Myr.

The initial condition resulting from this equilibration phase is in statistical steady-state for average mantle temperature and basal and surface heat flux. We computed the thermo-chemical evolution with tracer advection over ∼1,000 Myr, in order to compute statistics and observe a diversity of convective states. Although we used a 2D geometry, each of these models is computationally expensive, because of the long time of integration, high resolution and solving for large viscosity variations. The total computational time necessary for the 18 models presented in Fig 3.4a and Table 3.2 was about 775,000 CPU-hours.

We computed a series of models to find the parameter range for which models present (1) plate-like behaviour and (2) amplitudes of topography and surface heat flow comparable to observations (see Fig. 3.4 and Table 3.2). We varied Ra between 10^5 and 5×10^7. Basal heating represents on average 6% to 25% of the total surface heat flux (Table 3.2), depending on the presence of a basal thermo-chemical layer. Most estimates of Earth's core heat flow range between 7-17 TW (Olson, 2016), which would represent > 17 % of Earth's total heat flow, excluding crustal radioactive heat production. Therefore, most of our models have a core heat flow lower than inferred for Earth. We also varied the dimensional value of the yield stress at room pressure between 1 and 140 MPa (Fig. 3.4). These values are low

Table 3.2: Model input parameters and main resulting outputs. Ra is the Rayleigh number as defined in Eq. 3.3, H the internal heat production rate, CBL means Chemical Basal Layer, $\sigma_{Y_{oc}}$ is the surface oceanic lithosphere yield stress, P the plateness, M the mobility, Q_0 the surface heat flow, h_{RMS} the surface total RMS topography, Q_0/Q_{CMB} the ratio of CMB to surface heat flow, T_{LAB} the sub-lithospheric temperature, and η_0 the reference viscosity.

	Input parameters				Surface characteristics				Mantle properties		
Model	**Ra**	**H (W.kg^{-1})**	**$\sigma_{Y_{oc}}$ (MPa)**	**CBL**	**P**	**M**	**Q_0 (TW)**	**h_{RMS} (km)**	**Q_0/Q_{CMB}**	**T_{LAB}**	**η_0 (Pa s)**
Model 1	10^5	8.7×10^{-13}	6.37	Yes	0.13	0.16	22.7	7.28	6 %	0.78	1.1×10^{24}
Model 2	10^5	1.9×10^{-12}	70	Yes	0.94	0.97	6.9	6.53	19 %	0.72	1.2×10^{24}
Model 3	10^6	3.8×10^{-12}	139	Yes	0.88	0.47	10.6	4.41	25 %	0.72	1.2×10^{23}
Model 4	10^6	9.1×10^{-12}	26.2	Yes	0.86	1.01	39.7	5.30	7 %	0.76	1.1×10^{23}
Model 5	10^6	8.5×10^{-12}	24.8	No	0.91	1.13	38.4	6.13	7 %	0.80	1.0×10^{23}
Model 6	10^6	8.5×10^{-12}	37.1	Yes	0.93	0.93	35.7	5.02	8 %	0.80	1.0×10^{23}
Model 7	10^6	7.8×10^{-12}	57	No	0.97	0.86	37	5.15	8 %	0.86	9.5×10^{22}
Model 8	10^7	1.2×10^{-11}	7.42	Yes	0.88	1.15	46.4	4.27	8 %	0.68	1.2×10^{22}
Model 9	10^7	9.7×10^{-12}	16.9	Yes	0.93	0.97	38	3.98	10 %	0.74	1.2×10^{22}
Model 10	10^7	9.2×10^{-12}	27	Yes	0.97	0.85	37.5	3.72	9 %	0.75	1.1×10^{22}
Model 11	10^7	9.7×10^{-12}	28	No	0.95	1.03	36.5	3.79	15 %	0.71	1.2×10^{22}
Model 12	10^7	8.8×10^{-12}	38.2	Yes	0.97	0.88	35.9	3.70	8 %	0.78	1.1×10^{22}
Model 13	10^7	8.4×10^{-12}	48.8	Yes	0.96	0.80	36.5	3.55	9%	0.81	1.0×10^{22}
Model 14	10^7	8.2×10^{-12}	84.3	Yes	0.92	0.60	21.5	3.61	20 %	0.82	1.0×10^{22}
Model 15	10^7	7.8×10^{-12}	116	Yes	-0.1	0.00	20.6	3.47	7 %	0.85	9.7×10^{21}
Model 16	5×10^7	9.2×10^{-12}	5.3	Yes	0.87	1.25	83	4.77	10 %	0.75	2.2×10^{21}
Model 17	5×10^7	1.4×10^{-11}	1.25	Yes	0.91	1.08	64.1	5.28	13 %	0.65	2.6×10^{21}
Model 18	5×10^7	9.7×10^{-12}	25	Yes	0.97	0.82	38.9	3.79	13 %	0.65	2.6×10^{21}
Earth	**$10^{7.5}$-10^9**	**3-5 $\times 10^{-12}$** [a]	**10-500** [b]	**??**	**> 0.75**[c]	**??**	**37-41**[d]	**2.17**[e]	**17-35 %**[f]	**0.64**[g]	**??**

[a] Present-day heat production rate deduced from the activity of radioactive elements K,U and Th (Turcotte and Schubert, 2014)

[b] Stress release from earthquakes (Allmann and Shearer, 2009) and high-pressure high-temperature experiments (Brace and Kohlstedt, 1980)

[c] Earth's lowest bound plateness taken from f_{90} estimated by Kreemer et al. (2014)(at least 14%).

[d] Earth's total surface heat flow without continental lithosphere radioactive heat production (Jaupart et al., 2007).

[e] RMS-total topography of Earth from etopo1 (Amante and Eakins, 2009) after the removal of the loading of oceans.

[f] After removal of continental crust heat production, according to Olson (2016)

[g] Non dim. sub-lithospheric temperature assuming the isotherm 1600 K.

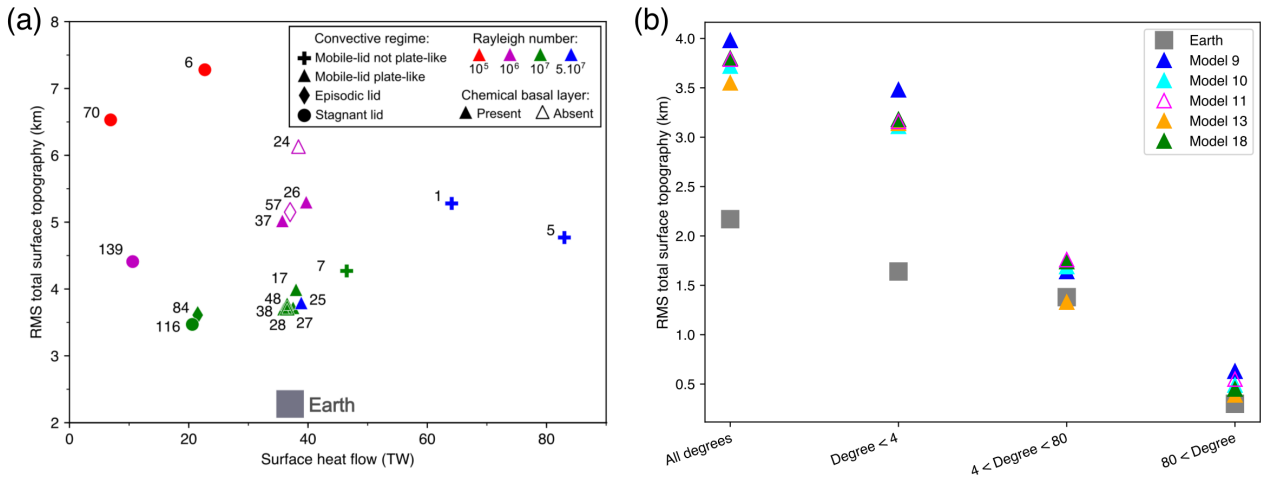


Figure 3.4: Regime diagram showing RMS-total surface topography and surface heat flow for all models. Symbols describe the tectonic regime of each model. Empty and filled symbols represent models respectively excluding and including a chemical basal layer. Colours represent the reference Rayleigh number, and numbers correspond to the dimensional yield-stress in MPa. For comparison to the models, Earth's surface heat flow is without the radioactive contribution of the continental crust radioactivity (37-41 TW, Jaupart et al., 2007), and Earth's surface RMS total topography (about 2.17 km, Amante and Eakins, 2009) is modified to air-loaded in the oceans. (b) Total and low-, band- and high-pass filtered RMS surface total topography for Earth and five models.

compared to laboratory experiments on mantle rocks (Brace and Kohlstedt, 1980), and close to the stress drop of earthquakes (Allmann and Shearer, 2009). The pseudo-plastic rheology used here is empirical, and probably represents homogenisation of a variety of processes (including two-phase flow, grain size evolution, and damage) that occur at smaller spatial scales than resolved in our models. We found that larger yield stresses result in the formation of a stagnant lid at the surface of the domain (Fig. 3.4a).

We determined models in plate-like behaviour using the same diagnostics as Tackley (2000). We measured the plateness P as:

$$P = 1 - \frac{f_{90}}{f_{90,iso}} \tag{3.8}$$

where f_{90} corresponds to the proportion of the surface localising 90 % of deformation, and the value of $f_{90,iso}$ is f_{90} for an isoviscous model. $f_{90,iso}$ is about 0.6 for models with Ra $\geq 10^6$ and 0.54 for models with Ra $= 10^5$. An ideal plate tectonic layout gives $P = 1$. We also measured the mobility that is the ratio of the RMS surface velocity to RMS velocity in the whole domain. Plate-like behaviour requires mobility close to or larger than 1. Among the models passing this test, we selected six models that displayed heat flow and total topography close to Earth's (see Fig. 3.4a and Table 3.2). However, those models present a RMS-total topography distribution about 1 km larger than

Earth's for spherical harmonic degrees < 4, while RMS-total topography for degrees > 4 matches Earth's intermediate and small wavelengths of RMS-total topography (Fig. 3.4b). This large-scale topography difference is caused by the overestimate of the density difference between continental and oceanic lithosphere in the models, as seen on the bimodal distribution of their surface topography (Fig. 3.5), which is responsible for large-scale isostatic topography.

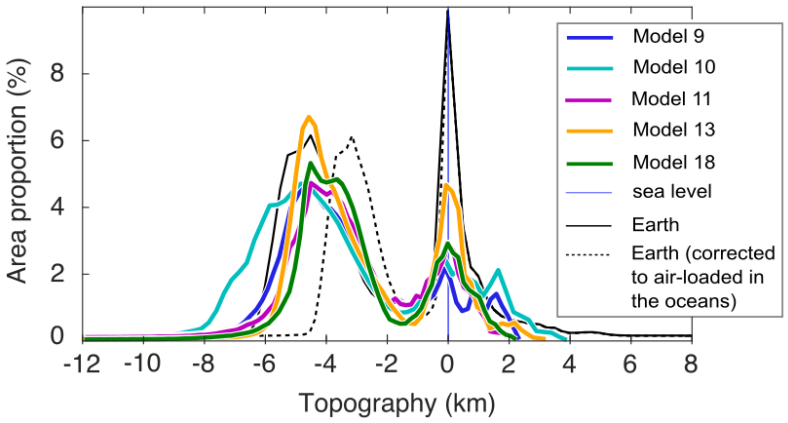


Figure 3.5: Time-averaged hypsometry for Models 9, 10, 11, 13 and 18 and Earth (etopo1 (Amante and Eakins, 2009), black solid line). The black dotted line is Earth's hypsometry corrected to air-loaded in oceans.

We focus on seven models: Model 8 ($\sigma_Y = 7$ MPa), Model 9 ($\sigma_Y = 18$ MPa), Model 10 ($\sigma_Y = 27$ MPa), Model 13 ($\sigma_Y = 48$ MPa), and Model 14 ($\sigma_Y = 84$ MPa), for which Ra $= 10^7$, include a basal layer; Model 11 ($\sigma_Y = 28$ MPa), for which Ra $= 10^7$, does not include a basal chemical layer; Model 18 ($\sigma_Y = 25$ MPa), for which Ra $= 5 \times 10^7$, includes a basal chemical layer (Table 3.2). Models 9, 10, 11, 13, and 18 are characterized by a mobile-lid plate-like behaviour. Model 8 is characterized by a mobile-lid but not plate-like convective regime. Model 14 is characterized by an episodic-lid convective regime. We consider these last two models to investigate the effect of different tectonic regimes on the spatial and temporal distribution of dynamic topography.

We focus on seven models. In Model 8 ($\sigma_Y = 7$ MPa), Model 9 ($\sigma_Y = 18$ MPa), Model 10 ($\sigma_Y = 27$ MPa), Model 13 ($\sigma_Y = 48$ MPa), and Model 14 ($\sigma_Y = 84$ MPa), Ra $= 10^7$ and a dense basal layer is included. In Model 11 ($\sigma_Y = 28$ MPa), $Ra = 10^7$ and a dense basal layer is not included. In Model 18 ($\sigma_Y = 25$ MPa), Ra $= 5 \times 10^7$ a dense basal layer is included (Table 3.2). Models 9, 10, 11, 13, and 18 are characterised by a mobile-lid plate-like behaviour. Model 8 is characterised by a mobile-lid but not plate-like convective regime. Model 14 is characterised by an episodic-lid convective regime. We consider these last two models to investigate the effect of different tectonic regimes on the

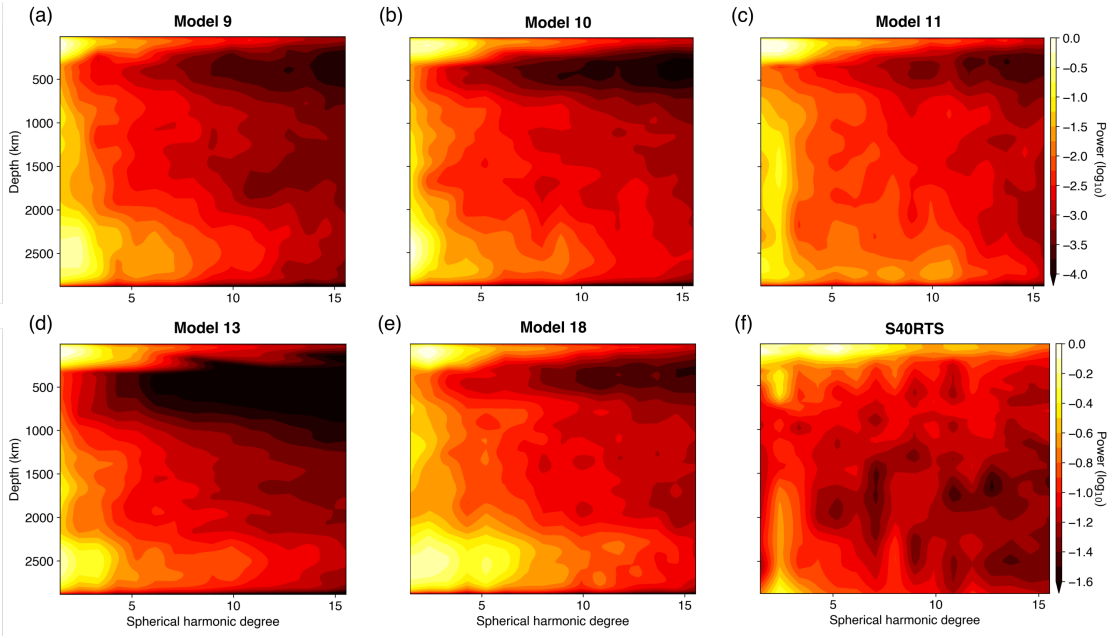


Figure 3.6: Temporal average of the thermal heterogeneity spectrum for (a) Model 9, (b) Model 10, (c) Model 11, (d) Model 13, and (e) Model 18 normalised by the highest power. (f) Shear wave velocity heterogeneity spectrum for seismic tomographic model S40RTS (Ritsema et al., 2011), also normalised by the highest power.

spatial and temporal distribution of dynamic topography.

The time-averaged power spectra of temperature heterogeneities in the five plate-like models display strong low degrees, and a contribution from smaller scales in the shallow mantle (Fig. 3.3a and 3.6), similar to seismic tomographic models such as S40RTS (Ritsema et al., 2011). This results from the large radial and lateral viscosity variations considered in our models (Coltice et al., 2017a, Huang et al., 2003, Moresi and Solomatov, 1995, Solomatov and Moresi, 2000). Degree 1 is dominant in the lower mantle for the spectra of Models 9, 10 and 13. As the yield stress increases, less power is present at intermediate scales (degrees 5-16) in the upper mantle. In Model 11, the spectrum in the lower mantle is dominated by degree 2. The presence of thermo-chemical heterogeneities enhances the power of degrees smaller than 4. Increasing Ra breaks the degree 1 symmetry of the thermo-chemical layer and leads to strong amplitudes up to degree 7 in the lowermost mantle.

3.3.2.2 Computing dynamic topography

Many studies compute dynamic topography from the normal stresses arising from the convecting mantle, excluding the density anomalies located above a depth of 220 km to 350 km from the flow calcuation, since the non-convecting lithosphere extends down to these depths in some places (Flament

et al., 2013, Lithgow-Bertelloni and Silver, 1998, Steinberger, 2007). Here, we compute dynamic topography in a similar fashion to present-day residual topography (*e.g.* Gvirtzman et al., 2016), because our numerical solutions include small-scale convection near the lithosphere-asthenosphere boundary. We define dynamic topography as the vertical motion of the surface induced by mantle flow below the lithosphere (which is the upper conductive thermal boundary layer), in contrast to isostatic topography occurring above the lithosphere-asthenosphere boundary. We first calculate total topography from normal stresses at the surface σ_{zz} following:

$$h = \frac{\sigma_{zz}}{\rho g} \tag{3.9}$$

where ρ is the density and g is the gravitational acceleration. The total topography predicted by the models averages to zero. In order to compare model topography and Earth's topography, we shift the total model topography by the average value of Earth's topography after removing water loading in the oceans. This value for a hydrosphere-free Earth is -2.3 km. We then calculate isostatic topography as the sum of all density contributions above a compensation depth, following the Airy condition (Fig. 3.7a). Since dynamic topography averages to zero to account for the conservation of the average radius of our models, and the total topography averages to -2.3 km by construction, isostatic topography also averages to -2.3 km. The compensation depth is taken as the inflection point of the average geotherm of the model at each timestep, and varies between 240 and 360 km depth depending on the temperature field. This method ensures that the modeled isostatic topography contains the density variations of both continental and oceanic lithospheres. We assume that the topography at subduction zones is completely dynamic since the Airy condition of pressure balance at the compensation depth cannot be satisfied there. We conservatively set isostatic topography to its average value within 500 km of subduction zones from the detection of their large negative normal velocity. This approach ensures that subduction topography is dynamic although the lateral extent of steeply dipping subduction zones is overestimated. We verify that increasing or decreasing the assumed lateral extent of subduction zones does not significantly affect the spatial distribution of dynamic topography. We obtain the dynamic component of topography by subtracting the isostatic topography from total topography.

On Fig. 3.7b, we decomposed total topography (blue curve) into its isostatic (red curve) and dynamic (yellow curve) components for a snapshot of Model 10. The isostatic topography follows the

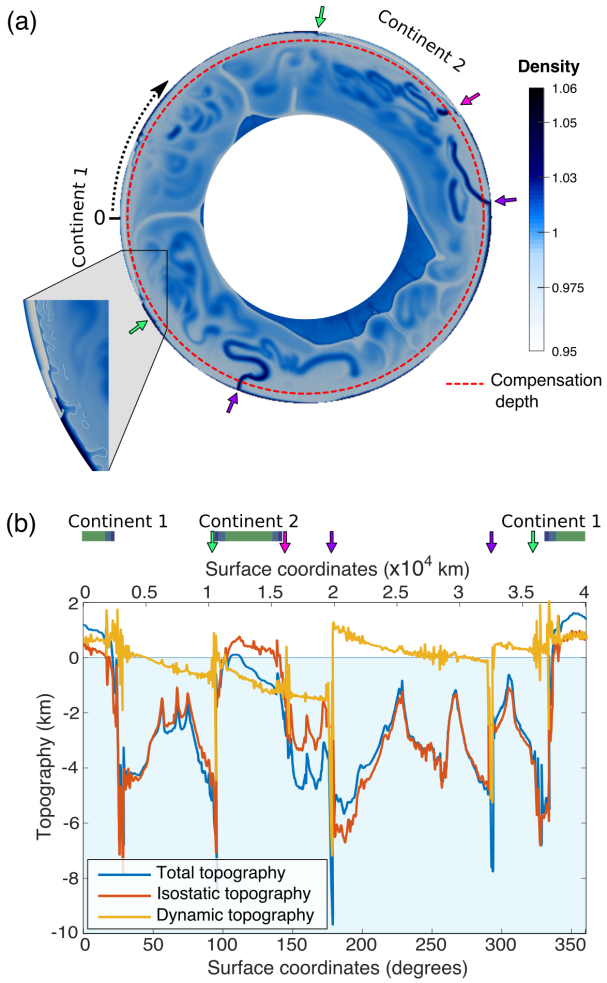


Figure 3.7: Total topography and its components for Model 10 for the same timestep as in Fig. 3.3. a) Non-dimensional mantle density field. The inset shows a closeup on small-scale convection, underlined by the white contour which represents the 0.75 non-dimensional isotherm. b) dimensionalised surface total topography (blue) and isostatic (red) and dynamic (yellow) components. Surface coordinates increase clockwise from the left side of the spherical annulus surface, as shown by the black arrow on a). Purple arrows show the locations of ongoing subduction zones, green arrows show the initiation position of future subduction zones and the pink arrow shows a slab break-off event.

shape of total topography, emphasising its dominant role in the generation of topography (Gvirtzman et al., 2016). The amplitude of dynamic topography is ±2 km at most, except at subduction zones that we have considered to be entirely dynamic, hence reaching -7 km. The long-wavelength trend of dynamic topography (>10,000 km) is consistent with the longest wavelength of mantle convection, outlined by the location of large-scale density anomalies in the model at that timestep (Fig. 3.7a).

Depending on the geometry of slabs sinking in the mantle, dynamic topography around subduction zones is generally asymmetric within 5,000 km from trenches, being more negative above the dense sinking material which generates downward radial stresses and velocities in the upper mantle

(Fig. 3.7b).

Short-wavelength (∼ 200-500 km) dynamic topography variations, which result from small-scale convection below the lithosphere (Fig. 3.3), coincide with continents and old oceanic lithosphere (Fig. 3.7b). Small-scale dynamic topography is also caused by small-scale convection at continental boundaries (also called edge-driven convection) and by artificial excessive stresses at the boundaries between the different continental belts. These artifacts, caused by compositional differences between continental and oceanic lithosphere, do not affect our conclusions, as we do not focus on processes affecting continental margins. The description of this snapshot confirms that the predicted dynamic topography is directly linked to density anomalies advected within the mantle, as expected.

3.3.3 Results

3.3.3.1 Spatial distribution of dynamic topography

Figure 3.8 shows the evolution of total topography and its components through time for Models 9, 10, 11, 13 and 18. In Models 10 and 18, the two continents move freely and never collide while in Models 9, 11 and 13, continents collide and form a supercontinent during the second half of the time integration. While supercontinent break-up is possible in principle, it was not observed in the time intervals considered. In all models, continental total topography decreases through time by about 1 km due to the combination of two phenomena. First, the presence of an initial hot area below continents, favoured by their fixity during the equilibration phase and their insulating effect (see Gurnis, 1993b), provides sub-continental positive buoyancy that decreases as continents start moving over 100 to 200 Myr. Continents present an average sligthly positive (78 m in average) dynamic topography throughout the time integration of each model due to this insulation characteristic (Fig. 3.8c). Second, the progressive basal erosion of continental lithosphere contributes to the decrease in their elevation through time, as shown by the decrease of isostatic topography on Fig. 3.8b. This is a model effect that may not apply to Earth. Continents also get deflected downwards at convergent margins.

In the oceanic domain, the total topography varies between ∼-1 km to -15 km. The highest topographies correspond to ridges dynamically supported by plumes. The total elevation of other ridges is around -2 km. The lowest areas correspond to trenches. The elevation decreases continuously from ridges to trenches as expected on Earth. In our models, trenches and ridges last between ten to several hundreds of millions of years (Fig. 3.8a and c). The average number of trenches decreases

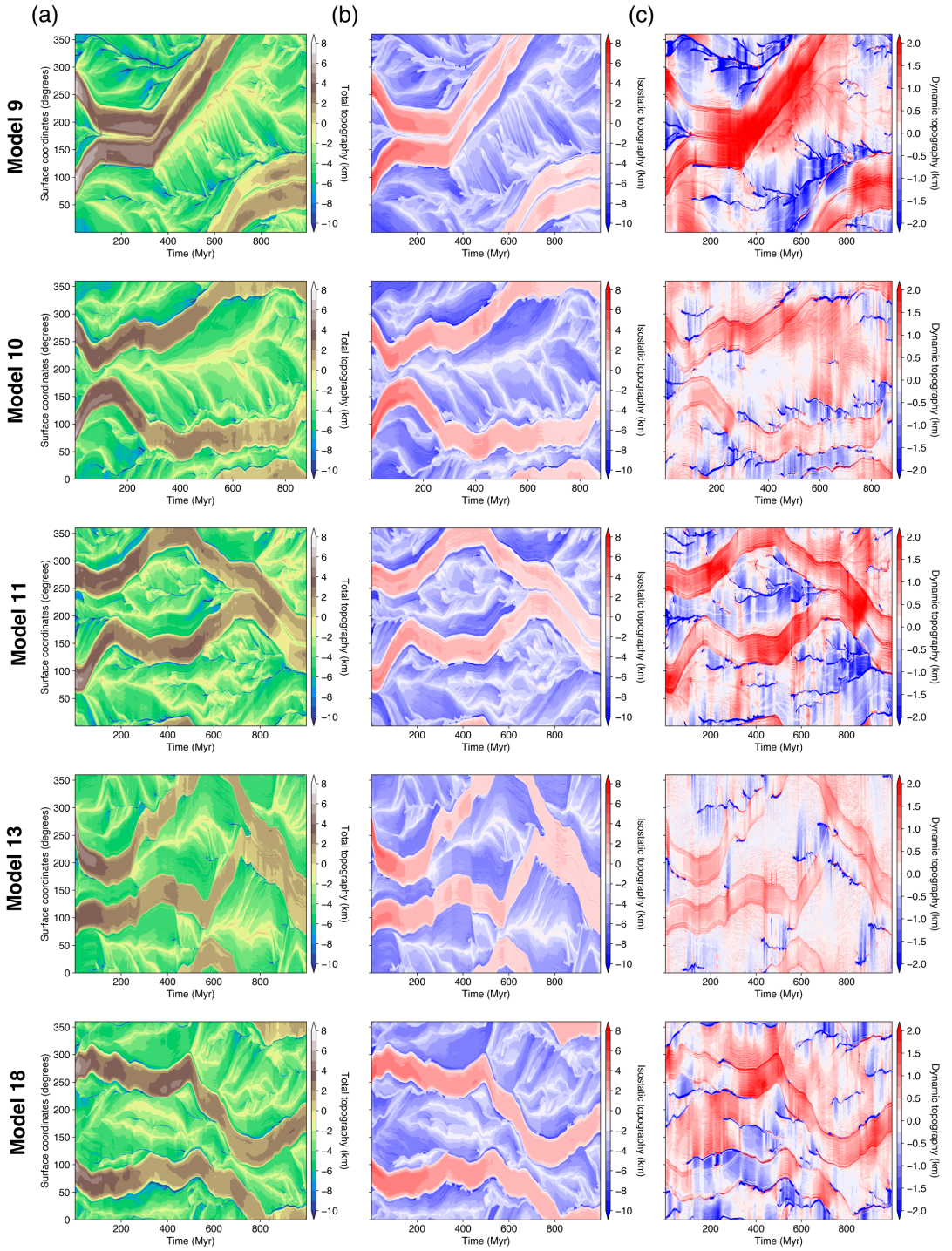


Figure 3.8: Temporal evolution of (a) total topography, (b) isostatic topography and (c) dynamic topography for Models 9, 10, 11, 13 and 18. In (c), we limit the dynamic topography scalebar to ± 2 km to enhance dynamic topography contrasts.

from about 15 to 1 as the yield stress increases from 7 to 84 MPa (Models 8, 9, 10, 13 and 14). The number of ridges evolves with that of trenches. As proposed by Mallard et al. (2016) for 3D spherical models, the number and spatial distribution of plate boundaries vary with the yield stress for a given

Rayleigh number in our models.

The spacing between trenches is rather even in Model 11, which is characterised by the absence of deep thermo-chemical heterogeneities. Keeping the same Rayleigh number and introducing thermo-chemical piles (Model 10 and 13), the spatial regularity is lost with subduction initiating closer to ocean-continent boundaries. Such models show a degree-1 dominant convection with a large-scale upwelling preferentially located below oceans. Increasing the Rayleigh number (Model 18) breaks the degree-1 and the models display a more even spacing between trenches.

In Model 11, positive dynamic topography areas are about 1 km higher than in Model 10 because heat loss is more efficient in the absence of deep thermo-chemical piles. We verify that the presence of dense material at the base of the mantle in Model 10 opposes the positive buoyancy of ascending plumes and limits their vertical velocity. As a result, in Model 11, plumes are more positively buoyant and deflect the surface more than in Model 10. Model 18, for which the Rayleigh number is increased, also shows higher dynamic topography highs. Increasing the Rayleigh number with mixed heating decreases the average temperature below the boundary layer (Sotin and Labrosse, 1999). Therefore, plumes have a larger excess temperature and hence produce stronger dynamic topography.

Small-scale convection develops below old oceanic lithosphere and continents, as expected for Earth (Haxby and Weissel (1986)). As the number of subduction zones decreases, small-scale convection and small-scale dynamic topography are more developed since older and thicker oceanic lithosphere are present (Models 10 and 13). Model 8 (yield stress equal to 7 MPa) is characterised by the quasi absence of small-scale topography, while small-scale topography is ubiquitous in Model 14 characterised by episodic-lid convection.

3.3.3.2 Spectral decomposition of dynamic topography

We compute the spatial Fourier power spectrum of the average dynamic topography for Models 9, 10, 11, 13 and 18 in order to characterise the spatial distribution of dynamic topography power in plate-like regime, and for Models 8 and 14 that present different convective regimes. To compare these Fourier power spectra with existing 3D spherical harmonics power spectra of global dynamic topography (*e.g.* Flament et al., 2013), we calculate and normalise the Fourier spectrum for our models following the method described in Appendix A.

The power spectrum of dynamic topography in our models with plate-like tectonics (Fig. 3.9) is characterised by a large power at low degrees (> 1 km^2, for degrees 1 to 4) and a substantial power

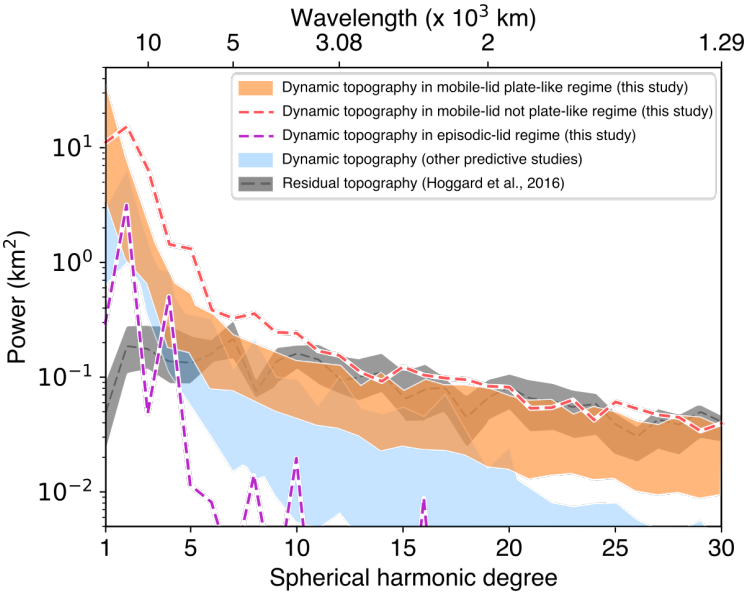


Figure 3.9: Temporal average of dynamic topography power spectra for Models 9, 10, 11, 13 and 18 with plate-like tectonics (orange shaded area). Temporal average of dynamic topography power spectra for Model 8 in mobile-lid tectonic regime without plate-like tectonics (orange dashed line) and Model 14 in episodic-lid regime (pink dashed line). The predictive dynamic topography spectra of Conrad and Husson (2009), Flament et al. (2013), Ricard et al. (1993), Spasojevic and Gurnis (2012), Steinberger (2007) are represented by the light blue envelope. The residual topography power spectrum obtained by regularised least-squares inversion from Hoggard et al. (2016) is shown as a dashed grey line, with the grey envelope representing associated uncertainties.

($> 2 \times 10^{-2}$ km^2) for intermediate scales of dynamic topography (degree 4-30). The average spectral power at degree 1 decreases from 10 km^2 for Model 11 (without thermo-chemical heterogeneities) to 4 km^2 for Model 10 (with thermo-chemical heterogeneities). At spherical harmonic degree 2, the average spectral power is 6 km^2 and 2.5 km^2 for Models 11 and 10, respectively. Basal thermo-chemical piles barely impact intermediate and small-scale dynamic topography. This decrease in amplitude of the largest scales of dynamic topography in Model 10 results from the fact that thermal buoyancy is partially compensated by the negative chemical buoyancy of basal thermo-chemical anomalies. Despite differences in the planform of convection between model cases (Fig. 3.6), the power of dynamic topography is always predicted to be greater than 1 km^2 at low spherical harmonic degrees.

Increasing the yield stress from 7 to 84 MPa while increasing the internal heating rate from 9×10^{-13} W·kg^{-1} to 1×10^{-11} W·kg^{-1} leads to a decrease in power at intermediate scales (from more than 10^{-1} km^2 for Model 8 to less than 10^{-3} km^2 for Model 14). Comparing the thermal heterogeneity spectra of Models 9, 10 and 13 (Fig. 3.6), reveals that increasing the yield stress leads to a decrease in power at intermediate wavelengths (spherical harmonic degrees 4-16), particularly in the upper mantle

since less subduction zones develop and the interior of the mantle heats up, prohibiting the rise of mantle plumes. Therefore, a larger part of topography is isostatic for a higher yield stress, and the dynamic topography spectral power decreases.

While increasing the Rayleigh number from 10^7 (Model 10) to 5×10^7 (Model 18) modifies the spatial distribution of dynamic topography by imposing more vigorous convection (Fig. 3.6 and 3.8), the average spectrum of dynamic topography from degree 1 to 40 is overall similar between these two models.

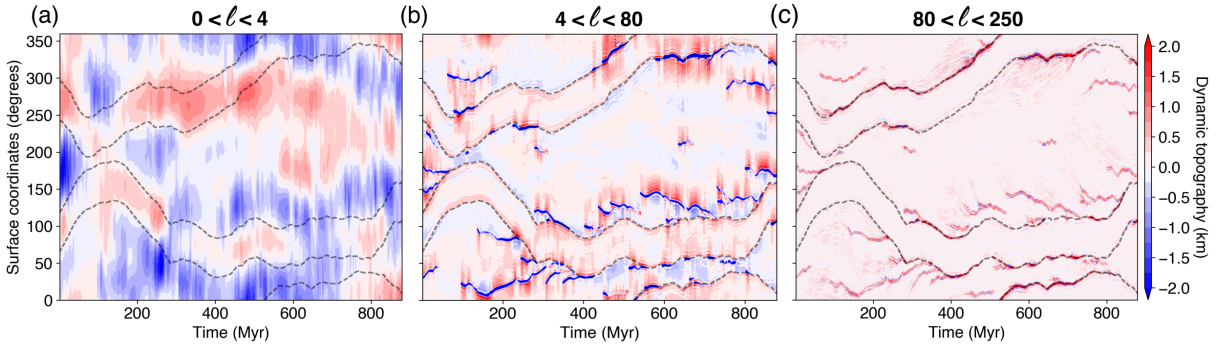


Figure 3.10: Low-pass, band-pass and high-pass filtered dynamic topography for Model 10. l is the spherical harmonic degree. Continent boundaries are delimitated with dashed lines. To enhance dynamic topography contrasts, we limit the dynamic topography scalebar to ± 2 km. The minimum and maximum amplitudes of dynamic topography are annotated in parentheses.

In order to identify the sources of the different spectral signatures of dynamic topography, we used an order-5 Butterworth filter (Butterworth, 1930) to decompose the dynamic topography component of Model 10 (Fig. 3.8c) into large (> 5,000 km - spherical harmonic degree $l < 4$), intermediate (between 5,000 km and 500 km - $4 < l < 80$) and small (< 500 km - $l > 80$) scales (Fig. 3.10). This filter has a flat response in the passband and a continuous slope decrease to the stopband frequency (no ripples), avoiding the addition of noise to the filtered signal.

In Model 10, large-scale dynamic topography highs (Fig. 3.10a) have a maximum amplitude of 1.4 km. Figure 3.11 shows that dynamic topography highs are correlated with the position of large-scale upwellings, which are linked with the position of dense basal structures in Model 10. Large-scale dynamic topography lows (maximum amplitude -2.1 km) occur at subduction zones, which generally initiate on the sides of dense basal structures before moving towards continental edges. In other plate-like models, the maximum peak-to-peak amplitude is -3.1/2.3 km.

Filtering dynamic topography for intermediate scales (Fig. 3.10b) shows that the main process controlling dynamic topography at these spatial scales is subduction. Slabs generally stagnate in the

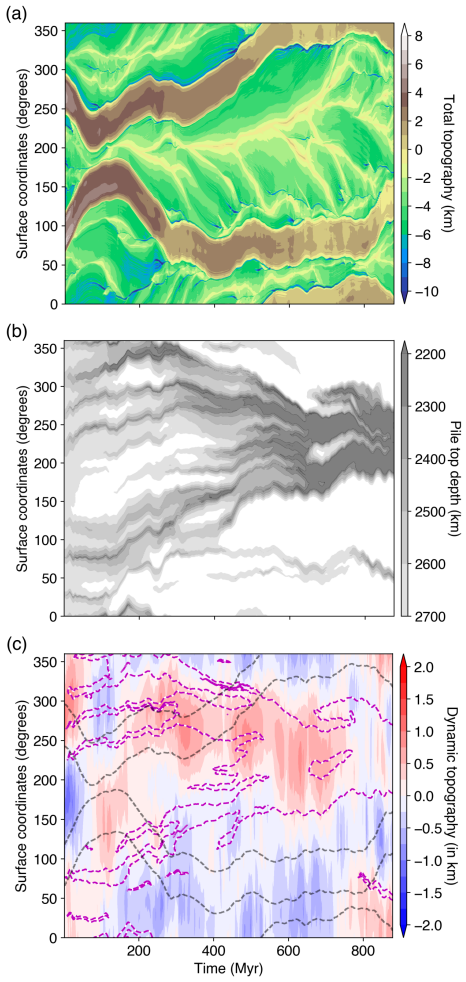


Figure 3.11: Temporal evolution of (a) total topography, (b) the depth of the top of thermo-chemical material and (c) degree-2 low-pass filtered dynamic topography for Model 10. In (c), continent boundaries are delimitated with grey dashed lines and the 2500 km pile depth contour is delimitated with magenta dashed lines. To enhance dynamic topography contrasts, we limit the dynamic topography scalebar to ± 2 km.

transition zone, which leads to changes in their dip-angle. This is reflected in the temporal changes of the spatial distribution of dynamic topography amplitudes on either side of subduction zones. Continents are also affected by intermediate- to large-scale dynamic topography highs when plumes reach their base and propagate laterally (Fig. 3.10b).

Finally, all models displaying plate-like tectonics predict small-scale dynamic topography (Fig. 3.10c), particularly developed below oceanic lithosphere near subduction zones, with an amplitude of ± 750 m at most and a wavelength of ∼200 km. It is characterised by two viscous bulges surrounding a depression directly above the trench, as described in Husson et al. (2012). Small-scale convection below continental lithosphere produces dynamic topography wavelengths of about 500 km. This is

larger scale than for the oceanic lithosphere, because continents are ten to a thousand times more viscous.

3.3.3.3 Temporal evolution of dynamic topography

Large-scale mantle convection drives the temporal evolution of large scale dynamic topography as highlighted by the superposition of the location of deep thermo-chemical heterogeneities, when present, and large-scale dynamic topography highs (Fig. 3.11). The progressive self-organisation of the basal thermo-chemical layer does not significantly affect the amplitude of large-scale dynamic topography (spherical harmonics of degree 1 and 2, Fig. 3.11c). In Models 9 and 11, the formation of a supercontinent is linked to an increase in the spectral power of dynamic topography at spherical harmonic degree 1. Such variations of large-scale dynamic topography occur on timescales of several hundreds of millions of years. In Model 13, this is not visible since one of the continents is surrounded by subduction zones, which generate a strong negative dynamic topography (Fig. 3.8). Therefore, the spectral power associated to degree 1 is not as large as in Models 9 and 11 that are characterised by large-scale positive dynamic topography above continents at the time of the collision.

Intermediate scales of dynamic topography are also subjected to variations through time, in connection with the temporal evolution of the number of subduction zones. As shown on Figure 3.12, the spectral power of intermediate spherical harmonic degrees varies over time by about one order of magnitude for Models 9, 10, 11, 13 and 18. In Models 10 and 13, the decrease in the power of intermediate scales is associated with a decrease in the number of subduction zones (Fig. 3.12d and h) whereas the initiation of subduction zones favours the development of intermediate wavelengths of dynamic topography. Such variations occur on timescales of about 50-100 Myr on average (Fig. 3.12c and g). These timescales increase for increasing yield stress. In Models 10 and 13, a maximum of six subduction zones exist at any time. As a consequence, any subduction initiation or slab break-off event significantly modifies the spatial distribution of dynamic topography at intermediate wavelengths. In Models 9, 11 and 18, changes in the dynamic topography power spectrum at intermediate scales are less correlated with changes in the number of subduction zones. In Models 9 (low yield stress) and 11 (absence of dense basal heterogeneities), up to 15 subduction zones exist at any time and they are distributed more homogeneously than in Models 10 and 13. Therefore, subduction initiation or slab break-off events have less impact on the spatial distribution of dynamic topography than in models with less subduction zones. Variations in the spectral power at intermediate scales can also be

as frequent as every 10-50 Myr in Models 9, 11 and 18 than in models 10 and 13 since subduction initiations and break-offs are more likely when the yield stress is lower than 20 MPa, in the absence of dense basal heterogeneities or for a Rayleigh number as high as 5×10^7. In Model 18, the large Rayleigh number leads to an homogeneous temporal distribution of subduction zones and relatively small changes in the temporal evolution of intermediate-scale dynamic topography as in Models 9 and 11.

The formation of a supercontinent in Models 9, 11 and 13 is associated with a strong decrease in the power at intermediate scales of dynamic topography. In Models 9 and 11, the decrease in dynamic topography power corresponds to subduction cessation due to continental collision. In Model 13, this decrease in the power spectrum of intermediate-scale dynamic topography occurs after the collision because a subduction zone persists at the margin of the newly formed supercontinent. Changes in the dip-angle of subduction zones also regionally modify dynamic topography on timescales of several tens of millions of years (Fig. 3.8 and 3.10b).

In all considered models, small-scale dynamic topography is linked to small-scale convection and subduction zones. Small-scale convection develops below moving plates and thus undergoes shearing deformation which deflects the moving cells (Fig. 3.3a). Short-lived cold droplets develop at the base of the lithosphere on timescales of the order of 1-10 Myr, thus deflecting the surface at this rhythm (Fig. 3.10c). In the models, once the lithosphere has been shaped by small-scale convection, subsequent instabilities initiate at the same location, which leads to long-lived stationary waves of small-scale dynamic topography (timescale of the order of ∼50-100 Myr, visible on Fig. 3.10c) that only disappear when absorbed by a subduction zone. Local disturbances in the planform of small-scale convection are caused by the interplay between small-scale convection and rising plumes beneath oceanic lithosphere, which 'rejuvenate' its base and temporarily erase small-scale convection in the direct vicinity of the plume conduit as described in Ballmer et al. (2011) and Coltice et al. (2017b).

3.3.4 Discussion

3.3.4.1 Model limitations

Because of the 2D-spherical annulus geometry of our models, temperature and density anomalies are still confined to a plane. Flow cannot propagate orthogonally to the 2D plane and thus generates dynamic topography wavelengths longer than expected since the rising material can only spread in one

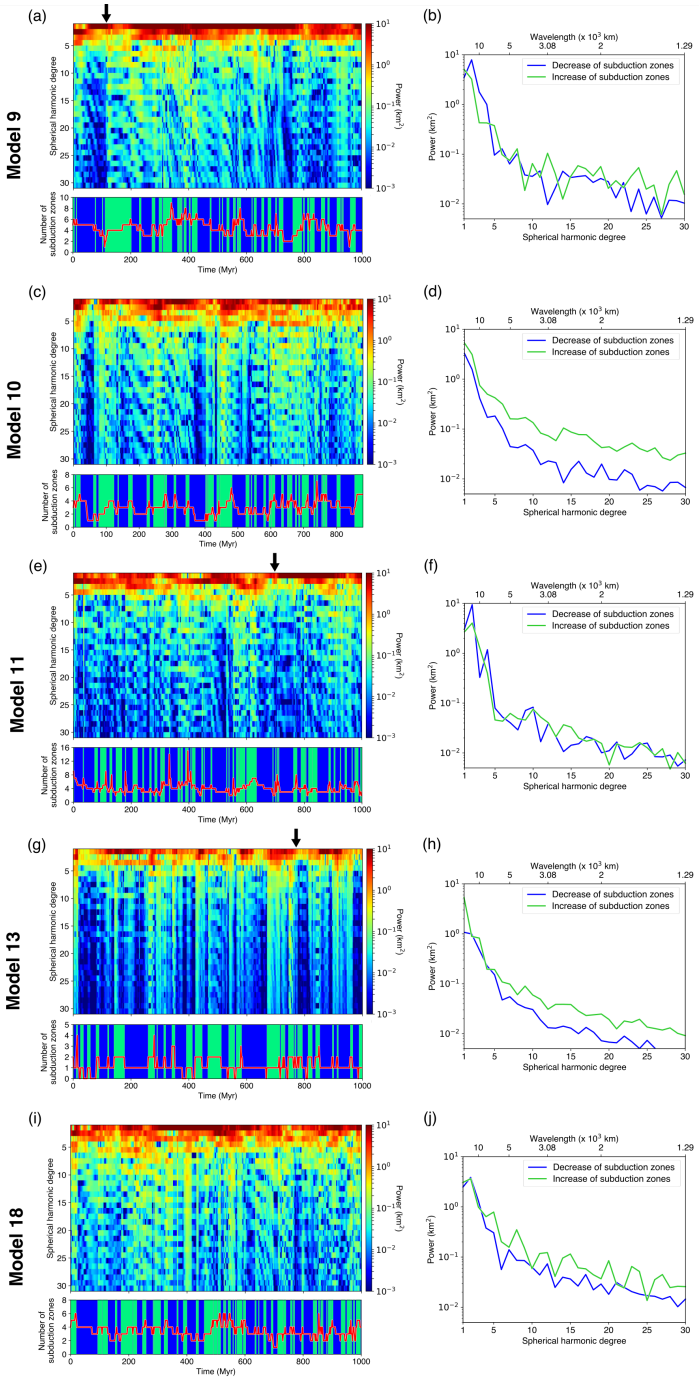


Figure 3.12: Temporal evolution of dynamic topography power spectrum and evolution of the number of subduction zones through time for Models 9 (a), 10 (c), 11 (e), 13 (g) and 18 (i). The blue zones are time intervals where the number of subduction zones decreases or has just decreased. The green regions show the timesteps during which an increase in the number of subduction zones is observed, or directly following an increase of the number of subduction zones. The black arrows indicate the formation of a supercontinent in Models 9, 11 and 13. Decomposition of the power spectra of dynamic topography for Models 9 (b), 10 (d), 11 (f), 13 (h) and 18 (j) according to the separation of spectra for the timesteps following a decrease in the number of subduction zones (blue curve), and those following an increase in the number of subduction zones (green curve).

dimension below the lithosphere. In particular, no toroidal flow is produced with this geometry. The effect of the resulting planform of convection on the amplitude of the dynamic topography spectrum of our models is difficult to estimate. Moreover, our spectral decomposition of dynamic topography assumes that the statistical distribution of dynamic topography is homogeneous in all directions on a complete sphere. Time-dependent 3D spherical mantle flow models with an Earth-like Rayleigh number and large radial and lateral viscosity variations are still a computational frontier.

Even though the Rayleigh number, total heat flow and surface plate velocities of our models approach Earth-like values, these models do not fully capture the convective and plate behaviour of Earth since assumptions and simplifications have been made to solve the problem of time-dependent convection. We do not consider mantle compressibility, which would affect the planform of convection, for computational reasons and not to add further complexity. However, we account for a thermal expansivity decrease with depth, which has the most important contribution on mantle convection planform in the lower mantle and therefore on large-scale dynamic topography (Hansen et al., 1993). Moreover, Steinberger (2016) showed that accounting for compressibility (which depends on both the depth-dependence of density and thermal expansivity) does not substantially modify large-scale dynamic topography in instantaneous flow models. Finally, we do not account for phase transitions in the mantle which possibly lead to a decrease in the amplitude of surface dynamic topography (Le Stunff and Ricard, 1997).

Our models employ a simplified and empirical rheology (for a review, see Coltice et al., 2017a), not accounting for the complexity of the coexisting deformation mechanisms at low temperature. Although the use of a power-law rheology should improve the plate-like behaviour of our models (Bercovici, 2003), Christensen (1984c) showed that the convection planform does not differ significantly from the use of a pseudo-plastic rheology such as the one used in this study. Also, we do not model the elasticity of lithosphere, which would at least partially filter out the shortest wavelengths of dynamic topography (Golle et al., 2012). Considering the elastic properties of the lithosphere would modify the behaviour of the highest-frequency surface deflections, depending on the modeled elastic thickness.

We used a free-slip condition at the surface. We thus derived dynamic topography from normal stresses acting on the top boundary, which can produce some artifacts, for example between continental belts or near subduction trenches. Crameri et al. (2012a) showed that the use of a free surface precludes the formation of excessive normal stresses and results in a better resolution of topography. However, this approach drastically increases the computation cost. Moreover, since our surface topography

amplitudes are small compared to the domain depth, using the free-slip simplification is still reasonable (Crameri et al., 2012a).

3.3.4.2 Spatial and temporal influence of dynamic topography on surface processes

The generation of multiple scales of dynamic topography induced by large viscosity contrasts reported herein provides a first step to the modeling of different scales of dynamic topography in 3D global mantle flow models with plate-like tectonics, and their interplay with surface processes. In the models presented, rapid flow reorganisations occur due to mantle-lithosphere interactions such as the evolution of the spatial distribution of subduction zones, subduction initiation or slab break-offs, changes in slab dip-angles, and interaction of small-scale convection and plume heads with the lithosphere. These processes produce dynamic topography over a range of spatial scales that cannot yet be taken into account in 3D global models because of computational limitations. Our models predict significant intermediate to small scales of dynamic topography, with a spectral distribution similar to the global residual topography spectrum of Hoggard et al. (2016) at spherical harmonic degrees larger than five (Fig. 3.9). The dynamic topography spectra that we obtained (Fig. 3.9) are comparable to those derived by recent inversions of present-day mantle structures (Yang and Gurnis, 2016) to simultaneously fit the long-wavelength geoid, free-air gravity anomalies, gravity gradients and residual topography point data (Hoggard et al., 2016), and of a high-resolution upper mantle tomography model (Steinberger et al., 2017). Nevertheless, we note a significant discrepancy at low spherical harmonic degrees (1-4) between global model dynamic topography spectra, including ours, and the residual topography spectrum of Hoggard et al. (2016), for which power is ten times lower (Fig. 3.9). The discrepancy between numerical models of dynamic topography and observation-derived present-day dynamic topography remains debated (*e.g.* Hoggard et al., 2016, Molnar et al., 2015, Yang and Gurnis, 2016, Hoggard et al., 2017, Yang et al., 2017, Steinberger et al., 2017, Watkins and Conrad, 2018). Indeed, Hoggard et al. (2016) and Hoggard et al. (2017) proposed from models of residual topography based on seismic profiles in the oceanic realm and free-air gravity anomalies in the continental domain that large-scale dynamic topography has an amplitude of $\pm$ 300 m at most. More recently, Steinberger et al. (2017) used a crustal model to estimate present-day continental residual topography and also found a limited degree 2 residual topography amplitude. Watkins and Conrad (2018) also inferred a degree 2 residual topography amplitude of about 500 km from the asymmetric subsidence of mid-ocean ridges.However, Yang and Gurnis (2016) and Yang et al. (2017)

advocate for low spherical degree of dynamic topography with amplitudes larger than ± 1 km, based on a different analysis of residual topography data and consistently with previous numerical models based on seismic tomography or slab assimilation. Our time-dependent models self-generating mantle convective scales with plate-like tectonics and basal chemical heterogeneities support the existence of large-scale dynamic topography of amplitude larger than ± 1 km.

Our models predict that the main geodynamic processes controlling the existence of intermediate wavelengths of dynamic topography are associated with plate boundaries, specifically subduction initiation or cessation, while Hoggard et al. (2016) identified intraplate intermediate scales of residual topography and explained them by distributed density anomalies in a fast moving asthenospheric channel. Although our models present large viscosity contrasts between the lithosphere and the asthenosphere, we only observe a significant effect of this low-viscosity layer on dynamic topography at scales smaller than 1,000 km (small-scale convection, Fig. 3.3). It is thought that subduction dynamics control continental sedimentation by favouring regional continental flooding (Mitrovica et al., 1989). In our models, the tilting of continents due to the presence of sinking slabs in the upper mantle can reach 5,000 km in lateral extent (depending on slab geometry), up to 1.5 km amplitude at continental margins and can last up to 50 Myr (Fig. 3.8c and Fig. 3.13). In the case of the tectonic motion of continents over slabs, we observe a propagation of topographic lows towards the centre of the continent, reminiscent of the migration of sedimentary depocentres towards the interior of North America (Liu and Gurnis, 2008).

Intermediate to long-wavelength dynamic topography variations caused by changes in the planform of convection due to supercontinent cycles or to the evolution of the number of subduction zones (Fig. 3.12) are likely to cause changes in the volume of ocean basins, leading to sea-level changes. For example, Conrad and Husson (2009) studied the effects of continents moving above downwellings, and the effect of Wilson cycles on sea-level variations. They showed that present-day seafloor is uplifted by 132 m (air-loaded) due to its preferred position on top on large-scale upwellings while continental areas are deflected by about 295 m because of the presence of dense mantle anomalies below them after the Pangea breakup. They estimated a sea-level rise of 0.44 ±0.22 m·Myr^{-1} due to this uplift. Such long-term variations in the seafloor depth occur throughout our models, due to long-term changes in the number of subductions linked with large-scale mantle flow reorganisations. For example, the long-term decrease in the average oceanic dynamic topography between 350 Myr and 750 Myr for Model 9 at a rate of about 1.5 m·Myr^{-1} (Fig.3.13a) and between 250 Myr and 650 Myr for Model 10 (Fig.

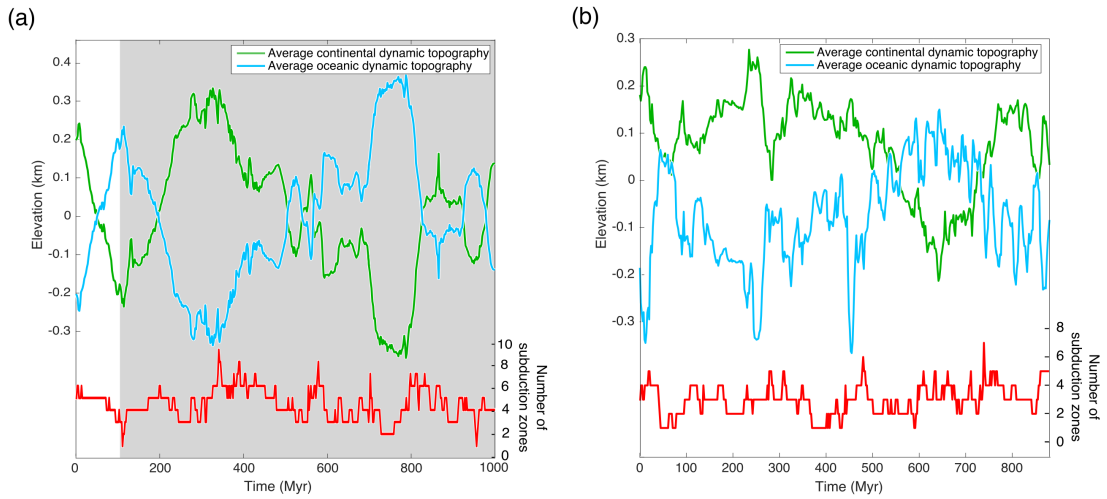


Figure 3.13: Temporal evolution of average oceanic dynamic topography (blue curve), continental dynamic topography (green curve) and the number of subduction zones in (a) Model 9 and (b) Model 10. The grey shaded area corresponds to the presence of a supercontinent in Model 9. The average continental dynamic topography evolution compensates the evolution of the average oceanic dynamic topography (the continental and oceanic area are not the same, which explains differences between the blue and green curves). Note the anticorrelation between the evolution of the number of subduction zones and the evolution of average oceanic dynamic topography.

3.13b) at a rate of about 0.75 m·Myr^{-1} correspond to the presence of a large-scale upwelling below the oceanic domain which prevents the initiation of subduction zones in this area at these periods (Fig. 3.8 and 3.11). Moreover, on Fig. 3.13a, we show that the formation of a supercontinent in Model 9 is associated with a 400 m decrease in the average depth of the seafloor over about 100 Myr (rate of change 4 m·Myr^{-1}), and that it is compensated by continental deflection over the same period. These amplitudes and rates of change are larger than estimated by Conrad and Husson (2009) and probably result from the 2D geometry of our models, which leads to higher amplitude and faster motion of the surface since changes in mantle flow are only accommodated along one direction. We therefore show that, in our models, the decrease in the number of subduction zones linked to large-scale reorganisations of mantle flow leads to shallower seafloor, which would increase long-term global sea-level.

Faster dynamic topography changes also occur on timescales of 5 Myr to tens of millions of years and can reach up to ±60 m·Myr^{-1} in average for both oceans and continents (Fig. 3.10c and Fig. 3.13). These are linked with abrupt changes in mantle dynamics, such as the initiation, change in the dip-angle or break-off of slabs and the rise of a plume head below the lithosphere. The amounts of vertical stress generated by such events on the lithosphere cause dynamic topography changes with

variable amplitude (Fig. 3.13). We expect local stratigraphic sequences with periods as short as ∼5 Myr to occur in response to those geodynamic processes. These intermediate scales of dynamic topography can locally modify shorelines, leading to changes in sedimentation at continental margins such as documented for the North-European margin in the vicinity of the Iceland plume (Hartley et al., 2011).

In our models, dynamic topography is controlled by small-scale convection at wavelengths shorter than 500 km, which is consistent with the study of Petersen et al. (2010) that predicts small-scale dynamic topography (< 500 km) with amplitudes of about ± 300 m and high-frequency variations (2-20 Myr). Our whole-mantle convection models suggest that small-scale convection induces dynamic topography that would affect sedimentation and continental flooding at spatial scales between 200-500 km, with maximal amplitude of ±750 m and period 2-50 Myr. Nevertheless, we observe a partial filtering of small-scale dynamic topography close to continents, which are stiffer and thicker. This could result from an attenuation for dynamic mantle tractions by the lithosphere rheology, as studied in laboratory experiments by Sembroni et al. (2017).

3.3.5 Conclusions

We explored the parameter space for convection models in 2D spherical annulus geometry in which we consider a viscosity jump by a factor of 30 at 660 km depth and an activation energy for the temperature dependence of viscosity of 142 kJ·mol^{-1}, which leads to a variation of viscosity over 6 orders of magnitude. We identified a range of models in a plate-like tectonic regime with Earth-like surface heat flow, surface velocities and hypsometric distribution. For these models the Rayleigh number ranges between $1 - 5 \times 10^7$, internal heating rates range between 9×10^{-13} and 1.4×10^{-11} W·kg^{-1} and the yield stress ranged between 17 MPa and 49 MPa.

We developed an analytical procedure to compare 2D spherical annulus power spectra to 3D spherical harmonic power spectra. The amplitude of large-scale dynamic topography (> 10^4 km) varies between -2.1 km and +1.4 km in Model 10 (with dense thermo-chemical piles), and between -3.1 km and +2.3 km in Model 11 (without dense thermo-chemical piles). In addition, all these models produce intermediate scales of dynamic topography (500 to 10^4 km - up to degree 30) with a spectral power consistent with those obtained from the study of the residual topography at present-day (Hoggard et al., 2016). These models also predict dynamic topography at wavelengths shorter than 500 km.

The longest wavelengths of dynamic topography represent the large-scale convective flow expressed by the large tectonic plates and distribution of lower mantle convective cells. The large-scale flow evolves with continental drift and global tectonic reorganisation at timescales >100 Myr. The intermediate scales of dynamic topography correspond to the flow in the upper mantle around subduction zones and depend on the geometry of slabs. In these models, subduction zones last between ten to several hundreds of Myr. The shortest scales of dynamic topography are generated by small-scale convection below oceanic and continental lithosphere. In our models, these instabilities evolve rapidly between five to tens of Myr.

The parameters we varied influence the distribution of dynamic topography, through the organization of the flow: increasing the Rayleigh number, decreasing the yield stress and removing deep dense chemical piles have the similar effect of increasing the number of slabs. In turn, this results in younger ocean floor and in less developed small-scale convection, because small-scale convection preferentially occurs under old seafloor. As a consequence, models with the smallest number of slabs display strong small-scale dynamic topography, and the spectral power of intermediate scales of dynamic topography fluctuates strongly with initiations and break-offs of slabs.

Our models suggest that the flow in the upper mantle, mostly driven by slab evolution over 10-100 Myr generates the intermediate scales of dynamic topography proposed by Hoggard et al. (2016). In the models, these scales occur due to the existence of large lateral viscosity contrasts in the upper mantle. Our models suggest that these intermediate scales coexist with strong large-scale dynamic topography ($> 10^4$ km). We propose that a significant decrease in the number of subduction zones linked with large-scale mantle flow reorganisations, for example related to supercontinent formation, could cause a substantial decrease of the spectral power of intermediate scales of dynamic topography linked with a significant decrease in the average seafloor depth, which would contribute to an increase of sea-level and of the area of continental sedimentary basins.

Our study suggests that the interpretation of surface processes, such as sedimentary strata deposition and sea-level change, should consider the effect of dynamic topography at all spatial and temporal scales.

Acknowledgments

We thank Mark Hoggard, an anonymous referee and the Associate Editor for their constructive reviews. The data used are listed in the references, tables, and Appendix. We thank S. Durand for sharing data used in Fig. 3.6. The research leading to these results has received funding from the European Research Council within the framework of the SP2-Ideas Program ERC-2013-CoG, under ERC grant agreement 617588. Calculations were performed on the Augury supercomputer at P2CHPD Lyon, and with the assistance of resources from the National Computational Infrastructure (NCI), which is supported by the Australian Government. M.A. benefited from funding provided by the grant n°15.007742.01 from Région Rhône-Alpes and a grant from Programme Avenir Lyon Saint-Etienne. N.F. was supported by ARC DE160101020. R.D.M. was supported by ARC IH130200012.

3.4 Conclusions and perspectives

Take-home message:

From this article, the main conclusions are:

- **We identified a parameter range for which 2D mantle convection models produce Earth-like tectonics, plate velocities, heat flow and topography**
- **In these models, dynamic topography is substantial at large, intermediate and small spatial scales**
- **Feedbacks between mantle flow and lithosphere dynamics control the spatio-temporal distribution of dynamic topography**

While it is known from kernel studies of Hager and Richards (1989) that intermediate and small scales of convection in the upper mantle play a significant role in the generation of dynamic topography, numerical models have mainly focussed on the study of large-scale dynamic topography (*e.g.* Steinberger, 2007). Observations of smaller-scale dynamic topography (see section 3.1) have only recently revived the need to account for asthenospheric and upper mantle flow in the modeling of surface dynamic topography (*e.g.* Steinberger et al., 2017, Watkins and Conrad, 2018, Tutu et al., 2018), although clear mechanisms still need to be resolved. The main contribution of this work is that time-dependent models of mantle convection with plate-like tectonics displaying strong radial and lateral viscosity contrasts make it possible to generate significant intermediate and small scales of dynamic topography, consistent with present-day observation-derived residual topography. Moreover, we propose a mechanism (the temporal evolution of subduction zones) controlling the generation of intermediate scales of dynamic topography.

Perspectives:

This work is only a first step to the understanding of how mantle properties and dynamics at all spatial and timescales control the presence of dynamic topography. As mentioned in section 3.3.4.1, the question of Earth's mantle and lithosphere rheology is important to tackle when we want to unravel the spatio-temporal evolution of dynamic topography patterns. For example, an important number of studies have focussed on the role of asthenospheric low-viscosity channels in the generation of

fast convective cells of intermediate scale, therefore leading to intermediate-scale dynamic topography (*e.g.* Hoggard et al., 2016). Steinberger et al. (2017) recently attempted to model large-scale dynamic topography with a small-amplitude. They propose to test different viscosity profiles, although it would alter the fit to the geoid. Likewise, the effect of compressibility in the lower mantle does not significantly reduce the amplitude of degree-2 dynamic topography (Rubey et al., 2017). Le Stunff and Ricard (1997) and Steinberger (2007) tested the possibility of an attenuation of large-scale lower mantle convective scales by phase transitions. As for lithosphere rheology, many studies show the importance of its elastic properties in filtering the different scales of dynamic topography (McKenzie, 2010, Golle et al., 2012). While the effect of viscoelasticity on lithospheric vertical deformations has only been studied in regional models displaying simple mantle convective scales (Petersen et al., 2010), the recent implementation of viscoelasticity in StagYY (Patocka et al., 2017) now makes it possible to envision the study of the influence of complex mantle convective patterns on the vertical response of a visco-elastic lithosphere.

Another area of focus is the validation of the results presented in section 3.3 in 3D-numerical models of mantle convection with plate-like tectonics. Here, the main barrier is the increase in the computational time required to equilibrate our models and study the evolution of dynamic topography over timescales of several hundreds of millions of years (this would require over two months of computation for each model on 128 processors, which limits the possibilities of testing a large range of model parameters). As described in Chapter 4, we have run a number of preliminary 3D numerical models with comparable parameters to the ones presented in section 3.3 (Fig. 4.31). However, the systematic study of dynamic topography predicted by those models still needs to be carried out.

Chapter 4

Some surface expressions of mantle plume dynamics

Contents

4.1 Introduction . . . 123

4.2 Sources of hotspot relative motions in whole-mantle convection models . . . 124

4.2.1 Introduction . . . 125

4.2.2 Modeling mantle plumes in 3D-whole mantle convection models . . . 128

4.2.2.1 Numerical models . . . 128

4.2.2.2 Plume tracking method . . . 131

4.2.2.3 Scaling of model velocities . . . 132

4.2.3 Mantle plume phenomenology . . . 134

4.2.3.1 Modeled mantle convective planform . . . 134

4.2.3.2 Characteristics of mantle plumes . . . 134

4.2.3.3 Temporal behaviour . . . 143

4.2.4 Analysis of the motion of mantle plumes . . . 147

4.2.4.1 Description . . . 147

4.2.4.1.1 Absolute motions of mantle plumes. . . . 147

4.2.4.1.2 Relative motions between mantle plumes . . . 149

4.2.4.1.3 Vertical deflection of mantle plumes . . . 150

4.2.4.2 Potential causes of mantle plumes motion . . . 151

4.2.4.2.1 Slow entrainment by global mantle flow . . . 151

4.2.4.2.2 Limited effect of return flow. . . . 152

4.2.4.2.3 No systematic shearing of plume conduits by surface plate motions. 154

4.2.4.2.4 No enhanced stabilization of mantle plumes located at ridges. . . . 155

4.2.4.2.5 Push induced by slabs. . . . 156

4.2.4.2.6 Rapid motions due to negative pressure gradients . . . 158

4.2.4.2.7 Relative motions between mantle plumes and the basal thermo-chemical layer . . . 158
4.2.5 Discussion . . . 160
4.2.5.1 Model limitations . . . 160
4.2.5.2 Comparison with the lateral motion of mantle plumes in other studies . . . 160
4.2.6 Conclusion . . . 162
4.3 Northward drift of the Azores plume in the Earth's mantle . . . 164
4.3.1 Abstract . . . 164
4.3.2 Introduction . . . 164
4.3.3 Results . . . 167
4.3.3.1 New evidence for a temperature asymmetry below the Azores plume . . . 167
4.3.3.2 Thermal asymmetry caused by relative motions between a ridge system and a plume . . . 169
4.3.3.3 Northward motion of the Azores plume . . . 170
4.3.4 Method . . . 173
4.3.4.1 PRIMELT . . . 173
4.3.4.2 Numerical modeling . . . 174
4.4 Conclusion and perspectives . . . 175
4.4.1 Conclusion . . . 175
4.4.2 Perspectives . . . 176
4.4.2.1 Lateral motions of mantle plumes and supercontinent cycles . . . 176
4.4.2.2 Definition of an absolute frame of reference based on hotspots . . . 180
4.4.2.3 Topography and geoid anomalies generated by mantle plumes . . . 181

4.1 Introduction

As described in Chapter 1, the surface expression of focused areas of mantle upwelling (mantle plumes) can take different forms. These include intraplate or near-ridge volcanism with a particular geochemical signature (OIB and MORB basalts, low He^4/He^3 ratio...), surface positive topography caused by mantle positive buoyancy flow and multiple interactions with plate boundaries (interaction with spreading ridges, participation in rifting). Nevertheless, the characteristics of mantle plumes are still poorly constrained. This partly stems from the difficulties in seismically imaging focused zones of

mantle upwelling, although recent models tend to favor the presence of broad (300-500 km) and rather vertical plume conduits below major hotspots (French and Romanowicz, 2015). Moreover, estimates of plume buoyancy force can vary by a factor of 10 for Iceland for example, depending on the use of V-shaped ridges or topographic swells for the calculation of its buoyancy flux (Crosby and McKenzie, 2009). Characterizing the phenomenology of Earth's mantle plumes is a critical step towards the understanding of mantle plume dynamics and interactions with multiple scales of mantle convection and plate tectonics. Moreover, geochemical dating and paleomagnetic analyses of hotspot tracks usually provide a reference frame for reconstructing the past lateral motions of Earth's lithosphere. Nevertheless, precise understanding of the possible lateral motions of mantle plume conduits due to mantle convection and plate tectonics still lacks.

In this Chapter, I first quantify the behaviour of the mantle plumes arising self-consistently in 3D spherical models of mantle convection with plate-like tectonics. Then, I quantify their stability in the mantle by characterizing their interactions with both mantle convection and plate tectonics. Finally, I compare the upper-mantle thermal wake of mantle plumes in models with petrological analyses of basaltic rocks sampled at the Mid-Atlantic Ridge axis in the vicinity of the Azores in order to propose a northward motion of the Azores hotspot along the ridge axis between 85 and 20 Myr.

4.2 Sources of hotspot relative motions in whole-mantle convection models

The following section is to be submitted as:

Arnould, M., Coltice, N., Flament, N., *in prep.*, Sources of relative motions between hotspots in whole-mantle convection models with plate-like tectonics

Abstract

Mantle plumes have been widely used as a fixed reference frame in order to calculate the motion of tectonic plates. However, some paleomagnetic and geochronological observations suggest that substantial relative motions between hotspots can occur. Sources for such rapid motions of hotspots are still debated. Here, we present a set of 3D numerical models of mantle convection self-generating

plate-like tectonics. In those models, drifting plumes fully-dynamically emerge and interact with moving density heterogeneities within the modeled self-organized convective system. We investigate the role of depth-dependent thermal expansivity, the yield stress and the presence or the absence of deep thermo-chemical piles on the properties and behaviour of mantle plumes. The model plumes present a shape, an excess temperature, a buoyant rising speed, a buoyancy flux, a surface heat flux and pulses of activity comparable to Earth's hotspots. In all models, mantle plumes can persist over a hundred of million years at least. Most mantle plumes move relatively to each other by less than 2 cm·yr^{-1} in all models. Such motions coincide with whole-mantle motions. In models without basal thermo-chemical heterogeneities, plume conduits are always near vertical and are not deflected by mantle return flow because of mantle plume rising speeds larger than 10 cm·yr^{-1} in the lower mantle and 30 cm·yr^{-1} in the upper mantle. The presence of basal thermo-chemical heterogeneities buffers the temperature excess of mantle plumes and results in weaker plumes, more likely to be deflected and advected by mantle flow. Intermediate lateral velocities (2-5 cm·yr^{-1}) result from slabs pushing or shearing the base of plume conduits over timescales of several tens of million years. Some plumes can move relatively to one another by up to 20 cm·yr^{-1} over timescales shorter than 5 Myr. Such motions are related to plume merging events guided by negative pressure gradients. This quantitative study of mantle plume behaviour and characteristics in self-consistent models of mantle convection with plate-like tectonics participates in improving our understanding of the sources of motion of hotspots and the time-dependence of mantle mass fluxes and heat flow from the core.

4.2.1 Introduction

Soon after the emergence of the plate tectonics theory, Wilson (1963) proposed that linear chains of volcanic islands and seamounts displaying an age progression (hotspot tracks) result from the relative motion between tectonic plates and focused spots of melting below the lithosphere. Morgan (1971) then assumed that hotspots derive from stationary mantle plumes anchored in the lower mantle. Minster et al. (1974), Morgan (1981) and Duncan (1981) suggested that hotspots moved by less than 5 mm·yr^{-1} during the last 100 Ma, at least in the Indian and Atlantic Ocean, using geochronological and paleomagnetic measurements at hotspot tracks to test the fixity of mantle plumes. Reconstruction errors and uncertainties within the plate reconstruction circuits were first invoked to account for discrepancies between Indo-Atlantic and Pacific hotspots (Duncan, 1981, Acton and Gordon, 1994, Cande et al., 1995, Stock and Molnar, 1988). Burke et al. (1973), Molnar and Francheteau (1975),

Molnar and Stock (1987) nevertheless showed that mantle plumes have moved by 1-2 cm·yr^{-1} on average during the last 65 Ma, by measuring the relative motion between Indo-Atlantic hotspots and the Hawaiian hotspot. McElhinny (1973), DiVenere and Kent (1999), Raymond et al. (2000), Besse and Courtillot (2002), Tarduno and Cottrell (1997), Tarduno et al. (2003, 2009), Wright et al. (2015) and Konrad et al. (2018) later confirmed that at least the Hawaiian hotspot moved southwards by up to 5 cm·yr^{-1} between 81 and 47 Ma, using different sets of paleomagnetic and geochronological data. On the contrary, Koivisto et al. (2014) invoked a True Polar Wander event and Morgan (1972) and Torsvik et al. (2017) proposed a change in the Pacific plate motion to explain the Hawaiian-Emperor bend.

Numerical and experimental models have also investigated the problem of hotspot motion by studying the possibility of fixed hotspots in a chaotic convective mantle. Jellinek and Manga (2002) proposed from analogue experiments that plumes originating from a thermo-chemical boundary layer remain spatially approximately fixed and last hundreds of millions of years. Davaille et al. (2002) proposed that plumes anchored at a basal thermo-chemical layer would drift following any potential motion of such a layer caused by large-scale mantle convection and Davaille and Vatteville (2005) proposed episodic activity of mantle plumes, with lifetimes of 10 to 200 Myr, depending on their viscosity contrasts. Kincaid et al. (1996), Jellinek et al. (2002, 2003), Jellinek and Manga (2004) and Gonnermann et al. (2004) studied the behaviour of thermal plumes in the context of vigorous mantle convection and plate tectonics in laboratory experiments. They showed that, depending of the viscosity contrast between plumes and the ambient mantle and the ratio of plate velocities compared to the plume rising speed, plumes can be advected towards regions of large-scale upwellings induced by plate motions. In these models, downwelling is therefore far from any plume (which is consistent with observations, Cazenave et al., 1989, Weinstein and Olson, 1989) and would contribute to localizing mantle plumes by causing the thinning of the thermal boundary layer, therefore preventing the formation of instabilities in the vicinity of downwelling areas .

A large number of plate tectonic reconstructions used fixed hotspots as a reference frame to reconstruct past plate tectonics (*e.g.* Morgan, 1971, Duncan, 1981, Müller et al., 1993). However, because of growing evidence of hotspot motions, especially on timescales larger than 100 Myr, attempts to account for moving hotspots in plate tectonic reconstructions arose (Steinberger and O'Connell, 2000, O'Neill et al., 2005). Steinberger and O'Connell (1998), Steinberger (2000) and Steinberger and O'Connell (2000) computed numerical models of mantle convection with layered viscosity, density anomalies

imposed from seismic tomography models and a surface driven by reconstructed plate velocities. By advecting mantle plumes from the core-mantle boundary, they observed substantial deflection of plume conduits due to mantle return flow. Steinberger and O'Connell (2002) and Steinberger et al. (2004) used that generation of models to fit observed hotspot tracks, and predicted mantle plume motions consistent with paleomagnetic and geochronological estimates. Doubrovine et al. (2012) used such models of moving hotspots in order to iteratively fit hotspots tracks and reconstruct past plate tectonics motions, while allowing mantle plume conduits deformations in the mantle. However, this model displays large net rotation compared to estimates derived from paleomagnetic reconstructions of plate tectonics (Williams et al., 2015, and Table 4.3). Using the same method as Steinberger and O'Connell (1998), O'Neill et al. (2005) studied the relative motion between Indo-Atlantic and Pacific hotspots since the Late Cretaceous by accounting for uncertainties in both hotspot reconstructions and mantle convection models. Their best fit to hotspot track geometries shows substantial motion of Indo-Atlantic hotspots before 80 Ma, while during the last 80 Ma, hotspot motions seem undistinguishable from uncertainties associated with paleomagnetic measurements and mantle convection models. Wang et al. (2018) recently combined the MORVEL plate kinematic model with seismic tomography results to build an absolute plate reconstruction by estimating geochronological uncertainties on 24 deep-rooted hotspot tracks data. They suggest plume motions opposite to plate motions and oriented towards spreading centers.

Several sources have been invoked to explain the presence or the absence of lateral motions of mantle plumes and are indicative of the difficulty to reconstruct the past motions of mantle plumes. Richards (1991) was the first to propose that the large increase in the lower mantle viscosity (necessary to fit Earth's geoid, Hager et al., 1985) could improve the fixity of mantle plumes in 2D numerical models of mantle convection. Burke et al. (2008) proposed that the Indo-Atlantic and the Pacific plumes are rooted on the edges (Plume Generation Zones, PGZs) of two large-scale thermo-chemical heterogeneities lying at the core-mantle boundary (Large Low Shear Velocity Provinces, LLSVPs). Torsvik et al. (2008b) advocated for the long-term stability of LLSVPs while Torsvik et al. (2012) suggested that the anchorage of plumes at PGZs could explain the observed limited motions inside the Pacific and the Indo-Atlantic clusters of hotspots and significant motions between the two clusters. Conrad et al. (2013) tested the stability of mantle plumes anchored at LLSVPs by comparing the dipolar and quadrupolar moments of plate reconstructions with the underlying mantle flow and showed that large-scale areas of upwelling have been stationary since the past 250 Ma. However, Flament et al.

(2017) proposed that basal thermo-chemical heterogeneities can move significantly due to large-scale mantle convection. McNamara and Zhong (2004) further investigated the role of the presence of deep-seated thermochemical heterogeneities on the lateral motion of hotspots and showed no significant difference in the behaviour of plumes in isochemical and thermochemical models. Besides, several alternatives or complementary sources of hotspot motions have been proposed to explain the diversity of geometries of the hotspot tracks that do not result from a change in plate velocities, such as the observed Emperor-Hawaiian bend (*e.g.* Torsvik et al., 2017, Hassan et al., 2016, Tarduno et al., 2009, Sharp and Clague, 2006, Richards and Lithgow-Bertelloni, 1996). These notably include shearing of plume heads by changes in plate motions (*e.g.* Jones et al., 2017), slab-induced lateral push of hot rising material (*e.g.* Hassan et al., 2016), plume-ridge interactions (*e.g.* Ribe, 1996, Tarduno et al., 2009) or the influence of the continental configuration on mantle flow, and therefore on the location of mantle plumes (Zhong et al., 2007). The debate on the degree of interaction between plumes and global or regional tectonics stems from the difficulty in finding clues of such interactions in the geological record and in modeling the dynamic interplay between mantle plumes and mantle convection with plate-like tectonics.

Here, we use 3D models of whole-mantle convection self-generating plate-like tectonics (Coltice et al., 2017a) in order to model drifting plumes. We first compare their characteristics with hotspot observations on Earth. We investigate the influence of the presence of deep thermochemical heterogeneities, the depth-dependent thermal expansivity and the plate tectonic layout on the spatio-temporal evolution of the lateral motion of mantle plumes across a series of models. Our modeled hotspots present a large variety of lateral motions, comparable to observations. We investigate the causes for such a diversity of behaviours, by analyzing the role of surface plate tectonics and convection dynamics on the lateral motion of plumes.

4.2.2 Modeling mantle plumes in 3D-whole mantle convection models

4.2.2.1 Numerical models

We solve the equations of mass, momentum, energy and advection of compositional fields conservation under the Boussinesq approximation in order to produce different models of 3D spherical mantle convection with plate-like tectonics with the code StagYY (Tackley, 2000). We use pseudo-plasticity to generate a surface plate layout (Tackley, 1998). We use a temperature, pressure and yield-stress

dependent viscosity law as described in section 3.3.2, which results in up to seven orders of magnitude of viscosity contrasts throughout the mantle (cf Fig. 4.1b). We also add a viscosity jump by a factor of 30 at the upper-lower mantle boundary, consistent with geoid and post-glacial rebound studies (Nakiboglu and Lambeck, 1980, Ricard et al., 1993).

Table 4.1: Non-dimensional and dimensional parameters

Parameter	**Non-dim. value**	**Dim. value**
Surface temperature (T_{top})	0.12	255 K
Basal temperature (T_{bot})	1.12	2240 K
Mantle domain thickness (D)	1	2890 km
Reference thermal expansivity (α)	1	3×10^{-5} K^{-1}
Reference density (ρ_0)	1	4400 kg·m^{-3}
Reference diffusivity (κ)	1	1×10^{-6} m^2·s^{-1}
Reference conductivity (c_p)	1	3.15 W·m^{-1}·K^{-1}
Reference viscosity (η_0)	1	1.03×10^{22} Pa·s
Internal heating rate (H)	40	6.81×10^{-12} W·kg^{-1}
Activation energy (E_a)	8	142 kJ·mol^{-1}
Activation volume (V_a)	3	13.8 cm^3·mol^{-1}
Maximum viscosity cut-off	10^4	10^{26} Pa·s
Viscosity increase at 660 km	30	
Yield stress gradient for all materials ($d\sigma_Y$)	2.34×10^6	1088 Pa·m^{-1}
Yield stress at the surface - oceanic lithosphere ($\sigma_{Y_{oc}}$)	$2 - 3.5 \times 10^4$	27 − 48 MPa
Yield stress at the surface - continental interior ($\sigma_{Y_{cont}}$)	7×10^5	932 MPa
Viscosity increase - continental interior	100	
Buoyancy number - continental interior (B_{cont})	−0.32	−150 kg·m^{-3}
Thickness - continental interior	0.0692	200 km
Yield stress at the surface - continental belt ($\sigma_{Y_{belt}}$)	3×10^5	400 MPa
Viscosity increase - continental belt	50	
Buoyancy number - continental belt (B_{belt})	−0.4	−188 kg·m^{-3}
Thickness - continental belt	0.0432	125 km
Buoyancy number - deep-seated thermo-chemical layer (B_{llsvp})	0.25	117 kg·m^{-3}
Initial thickness - deep-seated thermo-chemical layer	0.0692	200 km

We compute 4 models of mantle convection with a Rayleigh number of 10^7 to model Earth-like mantle convective vigor. Models 1, 2 and 4 consider a three times decrease of thermal expansivity throughout the mantle following the empiric law of Chopelas and Boehler (1992). This causes the lower mantle to move less vigorously than in a model with a constant depth-dependent thermal expansivity. Models 1, 3 and 4 have a dimensional yield stress of 48 MPa and Model 2 has a dimensional yield stress of 27 MPa, which causes the formation of smaller tectonic plates (Mallard et al., 2016). Model 4 presents basal thermo-chemical heterogeneities characterized by a density excess of 2.7%, a viscosity increase by a factor of 50 (to improve their stability, Heyn et al., 2018) and an initial uniform thickness

of 200 km. The presence of dense basal thermo-chemical heterogeneities causes the heat transfer between the base of the mantle and the surface to be more limited than in the other considered models since all other convective parameters are kept constant. Indeed, the basal heat flow represents only 10 % of the surface heat flow in Model 4, whereas is represents at least 17 % of the surface heat flow in Models 1, 2 and 3. As a consequence, Model 4 allows us to study the impact of the core heat flow on the behaviour of mantle plumes, all other parameters being comparable to Model 1.

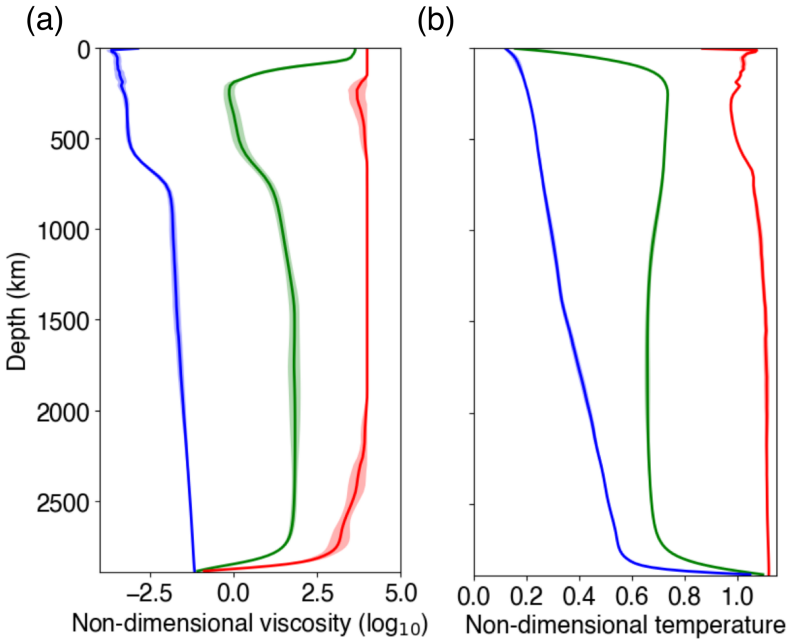


Figure 4.1: Temporal average of the minimum (blue), mean (green) and maximum (red) non-dimensional (a) viscosity and (b) temperature profiles for Model 1. The transparent envelopes indicate temporal variations in viscosity and temperature.

We fix all the compositional tracers during an equilibration phase, until the convective system reaches a quasi-stationary state, recognizable by stable mantle average temperature and basal and surface heat fluxes. We then let the tracers move during a time period of about 200 Myr before computing the model evolutions presented in the following sections. However, even after this time period of equilibration, the mantle average temperature keeps increasing in Model 4 because of the ongoing self-organization of the dense basal material at the base of the mantle throughout the time integration. The different parameters used are detailed in Table 4.1.

4.2.2.2 Plume tracking method

Localized hot upwellings naturally emerge from the core-mantle boundary and interact with other thermal heterogeneities in the mantle and surface tectonic plates (Fig. 4.2). In order to characterize the behaviour of mantle plumes, we first developed a plume detection scheme allowing to track their position and characteristics through time on mantle horizontal slices. Several methods of detection of mantle plumes in 3D numerical models of mantle convection already exist. For instance, Labrosse (2002) used a visual connectivity algorithm in order to detect mantle plumes throughout the mantle at a specific timestep, based on a temperature excess threshold. Hassan et al. (2015) used a *k-mean* clustering method on radial velocity gradient field to detect upwellings at 350 and 1,500 km at each timestep. Hassan et al. (2015) then follow plumes through time by detecting adjacent plumes located within a maximum radius of 500 km every 5 Myr.

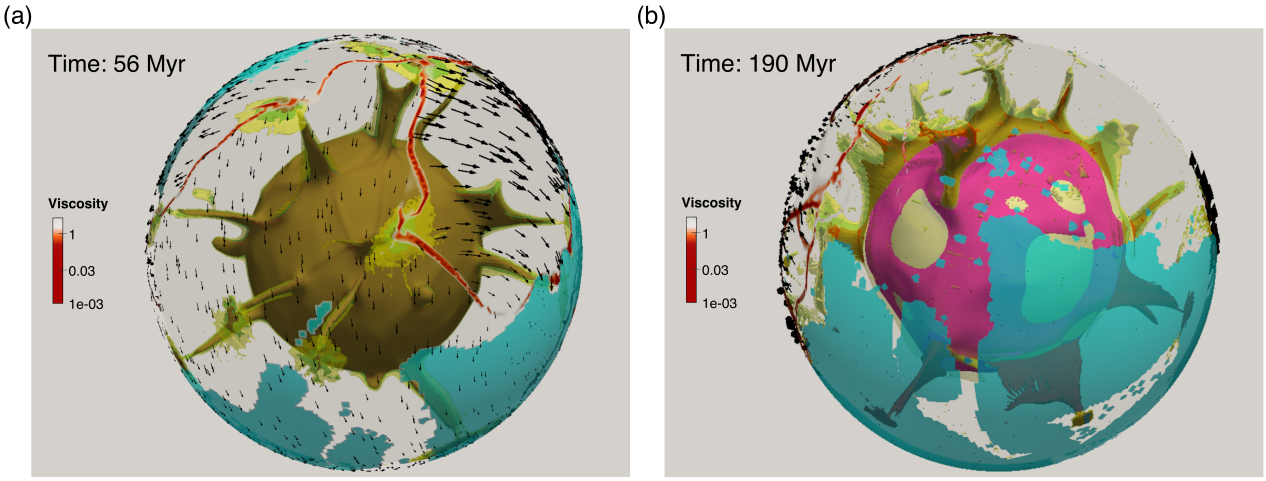


Figure 4.2: (a) 3D-hemispheric view of a timestep in Model 1 showing mantle plumes. Plumes are outlined by the brown (1,970 K), the green (1,860 K) and the yellow (1,750 K) isotherms. (b) 3D-hemispheric view of a timestep in Model 4 showing mantle plumes. Plumes are outlined by the brown (1,750 K), the green (1,700 K) and the yellow (1,690 K) isotherms. The magenta contour delimitates dense basal heterogeneities in Model 4. On both snapshots, surface continents are shown in blue, plate boundaries are outlined by the red lines corresponding to low viscosity areas, and plate velocities are shown by the black arrows.

Mantle plumes are characterized by a large temperature excess and large radial velocities compared to the ambient mantle. We therefore detect mantle plumes in the upper mantle (at 350 km depth) and in the lower mantle (at 1,000 km depth) from the radial heat advection field at considered depths, defined here as the temperature field x the vertical velocity field (Fig. 4.3(b) and (c)). The use of the temperature or the radial velocity field alone is not selective enough to detect mantle plumes. The

chosen depths allow to detect mantle plumes conduits only. We use different heat advection thresholds in order to isolate plumes from the ambient mantle depending on model parameters (Table 4.2). We use the connectivity method described in Labrosse (2002) in order to identify distinct plume conduits. We detect their geometrical centroid in order to localize them. Detecting their maximal temperature results in artificial wobbling of mantle plumes since the position of the maximal temperature of the conduits evolve on shorter timescales than the shape of the conduits. In Model 4, mantle plumes are weaker than in models without basal thermo-chemical heterogeneities since their excess temperature is buffered (cf section 4.2.3.2, Farnetani, 1997) and therefore, we stack the heat advection signal from about 600 km to 350 km depth in order to increase the signal-to-noise ratio by removing small-scale upwellings present only in the upper mantle. This is possible since mantle plume conduits are near vertical (Fig. 4.2). We then track plumes through time at 1 Myr interval by connecting plumes located within a radius of 500 km with a method similar to that of Hassan et al. (2015). We use a larger radius than in Hassan et al. (2015) to follow plumes potentially moving at velocities corresponding to several tens of cm·yr^{-1}. Our plume tracking method recovers plume positions and identities (IDs) in the upper and the lower mantle (Fig. 4.3).

Table 4.2: Non dimensional heat advection RMS and thresholds used for mantle plumes detection in the upper mantle (UM) and the lower mantle (LM)

Parameter	**Model 1**	**Model 2**	**Model 3**	**Model 4**
RMS non-dimensional UM heat advection	1277.3	1342.7	1362.5	956.7
Non-dimensional UM heat advection threshold	9000	10500	9000	4000
RMS non-dimensional LM heat advection	554.4	659	625.1	431.2
Non-dimensional LM heat advection threshold	2100	2500	2000	1200

4.2.2.3 Scaling of model velocities

We define mantle plumes' absolute lateral velocities as the speed reached by a considered plume averaged over 5 Myr. In our models, the motion of lithosphere is described in a no-net-rotation reference frame. As a consequence, net-rotation arises from the flow as opposed to surface motions. In the following, the absolute lateral velocities of mantle plumes that we describe comprise a net rotation component.

In order to compare the behaviour of modeled plumes with reconstructed plume motions, we calculate dimensionalized velocities by scaling the RMS-surface velocity of the models by Earth's present-day surface velocity, which is 3.96 cm·yr^{-1}. From the mantle plume detection algorithm de-

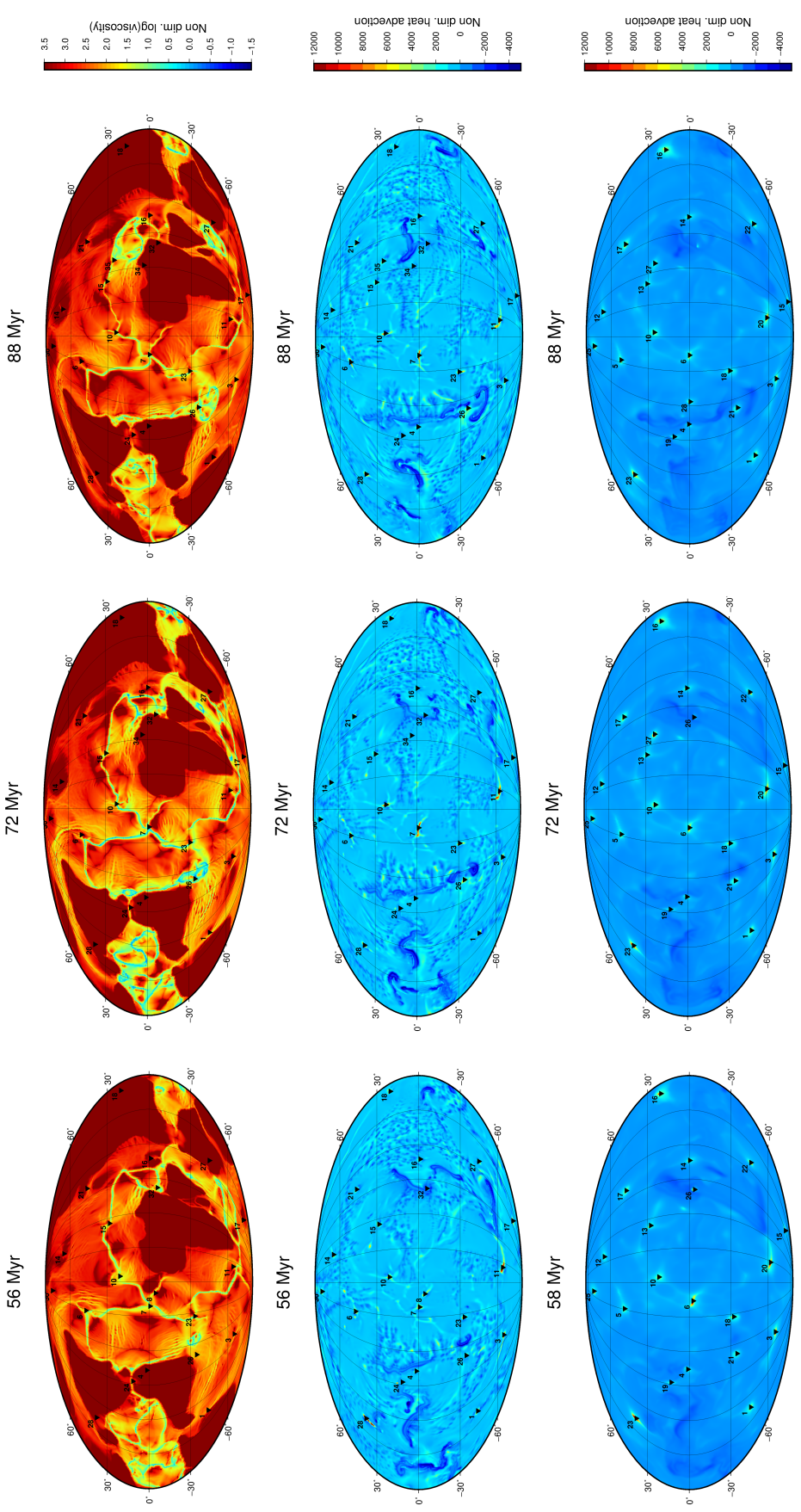


Figure 4.3: (a) Non-dimensional surface viscosity field for Model 1 at 56, 72 and 88 Myr. Continents are delimited by the dark red areas. Plate boundaries are shown in yellow-green. (b) Non-dimensional radial heat advection field at 350 km depth and (c) non dimensional radial heat advection field at 1,000 km depth at the same timesteps for Model 1. Areas of large positive heat advection correspond to mantle plumes. Areas of large negative heat advection represent regions of sinking lithosphere. Note the presence of small-scale convective instabilities in the upper mantle (b). The black triangles represent the hotspots detected in (a-b) the upper and (c) the lower mantle with the method described in section 4.2.2.2. The numbers are hotspot IDs, which allows to follow hotspots through time. Hotspot IDs are independent in the upper and the lower mantle.

scribed in section 4.2.2.2, we use the pyGPlates software to extract the temporal sequence of rotations of each mantle plume. We calculate absolute mantle plume velocities averaged over 5 Myr to eliminate artificial plume wobbling caused by rapid readjusments of plume conduit shape. We also calculate pair-wise mantle plume relative velocities at 5 Myr intervals in order to compare modeled plume relative motions with estimates for hotspot motions.

4.2.3 Mantle plume phenomenology

Here, we describe the phenomenology of all modeled mantle plumes in their mantle convective environment, in order to compare their characteristics with Earth's hotspot observations.

4.2.3.1 Modeled mantle convective planform

We first compare the temporal average of the thermal heterogeneity spectra of Models 1, 2, 3 and 4 with the seismic heterogeneity spectrum of the global seismic tomography model S40RTS for present-day Earth mantle (Fig. 4.4). In Model 2, mantle convective scales are smaller than in Model 1, especially in the lowermost mantle, where the dominant scales are at spherical harmonic degrees 4-6 whereas it is 1 in Model 1. In Model 4, the spherical harmonic power for low degrees is enhanced in the lowermost mantle due to the presence of deep thermo-chemical heterogeneities. In all models, the temporal average of thermal heterogeneities presents a low spectral power for harmonic degrees greater than six in the upper mantle, whereas such degrees are well represented in model S40RTS, which represents a present-day snapshot of Earth's convective scales. Indeed, in the models, upper-mantle convective scales smaller than spherical harmonic degree six evolve faster than in the lower mantle since upper-mantle convection is more vigorous. In the following, we investigate the influence of such differences in the convective planform of the models on the lateral motion of mantle plumes.

4.2.3.2 Characteristics of mantle plumes

Shape and diameter. Model plumes are characterized by individual vertical conduits, which is consistent with seismic tomography models (French and Romanowicz, 2015) that reveal vertical slow-seismic velocity anomalies below hotspots (Fig. 4.2). Several upper-mantle plume conduits are sometimes connected in the lower mantle. Such connections between plume roots are also observed on Earth in seismic tomography models between Ascension and St-Helena that would split from the transition zone (Montelli et al., 2006), between the Azores, Canaries and Cape-Verde that would be

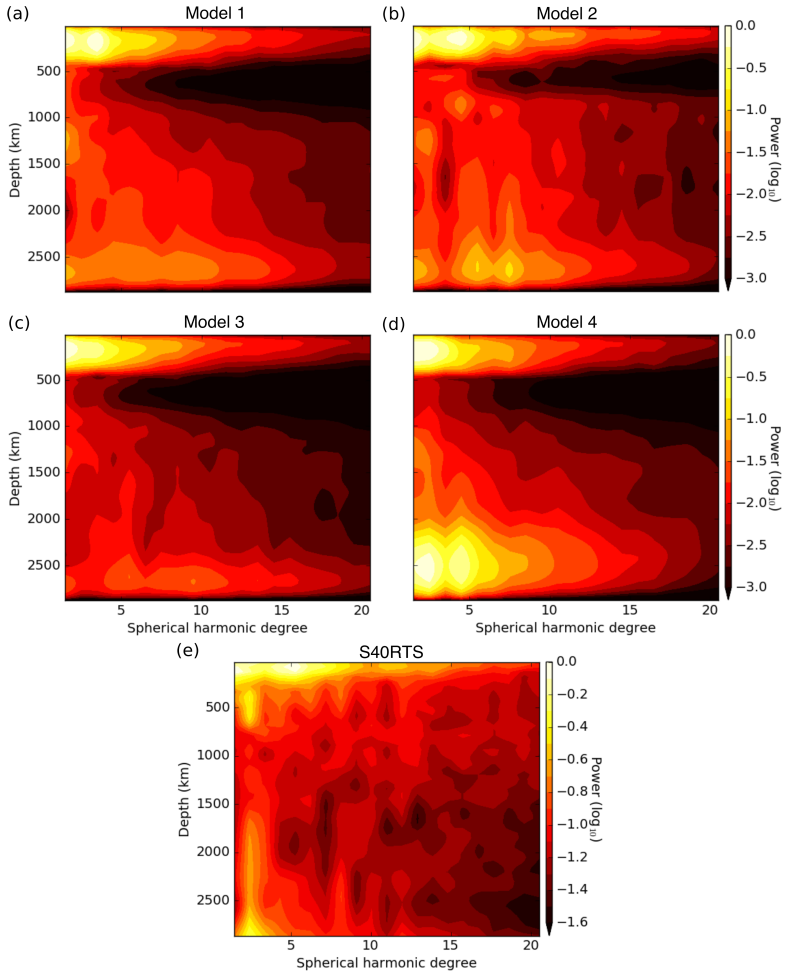


Figure 4.4: Temporal average of the thermal heterogeneity spectra for (a) Model 1, (b) Model 2, (c) Model 3 and (d) Model 4. The seismic velocity heterogeneity spectrum of seismic tomography model S40RTS is shown on (e) for comparison.

merged below 1,400 km depth and between Kerguelen and Crozet below 2,300 km depth (Davaille and Vatteville, 2005).

We calculate the cross-sectional area of the detected plumes from their anomalous radial heat advection flux. This cross-sectional area depends on the threshold that we define. The average cross-sectional area of upper mantle plumes varies from 2×10^4 km^2 (corresponding to a radius of about 60 km) for Models 3 and 4 to 6×10^4 km^2 for Model 2 (corresponding to a radius of about 80 km, Fig. 4.5). In the lower mantle, it varies between about 1×10^5 km^2 on average for Model 3 (corresponding to a radius of about 130 km) to 4×10^5 km^2 for Model 4 (corresponding to a radius of about 200 km).

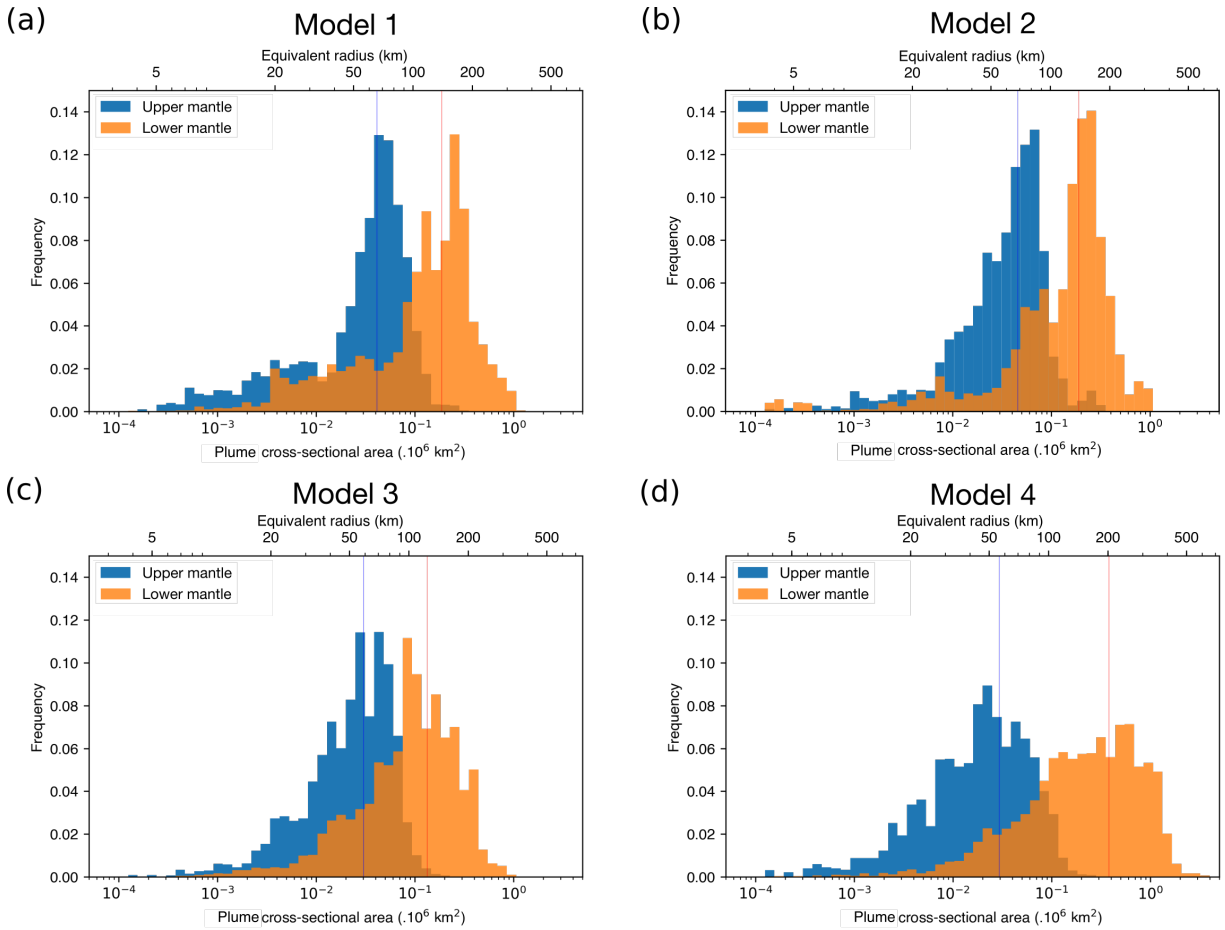


Figure 4.5: Distribution of plume cross-sectional area for all models in the upper mantle (blue histograms) and the lower mantle (orange histograms).

The thinning of plume conduits between the lower mantle and the upper mantle results from the applied 30 times viscosity difference between the upper and the lower mantle (Leng and Gurnis, 2012). The diameter of upper mantle plume conduits is estimated to be of the order of 200 km on average from the study of mantle plume buoyancy fluxes deduced from hotspot topographic swells (Turcotte and Schubert, 2014). Diameter is small compared to the resolution of seismic tomography models and probably explain difficulties in imaging plume conduits. Nevertheless, in their recent seismic tomography model, French and Romanowicz (2015) detect upper mantle conduits of about 600 km in diameter at least in the lower mantle. Davaille et al. (2018) explained the potential existence of such large plume conduits by a lower mantle visco-plastic rheology instead of the Newtonian rheology used in our models while Davaille and Vatteville (2005) invoked thermo-chemical heterogeneities in plumes.

The distribution of the detected plume conduits diameter is asymmetric (Fig. 4.5). In all models, most of the mantle plumes have a cross-sectional area of about 5×10^4 km^2 (corresponding to a

diameter of 140 km) while some mantle plumes present a cross-sectional area of less than 1×10^3 km^2 (which corresponds to a cross-sectional diameter of 20 km). Those correspond to dying plume conduits or detection errors. In this last case, detected anomalies of heat advection are short-lived and do not affect the analysis of mantle plume lateral motions (which are averaged on 5 Myr timescales, see section 4.2.4).

Plume excess temperature. The temperature excess distribution of the detected mantle plumes is averaged over the cross-sectional area of each of them. It varies between 350 and 400 K on average in Models 1, 2 and 3 in the lower mantle, and it is about 200 K on average in the upper mantle (Fig. 4.6). In Model 4, the upper and lower mantle temperature excesses are about 100 and 150 K respectively. Colder temperature excesses in Model 4 result from the presence of basal thermo-chemical heterogeneities (all other parameters being kept unchanged) which buffer the excess temperature of upwellings since heat is retained in the chemical layer as described in Farnetani (1997). The modeled upper mantle temperature excess range for Models 1, 2 and 3 corresponds to estimates of plume temperature obtained from the composition of olivine phenocrysts erupted at hotspots (Putirka, 2005).

The distributions of plume excess temperatures are less spread for Model 2, 3 and 4 than for Model 1, at least for the upper mantle. This results from the different thresholds used to detect mantle plumes in these models (Table 4.2). In Models 2, 3 and 4, the thresholds used to detect mantle plumes in the upper mantle are stricter than the one used for Model 1. Therefore, the distribution of plume excess temperature is less spread than is Model 1.

In all models, the temperature excess of mantle plumes located below continents is about 25 K greater than the temperature excess of mantle plumes located below oceanic lithosphere. However, the mantle temperature below continents is also 25 K greater than the oceanic asthenospheric mantle in these models because of the insulation properties of continents (Coltice et al., 2007). The temperature excess of plumes located below continents relatively to continental asthenosphere temperature is therefore comparable to the temperature excess of plumes located below oceans relatively to oceanic asthenosphere temperature.

Rising speed. In all models, plume material rises about three times faster in the upper mantle than in the lower mantle (Fig. 4.7). This is a consequence of the presence of a 30 times viscosity

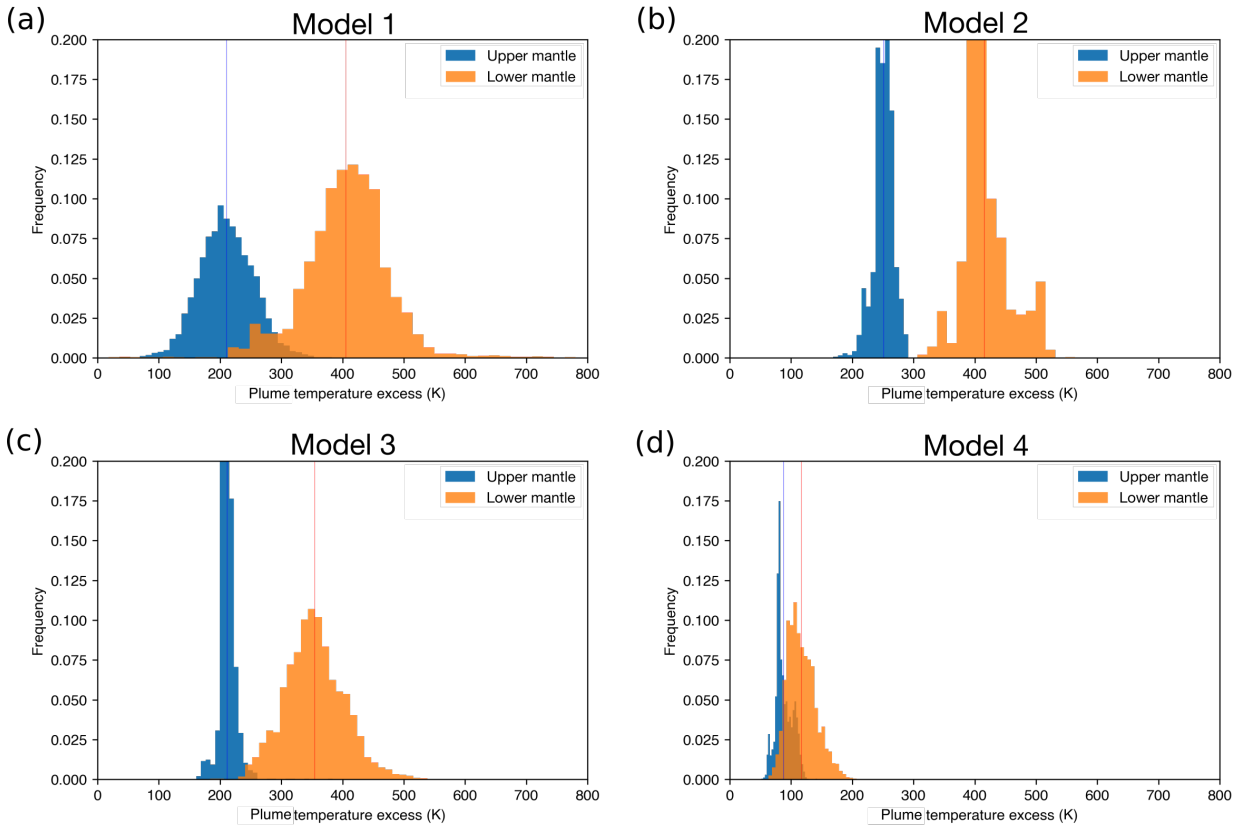


Figure 4.6: Distribution of temperature excess for all models in the upper mantle (blue histogram) and the lower mantle (orange histogram).

difference between the upper and the lower mantle, which causes the thinning of plume conduits in the upper mantle (Fig. 4.2 and 4.5, Ricard et al., 1993), and the acceleration of the hot material. In Models 1,2 and 3, plume material rises at a speed of about 10 cm·yr^{-1} in the lower mantle and 35-40 cm·yr^{-1} in the upper mantle on average. In these models, the maximum plume buoyant rising speed can reach up to 1 m·yr^{-1} in the upper mantle, for the largest plumes with the largest excess temperature and therefore an increased buoyancy. In Model 4, buoyant rising speeds are rather homogeneous and about 5 cm·yr^{-1} on average in the lower mantle and 15 cm·yr^{-1} in the upper mantle. This results from the presence of dense thermo-chemical heterogeneities. They cause a thermal weakening of plumes (Fig. 4.6), decreasing the buoyancy of plume material, and therefore, their ability to rise. Estimates of mantle plume rising speed from the study of hotspot topographic swells are 55 cm·yr^{-1} on average for major hotspots, with the approximation that plume material rises at Stokes velocity (Turcotte and Schubert, 2014).

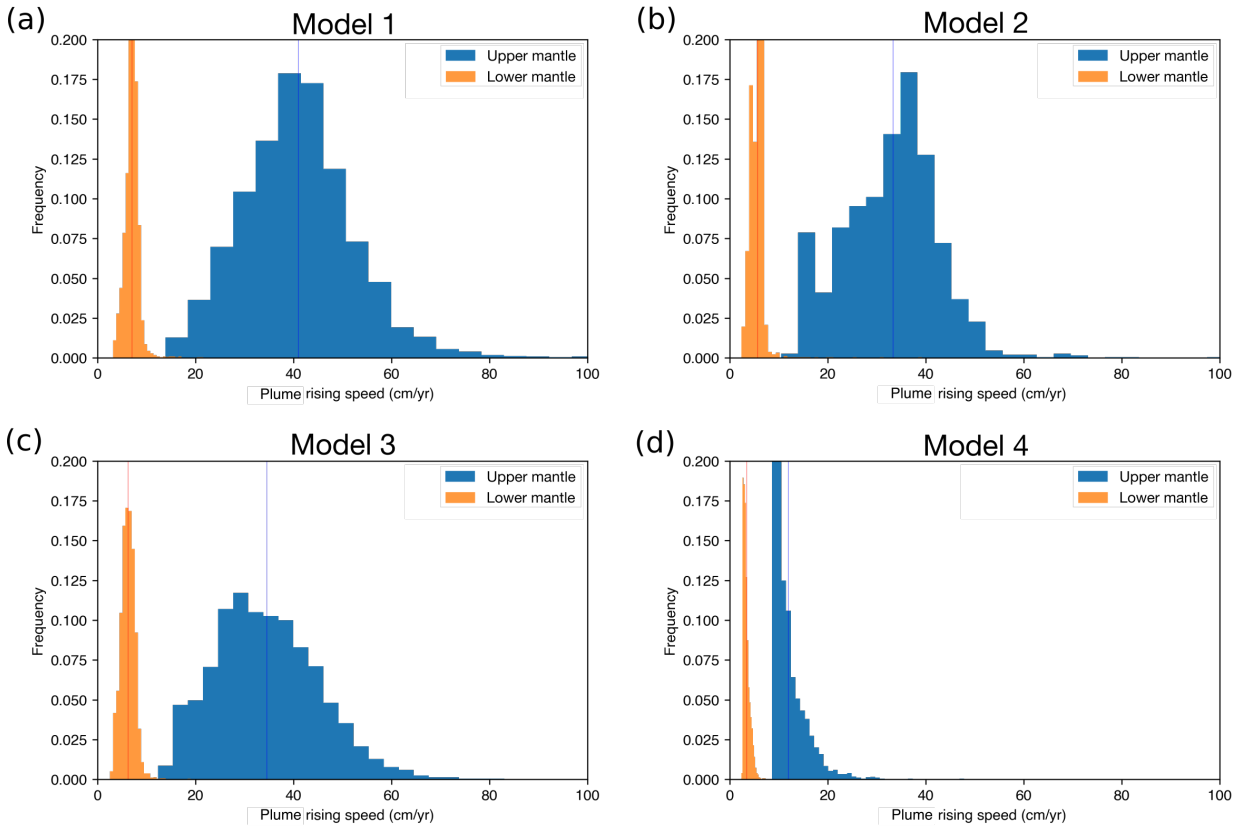


Figure 4.7: Distribution of buoyant rising speeds for all models in the upper mantle (blue histogram) and the lower mantle (orange histogram).

Richards and Griffiths (1988) experimentally linked the buoyant rising speed of chemical mantle plumes to a modified Stokes velocity:

$$v_p = \frac{k_p \Delta\rho g r_p^2}{\eta} \tag{4.1}$$

with v_p the plume buoyant rising speed, η the viscosity of the surrounding mantle, $k_p \approx 0.54$ a geometrical constant determined experimentally (Richards and Griffiths, 1988) for a viscosity contrast of a factor of 4-15 between the ambient mantle and the plume material; $\Delta\rho$ is the density contrast between mantle plumes and the surrounding upper mantle, g is the gravitational acceleration and r_p is the plume radius. In Models 1, 2 and 3, the upper mantle temperature excess is about 200 K (Fig. 4.6a, b and c), which leads to $\Delta\rho \approx 30$ kg·m^3 between mantle plume material and the ambient mantle, and the average equivalent radius of the conduits is $r_p \approx 70$ km. Using a value of 10^{20} Pa·s for the viscosity of the upper mantle, the modified Stokes velocity of upper mantle plumes would be ≈ 25 cm·yr^{-1}. In Model 4, the modified Stokes velocity of upper mantle plumes would be ≈ 8 cm·yr^{-1}, using a temperature excess of 100 K in the upper mantle (Fig. 4.6d), leading to $\Delta\rho \approx 15$ kg·m^3. Therefore,

the average plume rising speed in our models (Fig. 4.7) is comparable to the modified Stokes velocity law of Richards and Griffiths (1988), although Kerr and Mériaux (2004) and Kerr and Lister (2008) showed that thermal plume rising speed can be different from the analytical model of Richards and Griffiths (1988).

Volume and Buoyancy flux. We calculate the volume flux and the buoyancy flux of mantle plumes with the method described in Sleep (1990). The volume flux Q_p in $m^3 \cdot s^{-1}$ corresponds to:

$$Q_p = A_p v_p \tag{4.2}$$

with A_p the cross-sectional area of mantle plume conduits and v_p the buoyant rising speed. The buoyancy flux is obtained from:

$$B_p = \rho_m \alpha \Delta T Q_p \tag{4.3}$$

with ρ_m the reference mantle density, α the reference thermal expansivity and ΔT the mantle plume temperature excess. In Models 1, 2 and 3, the plume buoyancy flux extends between 0.1 and 10 $Mg \cdot s^{-1}$. It is lower than 1 $Mg \cdot s^{-1}$ in Model 4, because of a lower buoyancy of mantle plumes in that model. The buoyancy flux increases from the lower mantle to the upper mantle by a factor of 5-8 because of the viscosity jump at the transition zone, which favors plume conduits with a smaller diameter and an increased rising speed in the upper mantle.

Buoyancy fluxes for mantle plumes on Earth can be estimated from the topographic and gravity swell that they generate at the surface of the lithosphere (*e.g.* Davies, 1988a, Sleep, 1990, Schilling, 1991, Ribe et al., 1995, Crosby and McKenzie, 2009). The buoyancy flux of mantle plumes is calculated from estimates of the volumetric rate of swell creation:

$$B_p = \bar{D_H} \bar{W_H} v_{plate} (\rho_m - \rho_w) \tag{4.4}$$

with $\bar{D_H}$, the average hotspot swell height, $\bar{W_H}$ the average swell width, v_{plate} the plate speed and $\rho_m - \rho_w$ the density contrast between mantle and water. However, those estimates are poorly constrained. For example, Sleep (1990) expects the buoyancy flux to be of the order of 1.4 $Mg \cdot s^{-1}$ for the Iceland plume from plate spreading rates, while Poore et al. (2009) use the propagation velocity of V-shaped ridges to suggest a buoyancy flux of 22 $Mg \cdot s^{-1}$ for the Iceland plume. However, in the

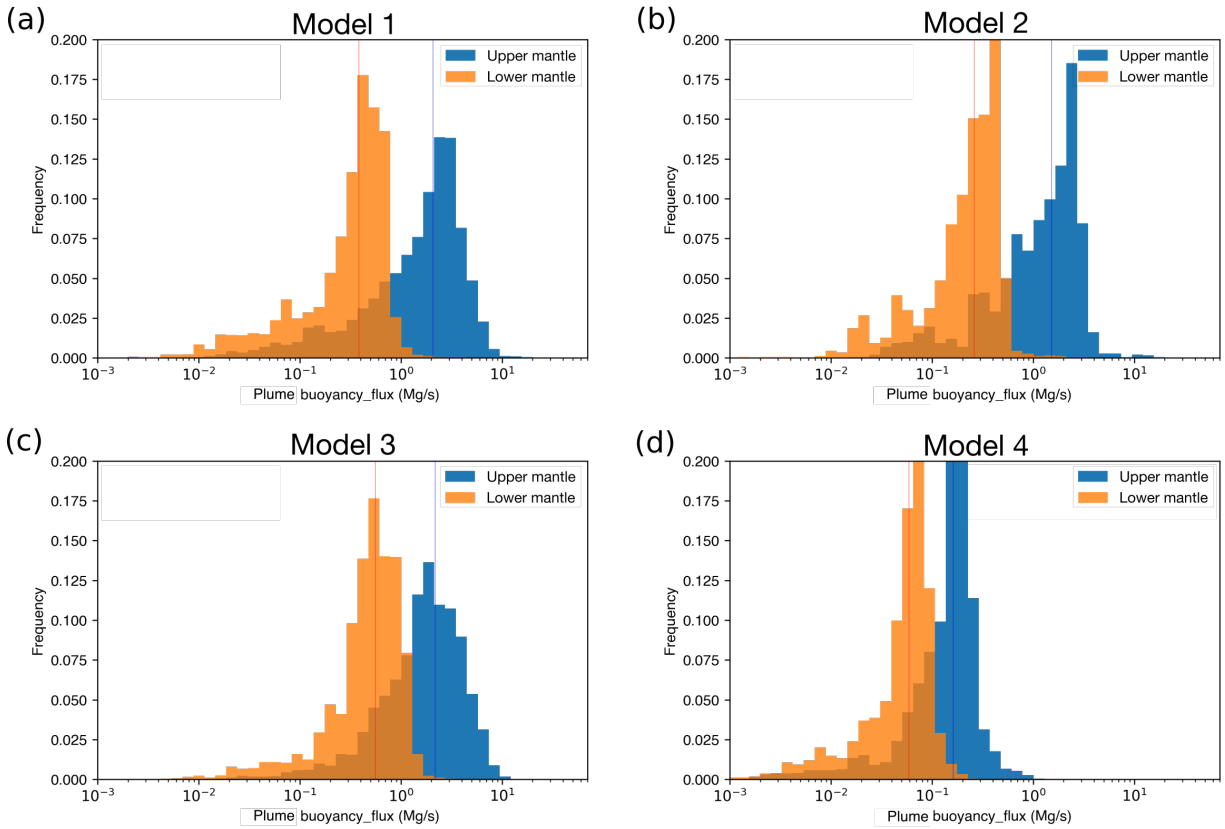


Figure 4.8: Distribution of buoyancy flux for all models in the upper mantle (blue histogram) and the lower mantle (orange histogram).

majority of cases, plume buoyancy fluxes range between 0.1 and 10 Mg·s^{-1} (Sleep, 1990, Crosby and McKenzie, 2009, Ito, 2001).

Heat flow. Plume heat flow can be deduced from the buoyancy flux as follows:

$$F_p = B_p \frac{c_p}{\alpha} \tag{4.5}$$

where c_p is the mantle heat capacity in J kg^{-1}K^{-1} (*e.g.* Sleep, 1990). In Models 1, 2 and 3, individual plumes carry about 0.05 TW on average. This value falls to about 0.007 TW on average in Model 4.

In all models, the total heat transferred from the core to the surface by mantle plumes is about 28% of the total surface heat flow in Model 1, 23% in Model 2, 20% in Model 3 and 5% in Model 4 (Fig. 4.10). Davies (1988a) and Sleep (1990) suggested a contribution of plumes to Earth's total heat flow of 2-4 TW from hotspot swells. Considering an upper bound of about 9±3 TW for the core heat flow (Buffett, 2003), this would mean that Earth's mantle plumes carry only about 20-50%

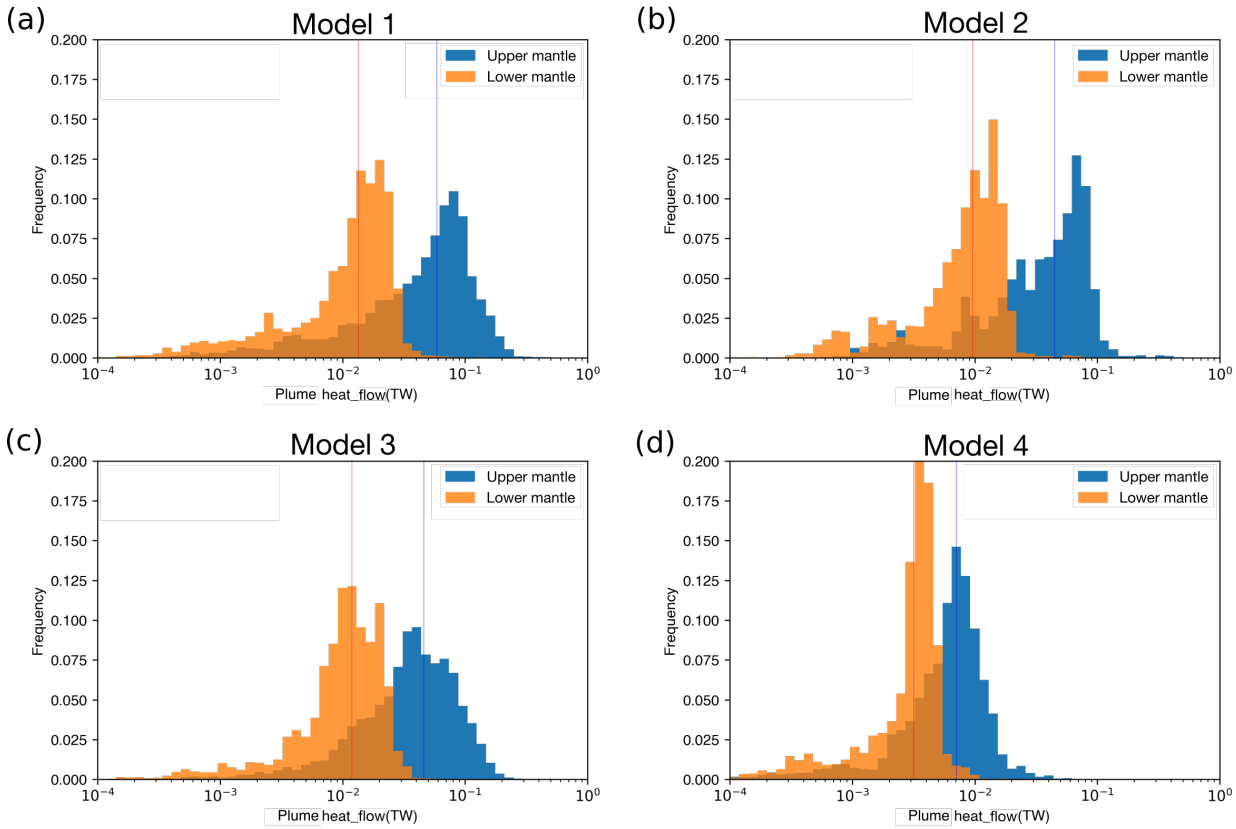


Figure 4.9: (a-d) Distribution of heat flow for all models in the upper mantle (blue histogram) and the lower mantle (orange histogram).

of the total heat extracted from the core. This small contribution was confirmed by plume heat flux estimates from numerical models of incompressible and isoviscous convection (Labrosse, 2002), although compressibility, plate tectonics, large-scale mantle convection or internal heating modes may alter those conclusions (*e.g.* Gonnermann et al., 2004).

In the models, mantle plumes are therefore not the only contributor to heat transport from the core to the surface. Several mechanisms have been invoked to explain this difference between the heat flow from mantle plumes and the core heat flow. Labrosse (2002) suggested that not all plumes reach the surface and proposed that most of the heat extracted from the core contributes to the heating of slabs in the lowermost mantle. Bunge (2005) and Zhong (2006) proposed that non-adiabaticity and thermal diffusion generate temperature contrast variations between mantle plumes and the ambient mantle and explain that the heat flow transported by plumes represents about 1/3 of the core heat flow near the surface. In the models presented here, all plumes reach the surface. Therefore 2/3 of the core heat flow is evacuated either by regions of passive and large-scale upwelling, heating of lower mantle slabs or non-adiabaticity.

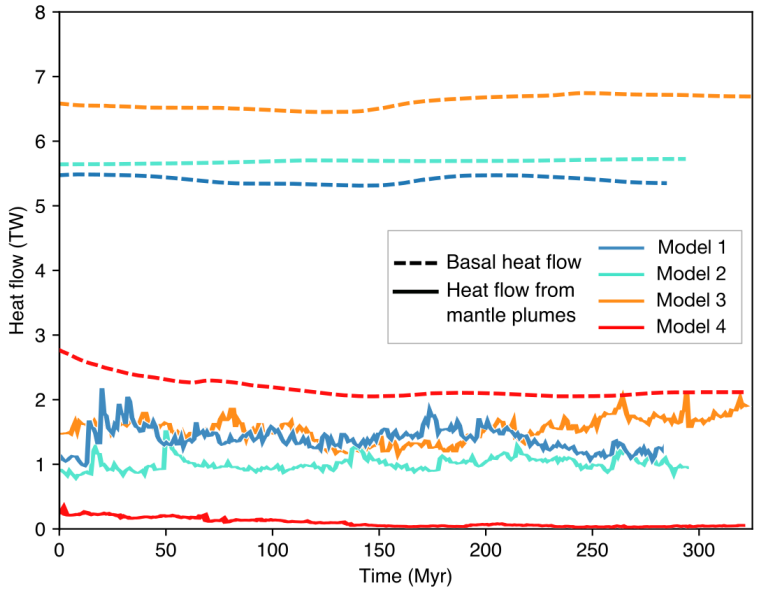


Figure 4.10: Temporal evolution of the total heat flow transferred by mantle plumes from the core.

4.2.3.3 Temporal behaviour

Number of plumes. In Models 1 and 2, the number of plumes varies between 15 and 25, independently of the yield stress (Fig. 4.11(a)). The slight increase through time correlates with a 50 K increase of the average mantle temperature throughout the evolution, which is therefore accomodated by the birth of new plumes. The number of mantle plumes detected in the lower mantle is slightly smaller than the number of plumes detected in the upper mantle. This results from the splitting or the merging of some mantle plumes in the upper mantle (Fig. 4.2). In Model 3, the number of mantle plumes detected is between 25 and 35 and is relatively constant through time. The larger number of plumes in Model 3 results from the constant thermal expansivity applied, which locally increases the Rayleigh number in the lower mantle compared to Models 1 and 2. As a consequence, convection is more vigorous in the lower mantle, and smaller scales develop at the base of the mantle, generating about 30 % more hot instabilities (Fig. 4.4). Moreover, the core heat flow is about 15% more important in Model 3 (Fig. 4.10), which also contributes to the rising of more plumes. Finally, in Model 4, the number of plumes detected in the lower mantle increases over time from 15 to 30, while it increases from about 5 to 45 in the upper mantle. This is related to the fact that 1/ mantle plumes are more difficult to distinguish from local hot anomalies in the upper mantle due to their reduced rising speed and temperature excess especially in the upper mantle; 2/ mantle plumes are more likely to be deflected and split in the upper mantle, since they are weaker than in Models 1, 2

and 3; 3/ the thermo-chemical heterogeneity is organized into proper piles at the start of the model, which prevents the rise of new plumes and 4/ the average mantle temperature increases throughout the evolution.

The number of plumes detected in our models is in agreement with other numerical models of whole-mantle convection although the model parameters differ (*e.g.* Davies and Davies, 2009, Hassan et al., 2015). On Earth, the number of hotspots with a lower mantle origin is still subjected to debate. Based on strict criteria (seismic tomography hot anomaly, topographic swell, rare gas anomalies and long-lived tracks starting with a large igneous province), Courtillot et al. (2003) showed that only seven hotspots have a deep origin. Using less strict criteria, Wang et al. (2018) recognizes 24 deep-rooted mantle plumes while Doubrovine et al. (2012) used five mantle plumes to build a plate tectonic reconstruction.

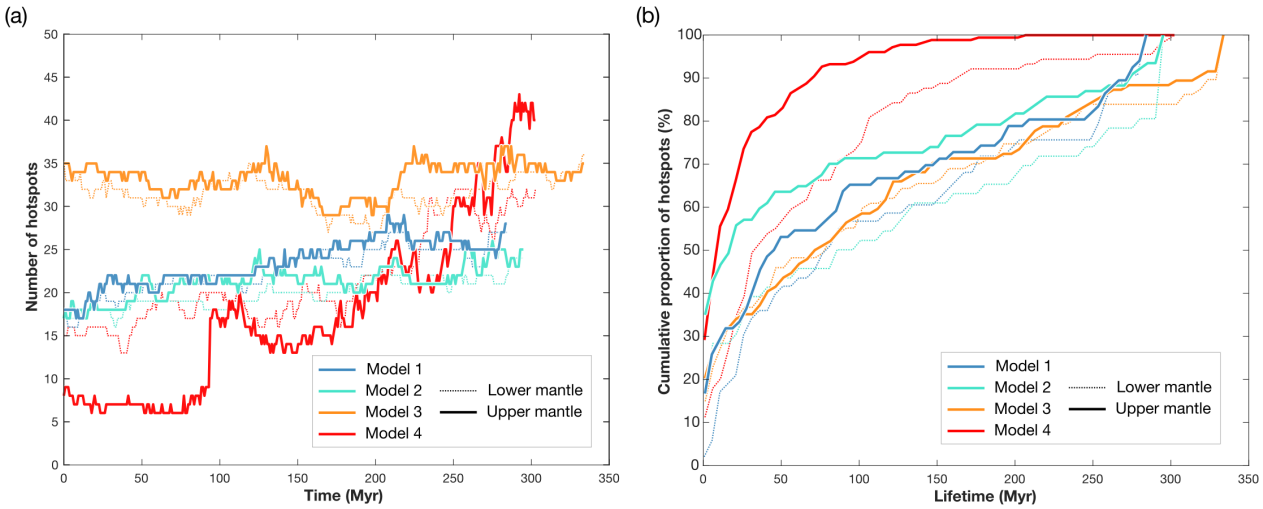


Figure 4.11: (a) Temporal evolution of the number of detected mantle plumes in the upper and the lower mantle for Models 1, 2, 3 and 4. (b) Cumulative lifetime distribution of detected mantle plumes in Model 1, 2, 3 and 4.

Lifetime. On Earth, hotspot tracks displaying a long age progression are usually considered to originate from deeply-rooted mantle plumes. The longest hotspot tracks correspond to Louisville (about 87 Ma), Hawaii (about 87 Ma) and New England (up to 130 Ma). In the case of Louisville and Hawaii though, the hotspot chains of volcanoes terminate at a subduction zone and it is therefore impossible to know their real lifetime, although Richards (1991), Tarduno et al. (1991), Clouard and Bonneville (2001) proposed a link with formation of the Ontong-Java plateau.

Model 1, 2 and 3 present a rather linear cumulative distribution of hotspot lifetime, with 30 % of

the detected plumes existing for at least 200 Myr (Fig. 4.11). In contrast, mantle plumes detected in Model 4 are characterized by shorter lifetimes, almost all of them becoming extinct within 150 Myr.

Pulses of activity. The activity of model mantle plumes fluctuates through time. This is recognizable in the cross-sectional area, the temperature excess, the rising speed, the buoyancy flux and the heat flux, as shown on Fig. 4.12 which presents the temporal evolution of those characteristics for one plume in Model 1. The presented temporal evolution of the characteristics of this mantle plume is representative of the behaviour of all the detected mantle plumes. Throughout the considered mantle plume lifetime (about 200 Myr), its flux decreases from about 4 Mg·s^{-1} to less than 1 Mg·s^{-1} and its average rising speed decreases from 50 cm·yr to about 20 cm·yr^{-1}. While the average temperature remains relatively stable, fluctuating around 200 K, the maximum temperature of the conduit decreases through time, from about 500 K to 200 K. A similar progressive decrease in temperature excess is suggested by geochemical evidence for Iceland and the Galapagos hotspots (Herzberg and Gazel, 2009).

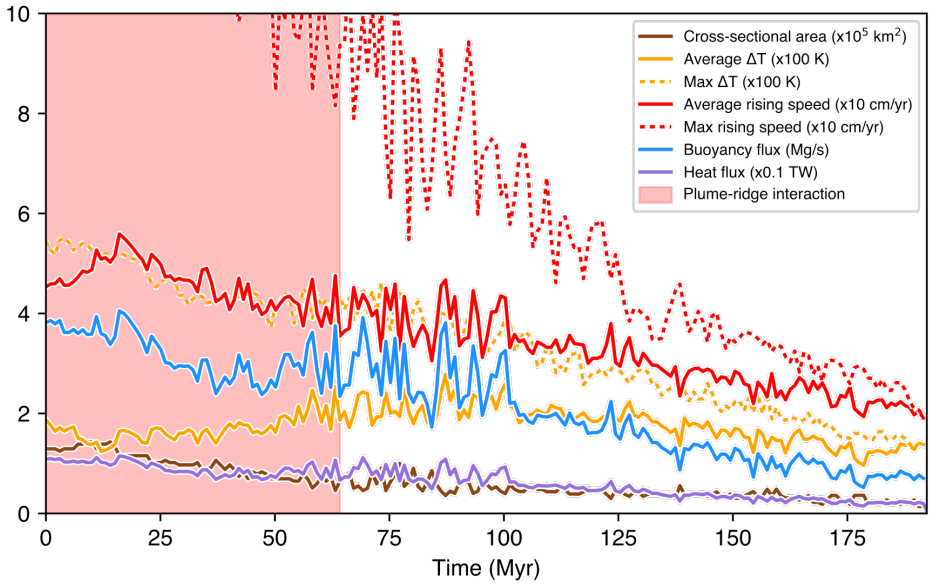


Figure 4.12: Temporal evolution of the cross-sectional area (brown), the average (orange) and maximum (orange, dashed) temperature excess, the average (red) and maximum (red, dashed) buoyant rising speed, the buoyancy flux (blue) and the heat flux (purple) for hotspot ID 6 in Model 1 (Fig. 4.3(a) and (b)). The duration of the plume-ridge interaction is highlighted by the pink area.

Short-term fluctuations also punctuate the long-term trend of mantle plumes activity: buoyancy flux variations of about ±1 Mg s^{-1} occur on timescales of 5 Myr to 10 Myr. The most rapid fluctuations of buoyancy flux correlate with bursts of temperature and rising speed, but are anti-correlated with changes in the cross-sectional area of the plume conduit. Fluctuations of activity increase when the

plume moves away from a spreading center (between 60 and 100 Myr, Fig. 4.12).

A large number of observations suggests that hotspots activity is subject to fluctuations. Ar^{40}/Ar^{39} geochronological dating of several LIPs shows evidence for pulses of activity over periods of tens of million years during flood basalt emplacement (*e.g.* Gibson et al., 2006, Neal et al., Fitton and Godard, 2004, Coffin et al., 2002). Similar studies on hotspots tracks also show pulses of volcanic production over periods of million years (*e.g.* White and Lovell, 1997, O'connor et al., 2000). Geochemical and geochronological data (Hanan and Schilling, 1997), seismic tomography models (cf Silveira et al., 2006, showing evidence for a dying Azores plume), gravity and topographic anomalies (Poore et al., 2009) and sedimentary sequences (White and Lovell, 1997, Hartley et al., 2011) also suggest the activity of mantle plumes can fluctuate through time, sometimes quite dramatically over periods as short as 2 Myr. Indeed, Vogt et al. (1971), White and McKenzie (1995), Ito (2001), Jones et al. (2002), Poore et al. (2009), Parnell-Turner et al. (2014) showed that the pattern of V-shaped ridges on both side of Iceland or south of the Azores (Cannat et al., 1999) could correspond to lithospheric deformations due to intermittent bursts of activity of the corresponding plumes, leading to fast lateral propagation of hot and buoyant material away from the plume conduit. Estimates of buoyancy fluxes from V-shaped ridges vary between 17-47 $Mg{\cdot}s^{-1}$ (Poore et al., 2009) to more than > 70 $Mg{\cdot}s^{-1}$ (Parnell-Turner et al., 2014) on a timescale of 10 Myr. Note that these values are at least one order greater than estimates of Sleep (1990) from eq. 4.4. Further analyses of sedimentation rates (*e.g.* Smallwood and White, 2002, Smallwood and Gill, 2002, Mudge and Jones, 2004, Hartley et al., 2011, Hardman et al., 2018) in the vicinity of hotspots show alternating episodes of emergence and drowning, linked with putative variations of dynamic support of plumes. For instance, Hartley et al. (2011) showed that the presence of a buried landscape in the North-Atlantic could be related to bursts of temperature excesses ranging from 15 and 130 K originating from the Iceland plume and propagating laterally at a speed of about 35 $cm{\cdot}yr^{-1}$. The source for such patterns is still discussed. They could be explained by fast convective lateral motions of hot fingers in the asthenosphere (Schoonman et al., 2017). Lin and van Keken (2006a), Lin and Van Keken (2006b) used numerical models of thermochemical convection in order to explain such fluctuations by the entrainment of dense material, which generates secondary instabilities. Schubert et al. (1989) showed that solitary waves of temperature variations can propagate throughout thermal plume conduits, while Whitehead (1982) suggested that plume conduit distortion by large-scale mantle flow can break plumes into rising drops. Ballmer et al. (2011) proposed that small-scale convection below the Pacific plate deforms the wake of the Hawaiian plume and generate

temporal and spatial geochemical and volume flux variations while O'Connor et al. (2018) suggested that the LLSVPs play a major role in generating pulsations of mantle plume material.

In Model 1, high-frequency fluctuations of mantle plume activity are not linked to the entrainment of chemically different material from the lower mantle. Bursts of buoyancy flux activity on Fig. 4.12 seem to be linked to the departure of the mantle plume conduit from the vicinity of a ridge. Stable upper mantle flow below the ridge likely contributes to the stability of the diameter of the considered mantle plume conduit whereas the lateral motion of the plume below older lithosphere may favour its interaction with vigorous upper-mantle convective scales. Moreover, the average temperature of the plume conduit is subjected to fluctuations about 5 Myr before the mantle plume starts moving away from the ridge, which also contributes to increased fluctuation of buoyancy flux.

4.2.4 Analysis of the motion of mantle plumes

4.2.4.1 Description

Table 4.3: Mantle ($\mathbf{v_{rms}}$) and plume absolute (with respect to mantle) and relative (with respect to other plumes) lateral speeds ($\mathbf{v_{h,p}}$) in the upper mantle (UM) and the lower mantle (LM)

Parameter	Model 1	Model 2	Model 3	Model 4	Doubrovine et al. (2012)
Non dim. surface $\mathbf{v_{rms}}$ [a]	2660	3475	3130	2110	
Mean UM absolute $\mathbf{v_{h,p}}$ (cm·yr^{-1})	1.99 ± 0.43	1.85 ± 0.78	2.26 ± 1.40	2.80 ± 1.20	1.42 ± 0.47
Mean LM absolute $\mathbf{v_{h,p}}$ (cm·yr^{-1})	1.69 ± 0.40	1.14 ± 0.22	1.83 ± 0.85	2.15 ± 0.68	
Mean UM relative $\mathbf{v_{h,p}}$ (cm·yr^{-1})	1.37 ± 0.40	1.70 ± 1.19	2.21 ± 2.08	2.29 ± 1.47	1.2 ± 0.57
Mean LM relative $\mathbf{v_{h,p}}$ (cm·yr^{-1})	1.15 ± 0.39	0.79 ± 0.18	1.72 ± 1.31	1.52 ± 0.80	
Average mantle $\mathbf{v_{rms}}$ (cm·yr^{-1})	2.03	1.61	1.8	2.3	
Average net rotation (cm·yr^{-1})	0.55 [b]	0.35 [b]	0.42 [b]	0.72 [b]	$2.05 - 5.36$

[a] The non dim. suface $\mathbf{v_{rms}}$ are all scales to 3.96 cm·yr^{-1})

[b] The net rotation indicated for our models corresponds to the net motion of the whole-mantle relatively to a no-net-rotation lithosphere.

4.2.4.1.1 Absolute motions of mantle plumes. In the upper mantle, the average absolute lateral velocity of the detected mantle plumes increases from 1.8 cm·yr^{-1} for Model 2 to 2.8 cm·yr^{-1} for Model 4. In the lower mantle, average lateral velocities are about 25 % smaller than in the upper mantle, increasing from 1.1 cm·yr^{-1} for Model 2 to 2.2 cm·yr^{-1} for Model 4 (Table 4.3). In the lower mantle, the range of mantle plume lateral velocities roughly corresponds to the average horizontal velocities at 1,000 km depth, while the range of mantle plume lateral velocities in the upper mantle is

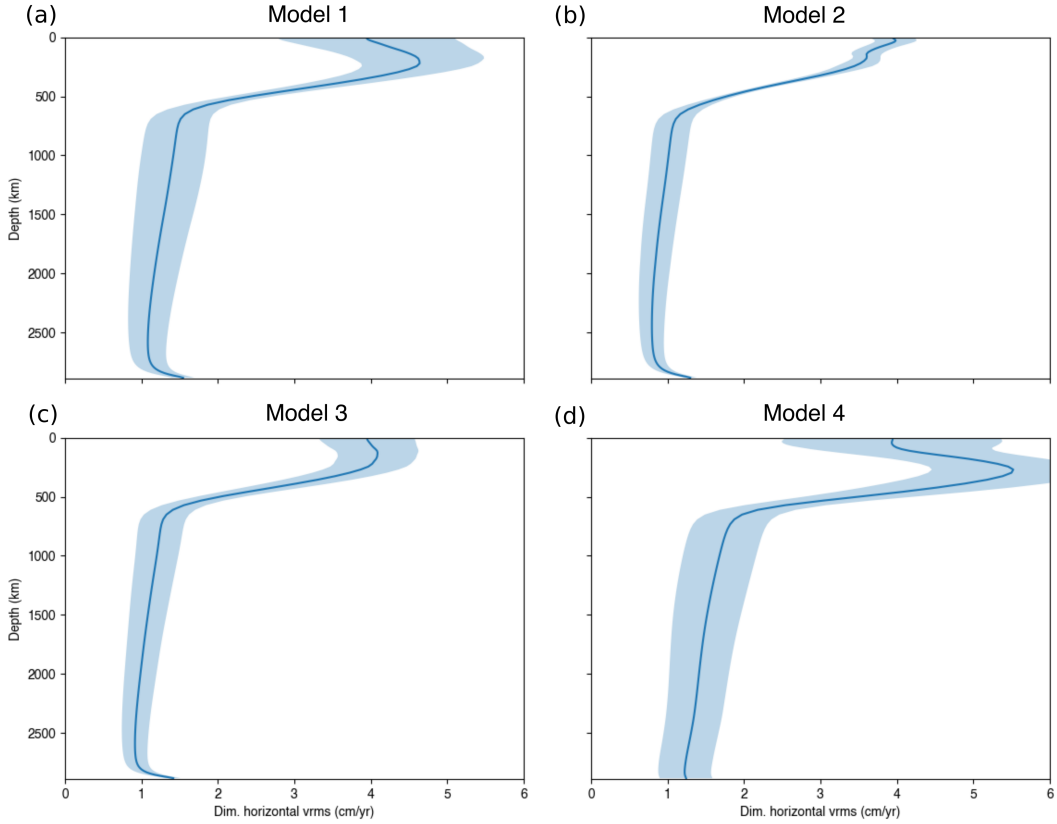


Figure 4.13: Dimensionalized horizontal RMS-velocity profiles in (a) Model 1, (b) Model 2, (c) Model 3 and (d) Model 4.

lower than the average lateral velocities of the mantle at that depth (350 km) (Fig. 4.13). Temporal variations on average absolute mantle plume velocities roughly correlate with variations in the net motion of mantle material compared to lithosphere, as seen on Fig. 4.14a ($r^2 = 0.4$). This correlation increases when accounting only for the slowest mantle plumes. In the lower mantle, it reaches its maximum when considering only mantle plumes moving slower than 2.5 cm·yr^{-1} ($r^2 = 0.57$, Fig. 4.14b). This suggests that some of the slowest mantle plume conduit motions in the lower mantle are driven by whole-mantle motions. In the upper mantle, the correlation between net rotation and mantle plume absolute lateral velocities reaches its maximum when absolute mantle plume lateral velocities are slower than 5 cm·yr^{-1} ($r^2 = 0.57$, Fig. 4.14b), which is a higher cutoff velocity than in the lower mantle. This probably results from the fact that choosing only mantle plumes moving at speeds lower than 2-4 cm·yr^{-1} in the upper mantle is too selective and therefore not representative of a potential coherent motion of the majority of plume conduits. In both the upper and the lower mantle, the correlation is never higher than 0.6, suggesting that net rotation is not the only process driving lateral plume motions.

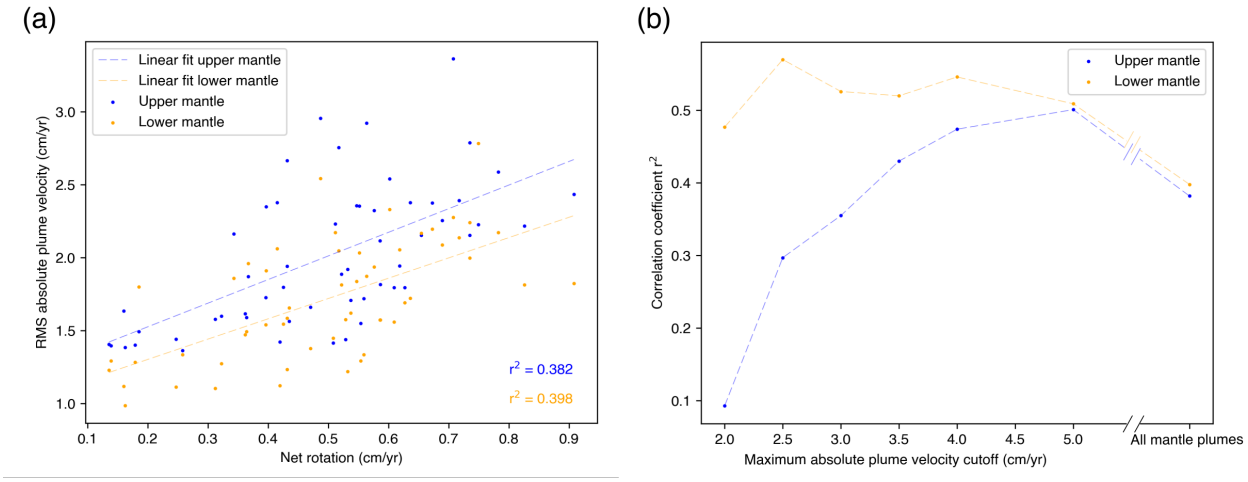


Figure 4.14: (a) Correlation between mantle plume RMS-absolute lateral velocities and net rotation in Model 1. (b) Correlation between mantle plume RMS-absolute lateral velocities and net rotation in Model 1 as a function of the maximum velocity cut-off of mantle plumes.

4.2.4.1.2 Relative motions between mantle plumes In Model 1, the majority of mantle plumes have limited pair-wise relative velocities, lower than 1 cm·yr^{-1} (Fig. 4.15a). However, a limited number of mantle plumes experiences relative lateral motions comprised between 4 and 10 cm·yr^{-1} in the upper mantle in Model 1. In Model 2, 3 and 4, upper mantle relative lateral velocities between mantle plumes can reach up to 20 cm·yr^{-1}, 24 cm·yr^{-1}, and 20 cm·yr^{-1} respectively. The most rapid motions between mantle plumes last less than 5 Myr and correlate with large buoyancy fluxes (Fig. 4.16).

In all models, the lateral velocities of mantle plumes in the upper mantle are usually less than 1 cm·yr^{-1}. Lateral relative motions of mantle plumes in the lower mantle are smaller than in the upper mantle for all models as expected from viscosity (Fig. 4.15b). Models 1, 2 and 3 have the same relative velocity distribution, with almost all mantle plumes having relative velocities lower than 3 cm·yr^{-1}. However, in Model 4, a significant number of mantle plumes have relative lateral velocities comprised between 2 and 5 cm·yr^{-1} in the upper mantle. The average relative velocities between mantle plumes in both the upper and the lower mantle are systematically lower than their average absolute motions (Table 4.3). This points to a coherent motion of mantle plumes by about 2 cm·yr^{-1} in our models. This '*net motion*' of mantle plumes is related to the net motion of the mantle as suggested by the correlation between mantle plume absolute velocities and net rotation (Fig. 4.14).

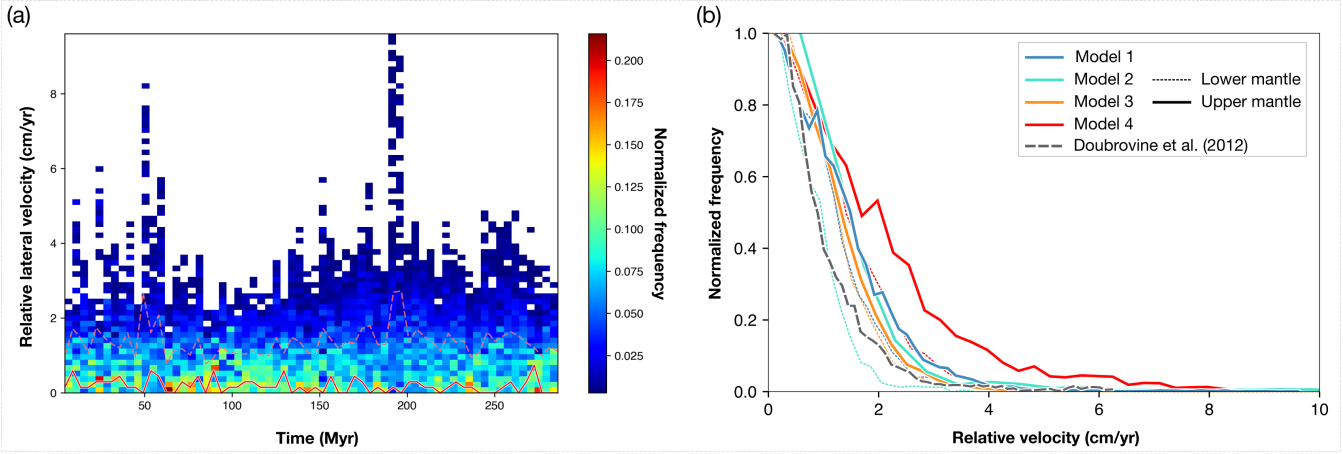


Figure 4.15: (a) Density plot showing the upper mantle RMS pair-wise lateral relative velocity distribution between mantle plumes through time in the upper mantle in Model 1. Relative velocities are calculated every 5 Myr interval. The thick red line represents the temporal evolution of the mode of mantle plumes' relative velocities. The dashed red line represents the temporal evolution of the average relative velocities between mantle plumes. (b) Density plot showing the time-average RMS pair-wise lateral relative velocity distribution between mantle plumes for all Models. Mantle plumes relative velocity distributions are normalized to their maximum frequency to allow model comparison. The relative RMS pair-wise lateral relative velocity between mantle plumes in the moving hotspot reconstruction model of Doubrovine et al. (2012) is shown in dashed grey for comparison.

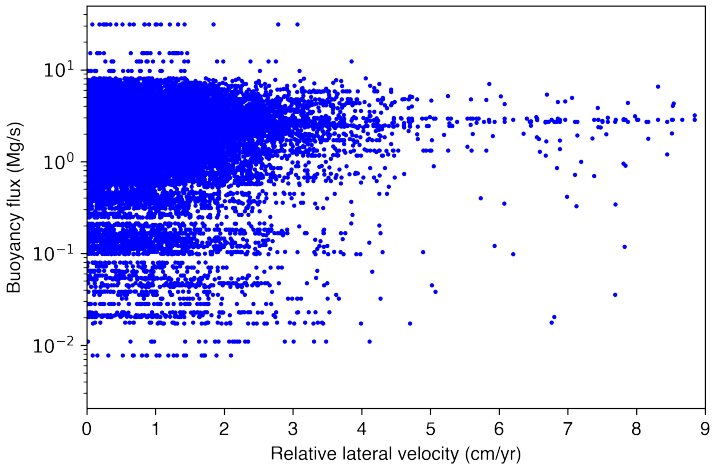


Figure 4.16: Correlation between mantle plumes relative velocities and their buoyancy flux in the upper mantle in Model 1. Each dot represents the lateral velocity and the corresponding buoyancy flux for each mantle plume at 5 Myr intervals. Note that when mantle plumes are moving fast, they tend to have an increased buoyancy flux compared to mantle plumes moving laterally at less than 2 cm·yr^{-1}.

4.2.4.1.3 Vertical deflection of mantle plumes We calculate the deflection angle of mantle plumes between the upper and the lower mantle by finding the minimum distance between each mantle plume located in the lower mantle and the upper mantle at each timestep (Fig. 4.17). We set an

upper limit at 9° for the detection of the nearest upper mantle plumes corresponding to lower mantle plumes locations. This corresponds to maximum deflections of 1,000 km between 1,000 km depth and the surface. In the case of split mantle plumes in the upper mantle, we only consider the minimum angle between lower mantle conduit location and upper mantle conduits.

In all models, mantle plumes define rather straight conduits, their deflection angle being about 2° on average (Fig. 4.17). This corresponds to a deflection of about 200 km between the surface and 1,000 km depth. However, in Models 3 and 4, mantle plume deflection angles are more spread, reaching 9° (1,000 km).

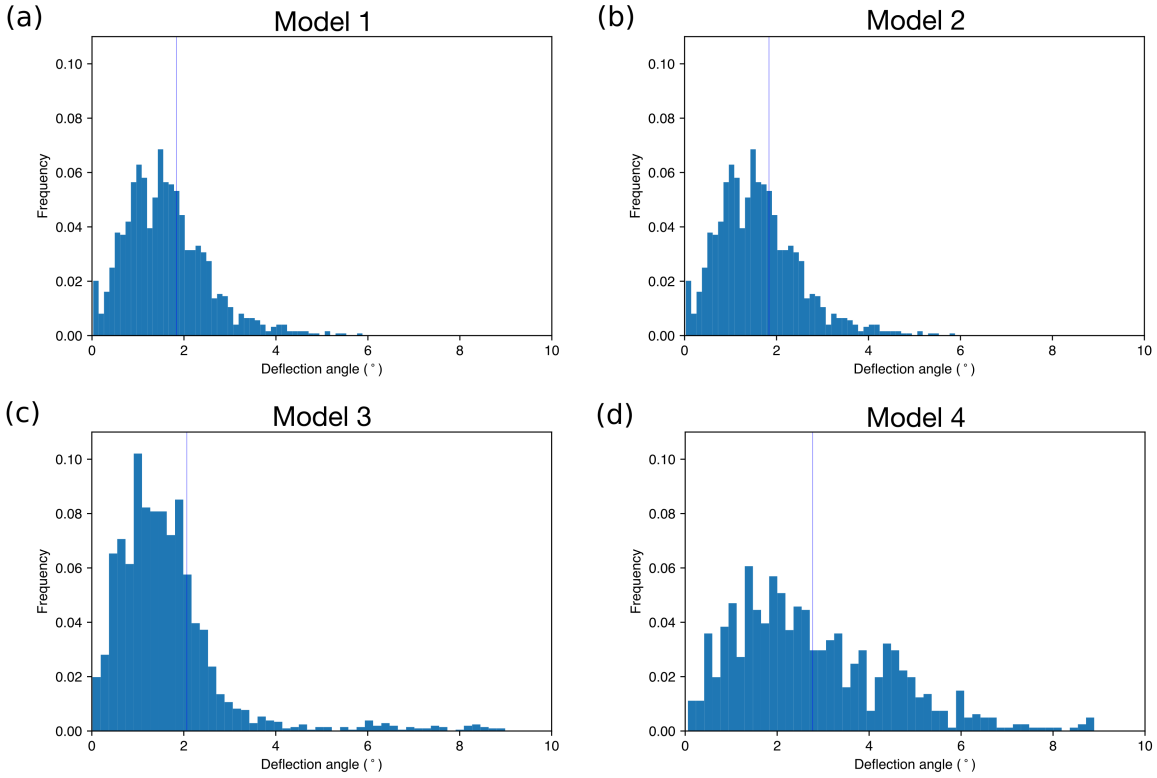


Figure 4.17: Mantle plume deflection angle distribution for all Models. For each model, the average deflection angle is outlined by the blue vertical line.

4.2.4.2 Potential causes of mantle plumes motion

4.2.4.2.1 Slow entrainment by global mantle flow In all models, most mantle plumes drift with relative velocities lower than 1-2 cm·yr^{-1} (Table 4.3 and Fig. 4.15). The absolute motion of mantle plumes in the upper mantle is smaller than the average upper mantle horizontal velocity (Fig. 4.13 and Table 4.3). Plume conduits are therefore poorly affected by upper mantle flow and their

motions seem to be mainly driven by lower mantle flow. Indeed, their limited velocities correspond to lowermost mantle average horizontal velocities and are roughly correlated with whole-mantle net motions, although mantle plume average velocities are larger (Fig. 4.14).

However, small differences in the absolute and relative motion of mantle plumes arise from the different model parameters used to compute the models. In Model 2, limited absolute motions of mantle plumes result from slower motions in the lower mantle (Fig. 4.13). This is because the lower mantle is more viscous on average than in Model 1, due to the presence of a larger number of cold material in the lowermost mantle since the yield stress is two times lower than in Model 1. In Model 3, the absence of depth-dependent thermal expansivity leads to more vigorous lower mantle convection, which causes mantle plumes to drift more rapidly on average. In Model 4, mantle plumes are more likely to be deflected by ambient mantle flow (Fig. 4.17). This results from their smaller temperature excess, rising speed and buoyancy flux. Indeed, a 100 K lower temperature excess than in Model 1 leads to a three times rising speed decrease compared to other models (Fig. 4.7) and a ten times viscosity decrease between the ambient mantle and plume conduits.

4.2.4.2.2 Limited effect of return flow. In plate reconstruction models based on a moving hotspot reference frame, Wang and Wang (2001), Wang et al. (2018) proposed that a significant number of mantle plumes move in an opposite direction from plate motions. This would result either from a lower mantle (Wang and Wang, 2001) or an asthenospheric (Wang et al., 2018) mantle return flow induced by subduction zones and necessary for mantle mass flux conservation, significantly deflecting mantle plumes. This corresponds to the proposed effect of the *mantle wind'* proposed by Steinberger and O'Connell (1998) to deflect moving mantle plume conduits to up to 60° (which also defines the upper limit for the existence of a coherent mantle plume in their models (Whitehead, 1982)) between the base of the mantle and the surface (Steinberger, 2000).

Combining analytical methods and laboratory experiments to study mantle plumes deflection, Richards and Griffiths (1988) showed that the shape of mantle plume conduits result from the combination between the horizontal mantle flow advection and the modified Stokes plume rising speed (Eq. 4.1). They developed analytical expressions to describe the maximal deflection of mantle plume conduits in the case of a simple return flow model with homogeneous mantle viscosity and strong viscosity contrasts between plume conduits and the ambient mantle. In this case, mantle plumes are deflected due to pressure gradients induced by mantle return flow. The shape of hotspot conduits is

bent in the direction of the return flow. The maximal deflection of mantle plume conduits throughout the mantle follows:

$$x_p(z) = -0.17 \frac{v_{plate}}{v_p} d \tag{4.6}$$

with x_p the horizontal deflection of the considered plume conduit, v_p the plume rising speed, v_{plate} the surface plate lateral velocity, z the depth and d the considered depth domain. Assuming an average rising speed v_p of about 20 cm·yr^{-1} for Models 1, 2 and 3 and 7 cm·yr^{-1} for Model 4, the maximal plume deflection due to mantle return flow would reach 100 km (about 0.9°) and 300 km (about 2.7°) respectively.

In our models, we do not observe significant deflection of mantle plumes related to a return flow in the lower mantle (Fig. 4.2). In the upper mantle, tilting of plume conduits due to a more vigorous convection is limited to 2° on average (corresponding to about 200 km), except in Models 3 and 4, in which mantle plumes can be more substantially tilted between the upper and the lower mantle (Fig. 4.17). in Model 3, slabs stronger than in Model 1 reach the lowermost mantle and can therefore contribute to deflect mantle plumes. In Model 4, mantle plumes are less hot and more viscous than in Models 1, 2 and 3. Therefore, they are less rapid and are more likely to be laterally entrained by ambient mantle convective cells.

The deflection angles measured in our models therefore correspond to the limited deflection proposed by the analytical solution of Richards and Griffiths (1988). In fact, Eq. 4.6 shows that the balance between mantle lateral velocities and plume rising speeds determine the amount of deflection of the conduits. In our models, the strong dependence of mantle viscosity on temperature makes it possible to generate low-viscosity mantle plumes with rising speeds reaching 10 times the average mantle. As a consequence, deflection due to mantle return flow is limited, unless plume rising speed (which depends on its viscosity and therefore on its excess temperature) is small. Therefore, mantle plume motions are not caused by internal mantle motions, but by processes modifying the location of the base or the top of the plume conduits.

This behaviour of mantle plume conduits is different from the models of Steinberger and O'Connell (1998), Steinberger (2000) and Steinberger and Antretter (2006). In the models of Steinberger and O'Connell (1998) and Steinberger (2000), mantle plumes are not explicitly modeled and result from a particle advection scheme. Mantle plume material is set to rise at a modified Stokes velocity (Richards and Griffiths, 1988) of 2.2 cm·yr^{-1} (corresponding to an ambient mantle viscosity of 10^{21} Pa·s), which

can lead to a maximal deflection of nearly 1000 km, and plume conduits are allowed to be distorted by 60° at most (Whitehead, 1982). From these modeled plume parameters, they concluded that important deflection of mantle plume conduits are caused by mantle return flow. Steinberger and Antretter (2006) corrected mantle plume rising speed to account for thermal plume rising speeds determined experimentally by Kerr and Mériaux (2004) instead of using the modified Stokes experimental law of Richards and Griffiths (1988) describing chemical plume behaviour and found similarly that the deflection of plume conduits results from mantle return flow. However, such a correction of modeled plume rising speed is not valid (Kerr and Lister, 2008).

4.2.4.2.3 No systematic shearing of plume conduits by surface plate motions. We calculate the distribution of angles between the surface plate velocities and upper mantle plume lateral velocities (at 350 km depth) at corresponding locations in all models. There is no significant trend in the orientation of upper mantle plume motions relatively to surface plate motions (Fig. 4.18). Indeed, the number of mantle plumes moving in the same direction as surface plates is similar to the number of mantle plumes moving opposite to surface plates. Mantle plumes are not all entrained by an upper mantle flow induced by surface plate motions because of the strong decoupling between the lithospheric mantle and the asthenosphere induced by large viscosity contrasts (Fig. 4.1). Therefore, the shearing of upper mantle flow by surface plate motions is limited to the uppermost mantle. Only the wake of mantle plumes (located at about 100 km depth below oceanic plates 200-250 km below continental plates) is substantially sheared by surface plate motions (Coltice et al., 2017b). Moreover, the rising speed of mantle plumes in the upper mantle is at least one order of magnitude faster than surface plates and upper mantle velocities (Fig. 4.7) due to their low viscosity. Mantle plume material thus crosses the upper mantle in about 1 Myr. As a consequence, potential shearing of plume material is limited.

This is consistent with the results of Richards and Griffiths (1988) who developed an analytical model of the deflection of mantle plume conduits due to a plate-driven shear flow. They found that mantle plumes develop a parabolic trajectory depending on the shear stress applied at the surface by the moving plate following:

$$x_p(z) = \frac{\eta}{k_p g \Delta\rho r_p^2} \frac{v_{plate}}{d} \frac{z^2}{2} \tag{4.7}$$

with all variables defined as in Eq. 4.1 and in Eq. 4.6. In Models 1, 2 and 3, assuming a constant upper mantle viscosity of 10^{20} Pa·s and an average surface plate velocity of 3.9 cm·yr^{-1}, the maximal

horizontal deflection of mantle plume conduits throughout the upper mantle due to plate shearing would be 51 km. In Model 4, it would be 169 km.

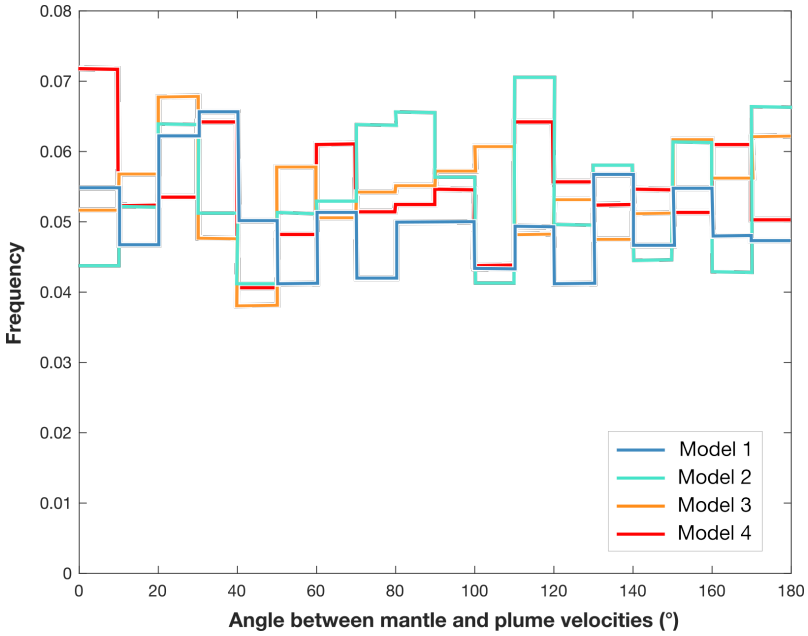


Figure 4.18: Distribution of angles between horizontal surface plate velocity and upper mantle plume lateral velocity for all Models.

4.2.4.2.4 No enhanced stabilization of mantle plumes located at ridges. On present-day Earth, a substantial number of mantle plumes interacts with mid-oceanic ridges. It was also proposed to be the case in the past (Whittaker et al., 2015). For example, Steinberger and O'Connell (1998) proposed that interactions between mantle plumes and spreading ridges are due to the impact of mantle return flow on the deflection of mantle plumes in an opposite direction to plate motion. However, as shown in section 4.2.4.2.2, we do not find such a behaviour in our models. Analytical studies quantified the activity of mantle plumes in the vicinity of stable or migrating ridges (*e.g.* Ribe et al., 1995, Ito and Lin, 1995, Albers and Christensen, 2001). Other studies proposed a link between mantle plumes and the formation of divergent plate boundaries (*e.g.* Morgan, 1971, Courtillot et al., 1999).

In all models, we detect mantle plumes interacting with ridges from the surface divergence field above the considered mantle plumes at each timestep. Throughout the model time integration, about 50% of the mantle plumes interact with surface divergent boundaries, either staying in the vicinity of oceanic ridges (as proposed for Tristan da Cunha, St-Helena or the Azores for example (see section 4.3)), crossing them (as it is the case for the Galapagos or Reunion hotspots), or participating to create new diverging boundaries (as the case of active rifting in the Afar). In the presented models,

we observe long-term plume-ridge interactions that can last more than 200 Myr.

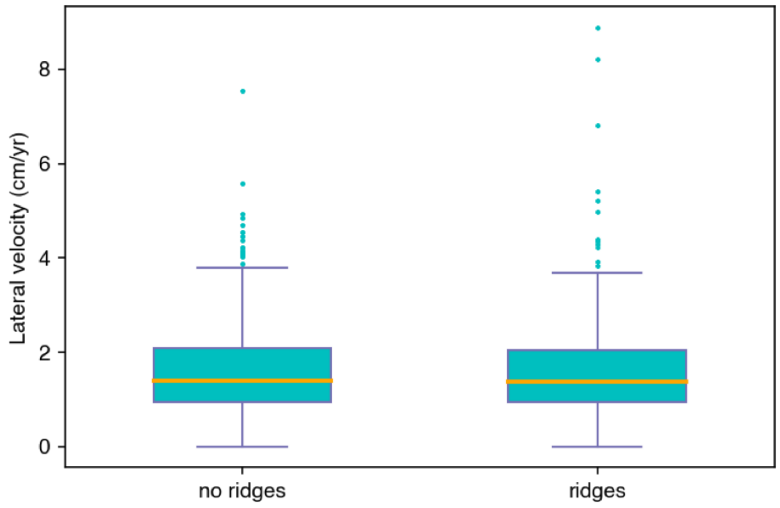


Figure 4.19: Distribution of upper-mantle absolute lateral velocities of mantle plumes interacting with ridges and mantle plumes not interacting with ridges in Model 1. The yellow lines correspond to the median lateral velocity of plumes, the rectangles delimitate the first quartile, purple horizontal lines show the third quartile and extreme lateral velocity values are represented by the cyan dots.

We compare the absolute lateral velocity distribution of mantle plumes located below ridges with the one of mantle plumes located elsewhere throughout Model 1 time integration. There is no significant increased stabilization of mantle plumes located below ridges relatively to intraplate hotspots (Fig. 4.19). Indeed, two mantle plume behaviours arise depending on the type of ridges they interact with. Mantle plumes can be stabilized during at least several tens of million years when they pond below long and stable ridges. On the contrary, mantle plumes interacting with fast-migrating ridges (which are usually located at the boundary of small plates which are affected by fast reorganisations (Mallard et al., 2016)) have the tendency to move laterally faster and more eratically. They therefore interact with spreading centers over shorter timescales. Such results are not contradictory with Jellinek et al. (2003) and Whittaker et al. (2015) who proposed that long-term interactions between ridges and mantle plumes are favoured at slow-spreading ridges.

4.2.4.2.5 Push induced by slabs. Existing scenarios to explain hotspot motions include an effect of slabs pushing mantle plume conduits. For example, Hassan et al. (2016) invoked the action of slabs pushing mantle plumes to explain horizontal velocities exceeding 4 cm·yr^{-1} between 81 and 47 Ma for the Hawaii hotspot.

In our models, subduction initiation as far as 5,000 km away from a stable mantle plume can modify

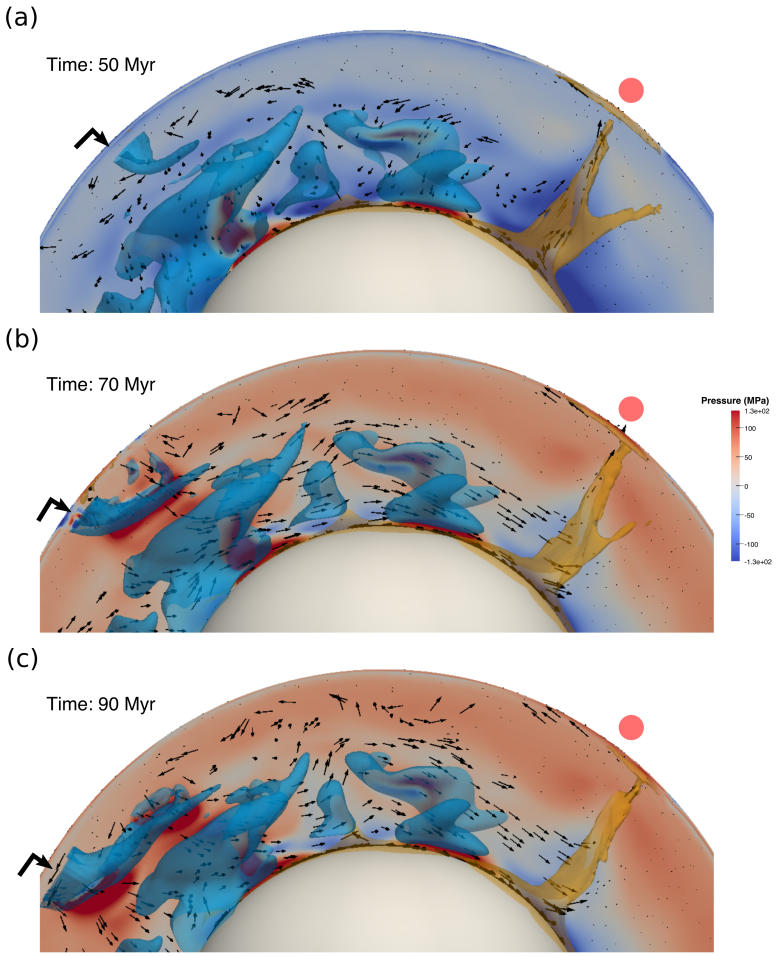


Figure 4.20: Pressure distribution in Model 1. A mantle plume is highlighted by the orange transparent isotherm. The initial position of the plume is shown at each timestep by the red circle. A subduction (blue transparent isotherm) initiates on the left, which results in far-field compression and a horizontal lower mantle flow directed towards the plume, as shown by the velocity field (black arrows). The thick black arrow shows the location of the subduction trench. Camera is fixed. Note that the pressure field is dominantly negative in (a) while it becomes positive in (b) and (c) as subduction zones initiate in Model 1.

mantle pressure field (Fig. 4.20a). It generates positive pressures in the mantle (Fig. 4.20b-c). Mantle therefore flows to the right, as outlined by the velocity field. These flow and pressure reorganizations generate lateral pressure gradients at the basal thermal boundary layer and also a possible shearing of this layer. As a consequence, the mantle plume is pushed towards the right, at a rate exceeding 2 cm·yr^{-1}. Moreover, because of a high mantle plume rising speed, the plume conduit is not deflected by the slab-induced flow in the lower mantle and remains vertical. In Model 1, this mechanism results in intermediate plume velocities, larger than 2 cm·yr^{-1}, which can last several tens of million years. In Model 2, the presence of a large number of ancient slabs in the lowermost mantle due to a reduced

surface yield stress results in a more limited action of slab-induced plume lateral motions, while in Model 3, stronger slabs reach the lowermost mantle, therefore pushing mantle plumes more efficiently.

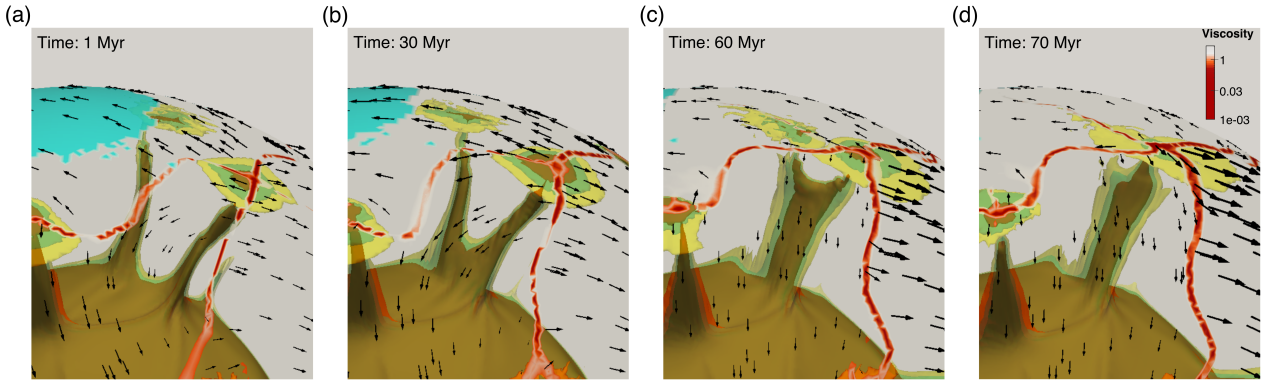


Figure 4.21: Temporal evolution of the merging between two plumes in Model 1 (cf hotspot IDs 7 and 8 on Fig. 4.3(a) and (b)). Plumes are outlined by the brown (1,750 K), the green (1,860 K) and the yellow (1,970 K) isotherms. Surface continents are shown in blue, plate boundaries are outlined by the red lines corresponding to low viscosity areas, and plate velocities are shown by the black arrows. Note that the merging starts from the base of the mantle and propagates upwards.

4.2.4.2.6 Rapid motions due to negative pressure gradients In the presented models, the fastest motions between mantle plumes occur when two close mantle plumes merge with each other. As seen on Fig. 4.21, the merging between two mantle plumes starts from the base of the mantle and then propagates to the surface. Such motions are related to negative pressure gradients between two close plume conduits, which lead to lateral motions larger than 5 cm·yr^{-1}, lasting less than 5 Myr (Fig. 4.22). Merging between two mantle plumes have been described in mantle convection models (Davies and Davies, 2009), who link them to some present-day seismic tomography models showing the apparent merging of some mantle plumes in the lower mantle (Ascension and St-Helena for example (Montelli et al., 2006)). However, fast lateral motions of merging mantle plumes have not been documented on Earth. This could be explained by the small probability of such an event. Indeed, in Model 1, merging events occur less than 10 times throughout the whole time integration (about 300 Myr).

4.2.4.2.7 Relative motions between mantle plumes and the basal thermo-chemical layer Burke et al. (2008) proposed that most mantle plumes on Earth are anchored at PGZs at located on the edges of thermo-chemical LLSVPs. Torsvik et al. (2010) then suggested that LLSVPs have remained stationary during the last 200 Ma at least, which Conrad et al. (2013) proposed to be evidence that

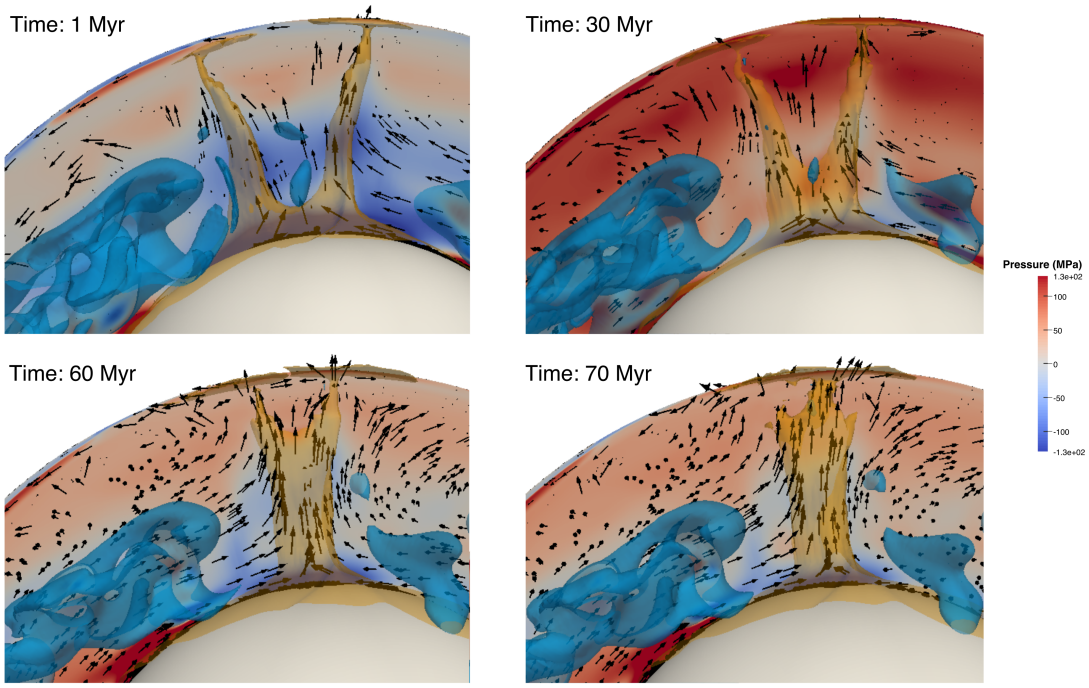


Figure 4.22: Pressure distribution in Model 1. The merging of two mantle plumes (orange transparent isotherm, cf Fig. 4.3 and 4.12) corresponds to an area of negative pressure. The action of slabs (blue transparent isotherms) pushing hot material in the lower mantle is highlighted by areas of compression and mantle velocity arrows.

large-scale mantle convective cells are long-lived. Therefore, mantle plumes would preferentially arise from defined locations in the vicinity of LLSVPs and move coherently and slowly within each of these large-scale upwelling areas (*e.g.* Jellinek and Manga, 2002, Davaille et al., 2002). However, the stability of LLSVPs is still debated (Tan et al., 2011, Zhong and Rudolph, 2015, Flament et al., 2017).

In Model 4, although all mantle plumes originate from the crests of basal thermo-chemical heterogeneities (Fig. 4.2), both absolute motions of mantle plumes and relative lateral motions between mantle plumes are enhanced compared to the other models (Table 4.3 and Fig. 4.15). This is because the presence of basal thermo-chemical heterogeneities is responsible for three times lower heat flow from the core (Fig. 4.10) and a plume temperature twice as cold in Model 4 as in Models 1, 2 and 3 in the upper mantle (Fig. 4.6d). Therefore, mantle plumes are less strong (Fig. 4.8d) and tend to be deflected more easily by mantle flow (Fig. 4.17), which generates faster lateral motions of conduits. In addition, the basal thermo-chemical heterogeneities form an initial uniform layer that continuously deforms throughout the time integration and therefore entrain mantle plumes laterally. Moreover, to compare Model 4 with Model 1, all parameters were kept constant besides the addition of a basal chemical layer, which results in a lower core heat flow than in other models. As a consequence, this

behaviour is contradictory with studies suggesting that thermo-chemical basal heterogeneities favour plume conduit fixity. A way to enhance plume fixity with the presence of thermo-chemical piles would be to increase the core heat flow, so that the temperature of plumes increases and they deflect less.

4.2.5 Discussion

4.2.5.1 Model limitations

Although this study provides a first step to the understanding of the lateral motions of naturally arising mantle plumes in mantle convection models with self-consistent generation of plate tectonics, the plume detection algorithm can be optimized in order to improve the quality of the comparison between different models. Indeed, in this study, the heat advection threshold used to detect mantle plumes was determined visually and independently for each model instead of fixing an arbitrary threshold for all models (Table 4.2). We could consider the use of an arbitrary amount of the average heat advection as a threshold in future studies.

Moreover, the conclusions relative to the presence of a basal thermo-chemical layer are strongly dependent on the lower heat flow than in models without basal chemical heterogeneities (Fig. 4.9). A future improvement would be to increase the amount of heat extracted from the core by decreasing the proportion of internal heating rate, in order to study the behaviour of mantle plumes arising from such a model. Moreover, although thermo-chemical material remains stable at the base of the mantle in Model 4 since it is weakly entrained by mantle plumes over the model time integration, the continuous deformation of this dense layer throughout the model time evolution impacts the ambient mantle behaviour. For example, the number of mantle plumes keeps increasing throughout the model time integration. This may be responsible for at least part of the important lateral motion of plumes in Model 4 (Fig. 4.15 and Table 4.3). To avoid such long-term reorganizations of mantle planform ans subsequent increased lateral mantle plume motions, we can consider future models with two initial domes of denser material at the base of the mantle instead of the uniform thermo-chemical basal layer used in Model 4.

4.2.5.2 Comparison with the lateral motion of mantle plumes in other studies

As stated above, due to the strong dependence of mantle viscosity on temperature, the rising speed of mantle plumes in our models can reach up to 1 $\mathrm{m{\cdot}yr^{-1}}$, which is consistent with some estimates

of Earth's mantle plume rising speed from hotspot topographic swells (Turcotte and Schubert, 2014). As a result, mantle plume conduits are near vertical and do not substantially deflect due to mantle return flow. Therefore, in our models, lateral motion of mantle plumes larger than 5 cm·yr^{-1} are due to pressure gradient forces (imposed by the flow induced by sinking slabs in the lower mantle pushing mantle plume conduits or by the merging of two plume conduits). Plume conduit motions at a rate of 1-2 cm·yr^{-1} are of the same order as mantle average lateral motions and correlate roughly with net rotation.

In our models, mantle plume rising speeds are at least five times larger than in other numerical models of mantle plumes. For example, Steinberger and O'Connell (1998) vertically advects plume tracers at a speed of 2.2 cm·yr^{-1}, Steinberger and Antretter (2006) uses an upper-mantle rising speed of 10 cm·yr^{-1}. As a consequence, their advected mantle plumes can be substantially deformed and tilted by mantle return flow, which is not the case in our models (up to 60° of lateral deflection is allowed instead of the 9° maximal deflection observed in our models). On the contrary, in their forward models of mantle convection using the extended Boussinesq approximation and reconstructed plate velocities, Hassan et al. (2015) measure a maximum plume rising speed of 1.39 m·yr^{-1}, resulting from large excess temperature (comprised between 300 and 700 K). As a consequence, mantle plume conduits are near vertical in their models, like in ours, and lateral motions are suggested to result from large-scale mantle convective processes. However, this proposed source of hotspot lateral motion stems from the fact that mantle flow is driven by imposed reconstructed plate velocities and slab-assimilation (Bower et al., 2015). Therefore, conclusions about the motion of mantle plumes induced by slab-induced flow in the lower mantle (Hassan et al., 2016) are highly dependent on the history of the surface used to drive mantle convection.

Several studies proposed that mantle plumes are not fixed but all move coherently (Zheng et al., 2018), or are grouped in independent clusters rooted to the Pacific and the African LLSVPs (Torsvik et al., 2012). Our study suggests that a coherent motion of all mantle plume conduits entrained by mantle net rotation is not likely, although a correlation of 0.6 is measured, showing that the slowest plume conduits can interact with degree-one mantle lateral flow. Our method does not allow us to compare the direction of mantle plume coherent motions with the direction of mantle flow, and so far, the thermo-chemical layer in Model 4 does not allow us to study the potential coherent motion of mantle plumes with LLSVP deformations. Nevertheless, implications of such coherent motions are critical for the building of plate reconstructions based on hotspot reference frames (Müller et al., 1993,

Doubrovine et al., 2012). Therefore, future work should focus more precisely on the characterization of the net motion of all mantle plumes or clusters of plumes in thermal or thermo-chemical fully-dynamic models of mantle convection with self-consistent plate tectonics.

4.2.6 Conclusion

In this study, we first characterized the phenomenology of the mantle plumes arising in our models of mantle convection self-generating plate-like tectonics and favorably compared them with observations at Earth's major hotspots. Our study confirms that the number, the lifetime, the shape, the temperature excess, the plume rising speed and the buoyancy flux of mantle plumes strongly depend on the presence of basal thermo-chemical heterogeneities. Depth-dependent thermal expansivity favours a smaller amount of mantle plumes in the models and changes in the lithosphere dynamics (yield stress variations) do not significantly affect mantle plume characteristics.

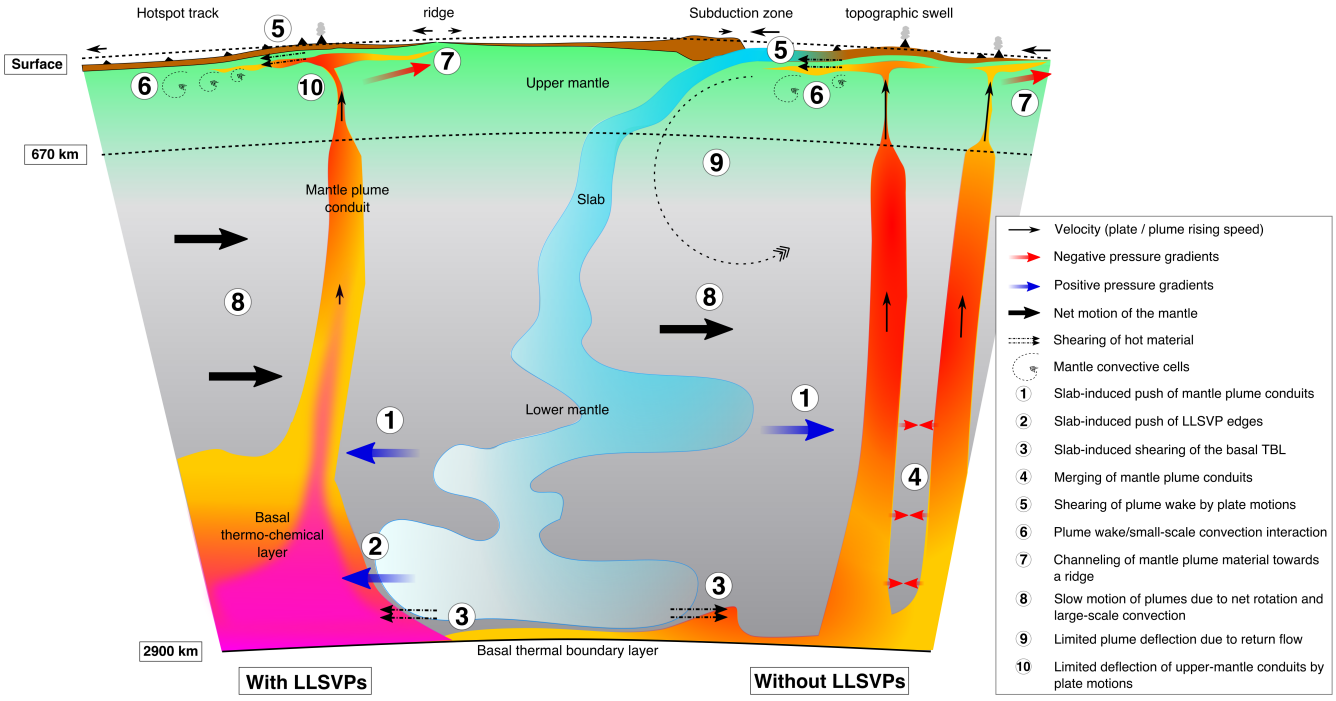


Figure 4.23: Schematic overview of the interaction of mantle plumes with mantle convection and plate-like tectonic processes in our models.

From the detection of mantle plumes through time, we measured a long-term decrease in mantle plume activity throughout their lifetime as well as shorter timescale pulsations of activity consistent with observations for Earth. The modeling of fully-dynamic mantle plumes and their interaction with self-consistent mantle flow and plate-like tectonics makes it possible to understand mantle plume

interactions with mantle convection and plate tectonics. Therefore, we characterized the absolute velocity, relative velocities and deflection angle of mantle plume conduits and identified the geodynamic processes from which they originate (Fig. 4.23). Absolute velocities are 1-2 cm·yr^{-1} on average and correlate with whole-mantle convection. Most of the mantle plumes move by less than 2 cm·yr^{-1} and are vertical throughout the mantle. In all models, mantle plume lateral motions faster than 3 cm·yr^{-1} are preferentially caused by processes acting on the source location of focused areas of upwelling: motions comprised between 3 and 5 cm·yr^{-1} are due to slab-induced push or shearing and can last several tens of Myr, which is a plausible mechanism to explain the Hawaiian bent, while motions larger than 7 cm·yr^{-1} are caused by the merging of two mantle plume conduits from their base and last less that 5 Myr. Contrary to existing studies (*e.g.* Steinberger and O'Connell, 1998, Steinberger, 2000, Steinberger and Antretter, 2006, Wang et al., 2018), mantle plumes are not substantially deflected by mantle return flow, unless basal thermo-chemical heterogeneities are present. This result from their large temperature excess and the strong temperature dependence of viscosity, which lead to plume rising speeds faster than inferred in other studies. This study provides an initial step towards the precise understanding of the sources and forces acting on mantle plume conduits and responsible for observed hotspot motions.

Take-home message:

From this study, the main conclusions are:

- **Plumes arising from 3D models of mantle convection models with plate-like tectonics present characteristics similar to Earth's plumes**
- **Most plumes move relatively to each other by less than 1-2 cm·yr^{-1} and are not deflected by mantle return flow**
- **Plume lateral accelerations result from merging events with other conduits or basal shearing and pressure gradients caused by slabs**

In the next section, I use the upper-mantle thermal signature of plumes interacting with ridges in 3D models of mantle convection with plate-like tectonics in order to reconstruct the relative motions between the Mid-Atlantic Ridge and the Azores mantle plume.

4.3 Northward drift of the Azores plume in the Earth's mantle

The following section is under review as:

Arnould, M., Ganne, J., Coltice, N., Feng, X., *in rev.*, Northward drift of the Azores plume in the Earth's mantle, *Nature Communications*

4.3.1 Abstract

The fixity of mantle plumes has been a cornerstone assumption for the reconstruction of tectonic plate motions (Morgan, 1972). However, paleomagnetic records and age progression along hotspot tracks have suggested substantial drift of plumes below the Pacific plate (Torsvik et al., 2002). Identifying the individual motion of a plume usually requires a long and continuous chain of seamounts, and precise geochronological and paleomagnetic data. Hence Hawaii is the only plume with clear evidence of drift so far (Konrad et al., 2018, Tarduno et al., 2003). Here, we use plume-derived basalts from the Mid-Atlantic ridge (MAR) to map the mantle temperature over a large region in the upper mantle centered on the Azores. We confirm that the thermal anomaly associated with the plume is asymmetric, spreading over 2,000 km southwards and 600 km northwards. Using for the first time a 3D spherical mantle convection where plumes, ridges and plates interact in a fully dynamic way, we show that the extent, shape and asymmetry of this anomaly is a consequence of the Azores plume moving northwards by 1-2 cm/yr, independently from other Atlantic plumes, possibly developing the Great-Meteor and Corner Rise volcanic chains.

4.3.2 Introduction

The Azores plateau is an oceanic area of about 150,000 km^2 (Vogt and Jung, 2018), with a magmatic center located about 100-200 km (Schilling, 1991, Ito and Lin, 1995) east from the MAR axis (Fig. 4.24a). The spatial correlation between bathymetric highs (Ito and Lin, 1995, Vogt, 1976), anomalously thick crust (Klein and Langmuir, 1987, Wang et al., 2011), gravity anomalies (Thibaud et al., 1998) and geochemical signatures (Dosso et al., 1999) along the MAR (Fig. 4.25c-e) point to an interaction between the ridge and a deep mantle plume. Both upper-mantle (Silveira et al., 2006, Dalton et al., 2014, Pilidou et al., 2005) and global seismic tomography studies (French and Romanowicz, 2015) describe the presence of a narrow and rather vertical low seismic velocity conduit beneath the Azores. This seismic anomaly extends in the lower mantle (French and Romanowicz,

2015) and the primitive $^4He/^3He$ ratios of the lavas (Moreira et al., 1999) further consolidate the deep origin of the Azores plume.

The symptoms of the plume-ridge interaction spread over a large region. The bathymetric high along the ridge forms an asymmetric bulge declining by 2.5 km over 500 km towards the North, and by 3 km over 2,000 km towards the South (Ito and Lin, 1995, Vogt, 1976), consistent with Bouguer anomalies (Thibaud et al., 1998) and plume geochemical fingerprints (Rare Earth ratios) (Dosso et al., 1999), (Fig. 4.25c-e). V-shaped gravity and topographic structures were detected only south of the Azores (Cannat et al., 1999), supporting the presence of a southwards elongated asymmetry. High resolution global **??** (Fig. 4.24b-d) and regional (Yang et al., 2006) tomographic models of the upper mantle show the asymmetric slow velocity region extends down to 200 km and spreads along the ridge over 3,000 km. The estimates for the Azores plume volume flux vary between 51 m^3/s, based on the spreading rate of the MAR (Sleep, 1990) to 90 m^3/s, deduced from the topographic swell around the hotspot (Crosby and McKenzie, 2009). Theories for interactions between a ridge and a static plume (Ribe et al., 1995, Ito et al., 1999, Albers and Christensen, 2001) fail to explain the extent of hot plume material spreading along the ridge (called waist) and its volume flux: accounting for a waist ¿ 2,000 km consistent with bathymetry (Ito and Lin, 1995), gravity (Thibaud et al., 1998), geochemistry (Dosso et al., 1999) (Fig. 4.25c) and seismic tomography (Debayle et al., 2016) (Fig. 4.24) would lead to an unrealistic volume flux of about 400 m^3/s (Ito et al., 2003). The presence of anomalously buoyant plume material more than 2,000 km south of the plume cannot either be explained by a burst of plume activity in the past. Such increase in the volume flux and temperature in the conduit was proposed for the Azores about 10 Ma ago based on V-shaped anomalies (Cannat et al., 1999), but would have led to a local increase of potential temperature of about 70°C, at about 600 km from the hotspot location and lasting only a few million years (Albers and Christensen, 2001).

Here we present first potential temperature (T_P) estimates along the MAR using the PRIMELT method that confirms the extent of the thermal waist of the Azores plume. We then investigate the dynamic connection between the plume asymmetry and relative plate-plume motions with 3D-spherical models of convection with plate-like behavior at Earth's-like convective vigor. Accounting for the kinematic context around the Azores, our model shows that only a northward motion of the plume $>$ 1 cm/yr can explain the geometry of the observed asymmetry.

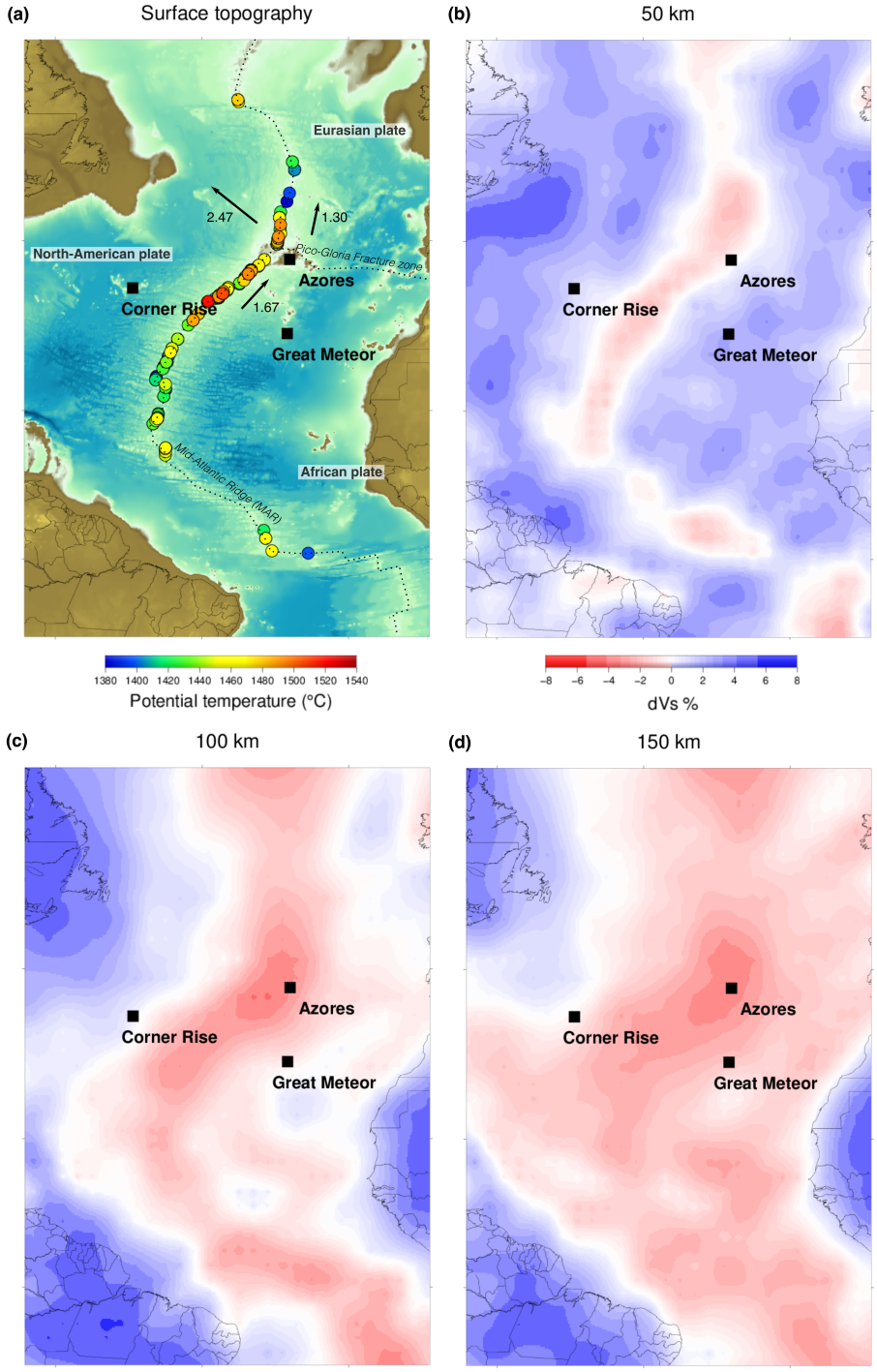


Figure 4.24: Geographical setting and seismic tomography of the upper mantle (a) Surface topography of the Central Atlantic Ocean and potential temperatures obtained from the PRIMELT method along the MAR (see Fig. 4.26). The direction and magnitude (in cm/yr) of plate velocities according to their absolute motions during the last 10 Ma in a moving hotspot reference frame (Torsvik et al., 2010) in the vicinity of the Azores are denoted by the black arrows and numbers. (b-d) Upper mantle shear wave tomography slices from the global upper mantle and transition zone model 3D2017_09SV (Debayle et al., 2016).

4.3.3 Results

4.3.3.1 New evidence for a temperature asymmetry below the Azores plume

MORBs are extracted from a partially melted region in the shallow ambient convective mantle. Their chemistry likely reflects the potential temperature (T_P) of this region, corresponding to the temperature that the ambient mantle would reach, should it raise adiabatically to the Earth surface without melting (McKenzie and Bickle, 1988). Global systematics of the chemistry of MORBs suggest T_P variations of 200°C to 250°C along, and immediately below, mid-oceanic ridges (Klein and Langmuir, 1987, Dalton et al., 2014), challenging some previous estimates ($\sim$ 100°C, Shen and Forsyth, 1995, Presnall et al., 2002). However, whether or not these variations simply reflect chemical heterogeneities in the mantle source, inappropriate corrections for fractionation (Niu and O'Hara, 2007) or the presence of fluids in the magmatic source (Cottrell and Kelley, 2013) remains a source of debate.

A more selective but secure approach relies on the chemical composition of primary magma formed by melting of dry, fertile peridotite, with limited fractional crystallization prior to magma emplacement in the crust. Inferences, though limited, already suggest that MORBs often appear too differentiated to yield T_P estimates with the PRIMELT method (Herzberg et al., 2007, Ganne and Feng, 2018). Conversely, intraplate volcanism, which also gives birth to primary magmas through decompression melting of deeper and hotter sections of the mantle (e.g. mantle plume), can provide about 10% of successful solutions of calculation with PRIMELT.

Geochemical data considered in this study come from Gale et al. (2013) who compiled an extensive chemical database of near zero-age (i.e. ¡ ca. 300 kyr) MORBs collected along the axis of mid-oceanic ridges (Fig. B.1 to B.7). We focus on the northern sections of the MAR (Fig. 4.25), from latitude 0 to 90°N where data is the most abundant. Fig. 4.25b illustrates the distribution of T_P obtained with PRIMELT along the MAR in the Azores area. A temperature anomaly spreads over 2,000 km southwards the Azores hotspot while it disappears about 500 km northwards of the hotspot. Fig. 4.25a-b and B.8 show that the temperature decrease correlates with a chemical depletion in calcium in the studied MORBs. Calcium depletion is indicative of a colder lithosphere or asthenospheric mantle below the MAR since it can result from (i) increasing melting of pyroxenite in the mantle favored by its lower solidus relative to peridotites; or (ii) increasing fractionation of magmatic pyroxenes during the ascent of primary melts through the lithospheric column, their crystallization being primarily controlled by the temperature of the mantle or the crustal section crossed by the melts. Petrological

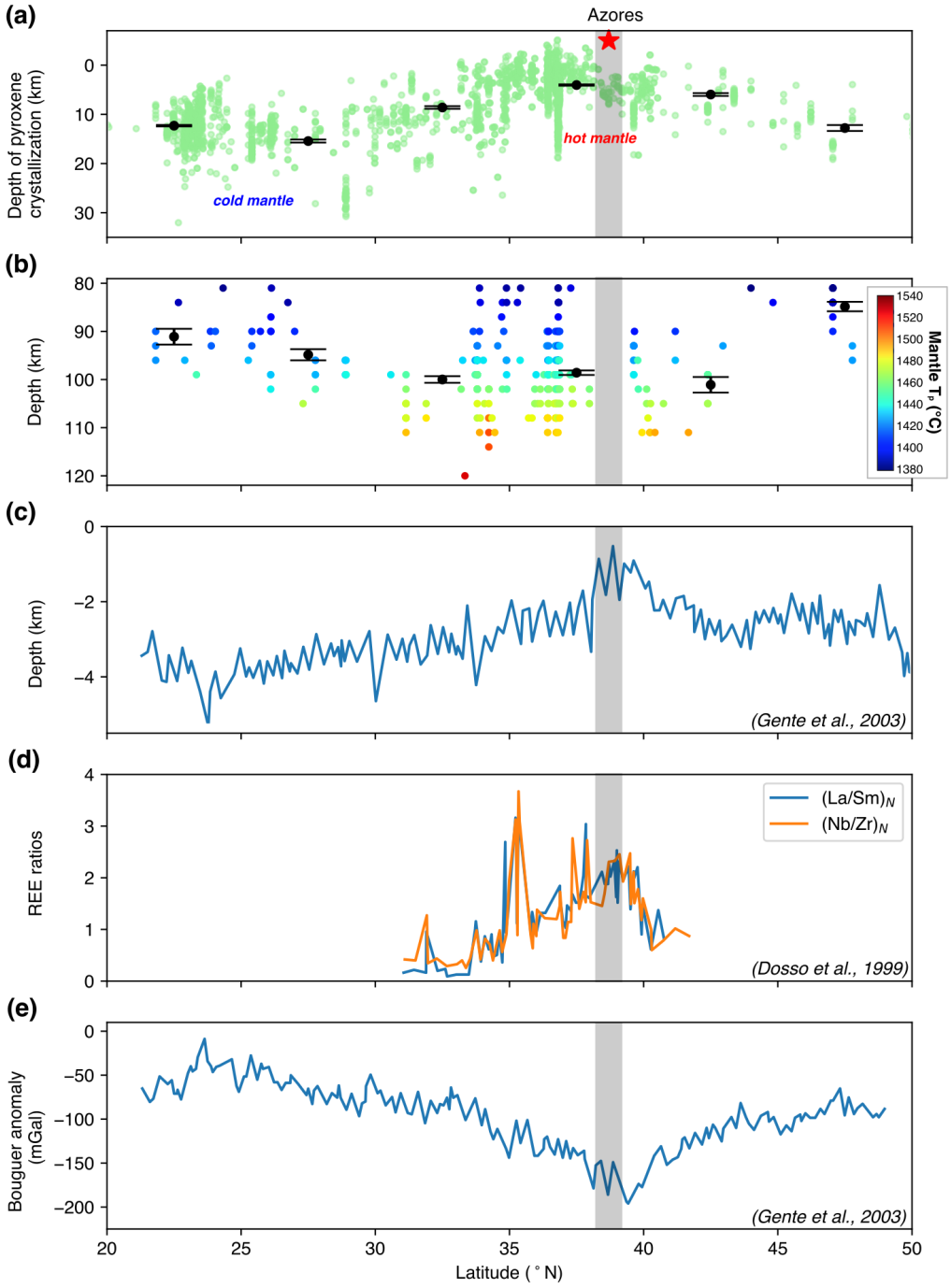


Figure 4.25: Chemical, thermal, bathymetric, geochemical and gravity asymmetry along the MAR (a) Depth of pyroxene crystallization then subtraction (e.g. fractionation) in a primary magma that, later, will give birth to MORBs, calculated using equation (6) in Herzberg (2004) and assuming a ratio of 1:3 between pressure (kb) and depth (km). (b) Depth at which adiabatically upwelling mantle bellow the MAR segments crossed their solidus, depending on their potential temperature (T_P) calculated with PRIMELT3 MEGA software (Herzberg and Asimow, 2015) using reduced conditions ($Fe^{2+}/\Sigma Fe = 0.9$) in the source. Solutions of calculation have been filtered for MgO < 8 wt% (blue dots in Fig. B.2). Mean values (black points) in (a) and (b) are obtained by bootstrap analysis, are reported at 5° step of latitude. (c) Ridge-axis depth in the region of the Azores (Gente et al., 2003). (d) Geochemical Rare-Earth-Elements (REE) ratios along the MAR (Dosso et al., 1999). (e) Ridge-axis Bouguer anomaly (Gente et al., 2003). Data have been plotted against latitude along the x-axis.

equilibrium curves (Herzberg, 2004) show that MORBs sampled away from the Azores crystallized pyroxenes at greater pressures and that the decrease in pressure correlates with the distance to the hotspot (Fig. 4.25a). This supports the idea of a temperature control on calcium depletion in MORBs and suggests that beneath the Azores, pyroxenes crystallize mainly in the oceanic crust due to the presence of anomalously hot mantle while further away, pyroxenes mostly crystallize in the mantle section (Fig. B.4 and B.5).

4.3.3.2 Thermal asymmetry caused by relative motions between a ridge system and a plume

We explore the hypothesis that the asymmetric thermal anomaly below the MAR corresponds to the thermal wake of the Azores plume, formed by shearing caused by the relative motion between the plate system around the ridge and the plume (Moore et al., 1998). To do so, we analyze the uppermost mantle thermal signature of drifting mantle plumes naturally emerging from a 3D spherical convection model with self-consistent plate-tectonics and interacting with ridges (see 4.3.4). In such models, plumes interact in a fully dynamic fashion with surface tectonics and convection currents at all scales (Coltice et al., 2017b). Hence, our model also takes into account in a fully dynamic way the effects of plume-ridge interactions described in previous regional models (Ribe et al., 1995, Ito et al., 1999, Albers and Christensen, 2001). Instead of using multiple regional models and imposing potentially unphysical constraints to our system to generate relative motions below a ridge, we are able to study a large number of self-evolving interactions between ridges and plumes by computing a global numerical model producing surface velocities, heat flow and plate size distributions comparable to Earth. We detect about 25 plumes on average at each time step. These plumes have a 210±45°C average temperature excess with respect to the ambient mantle, an upper mantle vertical velocity of 41±20 cm/yr, conduit diameters of 200±150 km, and volume fluxes of 40±15 m^3/s (Fig. B.9). We identify a total of 76 distinct plumes over the 320 Myr of model duration, moving laterally relative to a no-net-rotation surface at 1.75±0.38 cm/yr in average. Relative motions between hotspots are limited to 1.2±0.4 cm/yr. We observe that 46 of them interact at some point with ridges, either ponding below them or contributing to their propagation.

In our models, the relative motion between a considered plume and plates around the ridge shears the plume and generates thermal asymmetry. We identify four kinematic cases:

1. Fig. 4.26a. The plume moves along the ridge in the opposite direction to the average direction

of plate motion. Hence shearing always happens in the direction of plate motion, building up a highly asymmetric wake.

2. Fig. 4.26b. Both the plates and the plume move in the same direction. Shearing depends on which of the plates or the plume moves faster. If the plume does, like in Fig. 4.26b, shearing is opposite to the direction of the plates. If the plates do, shearing is in the direction of plate motion. If both move at about the same velocity, there is no asymmetry.

3. Fig. 4.26c. The plume moves perpendicularly to the ridge. Shearing along the ridge is then negligible and there is no asymmetry in this direction, although it can exist in the direction of seafloor spreading.

4. Fig. 4.26d. The plume lies below a ridge close to a ridge-ridge-ridge triple junction. The dominating effect causing the thermal asymmetry is the channeling of the wake material towards the triple junction.

Fig. 4.26f and Fig. B.11 show that temporal changes in the relative motion of the plate system and a plume can lead to a reversal of the asymmetry over a timescale of fifty million years.

4.3.3.3 Northward motion of the Azores plume

In the case of the Azores, the asymmetry of the thermal anomaly extends southwards. In a reference frame considering St-Helena and Tristan hotspots as fixed, explaining the asymmetry of the Azores plume would either require that the African and the North-American plates move southwards relatively to the Azores (case 1), or that both the Azores plume and those plates move northward, the plume moving at a faster pace (case 2). A southward motion of Africa was proposed by the NUVEL 1A-HS3 reference frame (Gripp and Gordon, 2002), based on Pacific hotspot tracks. However, this reference frame does not constrain the tracks of South-Atlantic hotspots. Using a moving hotspot reference accounting for both Pacific and Indo-Atlantic hotspot tracks, Steinberger et al. (2004), O'Neill et al. (2005) and Torsvik et al. (2008a, 2010) reconstructed a northward motion of Africa at a speed larger than 1 cm/yr in the vicinity of the Azores. Therefore, the Azores situation compares to modeled case 2 (Fig. 4.26b): the asymmetry results from a northward motion of the plume, at a faster velocity than the plates ($>$ 1 cm/yr). The northward motion of the Azores plume appears at odds with South-Atlantic hotspots (Fig. B.12), which are commonly viewed as stable, based on

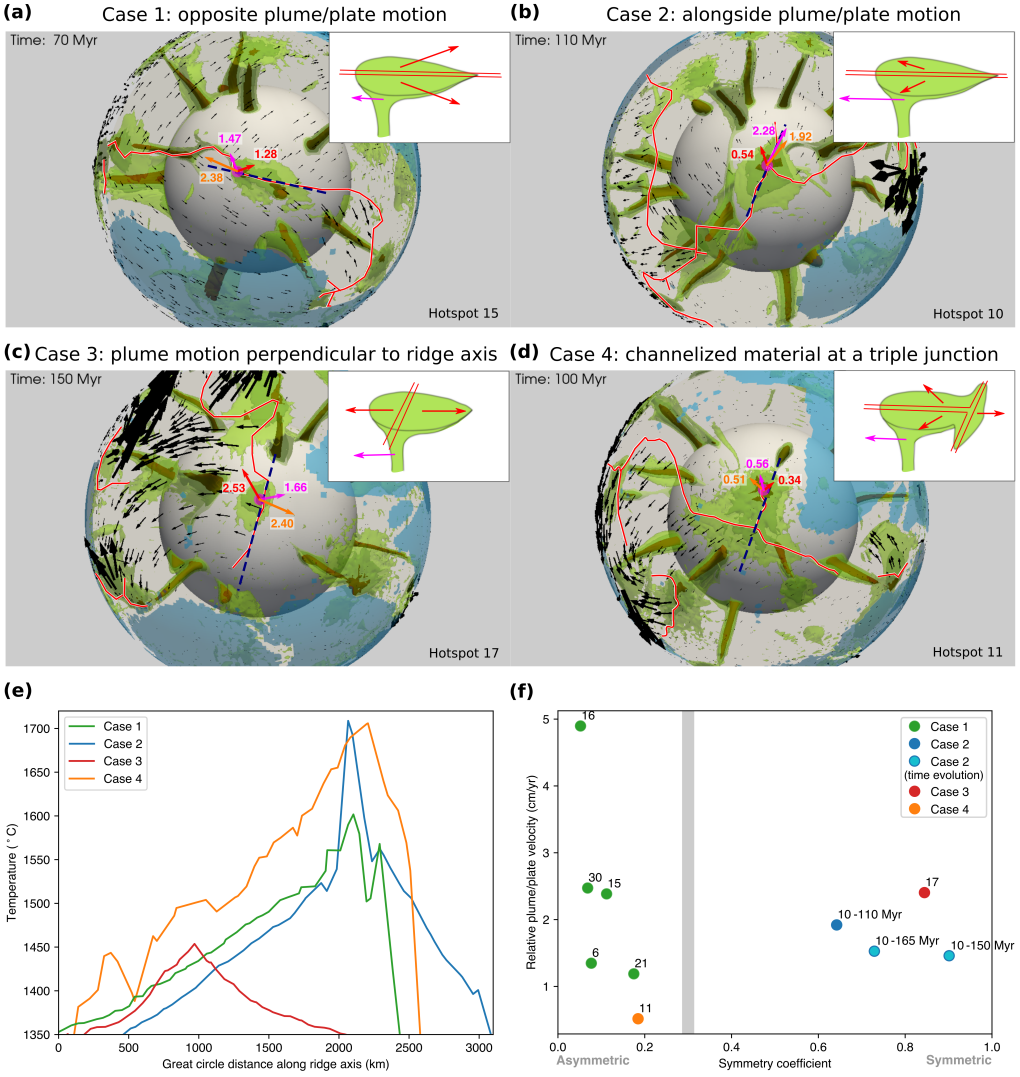


Figure 4.26: Modeled kinematic scenarii of the interaction between a plume and a ridge system. (a)-(d) Snapshots of four modeled cases of the relative motion between a ridge system (red lines) and a mantle plume (outlined by the light green (1,390°C), dark green (1,480°C) and brown (1,700°C) isotherms) in a global mantle convection model self-generating plate-like tectonics. Transparent magenta circles show the location of the plume thermal maximum. Colored arrows centered on the plume with magnitudes in cm/yr correspond to the plume absolute velocity (magenta), the average plates velocity within 500 km of the plume center (red) and the relative velocity between the plume and the average plates velocity (orange). Black arrows scale with surface plate velocities and blue transparent areas show the location of continents. Insets are schematic diagrams of the corresponding kinematic cases. (e) Temperature profiles across the plume waist at 100 km depth and along the modeled ridge (dark blue dashed lines in (a)-(d)). (f) Magnitude of the relative velocity between plumes and plate as a function of the symmetry of the temperature profiles of corresponding plumes (Fig. B.10). Symmetry coefficients correspond to the ratio of the extent of the thermal anomaly on each side of the corresponding plume thermal maximum. Numbers correspond to plume IDs. The vertical grey bar corresponds to the asymmetry observed at the Azores.

the geometry of their hotspot tracks (Duncan, 1981). This result differs from previous estimates of the Azores drift from numerical models of instantaneous flow induced by a density distribution based on seismic tomography (Steinberger, 2000), which favor a southwestward motion of the plume. However, in such models, the predicted flow close to the core-mantle boundary where the plume moves is very uncertain: (i) in the deepest mantle, tomographic models have relatively low resolution, show significant differences, and the conversion of seismic anomalies to density is ambiguous; (ii) the computed flows do not consider lateral viscosity variations, which are dominant in this area where cold slabs and hot plumes potentially interact; (iii) the ascent of plumes is not computed self-consistently in the flow model contrarily to our models. These models fail to explain both the vertical shape of plumes in the lower mantle recently unraveled by tomographic models (French and Romanowicz, 2015), and the southward elongated asymmetry across the Azores since they would predict an asymmetry in the opposite direction.

Since the Azores wake is highly asymmetric (Fig. 4.25 and 4.26f), it also suggests that the direction of the relative motion between the plume and the plates has remained stable over a timescale longer than a few tens of millions of years. A long-term northward motion of the Azores plume relative to the plate system is consistent with the proposed scenario of the Azores plume building up the Corner Rise and Great Meteor plateaus (Gente et al., 2003) (located about 1,000 km away from the present-day location of the plume, Fig. 4.24a). The indirect dating of these complexes (Tucholke and Smoot, 1990) was traditionally used to affiliate them to the New-England hotspot track mainly located on the North-American plate (Müller et al., 1993). However, recent tectonic (Gente et al., 2003) and geochemical (Pinto Ribeiro et al., 2017) studies bring complementary information for a genetic link with the Azores. A northward motion of the Azores plume at a rate of 1-2 cm/yr is consistent with such scenario of building a track from 85 Ma to 20 Ma and the proposed migration of the plume away from the MAR at 10±5 Ma (Gente et al., 2003).

Our study shows that characterizing thermal anomalies linked with plume-ridge interactions has the potential to unravel absolute plume motions, questioning our knowledge of mantle plumes. The proposed motion of the Azores plume is consistent with other evidence of moving mantle plumes (Tarduno et al., 2003, Molnar and Stock, 1987). Nevertheless, the causes for such motions are still unclear. The possible anchorage of the Azores plume on the edge of a dense and stable large low shear velocity province (LLSVP), as suggested in tomographic models (Thorne and Garnero, 2004), is not accounted by our convection model. However, convection calculations do not show enhanced fixity of

plumes with chemical anomalies at the core-mantle boundary (McNamara and Zhong, 2004). Also, slow deformation of the edges of LLSVPs produce plume motions of the order of 1 cm/yr (Flament et al., 2017), and plumes can propagate longitudinally along the edges of LLSVPs which undergo significant thermomechanical or thermochemical instabilities (Ni et al., 2002).

4.3.4 Method

4.3.4.1 PRIMELT

Mantle T_P calculation using PRIMELT is based on the MgO content of the primary magma, and MgO typically correlates with FeO. The calculations require that FeO be obtained from FeO_T (total iron reported as a single oxide) and this can be estimated assuming $Fe_2O_3/TiO_2 = 0.5$ or assuming a constant redox condition in the magmatic source ($Fe^{2+}/\ \Sigma Fe = 0.9$ or 0.8). We tested different hypotheses. Results are given in Fig. B.1. Uncertainties that arise by calculating FeO using Fe_2O_3/TiO_2=0.5 instead of $FeO/FeO_T = 0.9$ propagate to uncertainties in mantle T_P lower than 30°C for high-Ti type lavas ($TiO_2 > 1$ wt%) up to 60°C for low-Ti types ($TiO_2 < 0.5$ wt%). MORBs are dominantly characterized by Ti content > 1 wt% (Fig. B.1d). As such, the alternative adoption of a Ti-dependent redox condition is unlikely to affect our calculation toward more elevated T_P. Consistently, a more oxidizing ratio of $Fe^{2+}/\Sigma Fe = 0.8$ will decrease FeO in the primary magma, yielding lower MgO and lower mantle T_P but such general decrease will not change our general conclusions because it involves the whole set of data.

The petrological software is calibrated by anhydrous melting experiments on fertile peridotite, and its application to lavas assumes a similar fertile and dry peridotite source. Uncertainties in fertile peridotite composition do not lead to significant errors in mantle T_P(Herzberg and Asimow, 2008). Conversely, melting of wet peridotite is likely to result in MgO values that are too elevated. We excluded all samples that have undergone augite and/or plagioclase fractionation as indicated by depletion of CaO and Al_2O_3 or enrichment in FeO. Such discrepancies can be highlighted in a simple graph by plotting the chemistry of sample against its "liquid line of descent" (i.e. LLD, Fig. B.2c). Our calculations have been filtered according to a graphic procedure (Herzberg and Asimow, 2008) leading to reduced uncertainties that arise from pyroxenite source lithology, source volatile content from metasomatized peridotite, and clinopyroxene fractionation (Fig. B.3). We assume that the remaining samples have been affected only by minor amounts of olivine addition and subtraction.

Solutions of our calculation are provided in the supplementary material (Table B.1).

4.3.4.2 Numerical modeling

We use the thermochemical convection code StagYY (Tackley, 2008) to model mantle convection in 3D spherical geometry with continental lithospheric rafts and self-generation of plate-like tectonics at its surface. We solve the equations of mass, momentum and energy conservation under the Boussinesq approximation (see B for the equations and Table B.2 for parameters used). The Rayleigh number of the system, based on the temperature drop across the layer is 10^7, which results in a convective vigor comparable to the Earth. All mantle parameters are constant with depth, except the thermal expansivity coefficient (decreasing by a factor of 3 throughout the mantle), and the viscosity, which varies with temperature T and pressure P as in Arnould et al. (2018). The activation energy is 146 kJ/mol, implying 7 orders of viscosity variations throughout the domain. The activation volume is 13.8 cm^3/mol, and we impose a viscosity jump by a factor of 30 at 660 km, consistently with postglacial rebound and geoid modeling (Ricard et al., 1993, Nakiboglu and Lambeck, 1980). We introduce pseudo-plasticity (Tackley, 1998) to generate plate-like behaviour (plate boundaries emerge, they are not imposed). After exploration of the parameter space, we choose a yield stress value of 48 MPa for the oceanic lithosphere, so that the dynamic regime produces a plate-like behavior. The surface yield stress is 10 and 20 times higher for the margins and the interior of continental rafts respectively, to avoid their excessive mechanical erosion. The yield stress varies with depth by a factor of 1.8 MPa/km for all materials. We first run the model to reach a thermal statistical steady state. Then, we compute a total evolution of 400 Myr. Such model is at the limit of computation capabilities and required about 7 weeks of computing time on a parallel supercomputer of the National Computational Infrastructure (Australia). In the numerical solution, mantle plumes originate from the CMB where the heat flow is about 5 TW. Internal heat is produced at a rate of about 8.510^{-12} W/kg. Surface heat flow reaches 34 TW, and the root-mean square surface velocity is 3.26 cm/yr. Plumes and plate boundaries are emergent structures, not imposed in such models. All plumes can spontaneously move relatively to a no-net rotating surface. After the run, we examine these structures produced in a self-consistent manner by the system of equations.

Supplementary Information Supplementary Information is in Appendix B.

Acknowledgements The research leading to these results has received funding from the IRD, CNRS-INSU and the European Research Council within the framework of the SP2-Ideas Program ERC-2013-CoG, under ERC grant agreement 617588. Calculations were performed with the assistance of resources from the National Computational Infrastructure (NCI) through the National Computational Merit Allocation Scheme supported by the Australian Government.

Author contributions M.A. and J.G. conceived the study and wrote the paper. N.C. helped to generate the research idea and contributed to the writing and focusing of the paper. J.G. contributed with X.F. to the petrologic analysis and PRIMELT modelling. M.A and N.C. developed the numerical models and the kinematic analysis of the Azores plume motion. All authors contributed to the interpretation of results.

Take-home message:

From this article, the main conclusions are:

- **The petrological study of basalts sampled at the MAR near the Azores shows the existence of a shallow asymmetric mantle thermal anomaly**
- **The thermal wake of moving mantle plumes arising from numerical models of mantle convection with plate-like tectonics is consistent with observations**
- **The Azores hotspot moved northwards by 1-2 cm/yr from 85 Ma independently from other Atlantic hotspots and originated Great Meteor and Corner Rise**

4.4 Conclusion and perspectives

4.4.1 Conclusion

In this Chapter, I first characterized the behaviour of mantle plumes naturally arising from 3D numerical models of mantle convection. I showed that their temperature excess, conduit diameter, buoyant rising speed, buoyancy flux and heat flux are comparable to Earth's observations at major hotspots with a likely deep origin. I then tracked mantle plume conduits through time and showed that interactions with both mantle convective scales and plate tectonics are limited. Mantle plumes

move relatively to each other by less than 1-2 cm·yr^{-1} in average, and are not significantly deflected by mantle convective motions. Rapid lateral motions ($>$ 5 cm·yr^{-1}) of hotspots occur when two mantle plumes merge from their base. Intermediate lateral motions are due to the proximity of mantle plumes conduits with lower mantle slabs pushing their base. The models presented in this Chapter therefore suggest that mantle plumes' lateral motions are primarily initiated at the core-mantle boundary in models without basal thermo-chemical heterogeneities. When a basal thermo-chemical boundary layer is present, mantle plumes lateral motions coincide with the lateral deformations of the basal thermo-chemical layer by whole-mantle convective scales. Finally, this chapter proposes to use fully-dynamic 3D numerical models of mantle convection with plate-like tectonics in order to explain the spatial distribution of potential temperature anomalies in Earth's uppermost mantle at the axis of the Mid-Atlantic Ridge, in the vicinity of the Azores hotspot. I showed that the asymmetry and extent of such an anomaly cannot be explained by a stationary plume. I therefore proposed, from geodynamical and kinematic arguments that the Azores plume moved by 1-2 cm·yr^{-1} over the past 85 Ma. Its northward motion along the MAR axis contributed to the formation of Great Meteor and Corner Rise before the plume moved away from the axis of the Mid-Atlantic Ridge and created the Azores plateau. Moreover, this motion seems independent from the behaviour of other mantle plumes located in the South Atlantic (St Helena and Tristan da Cunha/Gough hotspots). The results presented in this Chapter are a first step towards the understanding of mantle plume conduits interactions with upper and lower mantle convective scales and plate tectonics.

4.4.2 Perspectives

4.4.2.1 Lateral motions of mantle plumes and supercontinent cycles

As stated in section 1.2.2.4 and shown in section 4.2, mantle plumes dynamics seems to be closely linked to diverging boundaries (*e.g.* Whittaker et al., 2015). Morgan (1971) proposed that mantle plumes contribute to supercontinental breakup by impinging the base of continental lithosphere. Amongst the observations in favor of plume-induced continental breakup, are the continental LIPs events, which are contemporaneous of rifting events (White and McKenzie, 1995), dyke swarms distribution and lithospheric deformations, which often draw triple junctions and therefore suggest plume head impingement below continental lithosphere (Gomez-Chavez, 2001), and *seaward-dipping reflectors* (SDRs) magmatic rocks underplating rift shoulders (Geoffroy (2005), although they are now

considered as independent of the mode of breakup). However, the precise timing of rifting and LIP eruption events is still questioned, since dyke swarms could reflect pre-existing lithospheric stresses (Jourdan et al., 2004), and some rifts seem to predate first flood basalts (Frizon de Lamotte et al., 2015). I propose to investigate the timing between supercontinent breakups and the surface arrival of new plumes at the surface in our models of mantle convection self-generating plate-like tectonics.

I analyzed a model of mantle convection with plate-like tectonics with a different parameterization from the one used throughout this Chapter. Indeed, the Rayleigh number is 10^6, thermal expansivity does not depend on depth, there are no basal thermo-chemical heterogeneities and the dimensionalized yield stress corresponds to 250 MPa, which results in a tectonic regime similar to Model 3 presented in section 4.2. Mantle plumes arising from this model have characteristics similar to the ones detailed in section 4.2. Since the Rayleigh number is ten times lower, plume conduits are about two times larger than in section 4.2. The total time of integration of this model is 450 Myr. The initial continental configuration corresponds to the position of Earth's continents 200 Ma ago (Pangea supercontinent, Fig. 4.28). After 310 Myr, the supercontinent starts to break-up.

Large-scale reorganization of mantle plumes during a supercontinent breakup

As shown on Fig. 4.27, the supercontinent breakup coincides with large-scale reorganization of whole-mantle convection. Indeed, on Fig. 4.27(a), the upper mantle is characterized by a dominance of degree-1 thermal anomalies corresponding to the fact that sub-continental mantle is hotter than sub-oceanic mantle due to its thermal insulation properties. On the contrary, the lower mantle is characterized by dominant degree-2 thermal anomalies. After the supercontinental breakup, degree-2 thermal anomalies become dominant in the upper mantle (since the supercontinent breaks into two major continental blocks) while degree-1 convection takes place in the upper mantle. This large-scale reorganization corresponds to the scenario proposed by Zhong et al. (2007) (see section 1.2.3) and therefore suggests that it is geodynamically plausible.

The large-scale reorganization of continental configuration and mantle convection also coincide with an enhanced motion of mantle plumes (Fig. 4.29). Indeed, even in the absence of basal thermo-chemical heterogeneities, mantle plumes tend to be clustered in areas of large-scale upwelling. Before the supercontinent breakup, two clusters of mantle plumes are present. When the supercontinent

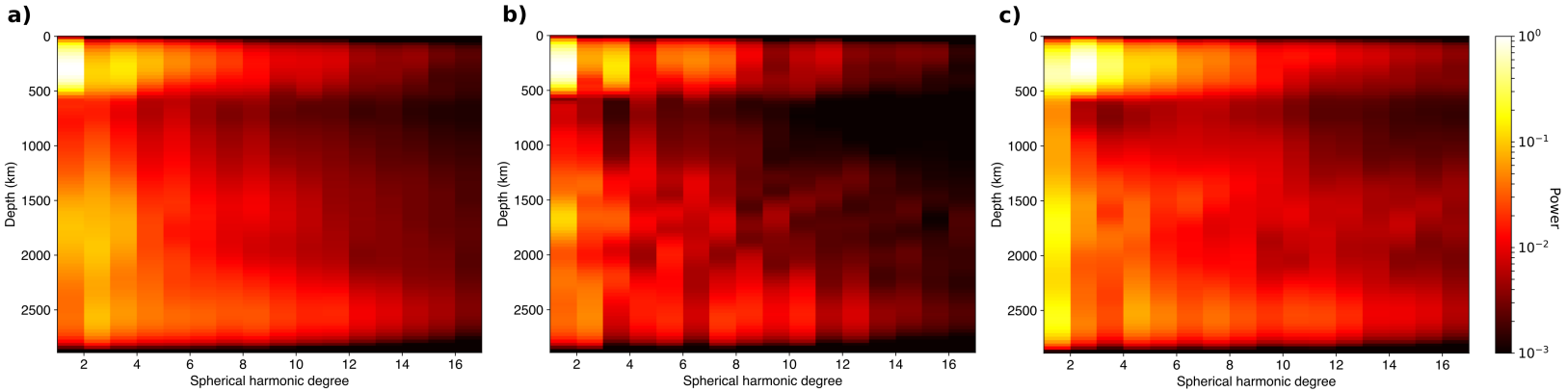


Figure 4.27: Evolution of the thermal heterogeneity spectrum of the model time-averaged over 3 stages: a) supercontinental stage, b) supercontinent breakup and c) separated continents. Note the change in the dominant largest spherical harmonic degree of thermal heterogeneities throughout the time integration, from a degree-2 to a degree-1 dominant convection in the lower mantle while the uppermost part of the mantle evolves from a dominant degree-1 to a dominant degree-2.

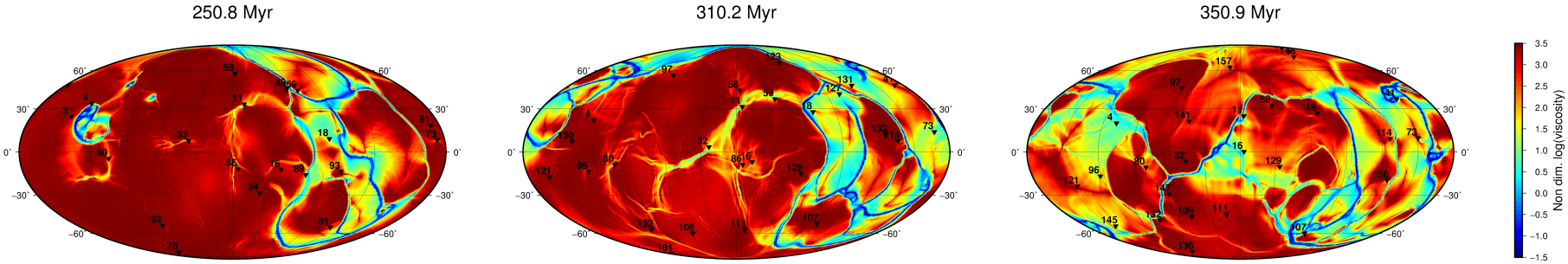


Figure 4.28: Surface viscosity field at 3 different timesteps. Note the preexistence of hotspots 11, 32 and 16 to the major episode of rifting occuring at about 310 Myr

breaks, existing plumes tend to aggregate in the area corresponding to the new ocean opening. Indeed, in this model, plumes location follow large-scale lower mantle flow (Fig. 4.27). In order to quantify the effect of supercontinents on the motion of mantle plumes and changes in large-scale mantle convection, further tests are needed (notably to investigate the effect of the presence of basal thermo-chemical heterogeneities or the effect of the initial configuration of continents) and longer time integrations are required. In the future, the identification of the scenario(s) of supercontinent cycles and corresponding changes in large-scale mantle convection will help to constrain the lateral motions between the Atlantic and the Pacific hotspots which are thought to move coherently since they are anchored to distinct LLSVPs. This might also make it possible to identify and use a population of mantle plumes that remained more stable than the others during Pangea breakup as an absolute reference for refining plate reconstructions for the last 200 Ma.

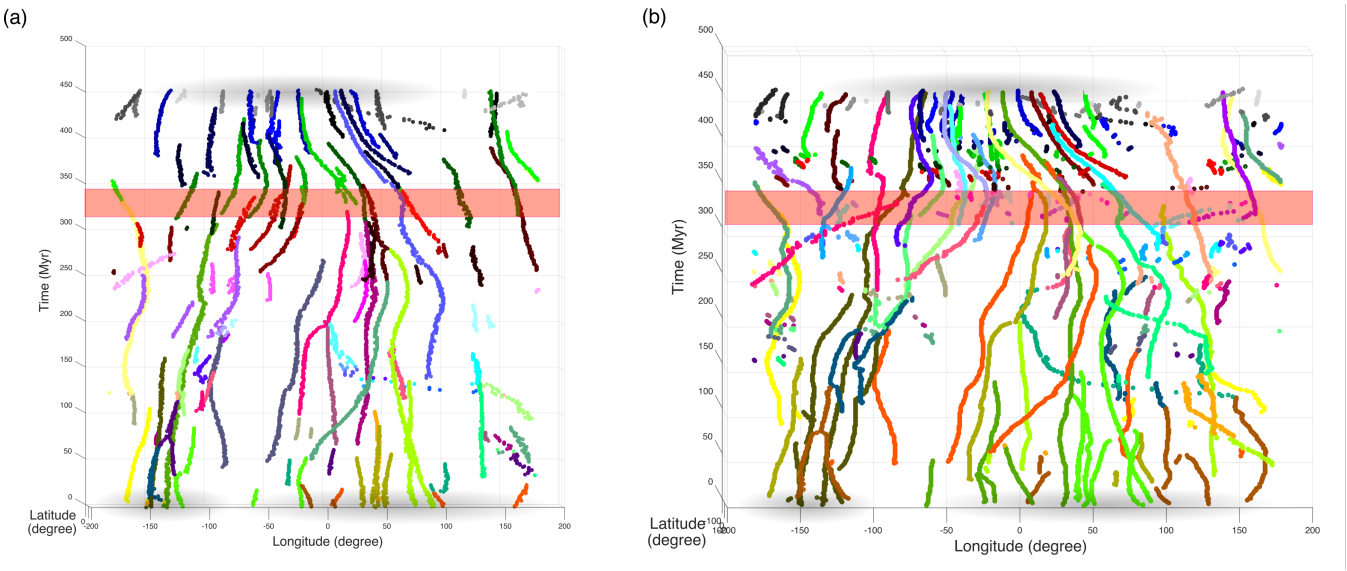


Figure 4.29: (a) Time evolution of the longitude of hotspots at (a) 1000 km depth (lower mantle) and (b) 350 km depth (upper mantle). The different colours show the temporal evolution of the position of individual hotspots. The red rectangle approximately shows the duration of the supercontinental breakup. After the supercontinental breakup, a global reorganization of hotspots occurs as new hotspots appear preferentially below the location of the former continent (top grey shaded area) and existing plumes converge towards this location whereas they were clustered into two groups at the beginning of the time integration.

A passive role of mantle plumes during the breakup?

Thanks to the generation of models used in this thesis, we can also quantify the timing between the supercontinental breakup and bursts of new mantle plumes in order to investigate the causes of such a breakup. To do so, we can quatify the temporal evolution of large igneous provinces (LIPs) that would be generated due to the arrival of a new plume detected in the upper mantle (Fig. 4.30). In the model presented here, the number of new LIPs increases gradually throughout the time integration. The supercontinental breakup is not preceded by an increased number of LIPs. However, the number of new mantle plumes detected in the upper mantle within 50-100 Myr after the supercontinental breakup increases from about 18 to 24. Therefore, in this model, the supercontinental breakup does not seem to be initiated by the impingement of new plume heads at the base of continental lithosphere. Indeed, long-lived plumes are already present long before the supercontinent breaks and the new rift propagates from areas thermally weakened by those plumes. The increase of the number of plumes following the supercontinent breakup corresponds to the relocation of areas of hot thermal instability initiation.

Dal Zilio et al. (2017) proposed that supercontinent breakup is initialized by mantle drag forces created by subductions located along the edges of Pangea. The model presented here also suggests that supercontinent breakup is not an active process, existing mantle plumes acting only as sources of thermal weakening of continental lithosphere, which is contradictory with the results of Zhang et al. (2018) who suggested an important role of mantle plumes below supercontinents. To draw conclusions about the mechanisms leading to supercontinental breakup, we need to analyze more models, by notably investigating the effect of the rheology of the supercontinent, the force-balance leading to supercontinental breakup and different large-scale mantle convection settings. Moreover, comparisons of the timing of LIPs/rifting with the geological record (*e.g.* de Gouveia et al., 2018) will help to better constrain the timing and mechanisms of rifting.

4.4.2.2 Definition of an absolute frame of reference based on hotspots

The study of the relative lateral motions of mantle plumes in Earth's mantle (Section 4.2) suggests that mantle plumes are not fixed in the mantle (Konrad et al., 2018). The use of hotspot tracks in order to derive the absolute motions of plate tectonics therefore requires precise knowledge on the behaviour

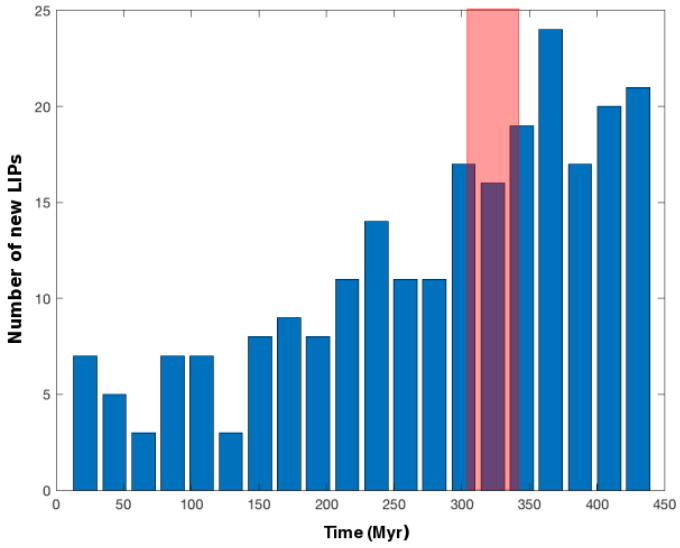


Figure 4.30: Temporal evolution of the probability of large igneous eruption. The number of new LIPs corresponds to the number of new plumes degtected in the upper mantle every 20 Myr. The red rectangle shows the approximate duration of the supercontinental breakup.

of all the individual hotspots used to reconstruct the past dynamics of the surface. It is still not clear, from the geological record, whether all mantle plumes move indepedently to each other, whether clusters of plumes anchored at LLSVPs move independently to one another, or whether all mantle plumes have a coherent net motion relatively to the lithosphere. Moreover, we have no clues about the possible existence of a net motion of all mantle plumes distinct from lithosphere/mantle net rotation, and about the potential mechanisms from which such motion would originate. The use of more fully-dynamic models of mantle convection with plate-like tectonics and mantle plumes arising naturally will ultimately help to test these hypotheses, understand the causes leading to coherent motions of hotspots and quantify the timescales and amplitudes of such motions, thanks to the development of a method of characterization of the correlation of the lateral motions of different mantle plumes.

4.4.2.3 Topography and geoid anomalies generated by mantle plumes

As described in section 1.2.2, one of the distinctive hints of the presence of mantle plumes on Earth is the upward deflection of Earth's surface by up to 1-2 km over 1,000 km from the considered hotspot (*e.g.* Crosby and McKenzie, 2009). These anomalous highs come along with positive geoid anomalies of 5-10 m high, indicating the presence of denser material below the surface, and larger crustal thickness linked to an increased magmatic production (Schilling, 1991). We calculate the surface total topography in Model 1 (see section 4.2) using the method described in Chapter 3 (Fig.

4.31). Areas corresponding to the presence of mantle plumes, are characterized by an anomalously high topography, reaching up to 2 km and extending up to 2,000 km in the oceanic domain (Fig. 4.31). In the continental domain which is characterized by a thicker and more viscous lithosphere, the topographic bulge induced by underlying mantle plumes is less prominent. From such results, I envision to quantify the temporal evolution of the dynamic topography generated by mantle plumes. From the systematic analysis of the patterns and timescales of dynamic uplifts at hotspots, it will be possible to characterize different periods of activity of mantle plumes from dynamic topography observations. It comprises the study of the birth of a mantle plume (Campbell, 2001), its fluctuations of activity (Hartley et al., 2011), its lateral motions (see hotspot 11 on Fig. 4.31: the mantle plume moves northeastwards from an island that it generated before 56 Myr but after 32 Myr of lateral drift of the plume, the island is still emerged) and its progressive decline of activity before its disappearance (Herzberg and Gazel, 2009).

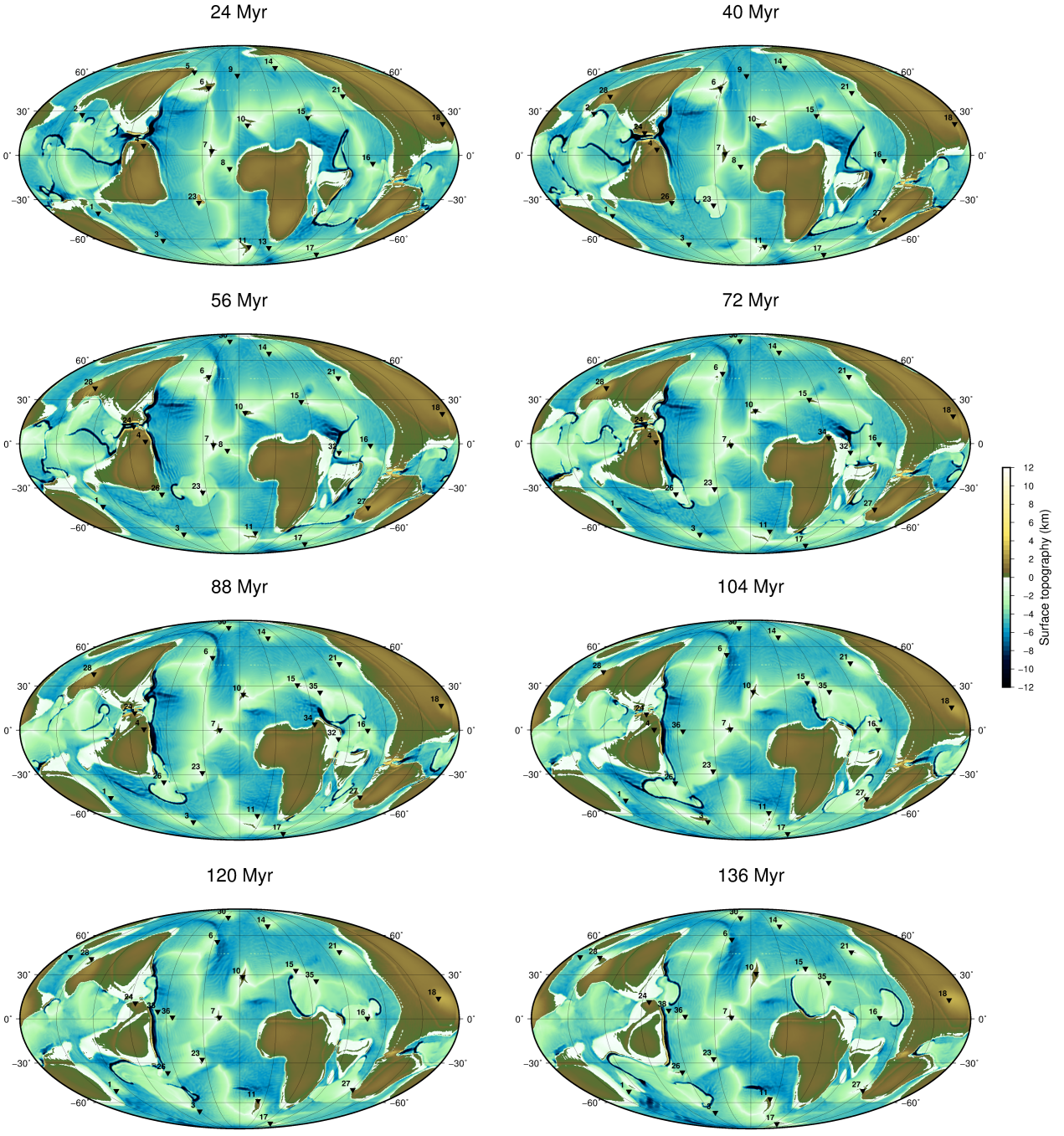


Figure 4.31: Surface topography at eight different timesteps in Model 1. Note the presence of topographic swells in areas surrounding mantle plumes, both in the continental and the oceanic domain.

Chapter 5

Conclusion and Perspectives

In this thesis, I used numerical models of mantle convection with plate-like tectonics in order to study some surface expressions of mantle convective instabilities. In particular, I focussed on the role of the different scales of mantle convective instabilities in the generation of dynamic topography at the surface of models and the interaction between mantle plumes with mantle convective scales and plate tectonics. Looking back at the challenges raised in the introduction of this thesis (Section 1.3.1), this work contributes to improving our understanding of the interactions between Earth's surface and mantle.

The first step of this work consisted in the development of numerical models of mantle convection self-generating plate-like tectonics in a regime allowing comparisons of surface heat flow, topography, and mantle and lithospheric velocities with observations for Earth. Since both mantle convection and plate-like tectonics dynamically arise in such models, the physical behaviour of mantle convection is preserved although the rheology used in the models presented in this thesis is highly simplified compared to the rheology of Earth materials as constrained by laboratory experiments (*e.g.* Kohlstedt et al., 1995). Therefore, those models are a powerful tool to study the interactions between Earth's lithosphere and mantle convection. However, describing the dynamics of the models requires original methods. These include statistical comparisons, detection and tracking methods and spectral comparisons.

In Chapter 3, I explored the influence of various scales of convection (scales smaller than 500 km arising from the modeling of large radial and lateral viscosity variations in the upper mantle to scales larger than 10,000 km) on the generation of dynamic topography. I showed that lithospheric vertical deformations are representative of all those spatial and temporal scales of convection. The spatial distribution of intermediate to small-scale dynamic topography (wavelengths smaller than

10,000 km) is consistent with observation-based present-day residual topography. In particular, the models suggest that the timing of subduction initiations and slab break-offs controls the existence of intermediate scales of dynamic topography. The potential existence of such fluctuations of intermediate scales of dynamic topography with subduction zones initiation and cessation events still needs to be tested in light of the geological records. The precise interpretation of surface processes such as sea-level variations, episodes of continental inundation or sedimentation rates requires to account for the interplay between local, regional and global tectonic and mantle convective motions.

In Chapter 4, I proposed to study the role of mantle dominant convective scales, the presence of basal chemical heterogeneities, and the decrease of thermal expansivity through depth on the behaviour of mantle plumes naturally arising from 3D models of whole-mantle convection with plate-like tectonics. In such models, the diameter of mantle plumes, temperature excess, rising speed, buoyancy flux and heat flux are comparable to Earth observations at major hotspots with a likely deep origin. I showed that in all the studied models, most of the mantle plumes move relatively to each other by less than 2 cm yr^{-1}. Nevertheless, some plumes can experience periods of rapid motions (up to about 20 cm$\cdot yr^{-1}$) over timescales shorter than 5 Myr. Such motions are due to plume merging events starting from the base of their conduits and caused by pressure gradients. Motions of intermediate speed (2-5 cm$\cdot yr^{-1}$) correspond to plume conduits base being pushed or sheared by slabs in the lowermost mantle. I showed that due to large viscosity contrasts caused by temperature excess between mantle plume material and the ambient mantle, plume rising speed is fast and deflections are rare in the case of purely thermal plumes. Conduit shearing by upper mantle flow induced by tectonic plate motions is also limited. This study provides starting clues in order to understand the behaviour of mantle plumes interacting with a dynamic environment. The models also make it possible to test the fixity of mantle plumes in Earth's mantle, through the comparison of plume-induced thermal anomalies deduced from petrological analyses of basalts sampled on the axis of the Mid-Atlantic Ridge (MAR) with thermal anomalies of plumes arising from numerical models. The study of the shape of thermal anomalies in the wake of modeled mantle plumes allowed to reconstruct the relative motions between the MAR and the Azores plume. Therefore, the numerical models developed in this thesis are a useful tool to interpret surface observations. Understanding the lateral motions of mantle plumes arising self-consistently from numerical models of mantle convection with plate-like tectonics can ultimately give geodynamical bounds on their lateral velocities in order to refine future reconstructions of past

plate tectonic motions.

This work falls within a larger project (called AUGURY) aiming at bridging the gaps between surface observations of the kinematics of plate tectonics and the physical framework of mantle convection on Earth thanks to the development of data assimilation methods (Bocher et al., 2015, 2018). As stated in this thesis, other methods based on the imposition of surface plate velocities (Bunge et al., 2002) and slab geometries (Bower et al., 2015) or the backward advection of seismic tomography anomalies (Conrad and Gurnis, 2003) become highly uncertain as the reconstruction time increases (Bello et al., 2014). Contrary to those methods, the data assimilation technique is based on the sequential inclusion of observations of past plate tectonic motions in numerical models of mantle convection, in a way that allows retroactions between new observations and the physics of convection. Indeed, the correction of surface velocities arising from mantle convection models by plate reconstructions velocities over periods of time shorter than 10 Myr limits the risks of propagating errors due to uncertainties in the model rheology or initial conditions through time (Coltice and Shephard, 2018). In order to build such integrated models, these methods nevertheless require that the initial convective and lithospheric state of the models is not too different from the actual state of Earth's lithosphere and mantle. Several studies conducted by the AUGURY team have already shown that the rheology and physical approximation (Boussinesq Approximation) used in models similar to the ones developed in this thesis are relevant for conducting data assimilation experiments, since they present seafloor age-area relationship (Coltice et al., 2013), continental motions (Rolf et al., 2014), plate-size distribution (Mallard et al., 2016) or even small-scale convection (Coltice et al., 2017b) similar to observations for Earth. In this thesis, I now consider the effect of highly vigorous mantle convection, the potential presence of basal thermo-chemical heterogeneities and a depth-dependent thermal expansivity in order to model mantle convection with plate-like tectonics that can be used in future data assimilation experiments. Moreover, Chapters 3 and 4 suggest that such models could be used as a fairly good initial condition for data assimilation experiments since they result in realistic dynamic topography and mantle plumes behaviour and characteristics. Further improvement of the quality of forward models of mantle convection requires the development of independent ways of testing the correspondence between numerical models and past geodynamical observations (such as past absolute motions of hotspots, temporal variations of net rotation or true polar wander). However, a balance needs to be found between the race for more complexity of the forward models of mantle convection

and the computational resources and time that such models would require.

Stemming for the work presented in this thesis, there are several axes that can be developed in future research projects:

- **Improving the quality and efficiency of models:** One of the possible improvements to the models developed in Chapter 3 is the effect of the **rheology** of the models on the scales of dynamic topography. In particular, the effect of a viscoelastic lithosphere can be quite important in order to resolve the smallest scales of dynamic topography that can arise from mantle convection. A future collaboration with V. Patocka who implemented the viscoelastic rheology in StagYY (Patocka et al., 2017) will be helpful in order to investigate the small-scale response of lithosphere to small-scale convection in the context of whole-mantle convection with plate-like tectonics. Moreover, the inclusion of **basal thermo-chemical heterogeneities** in the models presented in this thesis is not optimized so far. Indeed, basal thermo-chemical layers are initially defined as a uniform layer of finite thickness, which progressively deforms due to large-scale convective motions. This equilibration stage, which can take up to 200 Myr, requires extra computational time before carrying the model analysis. Future models of mantle convection with basal thermochemical layer could be defined by two discontinuous areas of finite thickness and with shapes corresponding to LLSVPs as seen through seismic tomography in order to decrease the equilibration time.

- **Improving our understanding of the feedbacks between mantle and lithosphere:**

  - A more precise description of **dynamic topography** in specific contexts is envisioned. This comprises a focus on the spatial and temporal scales of mantle-induced vertical deformations at passive margins (where most residual topography constraints are available) and continents. Indeed, although the dynamic topography signal is more difficult to isolate from tectonic and isostatic components on continents, increasing evidence in rather tectonic-inactive settings such as Africa (Guillocheau et al., 2018) and Australia (Müller et al., 2000, Sandiford, 2007, Czarnota et al., 2013, Barnett-Moore et al., 2014, Müller et al., 2016) show the existence of intermediate- to large-scale dynamic topography. Moreover, increasing attention is paid to measuring changes in mantle plume activity, and multiple observations (volcanism, uplift events, rare-gas isotopic signatures, geochemical tracers,

gravity anomalies, crustal thickness, heat flux) suggest the existence of pulses (*e.g.* Poore et al., 2009). The surface expressions of mantle plumes' activity below continental lithosphere are also poorly constrained. Therefore, the quantification in numerical models of the temporal evolution of oceanic and continental regional uplifts generated by fluctuations is mantle plume activity and their link with plume heat and buoyancy flux should help to interpret observations.

– A natural step forward arising from the description of dynamic topography from 3D models of mantle convection with plate-like tectonics is the consideration of **geoid and True Polar Wander**. Indeed, Earth's geoid results from both the presence of density anomalies in the mantle and the gravitational effect of their dynamic motions on the deflection of Earth's surface (self-gravitation). The temporal variations of Earth's degree-2 geoid (called True Polar Wander, which represents Earth's inertia and the relative motions between Earth's lithosphere/mantle and its rotation axis) are recorded in continental rocks as a paleomagnetic signal and provide clues about the temporal evolution of large-scale mantle anomalies and plate tectonic configuration (Greff-Lefftz and Besse, 2014). However, the True Polar Wander signal on Earth is difficult to extract from other sources of paleomagnetic anomalies and the wandering of the rotation axis relatively to Earth's mantle and lithosphere is still far from being completely understood. Therefore, the extraction of the True Polar Wander signal from mantle convection models with a plate-like tectonic history can provide insight on the physical mechanisms and mantle processes triggering such motion. Nevertheless, the development of gravity anomalies is really sensitive to the characteristics of the mantle thermal and thermo-chemical convective instabilities from which it originates. Therefore, such a study requires the prior development of complex models of convection with realistic isostatic and dynamic topography, and mantle density heterogeneities and viscosity structure.

– Another subject gaining more attention is understanding of the **feedbacks between changes of continental configuration and convective planform reorganizations**. Several scenarios of interaction between supercontinent cycles and mantle convection exist. For example, Zhong et al. (2007) suggested that the formation of supercontinents would strongly modify the location of mantle upwelling and downwelling areas by modifying mantle temperature distribution. This would cause large-scale mantle flow reorganizations,

likely to affect Earth's inertia and be paleomagnetically recorded in Earth's True Polar Wander path. The presence of large-scale upwelling beneath supercontinents could cause them to break apart (precise causes are still poorly understood) and lead to changes in the spatial distribution and length of subduction zones and spreading ridges, likely to affect large-scale mantle convection. More generally, supercontinent cycles have been decomposed into three types, depending on the way continents disperse and accrete. Gurnis (1988) proposed the *extroversion* mechanism in which continents accrete on the opposite side of Earth compared to the previous supercontinent. On the contrary, Dewey and Bird (1971), Worsley et al. (1984) proposed the *introversion* scenario, in which continents collide always on the same hemisphere of Earth. In addition to all possible combinations of both scenarios (Murphy and Nance, 2003), Mitchell et al. (2012) proposed *orthoversion* of continents (the new supercontinent forms 90° from the previous one). Depending on those different scenarios, plate boundaries distribution is different and mantle large-scale flow may reorganize differently, leading to different True Polar Wander paths and temporal evolution of LLSVPs spatial distribution in the lowermost mantle. Therefore, fully-dynamic numerical models of mantle convection with plate-like tectonics can help to test the validity of those scenarios, by comparing the timescales of changes in the thermal state of the mantle, the True Polar Wander signal, the location of plumes and LLSVPs, and the possible forces and mechanisms spearheading supercontinental breakup in models with petrological, paleomagnetic, geological and tectonic evidence on Earth.

- **Improving the quality of plate tectonic reconstructions:** Arising from better constraints on the feedbacks between the dynamics of mantle convective instabilities and plate tectonics, one of the ultimate goals is to improve models of past surface motions. A major task for the improvement of plate reconstruction is the definition of an absolute frame of reference for plate past motions. Several references have been defined in the past, based on fixed (Müller et al., 1993) or moving hotspots (Doubrovine et al., 2012), on the correspondance between LIPs and LLSVPs (Torsvik et al., 2008c) or on the fixity of LLSVPs through time (Torsvik et al., 2014), with (*e.g.* Becker et al., 2015) or without net rotation (Gripp and Gordon, 2002), or even correcting for True Polar Wander (Steinberger and Torsvik, 2008). Better physical constraints on True Polar Wander obtained from numerical models of mantle convection with plate-like tectonics can contribute

to improve the interpretation of paleomagnetism and refine plate reconstructions. Moreover, the quantification of hotspot motions, the understanding of their interactions with all scales of mantle convection and plate tectonics and the apprehension of the amount of net rotation and its possible variations through time would constrain plate reconstructions uncertainties and guide future global tectonic models.

Finally, this thesis underlines the importance and needs of forming bridges across various geoscience disciplines, in order to build closer links between sedimentology, paleomagnetism, petrology, geochemistry, gravimetry, seismology and geodynamical modeling. Indeed, fully-dynamic models of mantle convection with plate-like tectonics are an important tool to test the geodynamical behaviour of mantle convective instabilities against observation-based hypotheses of their effect on the surface of Earth.

Bibliography

Acton, G.D., Gordon, R.G., 1994. Paleomagnetic tests of pacific plate reconstructions and implications for motion between hotspots. Science 263, 1246–1254.

Airy, G., 1955. On the computation of the effect of the attraction of mountain-masses, as distributing the apparent astronomical latitude of stations in geodetic surveys. Philosophical Transactions of the Royal Society of London A: Mathematical, Physical and Engineering Sciences 145.

Al-Hajri, Y., White, N., Fishwick, S., 2009. Scales of transient convective support beneath africa. Geology 37, 883–886.

Albers, M., Christensen, U.R., 2001. Channeling of plume flow beneath mid-ocean ridges. Earth and Planetary Science Letters 187, 207–220.

Alboussière, T., Ricard, Y., 2017. Rayleigh–bénard stability and the validity of quasi-boussinesq or quasi-anelastic liquid approximations. Journal of Fluid Mechanics 817, 264–305.

Allmann, B.P., Shearer, P.M., 2009. Global variations of stress drop for moderate to large earthquakes. Journal of Geophysical Research: Solid Earth 114. doi:10.1029/2008JB005821.

Amante, C., Eakins, B.W., 2009. ETOPO1 1 arc-minute global relief model: procedures, data sources and analysis. US Department of Commerce, National Oceanic and Atmospheric Administration, National Environmental Satellite, Data, and Information Service, National Geophysical Data Center, Marine Geology and Geophysics Division Colorado. doi:10.1594/PANGAEA.769615.

Anderson, D., 2013. The persistent mantle plume myth. Australian Journal of Earth Sciences 60, 657–673.

Anderson, D.L., 1982. Hotspots, polar wander, mesozoic convection and the geoid. Nature 297, 391.

Anderson, D.L., 2001. Top-down tectonics? Science 293, 2016–2018.

Anonymous, Edo era - 1855. Shin Yoshiwara ōnamazu yurai - The cause of the great catfish at Shin Yoshiwara. Tokyo University Library.

Armitage, J.J., Collier, J.S., Minshull, T.A., 2010. The importance of rift history for volcanic margin formation. Nature 465, 913.

Arnould, M., Coltice, N., Flament, N., Seigneur, V., Muller, R.D., 2018. On the scales of dynamic topography in whole-mantle convection models. Geochemistry, Geophysics, Geosystems 19, 3140–3163.

Austermann, J., Kaye, B.T., Mitrovica, J.X., Huybers, P., 2014. A statistical analysis of the correlation between large igneous provinces and lower mantle seismic structure. Geophysical Journal International 197, 1–9.

Badro, J., Rueff, J.P., Vankó, G., Monaco, G., Fiquet, G., Guyot, F., 2004. Electronic transitions in perovskite: Possible nonconvecting layers in the lower mantle. Science 305, 383–386.

Bai, W., Vigny, C., Ricard, Y., Froidevaux, C., 1992. On the origin of deviatoric stresses in the lithosphere. Journal of Geophysical Research: Solid Earth 97, 11729–11737.

Ballmer, M., Van Hunen, J., Ito, G., Bianco, T., Tackley, P., 2009. Intraplate volcanism with complex age-distance patterns: A case for small-scale sublithospheric convection. Geochemistry, Geophysics, Geosystems 10.

Ballmer, M., Van Hunen, J., Ito, G., Tackley, P., Bianco, T., 2007. Non-hotspot volcano chains originating from small-scale sublithospheric convection. Geophysical Research Letters 34.

Ballmer, M.D., Ito, G., Van Hunen, J., Tackley, P.J., 2011. Spatial and temporal variability in hawaiian hotspot volcanism induced by small-scale convection. Nature Geoscience 4, 457.

Ballmer, M.D., Schmerr, N.C., Nakagawa, T., Ritsema, J., 2015. Compositional mantle layering revealed by slab stagnation at˜ 1000-km depth. Science advances 1, e1500815.

Barnett-Moore, N., Flament, N., Heine, C., Butterworth, N., Müller, R.D., 2014. Cenozoic uplift of south western australia as constrained by river profiles. Tectonophysics 622, 186–197.

Batchelor, G., . An introduction to fluid dynamics (cambridge up, cambridge, 1967). Google Scholar , 511–517.

Becker, T., Schaeffer, A., Lebedev, S., Conrad, C., 2015. Toward a generalized plate motion reference frame. Geophysical Research Letters 42, 3188–3196.

Becker, T.W., Boschi, L., 2002. A comparison of tomographic and geodynamic mantle models. Geochemistry, Geophysics, Geosystems 3.

Becker, T.W., Conrad, C.P., Buffett, B., Müller, R.D., 2009. Past and present seafloor age distributions and the temporal evolution of plate tectonic heat transport. Earth and Planetary Science Letters 278, 233–242.

Becker, T.W., Faccenna, C., 2011. Mantle conveyor beneath the tethyan collisional belt. Earth and Planetary Science Letters 310, 453–461.

Bello, L., 2015. Prediction des structures convectives terrestres. Ph.D. thesis. Unversity of Lyon.

Bello, L., Coltice, N., Rolf, T., Tackley, P.J., 2014. On the predictability limit of convection models of the earth's mantle. Geochemistry, Geophysics, Geosystems 15, 2319–2328.

Bello, L., Coltice, N., Tackley, P.J., Müller, R.D., Cannon, J., 2015. Assessing the role of slab rheology in coupled plate-mantle convection models. Earth and Planetary Science Letters 430, 191–201.

Bénard, H., 1900. Les tourbillons cellulaires dans une nappe liquide. Revue générale des Sciences Pures et Appliquées 11.

Bénard, H., 1901. Les tourbillons cellulaires dans une nappe liquide transportant la chaleur par convection en régime permanent. Annales de Chimie et de Physique .

Bercovici, D., 1993. A simple model of plate generation from mantle flow. Geophysical Journal International 114, 635–650.

Bercovici, D., 2003. The generation of plate tectonics from mantle convection. Earth and Planetary Science Letters 205, 107–121.

Bercovici, D., Ricard, Y., 2014. Plate tectonics, damage and inheritance. Nature 508, 513.

Bernard, P., 2003. Qu'est-ce qui fait trembler la Terre ? À l'origine des catastrophes sismiques. Belin.

Bertrand, M., 1900. Excursion nb xx. Livret-guide du 8e congrès géologique international , 7–44.

Besse, J., Courtillot, V., 2002. Apparent and true polar wander and the geometry of the geomagnetic field over the last 200 myr. Journal of Geophysical Research: Solid Earth 107.

Billen, M.I., Gurnis, M., 2001. A low viscosity wedge in subduction zones. Earth and Planetary Science Letters 193, 227–236.

Billen, M.I., Hirth, G., 2005. Newtonian versus non-newtonian upper mantle viscosity: Implications for subduction initiation. Geophysical Research Letters 32.

Bird, P., 2003. An updated digital model of plate boundaries. Geochemistry, Geophysics, Geosystems 4.

Bocher, M., Coltice, N., Fournier, A., Tackley, P.J., 2015. A sequential data assimilation approach for the joint reconstruction of mantle convection and surface tectonics. Geophysical Journal International 204, 200–214.

Bocher, M., Fournier, A., Coltice, N., 2018. Ensemble kalman filter for the reconstruction of the earth's mantle circulation. Nonlinear Processes in Geophysics 25, 99.

Boehler, R., 2000. High-pressure experiments and the phase diagram of lower mantle and core materials. Reviews of Geophysics 38, 221–245.

Boioli, F., Carrez, P., Cordier, P., Devincre, B., Gouriet, K., Hirel, P., Kraych, A., Ritterbex, S., 2017. Pure climb creep mechanism drives flow in earth's lower mantle. Science advances 3, e1601958.

Boioli, F., Carrez, P., Cordier, P., Devincre, B., Marquille, M., 2015. Modeling the creep properties of olivine by 2.5-dimensional dislocation dynamics simulations. Physical Review B 92, 014115.

Boschi, L., Becker, T., Steinberger, B., 2007. Mantle plumes: dynamic models and seismic images. Geochemistry, Geophysics, Geosystems 8.

Boschi, L., Faccenna, C., Becker, T., 2010. Mantle structure and dynamic topography in the mediterranean basin. Geophysical Research Letters 37.

Boussinesq, J., 1901. Théorie analytique de la chaleur mise en harmonie avec la thermodynamique et avec la théorie mécanique de la lumière. Gauthier-Villars.

Bower, D.J., Gurnis, M., Flament, N., 2015. Assimilating lithosphere and slab history in 4-d earth models. Physics of the Earth and Planetary Interiors 238, 8–22.

Bowie, W., 1927. The part played by isostasy in geophysics and geology. Journal of the Washington Academy of Sciences 17, 101–117.

Brace, W., Kohlstedt, D., 1980. Limits on lithospheric stress imposed by laboratory experiments. Journal of Geophysical Research: Solid Earth 85, 6248–6252. doi:10.1029/JB085iB11p06248.

Brandt, A., 1982. Guide to multigrid development, in: Multigrid methods. Springer, pp. 220–312.

Braun, J., 2010. The many surface expressions of mantle dynamics. Nature Geoscience 3, 825.

Braun, J., Thieulot, C., Fullsack, P., DeKool, M., Beaumont, C., Huismans, R., 2008. Douar: A new three-dimensional creeping flow numerical model for the solution of geological problems. Physics of the Earth and Planetary Interiors 171, 76–91.

Buffett, B.A., 2003. The thermal state of earth's core. Science 299, 1675–1677.

Bullen, K., 1956. Seismology and the broad structure of the earth's interior. Physics and Chemistry of the Earth 1, 68–93.

Bunge, H.P., 2005. Low plume excess temperature and high core heat flux inferred from non-adiabatic geotherms in internally heated mantle circulation models. Physics of the Earth and Planetary Interiors 153, 3–10.

Bunge, H.P., Ricard, Y., Matas, J., 2001. Non-adiabaticity in mantle convection. Geophysical research letters 28, 879–882.

Bunge, H.P., Richards, M., Baumgardner, J., 2002. Mantle–circulation models with sequential data assimilation: inferring present–day mantle structure from plate–motion histories. Philosophical Transactions of the Royal Society of London A: Mathematical, Physical and Engineering Sciences 360, 2545–2567.

Bunge, H.P., Richards, M.A., 1996. The origin of large scale structure in mantle convection: effects of plate motions and viscosity stratification. Geophysical Research Letters 23, 2987–2990.

Bunge, H.P., Richards, M.A., Baumgardner, J.R., 1997. A sensitivity study of three-dimensional spherical mantle convection at 108 rayleigh number: Effects of depth-dependent viscosity, heating mode, and an endothermic phase change. Journal of Geophysical Research: Solid Earth 102, 11991–12007.

Burke, K., 2001. Origin of the cameroon line of volcano-capped swells. The Journal of Geology 109, 349–362.

Burke, K., Kidd, W., Wilson, J.T., 1973. Relative and latitudinal motion of atlantic hot spots. Nature 245, 133.

Burke, K., Steinberger, B., Torsvik, T.H., Smethurst, M.A., 2008. Plume generation zones at the margins of large low shear velocity provinces on the core–mantle boundary. Earth and Planetary Science Letters 265, 49–60.

Burov, E., 2007. Plate rheology and mechanics. In Treatise of Geophysics. Crust and Lithospere Dynamics/Schubert G.(Ed.) .

Burov, E., 2010. The equivalent elastic thickness (te), seismicity and the long-term rheology of continental lithosphere: Time to burn-out "crème brûlée"?: Insights from large-scale geodynamic modeling. Tectonophysics 484, 4–26.

Burov, E., Diament, M., 1996. Isostasy, equivalent elastic thickness, and inelastic rheology of continents and oceans. Geology 24, 419–422.

Burov, E., Watts, A., et al., 2006. The long-term strength of continental lithosphere:" jelly sandwich" or" crème brûlée"? GSA today 16, 4.

Burov, E.B., 2011. Rheology and strength of the lithosphere. Marine and Petroleum Geology 28, 1402–1443.

Burov, E.B., Diament, M., 1995. The effective elastic thickness (t e) of continental lithosphere: what does it really mean? Journal of Geophysical Research: Solid Earth 100, 3905–3927.

Butterworth, N., Talsma, A., Müller, R., Seton, M., Bunge, H.P., Schuberth, B., Shephard, G., Heine, C., 2014. Geological, tomographic, kinematic and geodynamic constraints on the dynamics of sinking slabs. Journal of Geodynamics 73, 1–13.

Butterworth, S., 1930. On the theory of filter amplifiers. Wireless Engineer 7, 536–541.

Byerlee, J., 1978. Friction of rocks, in: Rock friction and earthquake prediction. Springer, pp. 615–626.

Cadek, O., Fleitout, L., 2003. Effect of lateral viscosity variations in the top 300 km on the geoid and dynamic topography. Geophysical Journal International 152, 566–580.

Campbell, I., 2001. Identification of ancient mantle plumes. Geological Society of America Inc. .

Campbell, I.H., Griffiths, R.W., 1990. Implications of mantle plume structure for the evolution of flood basalts. Earth and Planetary Science Letters 99, 79–93.

Canales, J.P., Ito, G., Detrick, R.S., Sinton, J., 2002. Crustal thickness along the western galápagos spreading center and the compensation of the galápagos hotspot swell. Earth and Planetary Science Letters 203, 311–327.

Cande, S.C., Raymond, C.A., Stock, J., Haxby, W.F., 1995. Geophysics of the pitman fracture zone and pacific-antarctic plate motions during the cenozoic. Science 270, 947–953.

Cande, S.C., Stegman, D.R., 2011. Indian and african plate motions driven by the push force of the reunion plume head. Nature 475, 47.

Cannat, M., Briais, A., Deplus, C., Escartin, J., Georgen, J., Lin, J., Mercouriev, S., Meyzen, C., Muller, M., Pouliquen, G., et al., 1999. Mid-atlantic ridge–azores hotspot interactions: along-axis migration of a hotspot-derived event of enhanced magmatism 10 to 4 ma ago. Earth and Planetary Science Letters 173, 257–269.

Cazenave, A., Dominh, K., Rabinowicz, M., Ceuleneer, G., 1988. Geoid and depth anomalies over ocean swells and troughs: evidence of an increasing trend of the geoid to depth ratio with age of plate. Journal of Geophysical Research: Solid Earth 93, 8064–8077.

Cazenave, A., Souriau, A., Dominh, K., 1989. Global coupling of earth surface topography with hotspots, geoid and mantle heterogeneities. Nature 340, 54.

Chopelas, A., Boehler, R., 1992. Thermal expansivity in the lower mantle. Geophysical Research Letters 19, 1983–1986. doi:10.1029/92GL02144.

Christensen, U., 1984a. Convection with pressure-and temperature-dependent non-newtonian rheology. Geophysical Journal International 77, 343–384.

Christensen, U., 1984b. Instability of a hot boundary layer and initiation of thermo-chemical plumes, in: Annales Geophysicae, pp. 311–319.

Christensen, U.R., 1984c. Heat transport by variable viscosity convection and implications for the earth's thermal evolution. Physics of the Earth and planetary interiors 35, 264–282.

Christensen, U.R., Hofmann, A.W., 1994. Segregation of subducted oceanic crust in the convecting mantle. Journal of Geophysical Research: Solid Earth 99, 19867–19884.

Christensen, U.R., Yuen, D.A., 1985. Layered convection induced by phase transitions. Journal of Geophysical Research: Solid Earth 90, 10291–10300.

Clouard, V., Bonneville, A., 2001. How many pacific hotspots are fed by deep-mantle plumes? Geology 29, 695–698.

Coffin, M.F., Pringle, M., Duncan, R., Gladczenko, T., Storey, M., Müller, R., Gahagan, L., 2002. Kerguelen hotspot magma output since 130 ma. Journal of Petrology 43, 1121–1137.

Cogné, J.P., Humler, E., 2004. Temporal variation of oceanic spreading and crustal production rates during the last 180 my. Earth and Planetary Science Letters 227, 427–439.

Colli, L., Ghelichkhan, S., Bunge, H.P., 2016. On the ratio of dynamic topography and gravity anomalies in a dynamic earth. Geophysical Research Letters 43, 2510–2516.

Coltice, N., Gérault, M., Ulvrová, M., 2017a. A mantle convection perspective on global tectonics. Earth-Science Reviews 165, 120–150. doi:10.1016/j.earscirev.2016.11.006.

Coltice, N., Larrouturou, G., Debayle, E., Garnero, E.J., 2017b. Interactions of scales of convection in the earth's mantle. Tectonophysics 746, 669–677.

Coltice, N., Phillips, B., Bertrand, H., Ricard, Y., Rey, P., 2007. Global warming of the mantle at the origin of flood basalts over supercontinents. Geology 35, 391–394.

Coltice, N., Ricard, Y., 1999. Geochemical observations and one layer mantle convection. Earth and Planetary Science Letters 174, 125–137.

Coltice, N., Rolf, T., Tackley, P., Labrosse, S., 2012. Dynamic causes of the relation between area and age of the ocean floor. Science 336, 335–338.

Coltice, N., Seton, M., Rolf, T., Müller, R., Tackley, P.J., 2013. Convergence of tectonic reconstructions and mantle convection models for significant fluctuations in seafloor spreading. Earth and Planetary Science Letters 383, 92–100. doi:10.1016/j.epsl.2013.09.032.

Coltice, N., Shephard, G.E., 2018. Tectonic predictions with mantle convection models. Geophysical Journal International 213, 16–29.

Conder, J.A., Scheirer, D.S., Forsyth, D.W., 2000. Seafloor spreading on the amsterdam-st. paul hotspot plateau. Journal of Geophysical Research: Solid Earth 105, 8263–8277.

Conrad, C.P., Behn, M.D., 2010. Constraints on lithosphere net rotation and asthenospheric viscosity from global mantle flow models and seismic anisotropy. Geochemistry, Geophysics, Geosystems 11.

Conrad, C.P., Bianco, T.A., Smith, E.I., Wessel, P., 2011. Patterns of intraplate volcanism controlled by asthenospheric shear. Nature Geoscience 4, 317.

Conrad, C.P., Gurnis, M., 2003. Seismic tomography, surface uplift, and the breakup of gondwanaland: Integrating mantle convection backwards in time. Geochemistry, Geophysics, Geosystems 4.

Conrad, C.P., Husson, L., 2009. Influence of dynamic topography on sea level and its rate of change. Lithosphere 1, 110–120. doi:10.1130/L32.1.

Conrad, C.P., Lithgow-Bertelloni, C., 2002. How mantle slabs drive plate tectonics. Science 298, 207–209.

Conrad, C.P., Lithgow-Bertelloni, C., 2004. The temporal evolution of plate driving forces: Importance of "slab suction" versus "slab pull" during the cenozoic. Journal of Geophysical Research: Solid Earth 109.

Conrad, C.P., Lithgow-Bertelloni, C., 2006. Influence of continental roots and asthenosphere on plate-mantle coupling. Geophysical Research Letters 33.

Conrad, C.P., Steinberger, B., Torsvik, T.H., 2013. Stability of active mantle upwelling revealed by net characteristics of plate tectonics. Nature 498, 479.

Corti, G., van Wijk, J., Cloetingh, S., Morley, C.K., 2007. Tectonic inheritance and continental rift architecture: Numerical and analogue models of the east african rift system. Tectonics 26.

Cottrell, E., Kelley, K.A., 2013. Redox heterogeneity in mid-ocean ridge basalts as a function of mantle source. Science , 1233299.

Courtillot, V., Davaille, A., Besse, J., Stock, J., 2003. Three distinct types of hotspots in the earth's mantle. Earth and Planetary Science Letters 205, 295–308.

Courtillot, V., Jaupart, C., Manighetti, I., Tapponnier, P., Besse, J., 1999. On causal links between flood basalts and continental breakup. Earth and Planetary Science Letters 166, 177–195.

Courtillot, V.E., Renne, P.R., 2003. On the ages of flood basalt events. Comptes Rendus Geoscience 335, 113–140.

Crameri, F., Lithgow-Bertelloni, C., Tackley, P., 2017. The dynamical control of subduction parameters on surface topography. Geochemistry, Geophysics, Geosystems .

Crameri, F., Schmeling, H., Golabek, G., Duretz, T., Orendt, R., Buiter, S., May, D., Kaus, B., Gerya, T., Tackley, P., 2012a. A comparison of numerical surface topography calculations in geodynamic modelling: an evaluation of the 'sticky air' method. Geophysical Journal International 189, 38–54. doi:10.1111/j.1365-246X.2012.05388.x.

Crameri, F., Tackley, P., Meilick, I., Gerya, T., Kaus, B., 2012b. A free plate surface and weak oceanic crust produce single-sided subduction on earth. Geophysical Research Letters 39. doi:10.1029/2011GL050046.

Crameri, F., Tackley, P.J., 2014. Spontaneous development of arcuate single-sided subduction in global 3-d mantle convection models with a free surface. Journal of Geophysical Research: Solid Earth 119, 5921–5942.

Crosby, A., McKenzie, D., 2009. An analysis of young ocean depth, gravity and global residual topography. Geophysical Journal International 178, 1198–1219.

Crough, S.T., 1978. Thermal origin of mid-plate hot-spot swells. Geophysical Journal International 55, 451–469.

Crough, S.T., 1983. Hotspot swells. Annual Review of Earth and Planetary Sciences 11, 165–193.

Czarnota, K., Hoggard, M., White, N., Winterbourne, J., 2013. Spatial and temporal patterns of cenozoic dynamic topography around australia. Geochemistry, Geophysics, Geosystems 14, 634–658.

Dal Zilio, L., Faccenda, M., Capitanio, F., 2017. The role of deep subduction in supercontinent breakup. Tectonophysics .

Dalton, C.A., Langmuir, C.H., Gale, A., 2014. Geophysical and geochemical evidence for deep temperature variations beneath mid-ocean ridges. Science 344, 80–83.

Davaille, A., 1999. Simultaneous generation of hotspots and superswells by convection in a heterogeneous planetary mantle. Nature 402, 756.

Davaille, A., Carrez, P., Cordier, P., 2018. Fat plumes may reflect the complex rheology of the lower mantle. Geophysical Research Letters 45, 1349–1354.

Davaille, A., Girard, F., Le Bars, M., 2002. How to anchor hotspots in a convecting mantle? Earth and Planetary Science Letters 203, 621–634.

Davaille, A., Jaupart, C., 1993. Transient high-rayleigh-number thermal convection with large viscosity variations. Journal of Fluid Mechanics 253, 141–166.

Davaille, A., Le Bars, M., Carbonne, C., 2003. Thermal convection in a heterogeneous mantle. Comptes Rendus Geoscience 335, 141–156. doi:10.1016/S1631-0713(03)00003-8.

Davaille, A., Smrekar, S., Tomlinson, S., 2017. Experimental and observational evidence for plume-induced subduction on venus. Nature Geoscience 10, 349.

Davaille, A., Vatteville, J., 2005. On the transient nature of mantle plumes. Geophysical Research Letters 32.

Davies, D.R., Davies, J.H., 2009. Thermally-driven mantle plumes reconcile multiple hot-spot observations. Earth and Planetary Science Letters 278, 50–54.

Davies, D.R., Goes, S., Davies, J., Schuberth, B., Bunge, H.P., Ritsema, J., 2012. Reconciling dynamic and seismic models of earth's lower mantle: The dominant role of thermal heterogeneity. Earth and Planetary Science Letters 353, 253–269.

Davies, D.R., Rawlinson, N., 2014. On the origin of recent intraplate volcanism in australia. Geology 42, 1031–1034.

Davies, G.F., 1981. Regional compensation of subducted lithosphere: effects on geoid, gravity and topography from a preliminary model. Earth and Planetary Science Letters 54, 431–441.

Davies, G.F., 1988a. Ocean bathymetry and mantle convection: 1. large-scale flow and hotspots. Journal of Geophysical Research: Solid Earth 93, 10467–10480.

Davies, G.F., 1988b. Ocean bathymetry and mantle convection: 2. small-scale flow. Journal od geophysical research 93.

Davies, G.F., 2001. Dynamic earth: plates, plumes and mantle convection.

Davies, G.F., 2007. Mantle regulation of core cooling: A geodynamo without core radioactivity? Physics of the Earth and Planetary Interiors 160, 215–229.

Davies, G.F., Pribac, F., 1993. Mesozoic seafloor subsidence and the darwin rise, past and present. The Mesozoic Pacific: Geology, Tectonics, and Volcanism , 39–52.

Davies, J.H., Davies, D.R., 2010. Earth's surface heat flux. Solid Earth 1, 5.

Debayle, E., Dubuffet, F., Durand, S., 2016. An automatically updated s-wave model of the upper mantle and the depth extent of azimuthal anisotropy. Geophysical Research Letters 43, 674–682.

Deschamps, F., Tackley, P.J., 2008. Searching for models of thermo-chemical convection that explain probabilistic tomography: I. principles and influence of rheological parameters. Physics of the Earth and Planetary Interiors 171, 357–373.

Deschamps, F., Tackley, P.J., 2009. Searching for models of thermo-chemical convection that explain probabilistic tomography. ii—influence of physical and compositional parameters. Physics of the Earth and Planetary Interiors 176, 1–18. doi:10.1016/j.pepi.2009.03.012.

Detrick, R.S., Crough, S.T., 1978. Island subsidence, hot spots, and lithospheric thinning. Journal of Geophysical Research: Solid Earth 83, 1236–1244.

Dewey, J., Bird, J., 1970. Mountain belts and the new global tectonics. Journal of Geophysical research 75, 2625–2647.

Dewey, J.F., Bird, J.M., 1971. Origin and emplacement of the ophiolite suite: Appalachian ophiolites in newfoundland. Journal of Geophysical Research 76, 3179–3206.

DiVenere, V., Kent, D.V., 1999. Are the pacific and indo–atlantic hotspots fixed? testing the plate circuit through antarctica. Earth and Planetary Science Letters 170, 105–117.

Doin, M.P., Henry, P., 2001. Subduction initiation and continental crust recycling: the roles of rheology and eclogitization. Tectonophysics 342, 163–191.

Dosso, L., Bougault, H., Langmuir, C., Bollinger, C., Bonnier, O., Etoubleau, J., 1999. The age and distribution of mantle heterogeneity along the mid-atlantic ridge (31–41 n). Earth and Planetary Science Letters 170, 269–286.

Doubrovine, P.V., Steinberger, B., Torsvik, T.H., 2012. Absolute plate motions in a reference frame defined by moving hot spots in the pacific, atlantic, and indian oceans. Journal of Geophysical Research: Solid Earth 117.

Dubuffet, F., Yuen, D.A., Yanagawa, T., 2000. Feedback effects of variable thermal conductivity on the cold downwellings in high rayleigh number convection. Geophysical Research Letters 27, 2981–2984.

Duncan, R., 1981. Hotspots in the southern oceans—an absolute frame of reference for motion of the gondwana continents. Tectonophysics 74, 29–42.

Dyment, J., 1998. Evolution of the carlsberg ridge between 60 and 45 ma: Ridge propagation, spreading asymmetry, and the deccan-reunion hotspot. Journal of Geophysical Research: Solid Earth 103, 24067–24084.

Dymkova, D., Gerya, T., 2013. Porous fluid flow enables oceanic subduction initiation on earth. Geophysical Research Letters 40, 5671–5676.

Elder, J.W., 1967. Steady free convection in a porous medium heated from below. Journal of Fluid Mechanics 27, 29–48.

Elsasser, W.M., 1969. Convection and stress propagation in the upper mantle., in: Runcorn, S. (Ed.), The Application of Modern Physics to the Earth and Planetary Interiors, pp. 223–246.

Farley, K., Neroda, E., 1998. Noble gases in the earth's mantle. Annual Review of Earth and Planetary Sciences 26, 189–218.

Farnetani, C., 1997. Excess temperature of mantle plumes: the role of chemical stratification across d". Geophysical Research Letters 24, 1583–1586.

Farnetani, C., Samuel, H., 2005. Beyond the thermal plume paradigm. Geophysical Research Letters 32.

Farnetani, C.G., Hofmann, A.W., 2011. Mantle plumes, in: Encyclopedia of Solid Earth Geophysics. Springer, pp. 857–869.

Fitton, J.G., Godard, M., 2004. Origin and evolution of magmas on the ontong java plateau. Geological Society, London, Special Publications 229, 151–178.

Flament, N., Gurnis, M., Müller, R.D., 2013. A review of observations and models of dynamic topography. Lithosphere 5, 189–210. doi:10.1130/L245.1.

Flament, N., Gurnis, M., Williams, S., Seton, M., Skogseid, J., Heine, C., Müller, R.D., 2014. Topographic asymmetry of the south atlantic from global models of mantle flow and lithospheric stretching. Earth and Planetary Science Letters 387, 107–119.

Flament, N., Williams, S., Müller, R., Gurnis, M., Bower, D.J., 2017. Origin and evolution of the deep thermochemical structure beneath eurasia. Nature communications 8, 14164.

Foley, B.J., Becker, T.W., 2009. Generation of plate-like behavior and mantle heterogeneity from a spherical, viscoplastic convection model. Geochemistry, Geophysics, Geosystems 10.

Forsyth, D., Uyeda, S., 1975. On the relative importance of the driving forces of plate motion. Geophysical Journal of the Royal Astronomical Society 43, 163–200.

Forsyth, D.W., Harmon, N., Scheirer, D.S., Duncan, R.A., 2006. Distribution of recent volcanism and the morphology of seamounts and ridges in the glimpse study area: Implications for the lithospheric cracking

hypothesis for the origin of intraplate, non–hot spot volcanic chains. Journal of Geophysical Research: Solid Earth 111.

Forte, A., Peltier, W., Dziewonski, A., Woodward, R., 1993. Dynamic surface topography: A new interpretation based upon mantle flow models derived from seismic tomography. Geophysical Research Letters 20, 225–228.

Foulger, G., Natland, J., 2003. Is "hotspot" volcanism a consequence of plate tectonics? Science 300, 921–922.

French, S.W., Romanowicz, B., 2015. Broad plumes rooted at the base of the earth's mantle beneath major hotspots. Nature 525, 95.

Fromm, T., Planert, L., Jokat, W., Ryberg, T., Behrmann, J.H., Weber, M.H., Haberland, C., 2015. South atlantic opening: A plume-induced breakup? Geology 43, 931–934.

Frost, D.A., Rost, S., 2014. The p-wave boundary of the large-low shear velocity province beneath the pacific. Earth and Planetary Science Letters 403, 380–392.

Fullsack, P., 1995. An arbitrary lagrangian-eulerian formulation for creeping flows and its application in tectonic models. Geophysical Journal International 120, 1–23.

Funiciello, F., Faccenna, C., Heuret, A., Lallemand, S., Di Giuseppe, E., Becker, T., 2008. Trench migration, net rotation and slab–mantle coupling. Earth and Planetary Science Letters 271, 233–240.

Gable, C.W., O'connell, R.J., Travis, B.J., 1991. Convection in three dimensions with surface plates: Generation of toroidal flow. Journal of Geophysical Research: Solid Earth 96, 8391–8405.

Gale, A., Dalton, C.A., Langmuir, C.H., Su, Y., Schilling, J.G., 2013. The mean composition of ocean ridge basalts. Geochemistry, Geophysics, Geosystems 14, 489–518.

Ganne, J., Feng, X., 2018. Magmatism: A crustal and geodynamic perspective. Journal of Structural Geology .

Garnero, E.J., McNamara, A.K., Shim, S.H., 2016. Continent-sized anomalous zones with low seismic velocity at the base of earth's mantle. Nature Geoscience doi:10.1038/ngeo2733.

Garnero, E.J., Revenaugh, J., Williams, Q., Lay, T., Kellogg, L.H., 1998. Ultralow velocity zone at the core-mantle boundary. The core-mantle boundary region 28, 319–334.

Gente, P., Dyment, J., Maia, M., Goslin, J., 2003. Interaction between the mid-atlantic ridge and the azores hot spot during the last 85 myr: Emplacement and rifting of the hot spot-derived plateaus. Geochemistry, Geophysics, Geosystems 4.

Geoffroy, L., 2005. Volcanic passive margins. Comptes Rendus Geoscience 337, 1395–1408.

Gérault, M., Husson, L., Miller, M.S., Humphreys, E.D., 2015. Flat-slab subduction, topography, and mantle dynamics in southwestern mexico. Tectonics 34, 1892–1909.

Gerya, T.V., Connolly, J.A., Yuen, D.A., 2008. Why is terrestrial subduction one-sided? Geology 36, 43–46.

Gerya, T.V., Stern, R.J., Baes, M., Sobolev, S.V., Whattam, S.A., 2015. Plate tectonics on the earth triggered by plume-induced subduction initiation. Nature 527, 221.

Gerya, T.V., Yuen, D.A., 2003. Characteristics-based marker-in-cell method with conservative finite-differences schemes for modeling geological flows with strongly variable transport properties. Physics of the Earth and Planetary Interiors 140, 293–318.

Gibson, S., Thompson, R., Day, J., 2006. Timescales and mechanisms of plume–lithosphere interactions: 40 ar/39 ar geochronology and geochemistry of alkaline igneous rocks from the paraná–etendeka large igneous province. Earth and Planetary Science Letters 251, 1–17.

Gillet, P., Daniel, I., Guyot, F., Matas, J., Chervin, J.C., 2000. A thermodynamic model for MgSiO3-perovskite derived from pressure, temperature and volume dependence of the raman mode frequencies. Physics of the Earth and Planetary Interiors 117, 361–384. doi:10.1016/S0031-9201(99)00107-7.

Glatzmaier, G.A., 1988. Numerical simulations of mantle convection: Time-dependent, three-dimensional, compressible, spherical shell. Geophysical & Astrophysical Fluid Dynamics 43, 223–264.

Goes, S., Agrusta, R., Van Hunen, J., Garel, F., 2017. Subduction-transition zone interaction: A review. Geosphere 13, 644–664.

Goetze, C., Evans, B., 1979. Stress and temperature in the bending lithosphere as constrained by experimental rock mechanics. Geophysical Journal International 59, 463–478.

Golle, O., Dumoulin, C., Choblet, G., Cadek, O., 2012. Topography and geoid induced by a convecting mantle beneath an elastic lithosphere. Geophysical Journal International 189, 55–72. doi:10.1111/j.1365-246X.2012.05364.x.

Gomez-Chavez, S., 2001. A catalogue of dykes from aeromagnetic surveys in eastern and southern Africa. International Institute for Aerospace Survey and Earth Sciences.

Gomi, H., Hirose, K., 2015. Electrical resistivity and thermal conductivity of hcp fe–ni alloys under high pressure: Implications for thermal convection in the earth's core. Physics of the Earth and Planetary Interiors 247, 2–10.

Gonnermann, H.M., Jellinek, A.M., Richards, M.A., Manga, M., 2004. Modulation of mantle plumes and heat flow at the core mantle boundary by plate-scale flow: results from laboratory experiments. Earth and Planetary Science Letters 226, 53–67.

Gordon, R.G., 1998. The plate tectonic approximation: Plate nonrigidity, diffuse plate boundaries, and global plate reconstructions. Annual Review of Earth and Planetary Sciences 26, 615–642.

de Gouveia, S.V., Besse, J., de Lamotte, D.F., Greff-Lefftz, M., Lescanne, M., Gueydan, F., Leparmentier, F., 2018. Evidence of hotspot paths below arabia and the horn of africa and consequences on the red sea opening. Earth and Planetary Science Letters 487, 210–220.

Graham, D.W., 2002. Noble gas isotope geochemistry of mid-ocean ridge and ocean island basalts: Characterization of mantle source reservoirs. Reviews in mineralogy and geochemistry 47, 247–317.

Greff-Lefftz, M., Besse, J., 2014. Sensitivity experiments on true polar wander. Geochemistry, Geophysics, Geosystems 15, 4599–4616.

Griggs, D., 1939. A theory of mounain building. American Journal of Science 237.

Gripp, A.E., Gordon, R.G., 2002. Young tracks of hotspots and current plate velocities. Geophysical Journal International 150, 321–361.

Guerri, M., Cammarano, F., Tackley, P.J., 2016. Modelling earth's surface topography: decomposition of the static and dynamic components. Physics of the Earth and Planetary Interiors 261, 172–186.

Guillocheau, F., Simon, B., Baby, G., Bessin, P., Robin, C., Dauteuil, O., 2018. Planation surfaces as a record of mantle dynamics: the case example of africa. Gondwana Research 53, 82–98.

Guillou, L., Jaupart, C., 1995. On the effect of continents on mantle convection. Journal of Geophysical Research: Solid Earth 100, 24217–24238.

Gurnis, M., 1988. Large-scale mantle convection and the aggregation and dispersal of supercontinents. Nature 332, 695.

Gurnis, M., 1990. Bounds on global dynamic topography from phanerozoic flooding of continental platforms. Nature 344, 754.

Gurnis, M., 1993a. Comment on "dynamic surface topography: a new interpretation based upon mantle flow models derived from seismic tomography" by AM Forte, WR Peltier, AM Dziewonski and RL Woodward. Geophysical research letters 20, 1663–1664.

Gurnis, M., 1993b. Phanerozoic marine inundation of continents driven by dynamic topography above subducting slabs. Nature 364, 589–593. doi:10.1038/364589a0.

Gurnis, M., Davies, G.F., 1986. Mixing in numerical models of mantle convection incorporating plate kinematics. Journal of Geophysical Research: Solid Earth 91, 6375–6395.

Gurnis, M., Hall, C., Lavier, L., 2004. Evolving force balance during incipient subduction. Geochemistry, Geophysics, Geosystems 5.

Gvirtzman, Z., Faccenna, C., Becker, T.W., 2016. Isostasy, flexure, and dynamic topography. Tectonophysics 683, 255–271. doi:10.1016/j.tecto.2016.05.041.

Hager, B., Richards, M., 1989. Long-wavelength variations in earth's geoid: physical models and dynamical implications. Philosophical Transactions of the Royal Society of London A: Mathematical, Physical and Engineering Sciences 328, 309–327. doi:10.1098/rsta.1989.0038.

Hager, B.H., 1984. Subducted slabs and the geoid: Constraints on mantle rheology and flow. Journal of Geophysical Research: Solid Earth 89, 6003–6015.

Hager, B.H., Clayton, R.W., Richards, M.A., Comer, R.P., Dziewonski, A.M., 1985. Lower mantle heterogeneity, dynamic topography and the geoid. Nature 313, 541–545. URL: http://dx.doi.org/10.1038/313541a0.

Hager, B.H., O'Connell, R.J., 1979. Kinematic models of large-scale flow in the earth's mantle. Journal of Geophysical Research: Solid Earth 84, 1031–1048.

Hager, B.H., O'Connell, R.J., 1981. A simple global model of plate dynamics and mantle convection. Journal of Geophysical Research: Solid Earth 86, 4843–4867.

Hanan, B.B., Schilling, J.G., 1997. The dynamic evolution of the iceland mantle plume: the lead isotope perspective. Earth and Planetary Science Letters 151, 43–60.

Hansen, U., Yuen, D., Kroening, S., Larsen, T., 1993. Dynamical consequences of depth-dependent thermal expansivity and viscosity on mantle circulations and thermal structure. Physics of the earth and planetary interiors 77, 205–223. doi:10.1016/0031-9201(93)90099-U.

Hardarson, B., Fitton, J., Ellam, R., Pringle, M., 1997. Rift relocation—a geochemical and geochronological investigation of a palaeo-rift in northwest iceland. Earth and Planetary Science Letters 153, 181–196.

Hardman, J.P., Schofield, N., Jolley, D.W., Holford, S.P., Hartley, A.J., Morse, S., Underhill, J.R., Watson, D.A., Zimmer, E.H., 2018. Prolonged dynamic support from the icelandic plume of the ne atlantic margin. Journal of the Geological Society , jgs2017–088.

Hart, S., Schilling, J.G., Powell, J., 1973. Basalts from iceland and along the reykjanes ridge: Sr isotope geochemistry. Nature Physical Science 246, 104.

Hartley, R.A., Roberts, G.G., White, N., Richardson, C., 2011. Transient convective uplift of an ancient buried landscape. Nature Geoscience 4, 562–565. doi:10.1038/NGEO1191.

Haskell, N., 1935. The motion of a viscous fluid under a surface load. Physics 6.

Hassan, R., Flament, N., Gurnis, M., Bower, D.J., Müller, D., 2015. Provenance of plumes in global convection models. Geochemistry, Geophysics, Geosystems 16, 1465–1489.

Hassan, R., Müller, R.D., Gurnis, M., Williams, S.E., Flament, N., 2016. A rapid burst in hotspot motion through the interaction of tectonics and deep mantle flow. Nature 533, 239–242.

Haxby, W.F., Weissel, J.K., 1986. Evidence for small-scale mantle convection from seasat altimeter data. Journal of Geophysical Research: Solid Earth 91, 3507–3520. doi:10.1029/JB091iB03p03507.

He, Y., Wen, L., Zheng, T., 2006. Geographic boundary and shear wave velocity structure of the "pacific anomaly" near the core–mantle boundary beneath western pacific. Earth and Planetary Science Letters 244, 302–314.

Heng, Z., 132. Replica of the Houfeng Didong Yi - instrument for measuring the seasonal winds and the movements of the Earth. Exhibition Hall, Museum of Chinese History, Beijing.

Hernlund, J.W., Tackley, P.J., 2008. Modeling mantle convection in the spherical annulus. Physics of the Earth and Planetary Interiors 171, 48–54. doi:10.1098/rsta.1989.0038.

Hernlund, J.W., Thomas, C., Tackley, P.J., 2005. A doubling of the post-perovskite phase boundary and structure of the earth's lowermost mantle. Nature 434, 882.

Herzberg, C., 2004. Partial crystallization of mid-ocean ridge basalts in the crust and mantle. Journal of Petrology 45, 2389–2405.

Herzberg, C., Asimow, P., 2015. PRIMELT3 MEGA.XLSM software for primary magma calculation: peridotite primary magma mgo contents from the liquidus to the solidus. Geochemistry, Geophysics, Geosystems 16, 563–578.

Herzberg, C., Asimow, P.D., 2008. Petrology of some oceanic island basalts: Primelt2. xls software for primary magma calculation. Geochemistry, Geophysics, Geosystems 9.

Herzberg, C., Asimow, P.D., Arndt, N., Niu, Y., Lesher, C., Fitton, J., Cheadle, M., Saunders, A., 2007. Temperatures in ambient mantle and plumes: Constraints from basalts, picrites, and komatiites. Geochemistry, Geophysics, Geosystems 8.

Herzberg, C., Condie, K., Korenaga, J., 2010. Thermal history of the earth and its petrological expression. Earth and Planetary Science Letters 292, 79–88.

Herzberg, C., Gazel, E., 2009. Petrological evidence for secular cooling in mantle plumes. Nature 458, 619.

Hess, H.H., 1946. Drowned ancient islands of the pacific basin. Eos Trans. AGU .

Hess, H.H., 1962. History of ocean basins. Petroligic studies: a volume in honnor to A. E. Buddington, The Geological Society of America .

Hey, R., 1977. A new class of "pseudofaults" and their bearing on plate tectonics: A propagating rift model. Earth and Planetary Science Letters 37, 321–325.

Heyn, B.H., Conrad, C.P., Trønnes, R.G., 2018. Stabilizing effect of compositional viscosity contrasts on thermochemical piles. Geophysical Research Letters 45, 7523–7532.

Van der Hilst, R., Widiyantoro, S., Engdahl, E., 1997. Evidence for deep mantle circulation from global tomography. Nature 386, 578.

Hilton, D., Barling, J., Wheller, G., 1995. Effect of shallow-level contamination on the helium isotope systematics of ocean-island lavas. Nature 373, 330.

Hirth, G., Kohlstedt, D., 2003. Rheology of the upper mantle and the mantle wedge: A view from the experimentalists. Inside the subduction Factory , 83–105.

Hofmeister, A., 1999. Mantle values of thermal conductivity and the geotherm from phonon lifetimes. Science 283, 1699–1706.

Hoggard, M., White, N., Al-Attar, D., 2016. Global dynamic topography observations reveal limited influence of large-scale mantle flow. Nature Geoscience doi:10.1038/NGEO2709.

Hoggard, M.J., Winterbourne, J., Czarnota, K., White, N., 2017. Oceanic residual depth measurements, the plate cooling model, and global dynamic topography. Journal of Geophysical Research: Solid Earth 122, 2328–2372. doi:10.1002/2016JB013457.

Höink, T., Lenardic, A., 2010. Long wavelength convection, poiseuille–couette flow in the low-viscosity asthenosphere and the strength of plate margins. Geophysical Journal International 180, 23–33.

Holmes, A., 1931. Xviii. radioactivity and earth movements. Transactions of the Geological Society of Glasgow 18, 559–606.

Honda, S., Yuen, D., Balachandar, S., Reuteler, D., 1993. Three-dimensional instabilities of mantle convection with multiple phase transitions. Science 259, 1308–1311.

Houseman, G., 1990. The thermal structure of mantle plumes: axisymmetric or triple-junction? Geophysical Journal International 102, 15–24.

Howard, L.N., 1966. Convection at high rayleigh number, in: Applied Mechanics. Springer, pp. 1109–1115.

Huang, J., Zhong, S., van Hunen, J., 2003. Controls on sublithospheric small-scale convection. Journal of Geophysical Research: Solid Earth 108.

Husson, L., 2006. Dynamic topography above retreating subduction zones. Geology 34, 741–744.

Husson, L., Bernet, M., Guillot, S., Huyghe, P., Mugnier, J.L., Replumaz, A., Robert, X., Van der Beek, P., 2014. Dynamic ups and downs of the himalaya. Geology 42, 839–842.

Husson, L., Guillaume, B., Funiciello, F., Faccenna, C., Royden, L.H., 2012. Unraveling topography around subduction zones from laboratory models. Tectonophysics 526, 5–15. doi:10.1016/j.tecto.2011.09.001.

Isacks, B., Oliver, J., Sykes, L., 1968. Seismology and the new global tectonics. Journal of Geophysical research 73.

Ita, J., King, S.D., 1994. Sensitivity of convection with an endothermic phase change to the form of governing equations, initial conditions, boundary conditions, and equation of state. Journal of Geophysical Research: Solid Earth 99, 15919–15938.

Ito, G., 2001. Reykjanes' v'-shaped ridges originating from a pulsing and dehydrating mantle plume. Nature 411, 681.

Ito, G., van Keken, P.E., 2007. Hotspots and melting anomalies. Treatise on Geophysics 7, 371–436.

Ito, G., Lin, J., 1995. Oceanic spreading center–hotspot interactions: constraints from along-isochron bathymetric and gravity anomalies. Geology 23, 657–660.

Ito, G., Lin, J., Graham, D., 2003. Observational and theoretical studies of the dynamics of mantle plume–mid-ocean ridge interaction. Reviews of Geophysics 41.

Ito, G., Shen, Y., Hirth, G., Wolfe, C.J., 1999. Mantle flow, melting, and dehydration of the iceland mantle plume. Earth and Planetary Science Letters 165, 81–96.

Jarvis, G.T., McKenzie, D., 1980. Convection in a compressible fluid with infinite prandtl number. Journal of Fluid Mechanics 96, 515–583.

Jarvis, G.T., Peltier, W., 1982. Mantle convection as a boundary layer phenomenon. Geophysical Journal International 68, 389–427.

Jaupart, C., Labrosse, S., Mareschal, J., 2007. 7.06-temperatures, heat and energy in the mantle of the earth. Treatise on geophysics 7, 223–270.

Jaupart, C., Mareschal, J.C., 2015. Heat flow and thermal structure of the lithosphere. Treatise of Geophysics .

Jaupart, C., Mareschal, J.C., Guillou-Frottier, L., Davaille, A., 1998. Heat flow and thickness of the lithosphere in the canadian shield. Journal of Geophysical Research: Solid Earth 103, 15269–15286.

Jeanloz, R., Morris, S., 1987. Is the mantle geotherm subadiabatic? Geophysical research letters 14, 335–338.

Jeffreys, H., 1923. Hypotheses of continental drift. Nature 111, 495.

Jeffreys, H., 1926. The rigidity of the earth's central core. Monthly notices of the Royal Astronomical Society, Geophysical supplements 1, 372–373.

Jellinek, A.M., Gonnermann, H.M., Richards, M.A., 2003. Plume capture by divergent plate motions: implications for the distribution of hotspots, geochemistry of mid-ocean ridge basalts, and estimates of the heat flux at the core–mantle boundary. Earth and Planetary Science Letters 205, 361–378.

Jellinek, A.M., Lenardic, A., Manga, M., 2002. The influence of interior mantle temperature on the structure of plumes: Heads for venus, tails for the earth. Geophysical Research Letters 29.

Jellinek, A.M., Manga, M., 2002. The influence of a chemical boundary layer on the fixity, spacing and lifetime of mantle plumes. Nature 418, 760.

Jellinek, A.M., Manga, M., 2004. Links between long-lived hot spots, mantle plumes, d , and plate tectonics. Reviews of Geophysics 42.

Jones, S.M., White, N., Maclennan, J., 2002. V-shaped ridges around iceland: Implications for spatial and temporal patterns of mantle convection. Geochemistry, Geophysics, Geosystems 3, 1–23.

Jones, T., Davies, D., Campbell, I., Iaffaldano, G., Yaxley, G., Kramer, S., Wilson, C., 2017. The concurrent emergence and causes of double volcanic hotspot tracks on the pacific plate. Nature 545, 472–476.

Jordan, T.H., 1979. Mineralogies, densities and seismic velocities of garnet lherzolites and their geophysical implications. The Mantle Sample: Inclusion in Kimberlites and Other Volcanics , 1–14.

Jourdan, F., Féraud, G., Bertrand, H., Kampunzu, A., Tshoso, G., Le Gall, B., Tiercelin, J., Capiez, P., 2004. The karoo triple junction questioned: evidence from jurassic and proterozoic 40 ar/39 ar ages and geochemistry of the giant okavango dyke swarm (botswana). Earth and Planetary Science Letters 222, 989–1006.

Kaban, M., Schwintzer, P., Reigber, C., 2004. A new isostatic model of the lithosphere and gravity field. Journal of Geodesy 78, 368–385.

Kageyama, A., Sato, T., 2004. "yin-yang grid": An overset grid in spherical geometry. Geochemistry, Geophysics, Geosystems 5.

Karato, S.I., Rubie, D.C., Yan, H., 1993. Dislocation recovery in olivine under deep upper mantle conditions: Implications for creep and diffusion. Journal of Geophysical Research: Solid Earth 98, 9761–9768.

Kellogg, L.H., Hager, B.H., van der Hilst, R.D., 1999. Compositional stratification in the deep mantle. Science 283, 1881–1884.

Kelvin, L., 1863. Dynamical Problem Regarding Elastic Spheroid Shell; On the Rigidity of the Earth'. volume 2. Phil. Trans. Roy. Soc. London, Treatise on Natural Philosophy.

Kerr, R.A., 1985. Plate tectonics goes back 2 billion years. Science 230, 1364–1367.

Kerr, R.C., Lister, J.R., 2008. Rise and deflection of mantle plume tails. Geochemistry, Geophysics, Geosystems 9.

Kerr, R.C., Mériaux, C., 2004. Structure and dynamics of sheared mantle plumes. Geochemistry, Geophysics, Geosystems 5.

Kincaid, C., Schilling, J.G., Gable, C., 1996. The dynamics of off-axis plume-ridge interaction in the uppermost mantle. Earth and Planetary Science Letters 137, 29–43.

King, S., 2007a. Mantle downwellings and the fate of subducting slabs: constraints from seismology, geoid topography, geochemistry, and petrology. Treatise of Geophysics .

King, S.D., 2002. Geoid and topography over subduction zones: The effect of phase transformations. Journal of Geophysical Research: Solid Earth 107.

King, S.D., 2007b. Hotspots and edge-driven convection. Geology 35, 223–226.

King, S.D., 2009. On topography and geoid from 2-d stagnant lid convection calculations. Geochemistry, Geophysics, Geosystems 10. doi:10.1029/2008GC002250.

King, S.D., Frost, D.J., Rubie, D.C., 2015. Why cold slabs stagnate in the transition zone. Geology 43, 231–234.

King, S.D., Raefsky, A., Hager, B.H., 1990. Conman: Vectorizing a finite element code for incompressible two-dimensional convection in the earth's mantle. Physics of the Earth and Planetary Interiors 59, 195–207.

King, S.D., Ritsema, J., 2000. African hot spot volcanism: small-scale convection in the upper mantle beneath cratons. Science 290, 1137–1140.

Kingsley, R.H., Schilling, J.G., 1998. Plume-ridge interaction in the easter-salas y gomez seamount chain-easter microplate system: Pb isotope evidence. Journal of Geophysical Research: Solid Earth 103, 24159–24177.

Kirby, S., Kronenberg, A., 1987. Rheology of the lithosphere: selected topics. Reviews of Geophysics 25, 1219–1244.

Kircher, A., 1665. Mundus subterraneus. Joannem Janssonium, from the collection of Roger Wagner.

Klein, E.M., Langmuir, C.H., 1987. Global correlations of ocean ridge basalt chemistry with axial depth and crustal thickness. Journal of Geophysical Research: Solid Earth 92, 8089–8115.

Kneller, E.A., Van Keken, P.E., 2007. Trench-parallel flow and seismic anisotropy in the mariana and andean subduction systems. Nature 450, 1222.

Koelemeijer, P., Deuss, A., Ritsema, J., 2017. Density structure of earth's lowermost mantle from stoneley mode splitting observations. Nature communications 8, 15241.

Kohlstedt, D., Evans, B., Mackwell, S., 1995. Strength of the lithosphere: Constraints imposed by laboratory experiments. Journal of Geophysical Research: Solid Earth 100, 17587–17602.

Koivisto, E.A., Andrews, D.L., Gordon, R.G., 2014. Tests of fixity of the indo-atlantic hot spots relative to pacific hot spots. Journal of Geophysical Research: Solid Earth 119, 661–675.

Konrad, K., Koppers, A.A., Steinberger, B., Finlayson, V.A., Konter, J.G., Jackson, M.G., 2018. On the relative motions of long-lived pacific mantle plumes. Nature communications 9, 854.

Koppers, A.A., Duncan, R.A., Steinberger, B., 2004. Implications of a nonlinear 40ar/39ar age progression along the louisville seamount trail for models of fixed and moving hot spots. Geochemistry, Geophysics, Geosystems 5.

Korenaga, T., Korenaga, J., 2008. Subsidence of normal oceanic lithosphere, apparent thermal expansivity, and seafloor flattening. Earth and Planetary Science Letters 268, 41–51.

Kowalik, Z., Murty, T.S., 1993. Numerical modeling of ocean dynamics. volume 5. World Scientific.

Kreemer, C., Blewitt, G., Klein, E.C., 2014. A geodetic plate motion and global strain rate model. Geochemistry, Geophysics, Geosystems 15, 3849–3889.

Labrosse, S., 2002. Hotspots, mantle plumes and core heat loss. Earth and Planetary Science Letters 199, 147–156.

Labrosse, S., 2007. Core-mantle boundary, heat flow across, in: Encyclopedia of Geomagnetism and Paleomagnetism. Springer, pp. 127–130.

Lachenbruch, A.H., Morgan, P., 1990. Continental extension, magmatism and elevation; formal relations and rules of thumb. Tectonophysics 174, 39–62.

Lallemand, S., Heuret, A., Boutelier, D., 2005. On the relationships between slab dip, back-arc stress, upper plate absolute motion, and crustal nature in subduction zones. Geochemistry, Geophysics, Geosystems 6.

Lambeck, K., 1990. Glacial rebound sea-level change and mantle viscosity. Quarterly Journal of the Royal Astronomical Society 31, 1.

Frizon de Lamotte, D., Fourdan, B., Leleu, S., Leparmentier, F., Clarens, P., 2015. Style of rifting and the stages of pangea breakup. Tectonics 34, 1009–1029.

Landau, L., Lifchitz, E., 1980. An introduction to fluid dynamics.

Lapusta, N., Rice, J., Ben-Zion, Y., Zheng, G., 2000. Elastodynamic analysis for slow tectonic loading with spontaneous rupture episodes on faults with rate- and state-dependent friction. Journal of Geophysical Research .

Laske, G., Masters, G., 1997. A global digital map of sediment thickness. Eos Trans. AGU 78, F483.

Le Bars, M., Davaille, A., 2004. Whole layer convection in a heterogeneous planetary mantle. Journal of Geophysical Research: Solid Earth 109.

Le Stunff, Y., Ricard, Y., 1995. Topography and geoid due to lithospheric mass anomalies. Geophysical Journal International 122, 982–990.

Le Stunff, Y., Ricard, Y., 1997. Partial advection of equidensity surfaces: A solution for the dynamic topography problem? Journal of Geophysical Research: Solid Earth 102, 24655–24667.

Lehmann, I., 1936. P'. Publications du Bureau Central Sismologique International, Série A, Travaux Scientifique 14, 87–115.

Lekic, V., Cottaar, S., Dziewonski, A., Romanowicz, B., 2012. Cluster analysis of global lower mantle tomography: A new class of structure and implications for chemical heterogeneity. Earth and Planetary Science Letters 357, 68–77.

Lenardic, A., Moresi, L.N., 1999. Some thoughts on the stability of cratonic lithosphere: Effects of buoyancy and viscosity. Journal of Geophysical Research: Solid Earth 104, 12747–12758. doi:10.1029/1999JB900035.

Leng, W., Gurnis, M., 2012. Shape of thermal plumes in a compressible mantle with depth-dependent viscosity. Geophysical Research Letters 39.

Leng, W., Zhong, S., 2008. Viscous heating, adiabatic heating and energetic consistency in compressible mantle convection. Geophysical Journal International 173, 693–702.

Li, M., Zhong, S., 2017. The source location of mantle plumes from 3d spherical models of mantle convection. Earth and Planetary Science Letters 478, 47–57.

Li, X., Kind, R., Yuan, X., Wölbern, I., Hanka, W., 2004. Rejuvenation of the lithosphere by the hawaiian plume. Nature 427, 827.

Li, X.D., Romanowicz, B., 1996. Global mantle shear velocity model developed using nonlinear asymptotic coupling theory. Journal of Geophysical Research: Solid Earth 101, 22245–22272.

Lin, S.C., van Keken, P.E., 2006a. Dynamics of thermochemical plumes: 1. plume formation and entrainment of a dense layer. Geochemistry, Geophysics, Geosystems 7.

Lin, S.C., Van Keken, P.E., 2006b. Dynamics of thermochemical plumes: 2. complexity of plume structures and its implications for mapping mantle plumes. Geochemistry, Geophysics, Geosystems 7.

Lister, C., Sclater, J., Davis, E., Villinger, H., Nagihara, S., 1990. Heat flow maintained in ocean basins of great age: investigations in the north-equatorial west pacific. Geophysical Journal International 102, 603–628.

Lithgow-Bertelloni, C., Richards, M.A., 1995. Cenozoic plate driving forces. Geophysical Research Letters 22, 1317–1320.

Lithgow-Bertelloni, C., Richards, M.A., Ricard, Y., O'Connell, R.J., Engebretson, D.C., 1993. Toroidal-poloidal partitioning of plate motions since 120 ma. Geophysical Research Letters 20, 375–378.

Lithgow-Bertelloni, C., Silver, P.G., 1998. Dynamic topography, plate driving forces and the african superswell. Nature 395, 269–272. doi:10.1038/26212.

Liu, L., Gurnis, M., 2008. Simultaneous inversion of mantle properties and initial conditions using an adjoint of mantle convection. Journal of Geophysical Research: Solid Earth 113.

Liu, L., Gurnis, M., 2010. Dynamic subsidence and uplift of the colorado plateau. Geology 38, 663–666.

Loper, D.E., Stacey, F.D., 1983. The dynamical and thermal structure of deep mantle plumes. Physics of the Earth and Planetary Interiors 33, 304–317.

Lourenco, D.L., Rozel, A., Tackley, P.J., 2016. Melting-induced crustal production helps plate tectonics on earth-like planets. Earth and Planetary Science Letters 439, 18–28.

Lowman, J.P., King, S.D., Gable, C.W., 2001. The influence of tectonic plates on mantle convection patterns, temperature and heat flow. Geophysical Journal International 146, 619–636.

Mainprice, D., Tommasi, A., Couvy, H., Cordier, P., Frost, D.J., 2005. Pressure sensitivity of olivine slip systems and seismic anisotropy of earth's upper mantle. Nature .

Malevsky, A.V., Yuen, D.A., 1993. Plume structures in the hard-turbulent regime of three-dimensional infinite prandtl number convection. Geophysical research letters 20, 383–386.

Mallard, C., Coltice, N., Seton, M., Müller, R.D., Tackley, P.J., 2016. Subduction controls the distribution and fragmentation of earth's tectonic plates. Nature .

Manga, M., Weeraratne, D., Morris, S., 2001. Boundary-layer thickness and instabilities in bénard convection of a liquid with a temperature-dependent viscosity. Physics of Fluids 13, 802–805.

Masters, G., Johnson, S., Laske, G., Bolton, H., 1996. A shear-velocity model of the mantle. Phil. Trans. R. Soc. Lond. A 354, 1385–1411.

Mattern, E., Matas, J., Ricard, Y., Bass, J., 2005. Lower mantle composition and temperature from mineral physics and thermodynamic modelling. Geophysical Journal International 160, 973–990.

Maus, S., 2001. New statistical methods in gravity and magnetics.

McElhinny, M., 1973. Mantle plumes, palaeomagnetism and polar wandering. Nature 241, 523.

McKenzie, D., 1977. The initiation of trenches. Island arcs, deep sea trenches and back-arc basins , 57–61.

McKenzie, D., 1978. Some remarks on the development of sedimentary basins. Earth and Planetary science letters 40, 25–32.

McKenzie, D., 1984. The generation and compaction of partially molten rock. Journal of Petrology 25, 713–765.

McKenzie, D., 2010. The influence of dynamically supported topography on estimates of Te. Earth and Planetary Science Letters 295, 127–138.

McKenzie, D., Bickle, M., 1988. The volume and composition of melt generated by extension of the lithosphere. Journal of petrology 29, 625–679.

McKenzie, D., Jackson, J., Priestley, K., 2005. Thermal structure of oceanic and continental lithosphere. Earth and Planetary Science Letters 233, 337–349.

McKenzie, D.P., 1967. Some remarks on heat flow and gravity anomalies. Journal of Geophysical Research 72, 6261–6273.

McKenzie, D.P., 1969. Speculations on the consequences and causes of plate motions. Geophysical Journal International 18, 1–32.

McKenzie, D.P., Roberts, J.M., Weiss, N.O., 1974. Convection in the earth's mantle: towards a numerical simulation. Journal of Fluid Mechanics 62, 465–538.

McNamara, A.K., Zhong, S., 2004. The influence of thermochemical convection on the fixity of mantle plumes. Earth and Planetary Science Letters 222, 485–500.

McNamara, A.K., Zhong, S., 2005. Degree-one mantle convection: Dependence on internal heating and temperature-dependent rheology. Geophysical research letters 32.

McNutt, M., 1987. Temperature beneath midplate swells: The inverse problem. Seamounts, Islands, and Atolls , 123–132.

McNutt, M., 1988. Thermal and mechanical properties of the cape verde rise. Journal of Geophysical Research: Solid Earth 93, 2784–2794.

McNutt, M.K., 1998. Superswells. Reviews of Geophysics 36, 211–244.

Melosh, H., Raefsky, A., 1980. The dynamical origin of subduction zone topography. Geophysical Journal International 60, 333–354.

Milelli, L., Fourel, L., Jaupart, C., 2012. A lithospheric instability origin for the cameroon volcanic line. Earth and Planetary Science Letters 335, 80–87.

Minster, J., Jordan, T., Molnar, P., Haines, E., 1974. Numerical modelling of instantaneous plate tectonics. Geophysical Journal International 36, 541–576.

Mitchell, R.N., Kilian, T.M., Evans, D.A., 2012. Supercontinent cycles and the calculation of absolute palaeolongitude in deep time. Nature 482, 208.

Mitrovica, J., Beaumont, C., Jarvis, G., 1989. Tilting of continental interiors by the dynamical effects of subduction. Tectonics 8, 1079–1094. doi:10.1029/TC008i005p01079.

Mitrovica, J.X., 1996. Haskell [1935] revisited. Journal of Geophysical Research: Solid Earth 101, 555–569.

Mitrovica, J.X., Forte, A.M., 1997. Radial profile of mantle viscosity: results from the joint inversion of convection and postglacial rebound observables. Journal of Geophysical Research: Solid Earth 102, 2751–2769.

Mohorovicic, A., 1992. Earthquake of 8 october 1909 (english translation from 1910). Geofyzica 9.

Molnar, P., England, P.C., Jones, C.H., 2015. Mantle dynamics, isostasy, and the support of high terrain. Journal of Geophysical Research: Solid Earth 120, 1932–1957.

Molnar, P., Francheteau, J., 1975. The relative motion of 'hot spots' in the atlantic and indian oceans during the cenozoic. Geophysical Journal International 43, 763–774.

Molnar, P., Stock, J., 1987. Relative motions of hotspots in the pacific, atlantic and indian oceans since late cretaceous time. Nature 327, 587–591.

Monnereau, M., Quéré, S., 2001. Spherical shell models of mantle convection with tectonic plates. Earth and Planetary Science Letters 184, 575–587.

Montelli, R., Nolet, G., Dahlen, F., Masters, G., 2006. A catalogue of deep mantle plumes: New results from finite-frequency tomography. Geochemistry, Geophysics, Geosystems 7.

Montelli, R., Nolet, G., Dahlen, F., Masters, G., Engdahl, E.R., Hung, S.H., 2004. Finite-frequency tomography reveals a variety of plumes in the mantle. Science 303, 338–343.

Moore, W.B., Schubert, G., Tackley, P., 1998. Three-dimensional simulations of plume-lithosphere interaction at the hawaiian swell. Science 279, 1008–1011.

Moreira, M., Doucelance, R., Kurz, M.D., Dupré, B., Allègre, C.J., 1999. Helium and lead isotope geochemistry of the azores archipelago. Earth and Planetary Science Letters 169, 189–205.

Moresi, L.N., Solomatov, V., 1995. Numerical investigation of 2d convection with extremely large viscosity variations. Physics of Fluids 7, 2154–2162. doi:10.1063/1.868465.

Morgan, W., 1968. Rises, trenches, great faults and crustal blocks. Journal od geophysical research 73.

Morgan, W.J., 1971. Convection plumes in the lower mantle. Nature 230, 42–43.

Morgan, W.J., 1972. Plate motions and deep mantle convection. Geological Society of America Memoirs 132, 7–22.

Morgan, W.J., 1981. Hotspot tracks and the opening of the atlantic and indian oceans. The oceanic lithosphere 7, 443.

Moucha, R., Forte, A.M., Mitrovica, J.X., Rowley, D.B., Quéré, S., Simmons, N.A., Grand, S.P., 2008. Dynamic topography and long-term sea-level variations: There is no such thing as a stable continental platform. Earth and Planetary Science Letters 271, 101–108.

Mudge, D.C., Jones, S.M., 2004. Palaeocene uplift and subsidence events in the scotland–shetland and north sea region and their relationship to the iceland plume. Journal of the Geological Society 161, 381–386.

Mueller, S., Phillips, R.J., 1991. On the initiation of subduction. Journal of Geophysical Research: Solid Earth 96, 651–665.

Müller, R.D., Lim, V.S., Isern, A.R., 2000. Late tertiary tectonic subsidence on the northeast australian passive margin: response to dynamic topography? Marine Geology 162, 337–352.

Müller, R.D., Roest, W.R., Royer, J.Y., Gahagan, L.M., Sclater, J.G., 1997. Digital isochrons of the world's ocean floor. Journal of Geophysical Research: Solid Earth 102, 3211–3214.

Müller, R.D., Royer, J.Y., Lawver, L.A., 1993. Revised plate motions relative to the hotspots from combined atlantic and indian ocean hotspot tracks. Geology 21, 275–278.

Müller, R.D., Seton, M., Zahirovic, S., Williams, S.E., Matthews, K.J., Wright, N.M., Shephard, G.E., Maloney, K.T., Barnett-Moore, N., Hosseinpour, M., et al., 2016. Ocean basin evolution and global-scale plate reorganization events since pangea breakup. Annual Review of Earth and Planetary Sciences 44, 107–138.

Mulyukova, E., Steinberger, B., Dabrowski, M., Sobolev, S.V., 2015. Survival of llsvps for billions of years in a vigorously convecting mantle: replenishment and destruction of chemical anomaly. Journal of Geophysical Research: Solid Earth 120, 3824–3847.

Murnaghan, F., 1951. Finite Deformation of an Elastic Solid. New York:John Wiley and Sons.

Murphy, J.B., Nance, R.D., 2003. Do supercontinents introvert or extrovert?: Sm-nd isotope evidence. Geology 31, 873–876.

Nakiboglu, S., Lambeck, K., 1980. Deglaciation effects on the rotation of the earth. Geophysical Journal International 62, 49–58. doi:10.1111/j.1365-246X.1980.tb04843.x.

Neal, C.R., Mahoney, J.J., Kroenke, L.W., Duncan, R.A., Petterson, M.G., . The ontong java plateau. Large Igneous Provinces: Continental, Oceanic, and Planetary Flood Volcanism , 183–216.

Newton, I., 1687. De Philosophiae Naturalis Principia Mathematica. London.

Ni, S., Tan, E., Gurnis, M., Helmberger, D., 2002. Sharp sides to the african superplume. science 296, 1850–1852.

Nishimura, C.E., Forsyth, D.W., 1989. The anisotropic structure of the upper mantle in the pacific. Geophysical Journal International 96, 203–229.

Niu, Y., O'Hara, M.J., 2007. Global correlations of ocean ridge basalt chemistry with axial depth: a new perspective. Journal of Petrology 49, 633–664.

Nyblade, A.A., Robinson, S.W., 1994. The african superswell. Geophysical research letters 21, 765–768.

O'Connell, R.J., Gable, C.W., Hager, B.H., 1991. Toroidal-poloidal partitioning of lithospheric plate motions, in: Glacial Isostasy, Sea-Level and Mantle Rheology. Springer, pp. 535–551.

O'Connor, J., Jokat, W., Wijbrans, J., Colli, L., 2018. Hotspot tracks in the south atlantic located above bands of fast flowing asthenosphere driven by waning pulsations from the african llsvp. Gondwana Research 53, 197–208.

O'connor, J., Stoffers, P., Wijbrans, J., Shannon, P., Morrissey, T., 2000. Evidence from episodic seamount volcanism for pulsing of the iceland plume in the past 70 myr. Nature 408, 954.

Ogawa, M., Schubert, G., Zebib, A., 1991. Numerical simulations of three-dimensional thermal convection in a fluid with strongly temperature-dependent viscosity. Journal of Fluid Mechanics 233, 299–328.

Ogura, Y., Phillips, N.A., 1962. Scale analysis of deep and shallow convection in the atmosphere. Journal of the atmospheric sciences 19, 173–179.

Oldham, R., 1906. The constitution of the interior of the earth, as revealed by earthquakes. Quaterly Journal of the Geological society 62, 456–475.

Olson, P., 1990. Hot spots, swells and mantle plumes. Magma transport and storage , 33–51.

Olson, P., 2016. Mantle control of the geodynamo: Consequences of top-down regulation. Geochemistry, Geophysics, Geosystems 17, 1935–1956.

Olson, P., Schubert, G., Anderson, C., 1987. Plume formation in the d -layer and the roughness of the core–mantle boundary. Nature 327, 409.

Olson, P., Yuen, D.A., Balsiger, D., 1984. Mixing of passive heterogeneities by mantle convection. Journal of Geophysical Research: Solid Earth 89, 425–436.

O'Neill, C., Müller, D., Steinberger, B., 2005. On the uncertainties in hot spot reconstructions and the significance of moving hot spot reference frames. Geochemistry, Geophysics, Geosystems 6.

Oxburgh, E., Turcotte, D., 1978. Mechanisms of continental drift. Reports on Progress in Physics 41, 1249.

Panet, I., Pajot-Métivier, G., Greff-Lefftz, M., Métivier, L., Diament, M., Mandea, M., 2014. Mapping the mass distribution of earth's mantle using satellite-derived gravity gradients. Nature Geoscience 7, 131.

Parish, J., Ziegler, A., Scotese, C., 1982. Rainfall patterns and the distribution of coals and evaporites in the mesozoic and cenozoic. Paleogeography, Paleoclimate, Paleoecology 40.

Parmentier, E., Sotin, C., 2000. Three-dimensional numerical experiments on thermal convection in a very viscous fluid: Implications for the dynamics of a thermal boundary layer at high rayleigh number. Physics of Fluids 12, 609–617.

Parmentier, E., Turcotte, D., Torrance, K., 1975. Numerical experiments on the structure of mantle plumes. Journal of Geophysical Research 80, 4417–4424.

Parnell-Turner, R., White, N., Henstock, T., Murton, B., Maclennan, J., Jones, S.M., 2014. A continuous 55-million-year record of transient mantle plume activity beneath iceland. Nature Geoscience 7, 914.

Parsons, B., McKenzie, D., 1978. Mantle convection and the thermal structure of the plates. Journal of Geophysical Research: Solid Earth 83, 4485–4496.

Patankar, S., 1980. Numerical heat transfer and fluid flow. CRC press.

Patocka, V., Cadek, O., Tackley, P.J., Cizkova, H., 2017. Stress memory effect in viscoelastic stagnant lid convection. Geophysical Journal International 209, 1462–1475.

Pavlis, N.K., Holmes, S.A., Kenyon, S.C., Factor, J.K., 2012. The development and evaluation of the earth gravitational model 2008 (egm2008). Journal of geophysical research: solid earth 117.

Pearson, J.R.A., 1958. On convection cells induced by surface tension. J. Fluid Mech 4, 489–500.

Pekeris, C.L., 1935. Thermal convection in the interior of the earth. Geophysical Journal International 3, 343–367. doi:10.1111/j.1365-246X.1935.tb01742.x.

Peltier, W., 1984. The thickness of the continental lithosphere. Journal of Geophysical Research: Solid Earth 89, 11303–11316.

Petersen, K.D., Nielsen, S., Clausen, O., Stephenson, R., Gerya, T., 2010. Small-scale mantle convection produces stratigraphic sequences in sedimentary basins. Science 329, 827–830. doi:10.1126/science.1190115.

Phipps Morgan, J., Morgan, W.J., Price, E., 1995. Hotspot melting generates both hotspot volcanism and a hotspot swell? Journal of Geophysical Research: Solid Earth 100, 8045–8062.

Picart, B., 1733. Temple of the Muses or the Principle Histories of fabulous Antiquity. Zachariah Chatelain.

Pilidou, S., Priestley, K., Debayle, E., Gudmundsson, O., 2005. Rayleigh wave tomography in the north atlantic: high resolution images of the iceland, azores and eifel mantle plumes. Lithos 79, 453–474.

Pinto Ribeiro, L., Martins, S., Hildenbrand, A., Madureira, P., Mata, J., 2017. The genetic link between the azores archipelago and the southern azores seamount chain (sasc): The elemental, isotopic and chronological evidences. Lithos 294, 133–146.

Pollack, H.N., Hurter, S.J., Johnson, J.R., 1993. Heat flow from the earth's interior: analysis of the global data set. Reviews of Geophysics 31, 267–280.

Poore, H., White, N., Jones, S., 2009. A neogene chronology of iceland plume activity from v-shaped ridges. Earth and Planetary Science Letters 283, 1–13.

Popov, A., Sobolev, S., 2008. Slim3d: A tool for three-dimensional thermomechanical modeling of lithospheric deformation with elasto-visco-plastic rheology. Physics of the Earth and Planetary Interiors 171, 55–75.

Pratt, J., 1959. On the deflection of the plumb-line in india, caused by the attraction of the himalaya mountains and of elevated regins beyond; and its modification by the compensating effect of a deficiency of matter below the mountain mass. Philosophical Transactions of the Royal Society of London 149.

Presnall, D.C., Gudfinnsson, G.H., Walter, M.J., 2002. Generation of mid-ocean ridge basalts at pressures from 1 to 7 gpa. Geochimica et Cosmochimica Acta 66, 2073–2090.

Pritchard, D., Roberts, G., White, N., Richardson, C., 2009. Uplift histories from river profiles. Geophysical Research Letters 36.

Putirka, K.D., 2005. Mantle potential temperatures at hawaii, iceland, and the mid-ocean ridge system, as inferred from olivine phenocrysts: Evidence for thermally driven mantle plumes. Geochemistry, Geophysics, Geosystems 6.

Rayleigh, L.J., 1916. On convection currents in a horizontal layer of fluid, when the higher temperature is on the underside. Philosophical Magazine 32.

Raymond, C.A., Stock, J.M., Cande, S.C., 2000. Fast Paleogene motion of the Pacific hotspots from revised global plate circuit constraints. Wiley Online Library.

Renne, P.R., Black, M.T., Zichao, Z., Richards, M.A., Basu, A.R., 1995. Synchrony and causal relations between permian-triassic boundary crises and siberian flood volcanism. Science 269, 1413–1416.

Rey, P.F., Coltice, N., Flament, N., 2014. Spreading continents kick-started plate tectonics. Nature 513, 405.

Ribe, N., 1996. The dynamics of plume-ridge interaction: 2. off-ridge plumes. Journal of Geophysical Research: Solid Earth 101, 16195–16204.

Ribe, N., Christensen, U., 1994. Three-dimensional modeling of plume-lithosphere interaction. Journal of Geophysical Research: Solid Earth 99, 669–682.

Ribe, N., Christensen, U., 1999. The dynamical origin of hawaiian volcanism. Earth and Planetary Science Letters 171, 517–531.

Ribe, N., Christensen, U., Theissing, J., 1995. The dynamics of plume-ridge interaction, 1: Ridge-centered plumes. Earth and Planetary Science Letters 134, 155–168.

Ricard, Y., 2007. Physics of mantle convection. Treatise of Geophysics .

Ricard, Y., 2015. Physics of mantle convection. Treatise of Geophysics , 23–71.

Ricard, Y., Doglioni, C., Sabadini, R., 1991. Differential rotation between lithosphere and mantle: a consequence of lateral mantle viscosity variations. Journal of Geophysical Research: Solid Earth 96, 8407–8415.

Ricard, Y., Fleitout, L., Froidevaux, C., 1984. Geoid heights and lithospheric stresses for a dynamic earth, in: Annales Geophysicae, pp. 267–286.

Ricard, Y., Richards, M., Lithgow-Bertelloni, C., Le Stunff, Y., 1993. A geodynamic model of mantle density heterogeneity. Journal of Geophysical Research: Solid Earth 98, 21895–21909. doi:10.1029/93JB02216.

Ricard, Y., Vigny, C., 1989. Mantle dynamics with induced plate tectonics. Journal of Geophysical Research: Solid Earth 94, 17543–17559.

Ricard, Y., Wuming, B., 1991. Inferring the viscosity and the 3-d density structure of the mantle from geoid, topography and plate velocities. Geophysical Journal International 105, 561–571.

Richards, M.A., 1991. Hotspots and the case for a high viscosity lower mantle, in: Glacial Isostasy, Sea-Level and Mantle Rheology. Springer, pp. 571–587.

Richards, M.A., Griffiths, R.W., 1988. Deflection of plumes by mantle shear flow: experimental results and a simple theory. Geophysical Journal International 94, 367–376.

Richards, M.A., Hager, B.H., 1984. Geoid anomalies in a dynamic earth. Journal of Geophysical Research: Solid Earth 89, 5987–6002.

Richards, M.A., Lithgow-Bertelloni, C., 1996. Plate motion changes, the hawaiian-emperor bend, and the apparent success and failure of geodynamic models. Earth and Planetary Science Letters 137, 19–27.

Richards, M.A., Yang, W.S., Baumgardner, J.R., Bunge, H.P., 2001. Role of a low-viscosity zone in stabilizing plate tectonics: Implications for comparative terrestrial planetology. Geochemistry, Geophysics, Geosystems 2.

Richter, F.M., McKenzie, D.P., 1981. On some consequences and possible causes of layered mantle convection. Journal of Geophysical Research: Solid Earth 86, 6133–6142.

Ritsema, J., Deuss, A., Van Heijst, H., Woodhouse, J., 2011. S40rts: a degree-40 shear-velocity model for the mantle from new rayleigh wave dispersion, teleseismic traveltime and normal-mode splitting function measurements. Geophysical Journal International 184, 1223–1236. doi:10.1111/j.1365-246X.2010.04884.x.

Roberts, G.G., Paul, J.D., White, N., Winterbourne, J., 2012. Temporal and spatial evolution of dynamic support from river profiles: a framework for madagascar. Geochemistry, Geophysics, Geosystems 13.

Rolf, T., Coltice, N., Tackley, P., 2014. Statistical cyclicity of the supercontinent cycle. Geophysical Research Letters 41, 2351–2358.

Romano, M., Cifelli, R.L., 2015. 100 years of continental drift. Science 350, 915–916.

Rossby, H., 1965. On thermal convection driven by non-uniform heating from below: an experimental study, in: Deep Sea Research and Oceanographic Abstracts, Elsevier. pp. 9–16.

Rowley, D.B., 2002. Rate of plate creation and destruction: 180 ma to present. Geological Society of America Bulletin 114, 927–933.

Rowley, D.B., Forte, A.M., Moucha, R., Mitrovica, J.X., Simmons, N.A., Grand, S.P., 2013. Dynamic topography change of the eastern united states since 3 million years ago. Science 340, 1560–1563.

Royden, L.H., Husson, L., 2006. Trench motion, slab geometry and viscous stresses in subduction systems. Geophysical Journal International 167, 881–905.

Rozel, A., Golabek, G., Jain, C., Tackley, P., Gerya, T., 2017. Continental crust formation on early earth controlled by intrusive magmatism. Nature 545, 332.

Rubey, M., Brune, S., Heine, C., Davies, D.R., Williams, S.E., Müller, R.D., 2017. Global patterns in earth's dynamic topography since the jurassic: the role of subducted slabs. Solid Earth 8, 899.

Rudolph, M.L., Lekić, V., Lithgow-Bertelloni, C., 2015. Viscosity jump in earth's mid-mantle. Science 350, 1349–1352.

Runcorn, S., 1959. Rock magnetization. Science 129.

Runcorn, S., 1967. Flow in the mantle inferred from the low degree harmonics of the geopotential. Geophysical Journal International 14, 375–384.

Ryberg, T., Haberland, C., Haberlau, T., Weber, M.H., Bauer, K., Behrmann, J.H., Jokat, W., 2015. Crustal structure of northwest namibia: Evidence for plume-rift-continent interaction. Geology 43, 739–742.

Rychert, C.A., Harmon, N., Armitage, J.J., 2018. Seismic imaging of thickened lithosphere resulting from plume pulsing beneath iceland. Geochemistry, Geophysics, Geosystems .

Samuel, H., Bercovici, D., 2006. Oscillating and stagnating plumes in the earth's lower mantle. Earth and Planetary Science Letters 248, 90–105.

Sandiford, M., 2007. The tilting continent: a new constraint on the dynamic topographic field from australia. Earth and Planetary Science Letters 261, 152–163.

Sandiford, M., Coblentz, D.D., Richardson, R.M., 1995. Ridge torques and continental collision in the indian-australian plate. Geology 23, 653–656.

Sandwell, D.T., Schubert, G., 1992. Evidence for retrograde lithospheric subduction on venus. Science 257, 766–770.

Schellart, W., Spakman, W., 2012. Mantle constraints on the plate tectonic evolution of the tonga–kermadec–hikurangi subduction zone and the south fiji basin region. Australian Journal of Earth Sciences 59, 933–952.

Schellart, W., Stegman, D., Freeman, J., 2008. Global trench migration velocities and slab migration induced upper mantle volume fluxes: Constraints to find an earth reference frame based on minimizing viscous dissipation. Earth-Science Reviews 88, 118–144.

Schilling, J.G., 1991. Fluxes and excess temperatures of mantle plumes inferred from their interaction with migrating mid-ocean ridges. Nature 352, 397.

Schmalholz, S., Podladchikov, Y., Schmid, D., 2001. A spectral/finite difference method for simulating large deformations of heterogeneous, viscoelastic materials. Geophysical Journal International .

Schmeling, H., 1989. Compressible convection with constant and variable viscosity: The effect on slab formation, geoid, and topography. Journal of Geophysical Research: Solid Earth 94, 12463–12481.

Schoonman, C., White, N., Pritchard, D., 2017. Radial viscous fingering of hot asthenosphere within the icelandic plume beneath the north atlantic ocean. Earth and Planetary Science Letters 468, 51–61.

Schubert, G., Olson, P., Anderson, C., Goldman, P., 1989. Solitary waves in mantle plumes. Journal of Geophysical Research: Solid Earth 94, 9523–9532.

Schubert, G., Turcotte, D., Olson, P., 2001. Mantle convection in the Earth and planets. Cambridge University Press.

Sclater, J., Jaupart, C., Galson, D., 1980. The heat flow through oceanic and continental crust and the heat loss of the earth. Reviews of Geophysics 18, 269–311.

Sembroni, A., Kiraly, A., Faccenna, C., Funiciello, F., Becker, T.W., Globig, J., Fernandez, M., 2017. Impact of the lithosphere on dynamic topography: Insights from analogue modeling. Geophysical Research Letters 44, 2693–2702. doi:10.1002/2017GL072668.

Sharp, W.D., Clague, D.A., 2006. 50-ma initiation of hawaiian-emperor bend records major change in pacific plate motion. Science 313, 1281–1284.

Shen, Y., Forsyth, D.W., 1995. Geochemical constraints on initial and final depths of melting beneath mid-ocean ridges. Journal of Geophysical Research: Solid Earth 100, 2211–2237.

Sidorin, I., Gurnis, M., 1998. Geodynamically consistent seismic velocity predictions at the base of the mantle. The core-mantle boundary region , 209–230.

Silveira, G., Stutzmann, E., Davaille, A., Montagner, J.P., Mendes-Victor, L., Sebai, A., 2006. Azores hotspot signature in the upper mantle. Journal of Volcanology and Geothermal Research 156, 23–34.

Sleep, N.H., 1990. Hotspots and mantle plumes: Some phenomenology. Journal of Geophysical Research: Solid Earth 95, 6715–6736.

Sleep, N.H., 1992. Hotspot volcanism and mantle plumes. Annual Review of Earth and Planetary Sciences 20, 19–43.

Smallwood, J., White, R., 2002. Ridge-plume interaction in the north atlantic and its influence on continental breakup and seafloor spreading. Geological Society, London, Special Publications 197, 15–37.

Smallwood, J.R., Gill, C.E., 2002. The rise and fall of the faroe–shetland basin: evidence from seismic mapping of the balder formation. Journal of the Geological Society 159, 627–630.

Smith, W.H., Sandwell, D.T., 1997. Global sea floor topography from satellite altimetry and ship depth soundings. Science 277, 1956–1962.

Smolarkiewicz, P.K., Margolin, L.G., 1998. Mpdata: A finite-difference solver for geophysical flows. Journal of Computational Physics 140, 459–480.

Sobolev, S.V., Sobolev, A.V., Kuzmin, D.V., Krivolutskaya, N.A., Petrunin, A.G., Arndt, N.T., Radko, V.A., Vasiliev, Y.R., 2011. Linking mantle plumes, large igneous provinces and environmental catastrophes. Nature 477, 312.

Solheim, L.P., Peltier, W., 1994. Avalanche effects in phase transition modulated thermal convection: A model of earth's mantle. Journal of Geophysical Research: Solid Earth 99, 6997–7018.

Solomatov, V., 2004. Initiation of subduction by small-scale convection. Journal of Geophysical Research: Solid Earth 109.

Solomatov, V., Moresi, L.N., 1996. Stagnant lid convection on venus. Journal of Geophysical Research: Planets 101, 4737–4753.

Solomatov, V., Moresi, L.N., 2000. Scaling of time-dependent stagnant lid convection: Application to small-scale convection on earth and other terrestrial planets. Journal of Geophysical Research: Solid Earth 105, 21795–21817.

Sotin, C., Labrosse, S., 1999. Three-dimensional thermal convection in an iso-viscous, infinite prandtl number fluid heated from within and from below: applications to the transfer of heat through planetary mantles. Physics of the Earth and Planetary Interiors 112, 171–190.

Sotin, C., Parmentier, E., 1989. Dynamical consequences of compositional and thermal density stratification beneath spreading centers. Geophysical Research Letters 16, 835–838.

Sparrow, E., Husar, R., Goldstein, R., 1970. Observations and other characteristics of thermals. Journal of Fluid Mechanics 41, 793–800.

Spasojevic, S., Gurnis, M., 2012. Sea level and vertical motion of continents from dynamic earth models since the late cretaceous. AAPG bulletin 96, 2037–2064. doi:10.1306/03261211121.

Spence, W., 1977. The aleutian arc: tectonic blocks, episodic subduction, strain diffusion, and magma generation. Journal of Geophysical Research 82, 213–230.

Stadler, G., Gurnis, M., Burstedde, C., Wilcox, L.C., Alisic, L., Ghattas, O., 2010. The dynamics of plate tectonics and mantle flow: From local to global scales. science 329, 1033–1038.

Stein, C.A., Stein, S., 1992. A model for the global variation in oceanic depth and heat flow with lithospheric age. Nature 359, 123.

Stein, C.A., Stein, S., 1993. Constraints on pacific midplate swells from global depth-age and heat flow-age models. The Mesozoic Pacific: geology, tectonics, and volcanism , 53–76.

Steinbach, V., Hansen, U., Ebel, A., 1989. Compressible convection in the earth's mantle: a comparison of different approaches. Geophysical Research Letters 16, 633–636.

Steinberger, B., 2000. Plumes in a convecting mantle: Models and observations for individual hotspots. Journal of Geophysical Research: Solid Earth 105, 11127–11152.

Steinberger, B., 2007. Effects of latent heat release at phase boundaries on flow in the earth's mantle, phase boundary topography and dynamic topography at the earth's surface. Physics of the Earth and Planetary Interiors 164, 2–20. doi:10.1016/j.pepi.2007.04.021.

Steinberger, B., 2016. Topography caused by mantle density variations: Observation-based estimates and models derived from tomography and lithosphere thickness. Geophysical Supplements to the Monthly Notices of the Royal Astronomical Society 205, 604–621.

Steinberger, B., Antretter, M., 2006. Conduit diameter and buoyant rising speed of mantle plumes: Implications for the motion of hot spots and shape of plume conduits. Geochemistry, Geophysics, Geosystems 7.

Steinberger, B., Conrad, C.P., Tutu, A.O., Hoggard, M.J., 2017. On the amplitude of dynamic topography at spherical harmonic degree two. Tectonophysics .

Steinberger, B., O'Connell, R.J., 1998. Advection of plumes in mantle flow: implications for hotspot motion, mantle viscosity and plume distribution. Geophysical Journal International 132, 412–434.

Steinberger, B., O'Connell, R.J., 2000. Effects of mantle flow on hotspot motion. The History and Dynamics of Global Plate Motions , 377–398.

Steinberger, B., O'Connell, R.J., 2002. The convective mantle flow signal in rates of true polar wander. Ice Sheets, Sea Level and the Dynamic Earth, Geodyn. Ser 29, 233–256.

Steinberger, B., Sutherland, R., O'connell, R.J., 2004. Prediction of emperor-hawaii seamount locations from a revised model of global plate motion and mantle flow. Nature 430, 167.

Steinberger, B., Torsvik, T.H., 2008. Absolute plate motions and true polar wander in the absence of hotspot tracks. Nature 452, 620.

Steinberger, B., Torsvik, T.H., 2012. A geodynamic model of plumes from the margins of large low shear velocity provinces. Geochemistry, Geophysics, Geosystems 13.

Stern, R.J., 2004. Subduction initiation: spontaneous and induced. Earth and Planetary Science Letters 226, 275–292.

Stern, R.J., Gerya, T., 2017. Subduction initiation in nature and models: A review. Tectonophysics .

Stock, J., Molnar, P., 1988. Uncertainties and implications of the late cretaceous and tertiary position of north america relative to the farallon, kula, and pacific plates. Tectonics 7, 1339–1384.

Storey, B.C., 1995. The role of mantle plumes in continental breakup: case histories from gondwanaland. Nature 377, 301.

Su, W.j., Woodward, R.L., Dziewonski, A.M., 1994. Degree 12 model of shear velocity heterogeneity in the mantle. Journal of Geophysical Research: Solid Earth 99, 6945–6980.

Suess, E., 1904-1924. The face of the earth (trans. of das antlitz der erde, 1885-1909). Oxford : Clarendon Press .

Tackley, P.J., 1998. Self-consistent generation of tectonic plates in three-dimensional mantle convection. Earth and Planetary Science Letters 157, 9–22.

Tackley, P.J., 2000. Self-consistent generation of tectonic plates in time-dependent, three-dimensional mantle convection simulations. Geochemistry, Geophysics, Geosystems 1.

Tackley, P.J., 2008. Modelling compressible mantle convection with large viscosity contrasts in a three-dimensional spherical shell using the yin-yang grid. Physics of the Earth and Planetary Interiors 171, 7–18.

Tackley, P.J., King, S.D., 2003. Testing the tracer ratio method for modeling active compositional fields in mantle convection simulations. Geochemistry, Geophysics, Geosystems 4. doi:10.1029/2001GC000214.

Tackley, P.J., Stevenson, D.J., Glatzmaier, G.A., Schubert, G., 1993. Effects of an endothermic phase transition at 670 km depth in a spherical model of convection in the earth's mantle. Nature 361, 699.

Tackley, P.J., Stevenson, D.J., Glatzmaier, G.A., Schubert, G., 1994. Effects of multiple phase transitions in a three-dimensional spherical model of convection in earth's mantle. Journal of Geophysical Research: Solid Earth 99, 15877–15901.

Tan, E., Leng, W., Zhong, S., Gurnis, M., 2011. On the location of plumes and lateral movement of thermochemical structures with high bulk modulus in the 3-d compressible mantle. Geochemistry, Geophysics, Geosystems 12.

Tarduno, J., Bunge, H.P., Sleep, N., Hansen, U., 2009. The bent hawaiian-emperor hotspot track: Inheriting the mantle wind. Science 324, 50–53.

Tarduno, J., Sliter, W., Kroenke, L., Leckie, M., Mayer, H., Mahoney, J., Musgrave, R., Storey, M., Winterer, E., 1991. Rapid formation of ontong java plateau by aptian mantle plume volcanism. Science 254, 399–403.

Tarduno, J.A., Cottrell, R.D., 1997. Paleomagnetic evidence for motion of the hawaiian hotspot during formation of the emperor seamounts. Earth and Planetary Science Letters 153, 171–180.

Tarduno, J.A., Duncan, R.A., Scholl, D.W., Cottrell, R.D., Steinberger, B., Thordarson, T., Kerr, B.C., Neal, C.R., Frey, F.A., Torii, M., et al., 2003. The emperor seamounts: Southward motion of the hawaiian hotspot plume in earth's mantle. Science 301, 1064–1069.

Thibaud, R., Gente, P., Maia, M., 1998. A systematic analysis of the mid-atlantic ridge morphology and gravity between 15 n and 40 n: Constraints of the thermal structure. Journal of Geophysical Research: Solid Earth 103, 24223–24243.

Thielmann, M., Kaus, B.J., 2012. Shear heating induced lithospheric-scale localization: Does it result in subduction? Earth and Planetary Science Letters 359, 1–13.

Thielmann, M., Kaus, B.J., Popov, A.A., 2015. Lithospheric stresses in rayleigh–bénard convection: effects of a free surface and a viscoelastic maxwell rheology. Geophysical Supplements to the Monthly Notices of the Royal Astronomical Society 203, 2200–2219.

Thoraval, C., Richards, M.A., 1997. The geoid constraint in global geodynamics: viscosity structure, mantle heterogeneity models and boundary conditions. Geophysical Journal International 131, 1–8.

Thorne, M.S., Garnero, E.J., 2004. Inferences on ultralow-velocity zone structure from a global analysis of spdks waves. Journal of Geophysical Research: Solid Earth 109.

Torrance, K., Turcotte, D., 1971. Thermal convection with large viscosity variations. Journal of Fluid Mechanics 47, 113–125.

Torsvik, T., Van der Voo, R., Redfield, T., 2002. Relative hotspot motions versus true polar wander. Earth and Planetary Science Letters 202, 185–200.

Torsvik, T.H., Burke, K., Steinberger, B., Webb, S.J., Ashwal, L.D., 2010. Diamonds sampled by plumes from the core-mantle boundary. Nature 466, 352.

Torsvik, T.H., Doubrovine, P.V., Steinberger, B., Gaina, C., Spakman, W., Domeier, M., 2017. Pacific plate motion change caused the hawaiian-emperor bend. Nature Communications 8, 15660.

Torsvik, T.H., Müller, R.D., Van der Voo, R., Steinberger, B., Gaina, C., 2008a. Global plate motion frames: toward a unified model. Reviews of geophysics 46.

Torsvik, T.H., Smethurst, M.A., Burke, K., Steinberger, B., 2008b. Long term stability in deep mantle structure: Evidence from the˜ 300 ma skagerrak-centered large igneous province (the sclip). Earth and Planetary Science Letters 267, 444–452.

Torsvik, T.H., Steinberger, B., Cocks, L.R.M., Burke, K., 2008c. Longitude: linking earth's ancient surface to its deep interior. Earth and Planetary Science Letters 276, 273–282.

Torsvik, T.H., van der Voo, R., Doubrovine, P.V., Burke, K., Steinberger, B., Ashwal, L.D., Trønnes, R.G., Webb, S.J., Bull, A.L., 2014. Deep mantle structure as a reference frame for movements in and on the earth. Proceedings of the National Academy of Sciences 111, 8735–8740.

Torsvik, T.H., Van der Voo, R., Preeden, U., Mac Niocaill, C., Steinberger, B., Doubrovine, P.V., van Hinsbergen, D.J., Domeier, M., Gaina, C., Tohver, E., et al., 2012. Phanerozoic polar wander, palaeogeography and dynamics. Earth-Science Reviews 114, 325–368.

Tosi, N., Yuen, D.A., de Koker, N., Wentzcovitch, R.M., 2013. Mantle dynamics with pressure-and temperature-dependent thermal expansivity and conductivity. Physics of the Earth and Planetary Interiors 217, 48–58. doi:10.1016/j.pepi.2013.02.004.

Toth, J., Gurnis, M., 1998. Dynamics of subduction initiation at preexisting fault zones. Journal of Geophysical Research: Solid Earth 103, 18053–18067.

Tucholke, B.E., Smoot, N.C., 1990. Evidence for age and evolution of corner seamounts and great meteor seamount chain from multibeam bathymetry. Journal of Geophysical Research: Solid Earth 95, 17555–17569.

Turcotte, D., Oxburgh, E., 1967. Finite amplitude convective cells and continental drift. Journal of Fluid Mechanics 28, 29–42.

Turcotte, D., Schubert, G., 2014. Geodynamics. Cambridge University Press.

Turcotte, D., Torrance, K., Hsui, A., 1973. Convection in the earth's mantle. Methods in Computational Physics 13, 431–454.

Tutu, A.O., Steinberger, B., Sobolev, S.V., Rogozhina, I., Popov, A.A., 2018. Effects of upper mantle heterogeneities on the lithospheric stress field and dynamic topography. Solid Earth 9, 649.

Ueda, K., Gerya, T., Sobolev, S.V., 2008. Subduction initiation by thermal–chemical plumes: numerical studies. Physics of the Earth and Planetary Interiors 171, 296–312.

Van Der Meer, D.G., Spakman, W., Van Hinsbergen, D.J., Amaru, M.L., Torsvik, T.H., 2010. Towards absolute plate motions constrained by lower-mantle slab remnants. Nature Geoscience 3, 36.

Van Dinther, Y., Gerya, T.V., Dalguer, L.A., Mai, P.M., Morra, G., Giardini, D., 2013. The seismic cycle at subduction thrusts: Insights from seismo-thermo-mechanical models. Journal of Geophysical Research: Solid Earth 118, 6183–6202.

Van Heck, H., Tackley, P., 2008. Planforms of self-consistently generated plates in 3d spherical geometry. Geophysical Research Letters 35.

Van Keken, P., King, S., Schmeling, H., Christensen, U., Neumeister, D., Doin, M.P., 1997. A comparison of methods for the modeling of thermochemical convection. Journal of Geophysical Research: Solid Earth 102, 22477–22495.

Van Summeren, J., Conrad, C.P., Lithgow-Bertelloni, C., 2012. The importance of slab pull and a global asthenosphere to plate motions. Geochemistry, Geophysics, Geosystems 13.

Vening-Meinesz, F.A., 1941. Gravity over the Hawaiian Archipelago and over the Madeira area; conclusions about the Earth's crust. Proceedings of the Koninklijke Nederlandse Academie, Wetensia.

Verne, J., 1864. Voyage au centre de la Terre. Librairie Hachette, collection Hetzel.

Vine, F., Matthews, D., 1963. Magnetic anomalies over oceanic ridges. Nature .

Vogt, P., 1981. On the applicability of thermal conduction models to mid-plate volcanism: Comments on a paper by gass et al. Journal of Geophysical Research: Solid Earth 86, 950–960.

Vogt, P., Johnson, G., Holcombe, T., Gilg, J., Avery, O., 1971. Episodes of sea-floor spreading recorded by the north atlantic basement. Tectonophysics 12, 211–234.

Vogt, P.R., 1976. Plumes, subaxial pipe flow, and topography along the mid-oceanic ridge. Earth and Planetary Science Letters 29, 309–325.

Vogt, P.R., Jung, W.Y., 2018. The "azores geosyndrome" and plate tectonics: Research history, synthesis, and unsolved puzzles, in: Volcanoes of the Azores. Springer, pp. 27–56.

Von Rebeur-Paschwitz, E., 1889. The earthquake of tokio, april 18, 1889. Nature .

Walcott, R., 1970. Flexural rigidity, thickness, and viscosity of the lithosphere. Journal of Geophysical Research 75, 3941–3954.

Wallace, P.J., 1998. Water and partial melting in mantle plumes: Inferences from the dissolved h2o concentrations of hawaiian basaltic magmas. Geophysical Research Letters 25, 3639–3642.

Wang, S., Wang, R., 2001. Current plate velocities relative to hotspots: implications for hotspot motion, mantle viscosity and global reference frame. Earth and Planetary Science Letters 189, 133–140.

Wang, S., Yu, H., Zhang, Q., Zhao, Y., 2018. Absolute plate motions relative to deep mantle plumes. Earth and Planetary Science Letters 490, 88–99.

Wang, T., Lin, J., Tucholke, B., Chen, Y.J., 2011. Crustal thickness anomalies in the north atlantic ocean basin from gravity analysis. Geochemistry, Geophysics, Geosystems 12.

Watkins, C.E., Conrad, C.P., 2018. Constraints on dynamic topography from asymmetric subsidence of the mid-ocean ridges. Earth and Planetary Science Letters 484, 264–275.

Watts, A.B., 2001. Isostasy and Flexure of the Lithosphere. Cambridge University Press.

Watts, A.B., Schubert, G., 2007. Treatise on geophysics. 6. Crust and lithosphere dynamics. Elsevier.

Weertman, J., Weertman, J.R., 1975. High temperature creep of rock and mantle viscosity. Annual Review of Earth and Planetary Sciences 3, 293–315.

Wegener, A., 1924. The origin of continents and oceans. Trans. JGA Skerl. Originally published as Die Entstehung der Kontinente und Ozeane, 3rd ed. (Braunschweig: Friedrich Vieweg und Sohn Akt. Ges., 1922) .

Weimer, R.J., 1970. Rates of deltaic sedimentation and intrabasin deformation, upper cretaceous of rocky mountain region. Deltaic Sedimentation, Modern and Ancient .

Weinstein, S.A., Olson, P., 1990. Planforms in thermal convection with internal heat sources at large rayleigh and prandtl numbers. Geophysical Research Letters 17, 239–242.

Weinstein, S.A., Olson, P.L., 1989. The proximity of hotspots to convergent and divergent plate boundaries. Geophysical Research Letters 16, 433–436.

Weinstein, S.A., Olson, P.L., 1992. Thermal convection with non-newtonian plates. Geophysical Journal International 111, 515–530.

Wen, L., Silver, P., James, D., Kuehnel, R., 2001. Seismic evidence for a thermo-chemical boundary at the base of the earth's mantle. Earth and Planetary Science Letters 189, 141–153.

Wesseling, P., Oosterlee, C.W., 2001. Geometric multigrid with applications to computational fluid dynamics, in: Partial Differential Equations. Elsevier, pp. 311–334.

Whattam, S.A., Stern, R.J., 2015. Late cretaceous plume-induced subduction initiation along the southern margin of the caribbean and nw south america: The first documented example with implications for the onset of plate tectonics. Gondwana Research 27, 38–63.

White, N., Lovell, B., 1997. Measuring the pulse of a plume with the sedimentary record. Nature 387, 888.

White, R., 1989. Initiation of the iceland plume and opening of the north atlantic: Chapter 10: North atlantic perspectives. Extensional Tectonics and Stratigraphy of the North Atlantic Margins .

White, R., McKenzie, D., 1995. Mantle plumes and flood basalts. Journal of Geophysical Research: Solid Earth 100, 17543–17585.

Whitehead, J., 1972. Moving heaters as a model of continental drift. Physics of the Earth and Planetary Interiors 5, 199–212.

Whitehead, J.A., 1982. Instabilities of fluid conduits in a flowing earth—are plates lubricated by the asthenosphere? Geophysical Journal International 70, 415–433.

Whitehead Jr, J.A., 1976. Convection models: Laboratory versus mantle. Tectonophysics 35, 215–228.

Whittaker, J., Afonso, J., Masterton, S., Müller, R., Wessel, P., Williams, S., Seton, M., 2015. Long-term interaction between mid-ocean ridges and mantle plumes. Nature Geoscience 8, 479–483.

Williams, S., Flament, N., Müller, R.D., Butterworth, N., 2015. Absolute plate motions since 130 ma constrained by subduction zone kinematics. Earth and Planetary Science Letters 418, 66–77.

Wilson, D.S., Hey, R.N., 1995. History of rift propagation and magnetization intensity for the cocos-nazca sspreading center. Journal of Geophysical Research: Solid Earth 100, 10041–10056.

Wilson, J.T., 1963. A possible origin of the hawaiian islands. Canadian Journal of Physics 41, 863–870.

Wilson, J.T., et al., 1966. Did the atlantic close and then re-open? Nature 211, 676–681.

Winterbourne, J., White, N., Crosby, A., 2014. Accurate measurements of residual topography from the oceanic realm. Tectonics 33, 982–1015.

Worsley, T., Nance, R., Moody, J., 1982. Plate tectonic episodicity: a deterministic model for periodic "pangeas". Eos, Transactions of the American Geophysical Union 65, 1104.

Worsley, T.R., Nance, D., Moody, J.B., 1984. Global tectonics and eustasy for the past 2 billion years. Marine Geology 58, 373–400.

Wright, N.M., Müller, R.D., Seton, M., Williams, S.E., 2015. Revision of paleogene plate motions in the pacific and implications for the hawaiian-emperor bend. Geology 43, 455–458.

Yang, T., Gurnis, M., 2016. Dynamic topography, gravity and the role of lateral viscosity variations from inversion of global mantle flow. Geophysical Journal International 207, 1186–1202. doi:10.1093/gji/ggw335.

Yang, T., Moresi, L., Müller, R.D., Gurnis, M., 2017. Oceanic residual topography agrees with mantle flow predictions at long wavelengths. Geophysical Research Letters 44, 10,896–10,906.

Yang, T., Shen, Y., van der Lee, S., Solomon, S.C., Hung, S.H., 2006. Upper mantle structure beneath the azores hotspot from finite-frequency seismic tomography. Earth and Planetary Science Letters 250, 11–26.

Yoshida, M., 2017. On approximations of the basic equations of terrestrial mantle convection used in published literature. Physics of the Earth and Planetary Interiors 268, 11–17.

Yuen, D., Peltier, W., 1980. Mantle plumes and the thermal stability of the d layer. Geophysical Research Letters 7, 625–628.

Zatman, S., Gordon, R.G., Mutnuri, K., 2005. Dynamics of diffuse oceanic plate boundaries: insensitivity to rheology. Geophysical Journal International 162, 239–248.

Zhang, N., Dang, Z., Huang, C., Li, Z.X., 2018. The dominant driving force for supercontinent breakup: Plume push or subduction retreat? Geoscience Frontiers .

Zhang, N., Zhong, S., Leng, W., Li, Z.X., 2010. A model for the evolution of the earth's mantle structure since the early paleozoic. Journal of Geophysical Research: Solid Earth 115.

Zhang, S., Christensen, U., 1993. Some effects of lateral viscosity variations on geoid and surface velocities induced by density anomalies in the mantle. Geophysical Journal International 114, 531–547.

Zhang, S., Yuen, D.A., 1996. Various influences on plumes and dynamics in time-dependent, compressible mantle convection in 3-d spherical shell. Physics of the earth and planetary interiors 94, 241–267.

Zheng, L., Gordon, R.G., Woodworth, D., 2018. Pacific plate apparent polar wander, hotspot fixity, and true polar wander during the formation of the hawaiian island and seamount chain from an analysis of the skewness of magnetic anomaly 20r (44 ma). Tectonics .

Zhong, S., 2002. Effects of lithosphere on the long-wavelength gravity anomalies and their implications for the formation of the tharsis rise on mars. Journal of Geophysical Research: Planets 107.

Zhong, S., 2006. Constraints on thermochemical convection of the mantle from plume heat flux, plume excess temperature, and upper mantle temperature. Journal of Geophysical Research: Solid Earth 111.

Zhong, S., Gurnis, M., 1992. Viscous flow model of a subduction zone with a faulted lithosphere: long and short wavelength topography, gravity and geoid. Geophysical Research Letters 19, 1891–1894.

Zhong, S., Gurnis, M., 1994. Controls on trench topography from dynamic models of subducted slabs. Journal of Geophysical Research: Solid Earth 99, 15683–15695.

Zhong, S., McNamara, A., Tan, E., Moresi, L., Gurnis, M., 2008. A benchmark study on mantle convection in a 3-d spherical shell using citcoms. Geochemistry, Geophysics, Geosystems 9.

Zhong, S., Rudolph, M.L., 2015. On the temporal evolution of long-wavelength mantle structure of the earth since the early paleozoic. Geochemistry, Geophysics, Geosystems 16, 1599–1615.

Zhong, S., Zhang, N., Li, Z.X., Roberts, J.H., 2007. Supercontinent cycles, true polar wander, and very long-wavelength mantle convection. Earth and Planetary Science Letters 261, 551–564.

Zhong, S., Zuber, M.T., Moresi, L., Gurnis, M., 2000. Role of temperature-dependent viscosity and surface plates in spherical shell models of mantle convection. Journal of Geophysical Research: Solid Earth 105, 11063–11082.

Appendix A

Comparison of a 1D discrete signal with a 2D signal defined on the sphere $\mathbb{S}^2$

A.1 Notations

We consider a real signal $f : \mathbb{S}^2 \longrightarrow \mathbf{R}$. Its spherical harmonic decomposition can be written:

$$f(\theta, \varphi) = \sum_{l=0}^{\infty} \sum_{m=-l}^{l} f_{l,m} Y_{l,m}(\theta, \varphi),$$

where

$$Y_{l,m}(\theta, \varphi) = \overline{P}_{l,m}(\cos(\theta)) cos(m\varphi)$$

if $m \geq 0$ and

$$Y_{l,m}(\theta, \varphi) = \overline{P}_{l,|m|}(\cos(\theta)) \sin(|m|\varphi)$$

if $m < 0$. We denote by θ the co-latitude, by φ the longitude, and by $\overline{P}_{l,m}$ the Legendre polynomials. We note $g_m(\varphi) = \cos(m\varphi)$ if $m \geq 0$ and $g_m(\varphi) = \sin(|m|\varphi)$ if $m < 0$. We use the fully-normalised Legendre polynomials:

$$\overline{P}_{l,m}(x) = \sqrt{\frac{(2 - \delta_{0,m})(2l+1)}{4\pi} \frac{(l-m)!}{(l+m)!}} P_{l,m}(x),$$

$$P_{l,m}(x) = (1 - x^2)^{\frac{m}{2}} \frac{d^m}{dx^m} P_l(x),$$

and

$$P_l(x) = \frac{1}{2^l l!} \frac{d^l}{dx^l} (x^2 - 1)^l.$$

$(Y_{l,m})_{l\in\mathbb{N},m\in\{-l,\dots,l\}}$ define an orthonormal base for the scalar product $L^2(\mathbb{S}^2, d\Omega)$, with the volume form $d\Omega = |\sin(\theta)|d\theta d\varphi$, where $\theta \in [0,\pi]$ and $\varphi \in [0, 2\pi]$.

A.2 Approximation of a function on a sphere by longitudinal functions

The aim here is to show that we can recover a spherical harmonic spectrum from a function defined on a sphere by summing the Fourier spectra of the same function sampled on a large range of great circles.

Let l be an integer, and ϕ_k a group of longitudes respectively equal to $\frac{2\pi k}{N}$, for a large and fixed N. If $f : \mathbb{S}^2 \longrightarrow \mathbf{R}$ is a function defined on the sphere, we can define the function f_l by:

$$f_l(\theta,\varphi) := \sum_{m=-l}^{l} f_{l,m} Y_{l,m}(\theta,\varphi),$$

and for a fixed longitude φ_k, we can define the function f_{l,φ_k} for $\theta \in [-\frac{\pi}{2}, \frac{\pi}{2}]$:

$$f_{l,\varphi_k}(\theta) := f_l(\theta,\varphi_k),$$

and for $\theta \in [-\frac{\pi}{2}, \frac{3\pi}{2}]$:

$$f_{l,\varphi_k}(\theta) := f_l(-\theta+\pi, \pi+\varphi_k)$$

We can extend f_{l,φ_k} to a 2π-periodic function, simply representing the function f_l restricted to the two half-great circles defined by the longitudes φ_k and $\varphi_{k+\frac{N}{2}}$.

We can define, for $j \neq 0$:

$$a_{(l,m),(j,k)} = \frac{1}{\pi}\int_0^{2\pi} Y_{l,m,\varphi_k}(\theta)\sqrt{|\sin(\theta)|}\cos(j\theta)d\theta$$

and

$$b_{(l,m),(j,k)} = \frac{1}{\pi}\int_0^{2\pi} Y_{l,m,\varphi_k}(\theta)\sqrt{|\sin(\theta)|}\sin(j\theta)d\theta,$$

and for $j = 0$:

$$a_{(l,m),(0,k)} = \frac{1}{2\pi}\int_0^{2\pi} Y_{l,m,\varphi_k}(\theta)\sqrt{|\sin(\theta)|}d\theta$$

and

$$b_{(l,m),(0,k)} = 0,$$

the real Fourier coefficients of the θ-dependent function given by $Y_{l,\varphi_k}(\theta)\sqrt{|\sin(\theta)|}$.

The separation of the variables θ and φ in the expression of $Y_{l,m}(\theta,\phi)$ leads to, for any j, k and l:

$$a_{l,(j,k)} = \sum_{m=-l}^{l} g_m(\varphi_k)\frac{2-\delta_{0,j}}{2\pi}\int_0^{2\pi}\overline{P}_{l,m}(\cos(\theta))\sqrt{|\sin(\theta)|}\cos(j\theta)d\theta,$$

and to:

$$b_{l,(j,k)} = \sum_{m=-l}^{l} g_m(\varphi_k)\frac{1}{\pi}\int_0^{2\pi}\overline{P}_{l,m}(\cos(\theta))\sqrt{|\sin(\theta)|}\sin(j\theta)d\theta.$$

Let $\alpha_{j,(l,m)}$ be the Fourier coefficient:

$$\alpha_{j,(l,m)} := \frac{2-\delta_{0,j}}{2\pi}\int_0^{2\pi}\overline{P}_{l,m}(\cos(\theta))\sqrt{|\sin(\theta)|}\cos(j\theta)d\theta$$

and $\beta_{j,(l,m)}$ the coefficient:

$$\beta_{j,(l,m)} := \frac{1}{\pi}\int_0^{2\pi}\overline{P}_{l,m}(\cos(\theta))\sqrt{|\sin(\theta)|}\sin(j\theta)d\theta.$$

We want to compare the spherical harmonic power spectrum of f_l given by $S(f_l) = \sum_{m=-l}^{l} f_{l,m}^2$ (with the chosen normalisation conventions), and the k-averaged from 0 to $\frac{N}{2}$ of the Fourier power spectrum of $f_{l,\varphi_k}(\theta)\sqrt{|sin(\theta)|}$.

Therefore, we consider the sum over each k:

$$s_k(f)(\theta) := \sum_{j=0}^{\infty}\sum_{m=-l}^{l} f_{l,m}(a_{j,k}\cos(j\theta) + b_{j,k}\sin(j\theta))$$

for which we want to calculate the spectral power. Its Fourier coefficients are: $\sum_{m=-l}^{l} f_{l,m}a_{j,k}$ and $\sum_{m=-l}^{l} b_{j,k}f_{l,m}$.

Parseval's identity gives:

$$\frac{1}{2\pi}\int_0^{2\pi} s_k(f)(\theta)^2 d\theta = \left(\sum_{m=-l}^{l} f_{l,m}a_{0,k}\right)^2 + \frac{1}{2}\sum_{j=0}^{\infty}\left(\left(\sum_{m=-l}^{l} f_{l,m}a_{j,k}\right)^2 + \left(\sum_{m=-l}^{l} f_{l,m}b_{j,k}\right)^2\right).$$

We name this expression $P_F(s_k(f))$. Let's consider the first sum of the second member of this identity.

By taking its square and its average over k, we get:

$$\begin{aligned}\frac{2}{N}\sum_{k=0}^{\frac{N}{2}-1}\sum_{m=-l}^{l}\sum_{m'=-l}^{l} f_{l,m}f_{l,m'}a_{0,k}^2 &= \sum_{m=-l}^{l}\sum_{m'=-l}^{l} f_{l,m}f_{l,m'}\frac{2}{N}\sum_{k=0}^{\frac{N}{2}-1} a_{0,k}^2 \\ &= \sum_{m=-l}^{l}\sum_{m'=-l}^{l} f_{l,m}f_{l,m'}\alpha_{0,(l,m)}\alpha_{0,(l,m')}\frac{2}{N}\sum_{k=0}^{\frac{N}{2}-1} g_m(\varphi_k)g_{m'}(\varphi_k)\end{aligned}$$

This last equation contains a Riemann sum for each m, for which the convergence rate only depends on m and thus on l. We therefore have:

$$\frac{2}{N}\sum_{k=0}^{\frac{N}{2}-1} g_m(\varphi_k)g_{m'}(\varphi_k) = \frac{2}{N}\sum_{k=0}^{\frac{N}{2}-1} g_m(\pi k\frac{2}{N})g_{m'}(\pi k\frac{2}{N}),$$

For a large N, this gives:

$$\frac{2}{N}\sum_{k=0}^{\frac{N}{2}-1} g_m(\varphi_k)g_{m'}(\varphi_k) \approx \int_0^1 g_m(\pi t)g_{m'}(\pi t)dt$$

(we can replace the '$\approx$' sign by an '=' sign only if N tends to infinity.) After a simple calculation, this gives:

$$\frac{2}{N}\sum_{k=0}^{\frac{N}{2}-1} g_m(\varphi_k)g_{m'}(\varphi_k) \approx \delta_{m,m'}\int_0^1 g_m(\pi t)^2dt$$

We recall that $g_m(\pi t)^2$ is equal to $\cos(m\pi t)^2$ for any positive m and to $\sin(m\pi t)^2$ for any negative m. We therefore have, for any $m \neq 0$:

$$\int_0^1 g_m(\pi t)^2dt = \frac{1}{2}$$

and

$$\int_0^1 g_0(\pi t)^2dt = 1.$$

The sum over m and m' then leads to:

$$\sum_{m=-l}^{l}\sum_{m'=-l}^{l} f_{l,m}f_{l,m'}\alpha_{0,(l,m)}\alpha_{0,(l,m')}\frac{2}{N}\sum_{k=0}^{\frac{N}{2}-1} g_m(\varphi_k)g_{m'}(\varphi_k) \approx \sum_{m=0}^{l}\alpha_{0,(l,m)}^2\frac{1}{2}(f_{l,m}^2 + f_{l,-m}^2).$$

The approximation is valid because the rate of convergence only depends on l.

We can do the same calculations for any j. We then get, for any $j \geq 1$:

$$\frac{2}{N}\sum_{k=0}^{\frac{N}{2}-1}\left(\sum_{m=-l}^{l} f_{l,m}a_{j,k}\right)^2 \approx \sum_{m=0}^{l}\alpha_{j,(l,m)}^2\frac{1}{2}(f_{l,m}^2+f_{l,-m}^2)$$

and

$$\frac{2}{N}\sum_{k=0}^{\frac{N}{2}-1}\left(\sum_{m=-l}^{l} f_{l,m}b_{j,k}\right)^2 \approx \sum_{m=0}^{l}\beta_{j,(l,m)}^2\frac{1}{2}(f_{l,m}^2+f_{l,-m}^2).$$

Finally, this leads to:

$$\frac{2}{N}\sum_{k=0}^{\frac{N}{2}-1} P_F(s_k(f)) \approx$$
$$\sum_{m=0}^{l}\alpha_{0,(l,m)}^2\frac{1}{2}(f_{l,m}^2+f_{l,-m}^2)+\frac{1}{2}\sum_{j=1}^{\infty}\left(\sum_{m=0}^{l}\alpha_{j,(l,m)}^2\frac{1}{2}(f_{l,m}^2+f_{l,-m}^2)+\sum_{m=0}^{l}\beta_{j,(l,m)}^2\frac{1}{2}(f_{l,m}^2+f_{l,-m}^2)\right).$$

By inverting the two sums, we have:

$$\frac{2}{N}\sum_{k=0}^{\frac{N}{2}-1} P_F(s_k(f)) \approx \sum_{m=0}^{l}\frac{1}{2}(f_{l,m}^2+f_{l,-m}^2)\left(\alpha_{0,(l,m)}^2+\frac{1}{2}\sum_{j=1}^{\infty}\alpha_{j,(l,m)}^2+\beta_{j,(l,m)}^2\right).$$

The sum over j contains the Fourier development of $\overline{P}_{l,m}(\cos(\theta)\sqrt{|\sin(\theta)|}$. Thanks to the Parseval's identity, we know that this sum equals to:

$$\frac{1}{2\pi}\int_{-\pi}^{\pi}\overline{P}_{l,m}(\cos(\theta))^2|\sin(\theta)|d\theta.$$

The change of variables $u = \cos(\theta)$ leads to:

$$\frac{1}{\pi}\int_{-1}^{1}\overline{P}_{l,m}(u)^2du$$

which is equal to $\frac{2(2-\delta_{0,m})}{4\pi^2}$.

Finally, we get, by dividing the sum with the part of negative m:

$$\frac{2}{N}\sum_{k=0}^{\frac{N}{2}-1} P_F(s_k(f)) \approx \frac{1}{2\pi^2}\sum_{m=-l}^{l} f_{l,m}^2.$$

Therefore,

$$\frac{2}{N}\sum_{k=0}^{\frac{N}{2}-1}\int_0^{2\pi} s_k(f)(\theta)^2 d\theta \approx \frac{1}{\pi}\times S(f_l).$$

In conclusion, in order to retrieve the spherical harmonic power of a 2D signal f_l defined on the sphere $\mathbb{S}^2$ from Fourier power spectra of the same signal f_{l,φ_k} restricted to two half great-circles defined by the longitudes φ_k and $\varphi_{k+\frac{N}{2}}$, we need to consider the sum over a large range N of longitudes of the Fourier spectral power coefficients of the following function $f_{l,\varphi_k}\sqrt{|sin(\theta)|}$, then divided by $\frac{1}{\pi}$.

We applied this method to the dynamic topography field of Flament et al. (2013). We decomposed this field into 180 signals defined on longitudinal great circles. We then calculated their corresponding Fourier spectra accordingly to the method described before. We averaged the resulting power spectral coefficients of all great circles for each frequency k and compared the resulting spectrum with the known spherical harmonic spectrum of the whole field (Fig. A.1).

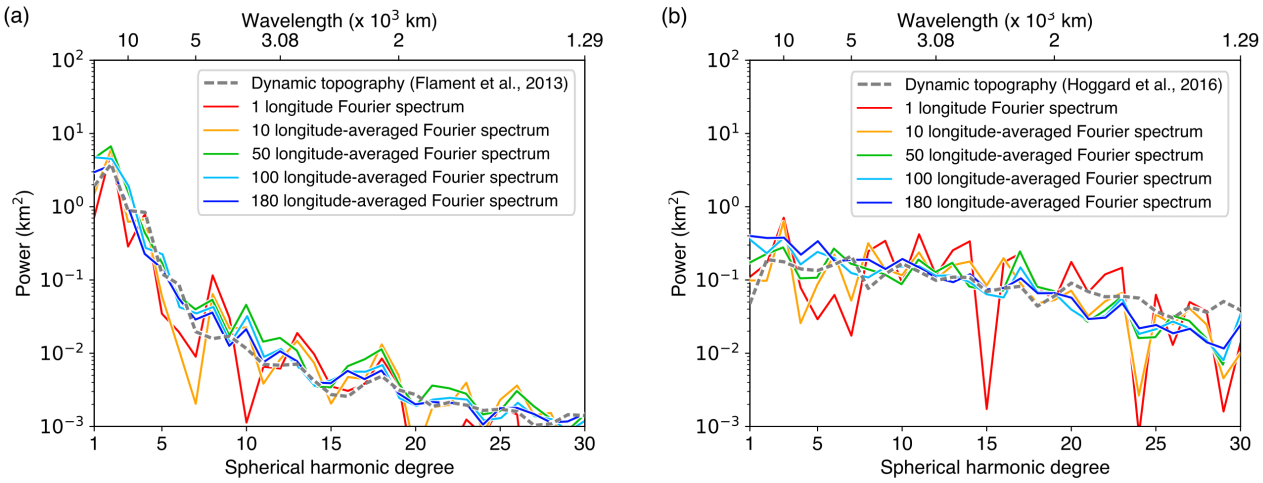


Figure A.1: Comparison of the spherical harmonic spectrum of dynamic topography from (a) Flament et al. (2013) and (b) Hoggard et al. (2016) with the longitudinal average of the Fourier power spectra of dynamic topography by Flament et al. (2013) and Hoggard et al. (2016) resp., sampled over 1, 10, 50, 100 and 180 longitudinal great circles

From Fig. A.1(a), we show that we successfully recover the spherical harmonic power spectrum of Flament et al. (2013) by using the method described before. The two curves are not exactly superposed because we only averaged Fourier spectra over 180 great circles. However, the method described before is exact for an infinite number of signals restricted to longitudinal great circles.

We repeated the same process for different dynamic topography global fields (Ricard et al., 1993, Steinberger, 2007, Conrad and Husson, 2009, Spasojevic and Gurnis, 2012) and Yang and Gurnis (2016), with the same positive conclusions. The same process applied to the residual topography field

of Hoggard et al. (2016) which has more signal in the small-wavelengths reveals that the recovery of the initial signal is consistent but not fully complete: the spectral power of the largest scales of dynamic topography (degrees > 6) is slightly overestimated by about 0.3 km^2 while the power at degrees < 20 is slightly underestimated by about 0.05 km^2.

When we calculate dynamic topography power spectra for our models, we repeat the procedure described above and add a correction of the slope of the Fourier power spectra by dividing the amplitude of each spherical harmonic degree l by $2l + 1$ to account for the degree-dependent slope of spherical harmonics decomposition (Maus, 2001).

Appendix B

Supplementary Information for: Northward drift of the Azores plume in the Earth's mantle

---

B.1 Petrological analysis of along-axis MAR basalts

Table B.1: Samples used in this study. See separate file.

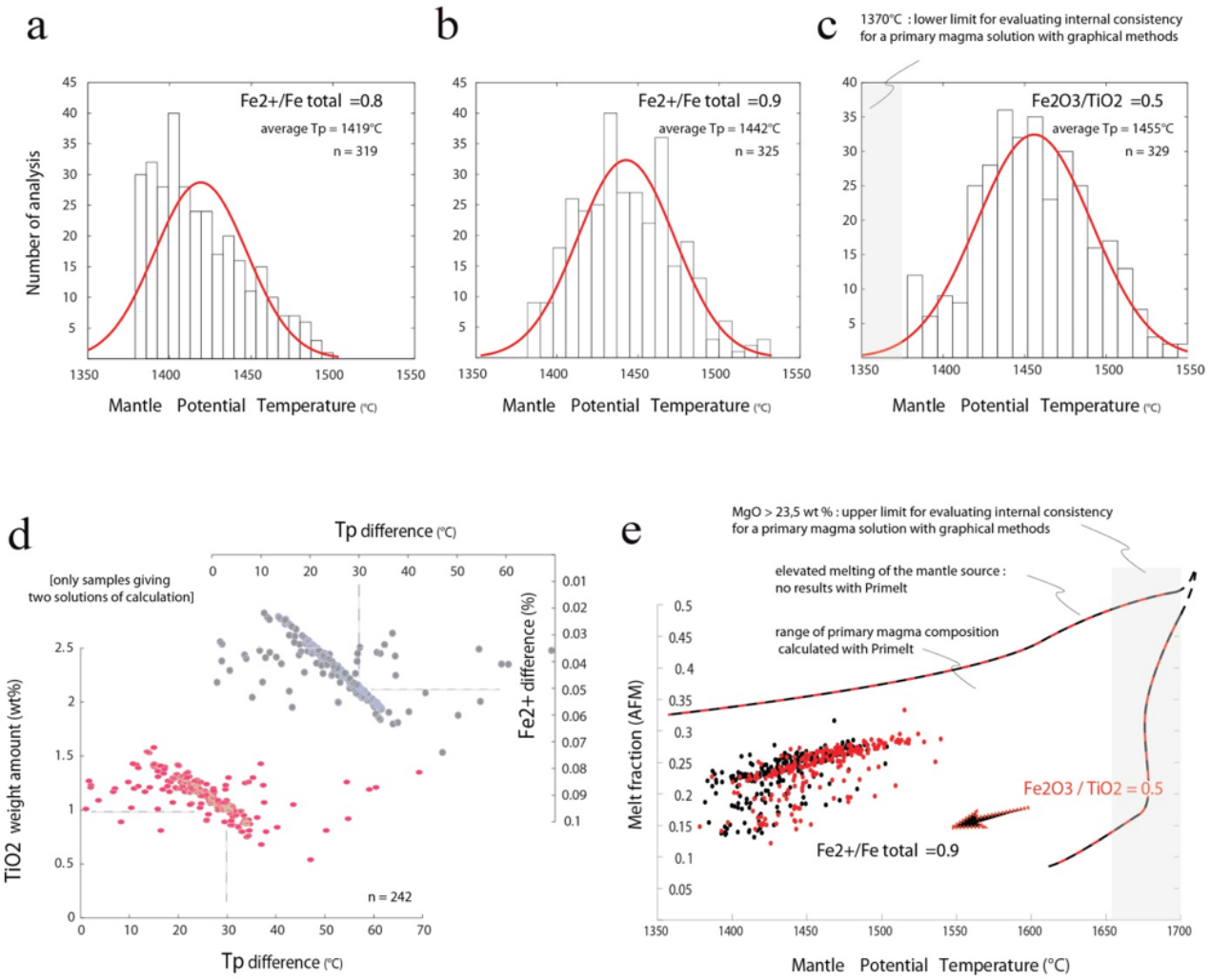


Figure B.1: Addressing redox conditions in the magmatic source. (a, b, c) Comparative distribution (histograms) of potential temperature (T_P) of mantle depicted from the composition of MORBs using PRIMELT3 MEGA software (Herzberg and Asimow, 2015) and different redox conditions in the source. In (c), the average redox condition ($Fe^{2+}/\Sigma Fe$ ratio) in the source is positioned at $\sim$ 0.95, depending of the titanium content of samples ($Fe_2O_3/TiO_2 = 0.5$); in (a) and (b) the redox condition in the mantle source is fixed at 0.8 and 0.9, respectively. (d) 242 samples yielded a solution of calculation when PRIMELT was running with a fixed (0.9) or Ti-dependent redox value (overlaps > 74 %). Uncertainties that arise by calculating FeO using Fe_2O_3/TiO_2=0.5 instead of FeO/FeO_T=0.9 (Herzberg et al., 2010) propagate to uncertainties (SEM) in mantle T_P lower than 30°C for high-Ti type lavas (TiO_2 > 1 wt% with FeO/FeO_T < 0.95) up to 60°C for low-Ti types (TiO_2 < 0.5 wt% with FeO/FeO_T > 0.95). (e) Uncertainties that arise by calculating FeO using Fe_2O_3/TiO_2=0.5 instead of FeO/FeO_T=0.9 propagate to uncertainties (SEM) in melt fraction (AFM) lower than 1% for high-Ti type lavas (TiO_2 >1 wt% with FeO/FeO_T < 0.95) up to 2% for low-Ti types (TiO_2 < 0.5 wt% with FeO/FeO_T > 0.95).

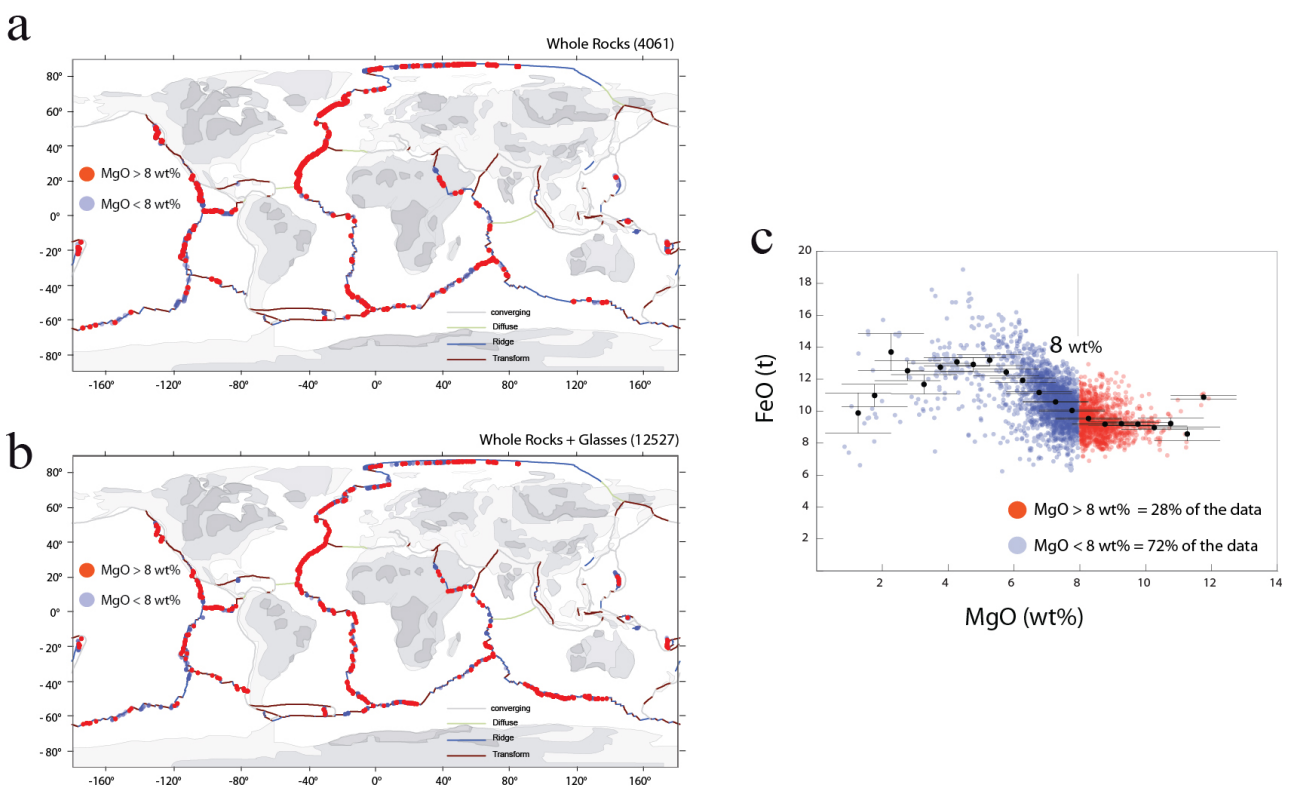


Figure B.2: Distribution of (zero-age) MORBs (Gale et al., 2013). (a) Whole-rock analyses only (25% of the dataset). (b) Whole-rock and glass analyses (100% of the dataset). (c) MgO-FeO_T liquid lines of descent for MORBs. The blue points correspond to more evolved liquids where clinopyroxene fractionated, leading to an increase of FeO_T in magma with increasing differentiation (MgO decrease). A statistical assessment of their averaged evolution (black points) through magma differentiation is given by the black drawbars (uncertainty bars correspond to $\pm$ 1σ standard deviation for a step of 0.5 wt%).

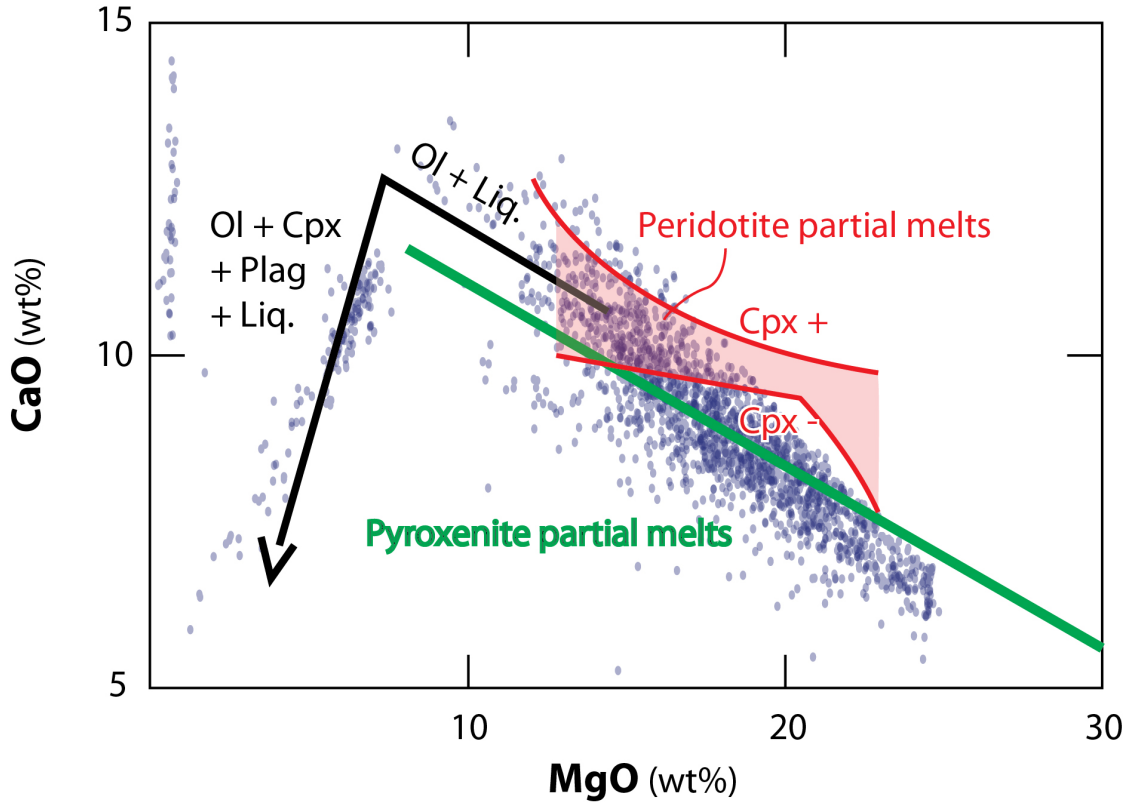


Figure B.3: CaO and MgO contents of primary magmas calculated with PRIMELT3 software (Herzberg and Asimow, 2015) using MORB compositions and reduced condition in the source ($Fe^{2+}/\Sigma Fe = 0.9$). Successful and unsuccessful solutions of calculation have been reported on the graph. Red lines are described by equations (9), (10), and (11) in Herzberg and Asimow (2008). They define upper and lower CaO filters of primary magmas of fertile peridotite produced by accumulated fractional melting. Primary magma with CaO contents lower than those defined by the green line are potential pyroxenite partial melts; they can also be peridotite partial melts that had clinopyroxene (Cpx) removed. The black broken arrow corresponds to the typical liquid line of descent for primary magmas that crystallize gabbro in the crust; the drop in CaO often occurs at MgO < 7–10%. However, Cpx can also crystallize in the mantle and affect magmas with MgO > 10%. Here, only ∼ 25% of the dataset have been reported (whole-rock analyses only, see Fig. B.2a).

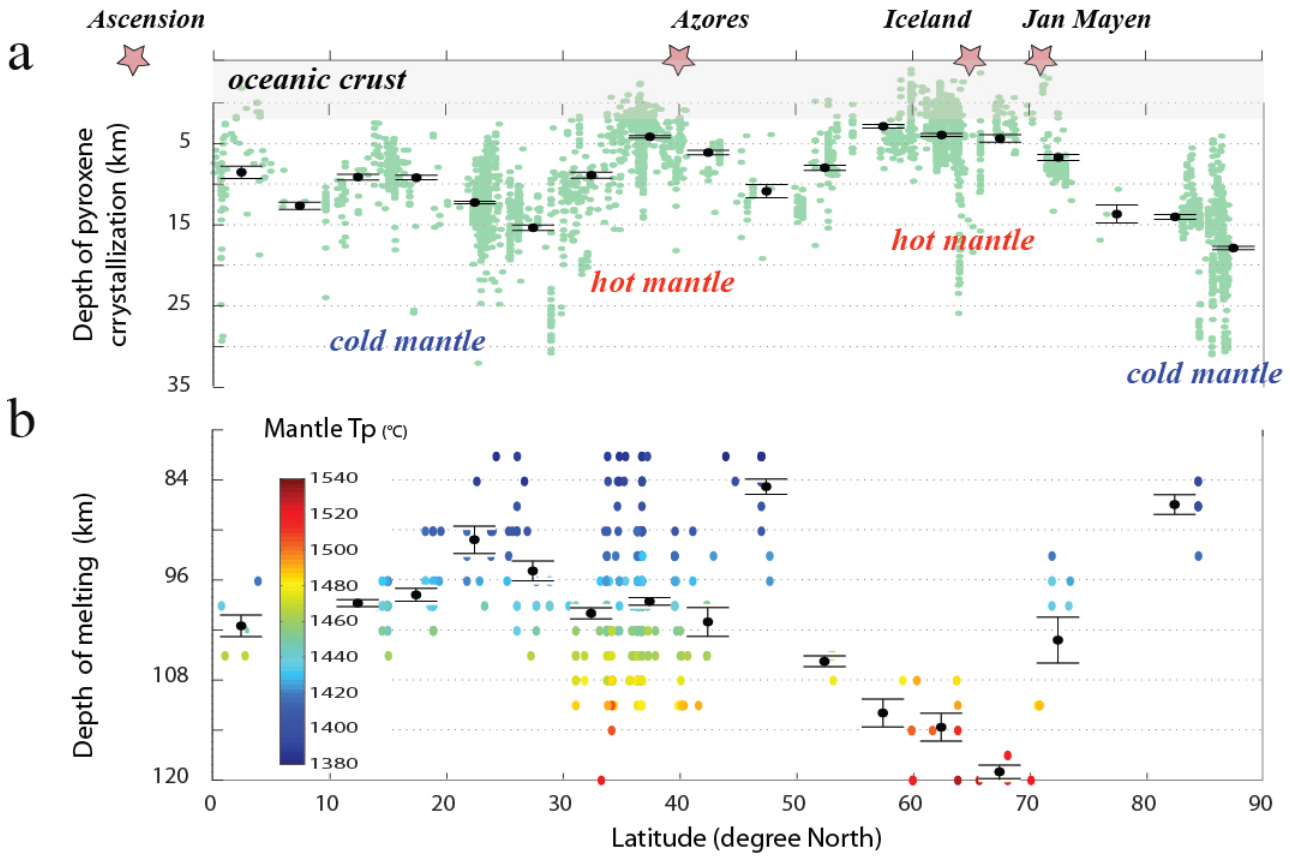


Figure B.4: Latitudinal distribution of pyroxene crystallization depth and T_P estimates along the northern section of the MAR (a) Depth of pyroxene crystallization then subtraction (e.g. fractionation) in a primary magma that, later, will give birth to MORBs, calculated using equation (6) in Herzberg (2004) and assuming a ratio of 1:3 between pressure (kb) and depth (km). (b) Depth at which adiabatically upwelling mantle below the MAR segments crossed their solidus, depending on their potential temperature (T_P) calculated with PRIMELT3 MEGA software (Herzberg and Asimow, 2015) using reduced conditions ($Fe^{2+}/\Sigma Fe = 0.9$) in the source. Solutions of calculation have been filtered for MgO < 8 wt% (blue dots in Fig. B.2). The Jan Mayen, Iceland and Azores plume-like volcanic edifices forming on the ridge are indicated. The lowest pressures are observed close to Iceland where elevated T_P have been calculated. The highest pressures are observed for MORB associated with ridge segment terminations, especially segments $> 70°$N (e.g. Gakkel ridge). Data are plotted against latitude.

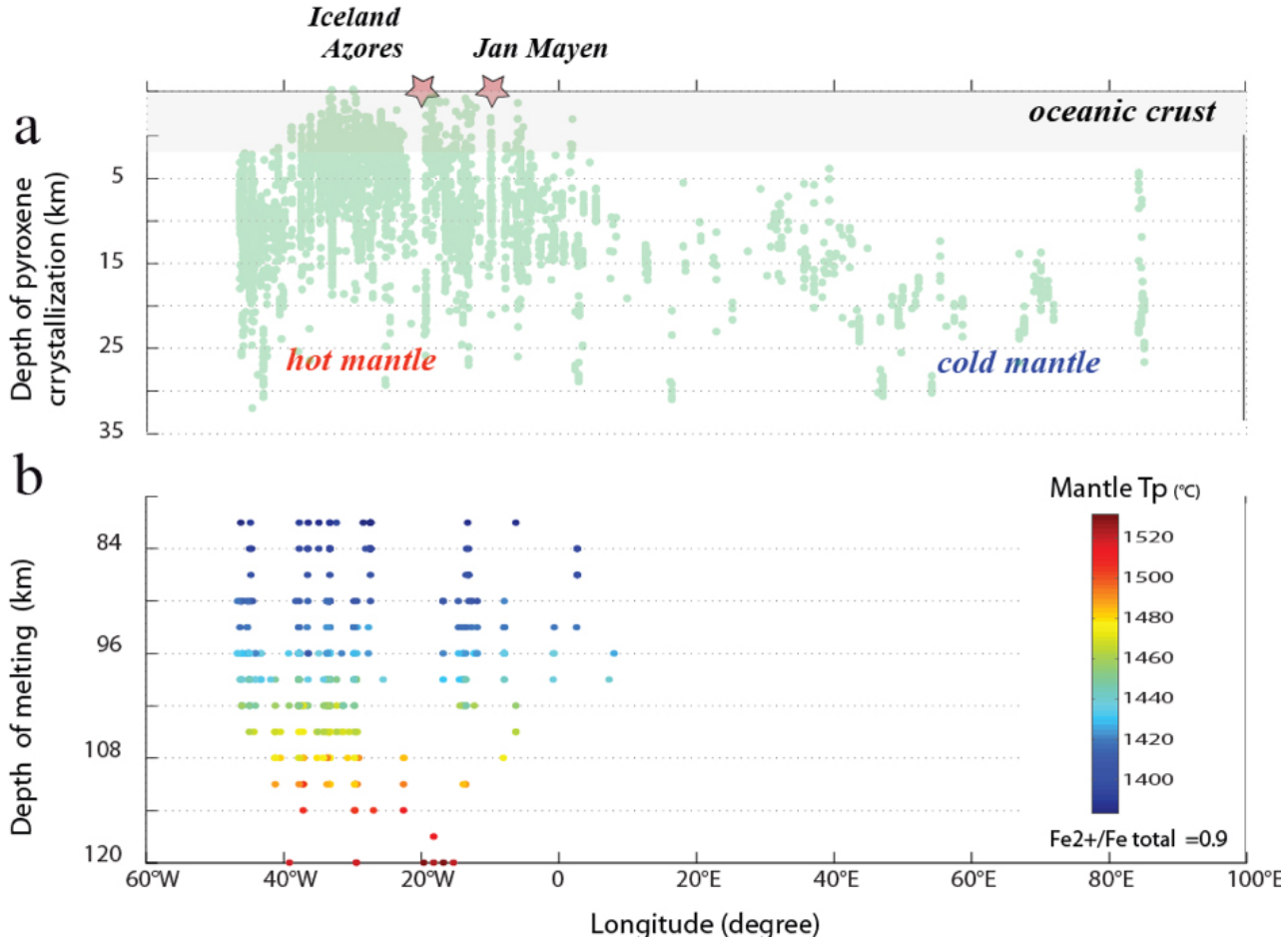


Figure B.5: Longitudinal distribution of pyroxene crystallization depth and T_P estimates along the northern section of the MAR (a) Depth of crystallization then subtraction (e.g. fractionation) of pyroxene in a primary magma, that later will give birth to MORBs, calculated using equation (6) in Herzberg (2004) and assuming a ratio 1:3 between pressure (kb) and depth (km). (b) Depth at which adiabatically upwelling mantle below the MAR segments crossed their solidus, depending on their potential temperature (T_P) calculated with PRIMELT3 Mega software (Herzberg and Asimow, 2015) using reduced conditions ($Fe^{2+}/\Sigma Fe = 0.9$) in the source. Solutions of calculation have been filtered for MgO $<$ 8 wt% (blue dots in Fig. B.2). MORBs for which Ol - Plag fractionation was likely have been filtered out as discussed in Herzberg (2004) ; these have CaO $>$ -0.3 x MgO + 14.55. Data are plotted against longitude. The longitude 0° corresponds to the Greenwich meridian.

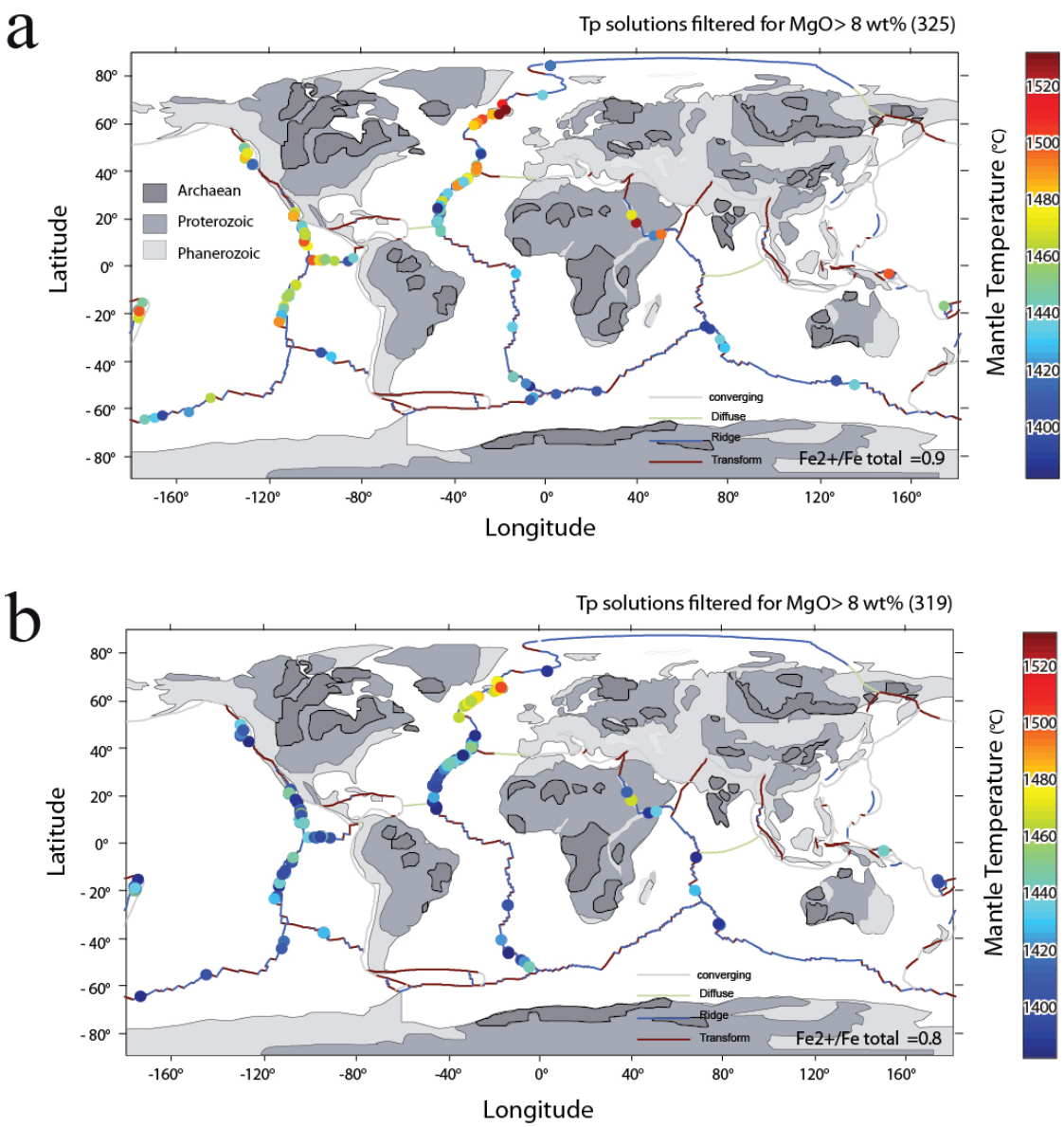


Figure B.6: Distribution of filtered T_P solutions. (a) Distribution of (zero-age) MORBs giving a solution of calculation with PRIMELT3 (Herzberg and Asimow, 2015). Mantle potential temperatures (T_P) were calculated with reduced conditions ($Fe^{2+}/\Sigma Fe = 0.9$ or 0.8) in the source and filtered with MgO < 8 wt% (blue dots in Fig. B.2). Here, only $\sim$ 25% of the dataset have been reported (whole-rock analyses only, see Fig. B.2a).

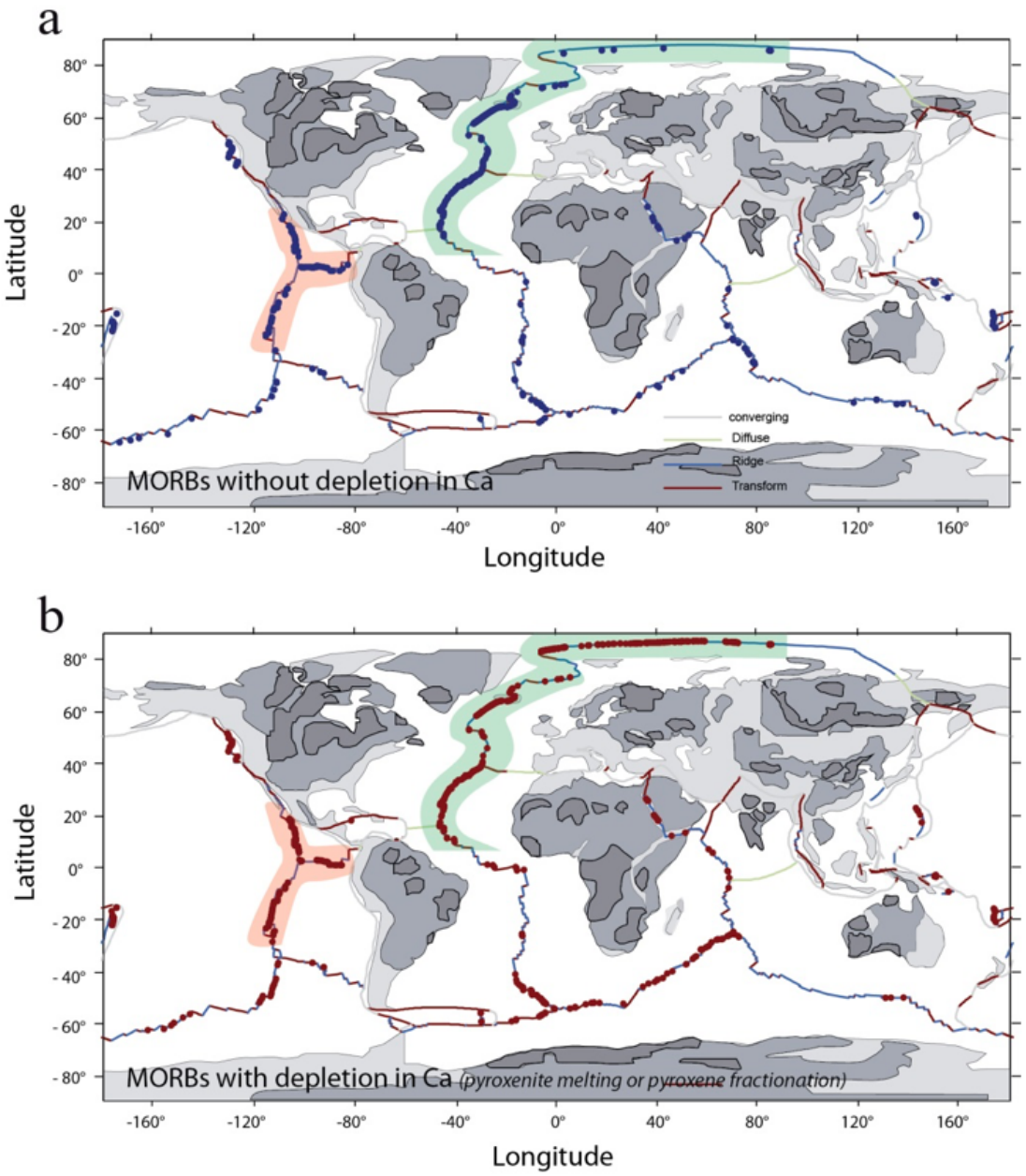


Figure B.7: – Distribution of (zero-age) MORBs deriving from a primary magma (a) that is not depleted in CaO and (b) depleted in CaO. A ratio of $\sim$ 32% is observed between CaO-depleted and -undepleted primary magma for the East Pacific Rise, between 30°S and 25°N (colored in orange on the map). The northern sections of the MAR (colored in green on the map) are characterized by a different ratio (57%), with significant variations along the strike of the ridge. Segments of ridges characterized by a dominant record of CaO-undepleted magma are positioned close to plume-like volcanic edifices (Iceland, Azores) whereas depleted magma are dominantly observed in ridge segment terminations, especially segments > 70°N (e.g. Gakkel ridge). Here, only $\sim$ 25% of the dataset have been reported (whole-rock analyses only, see Fig. B.2a).

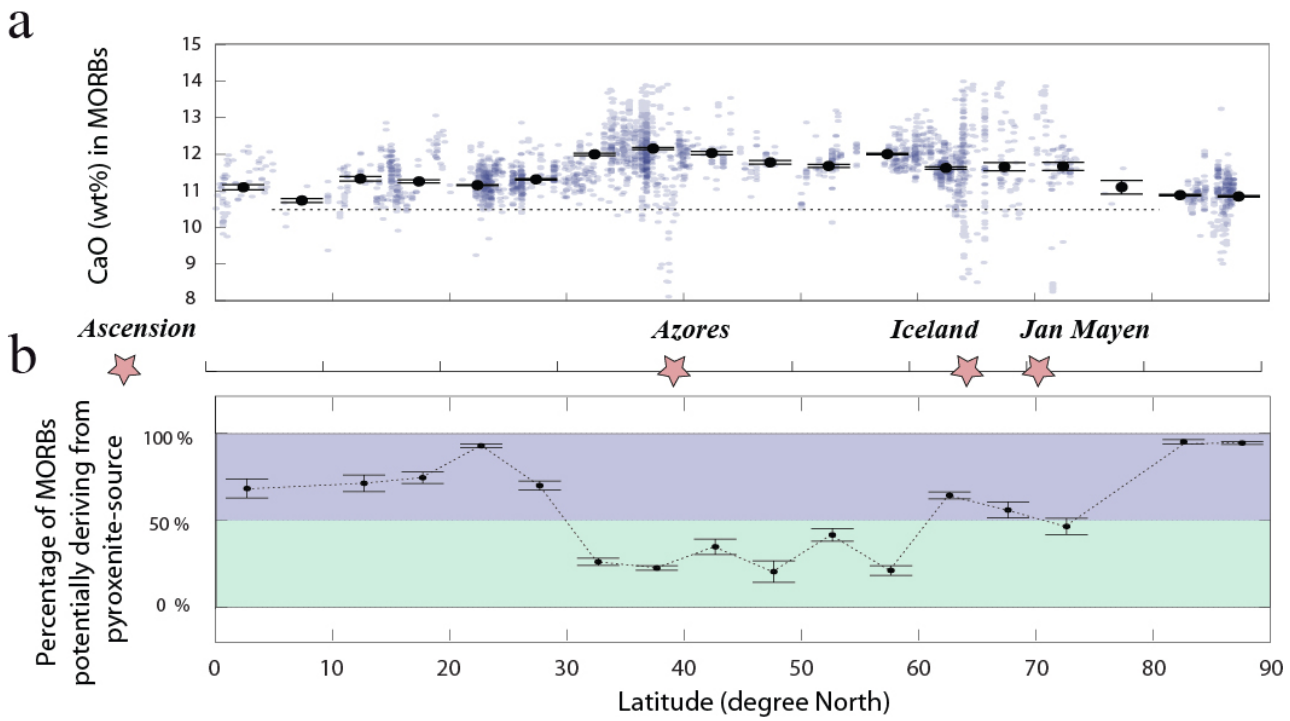


Figure B.8: Chemical depletion in CaO along the northern section of the MAR (a) Chemical evolution of (near zero-age) MORBs sampled along the Mid-Atlantic Ridge. Data have been plotted against the latitudes between 0 and 90°N along the x-axis. The Jan Mayen, Iceland and Azores plume-like volcanic edifices forming on the ridges are indicated. (b) Percentage of MORBs for which PRIMELT predicts a primary magma composition depleted in calcium. Mean values (black points), obtained by bootstrap analysis, are reported at 5° step of latitude.

Fig. 4.25a and B.8 unravel chemical changes of MORBs along the MAR. The database records slightly elevated CaO (wt%) values for MORBs centered on Azores (∼40°N) and a progressive decrease further south and north of the archipelago, following a bell-shaped evolution. The percentage of samples for which PRIMELT predicts a primary magma composition depleted in calcium, by comparison with primary magmas deriving from peridotite-source, is given in Fig. B.8b. Ca-depletion is minimal in the Azores region. It progressively increases in the south and north of the archipelago, reaching its maximum values (∼ 100%) along the Gakkel ridge which is on the northern segment of the MAR (Fig. B.5). Such differences in calcium cannot solely be explained by a fractionation of olivine (forsterite: Mg-rich endmember) and either require an increasingly subtraction of pyroxene (diopside : Mg-Ca-rich endmember) from the primary magma and/or an increasingly melting of Ca-depleted source (pyroxenites) in the mantle (Herzberg and Asimow, 2008) which, we infer, must be related to changes in the mantle temperature below the MAR.

A cooler mantle will promote pyroxenite melting over peridotite because of its lower temperature.

Likewise, low thermal gradients in a mantle section will promote the crystallization and sequestration of pyroxene at deeper levels, decreasing the content of Ca in the residual melt. Elevated T_P values ($> 1500°C$) are observed in the north of the Azores archipelago, extending to Iceland. A progressive decrease in temperature is observed southwards of the Azores and a marked decrease northwards of the Azores, giving the appearance of asymmetric thermal structure. However, a gap of data exists between 45°N and 55°N of latitude (Fig. B.6 and B.7). This section is associated with a change in the orientation of the ridge, which here operates with a strong strike-slip component (e.g. Charlie Gibbs's fault). The depth of pyroxene fractionation for MORBs was estimated using the equation (6) of Herzberg (2004) and results are given in Fig. 4.25a, B.4a and B.5a. MORBs in which olivine and plagioclase fractionation likely occurred have been filtered out as discussed in Herzberg (2004), these have CaO > -0.3 x MgO + 14.5. As expected, lower pressures of crystallization are observed around Azores and Iceland where elevated T_P have been calculated. The pressures of crystallization increase with decreasing T_P, as observed in the south of Azores. The highest pressures are observed for MORBs associated with ridge segment terminations (e.g. Gakkel ridge).

B.2 Analysis of the thermal imprint of modelled plumes

B.2.1 Numerical set up

The model equations and parameters correspond to the model set up fully-described in Arnould et al. (2018), although the presented model is in 3D-spherical geometry:

We solve the following equations of conservation of mass, momentum, energy and composition under the Boussinesq approximation (e.g. Ricard (2015)):

$$\begin{aligned} \nabla \cdot \mathbf{v} &= 0 \\ \nabla p - \nabla \cdot \left[\eta(\underline{\nabla \mathbf{v}} + (\underline{\nabla \mathbf{v}})^T)\right] &= \mathrm{Ra}(\alpha(z)T + BC)\mathbf{e_r} \\ \frac{\mathrm{D}T}{\mathrm{D}t} &= -\nabla \cdot (\nabla T) + H \\ \frac{\mathrm{D}C}{\mathrm{D}t} &= 0 \end{aligned} \tag{B.1}$$

where v is velocity, p is pressure, η is viscosity, T is temperature and C is composition. H is the mantle internal heat production rate, α is a depth-dependent thermal expansivity coefficient set as in Arnould et al. (2018), B is the chemical buoyancy ratio and $\mathbf{e_r}$ is the radial unit vector. Ra is the Rayleigh number:

$$\mathrm{Ra} = \frac{\alpha_0 g \Delta T \rho_0 h^3}{\eta_0 \kappa_0} \tag{B.2}$$

where α_0 is the surface thermal expansivity, D the mantle's thickness, g the gravitational acceleration, ΔT the temperature gradient across the mantle, ρ_0 the reference density, η_0 the reference viscosity and κ the reference thermal diffusivity. In the studied model, Ra is 10^7. We use the following viscosity law depending of pressure and temperature:

$$\eta(z,T) = \eta_0(z).\exp\left(A + \frac{E_a + \Pi(z)V_a}{RT}\right) \tag{B.3}$$

where A is a constant so that $\eta = \eta_0$ for $T = 0.64$ (corresponding to 1600 K), which is the a priori temperature at the lithosphere-asthenosphere boundary, E_a the activation energy, $\Pi(z)$ the static pressure, V_a the activation volume, R is the gas constant and T the temperature. We define an upper-lower mantle viscosity jump by a factor of 30, as suggested in geoid and post-glacial rebound studies (Nakiboglu and Lambeck, 1980, Ricard et al., 1993).

In order to model a plate-like behavior, we use a pseudo-plastic rheological law based on a yield-

stress induced viscosity drop enabling strain localization (Tackley, 2000).

The parameters are described in Table B.2.

Table B.2: Numerical modeling parameters

Parameter	**Non-dim. value**	**Dim. value**
Surface temperature (T_{top})	0.12	255 K
Basal temperature (T_{bot})	1.12	2240 K
Mantle domain thickness (D)	1	2890 km
Reference thermal expansivity (α)	1	3×10^{-5} K^{-1}
Reference density (ρ_0)	1	4400 $kg{\cdot}m^{-3}$
Reference diffusivity (κ)	1	1×10^{-6} $m^2{\cdot}s^{-1}$
Reference conductivity (c_p)	1	3.15 $W{\cdot}m^{-1}{\cdot}K^{-1}$
Reference viscosity (η_0)	1	1.03×10^{22} Pa·s
Internal heating rate (H)	40	6.81×10^{-12} $W{\cdot}kg^{-1}$
Activation energy (E_a)	8	142 $kJ{\cdot}mol^{-1}$
Activation volume (V_a)	3	13.8 $cm^3{\cdot}mol^{-1}$
Maximum viscosity cut-off	10^4	10^{26} Pa·s
Viscosity increase at 660 km	30	
Yield stress gradient for all materials ($d\sigma_Y$)	2.34×10^6	1088 $Pa{\cdot}m^{-1}$
Yield stress at the surface - oceanic lithosphere ($\sigma_{Y_{oc}}$)	3.5×10^4	48 MPa
Yield stress at the surface - continental interior ($\sigma_{Y_{cont}}$)	7×10^5	932 MPa
Viscosity increase - continental interior	100	
Buoyancy number - continental interior (B_{cont})	-0.32	-150 $kg{\cdot}m^{-3}$
Thickness - continental interior	0.0692	200 km
Yield stress at the surface - continental belt ($\sigma_{Y_{belt}}$)	3×10^5	400 MPa
Viscosity increase - continental belt	50	
Buoyancy number - continental belt (B_{belt})	-0.4	-188 $kg{\cdot}m^{-3}$
Thickness - continental belt	0.0432	125 km

B.2.2 Characteristics of modelled plumes

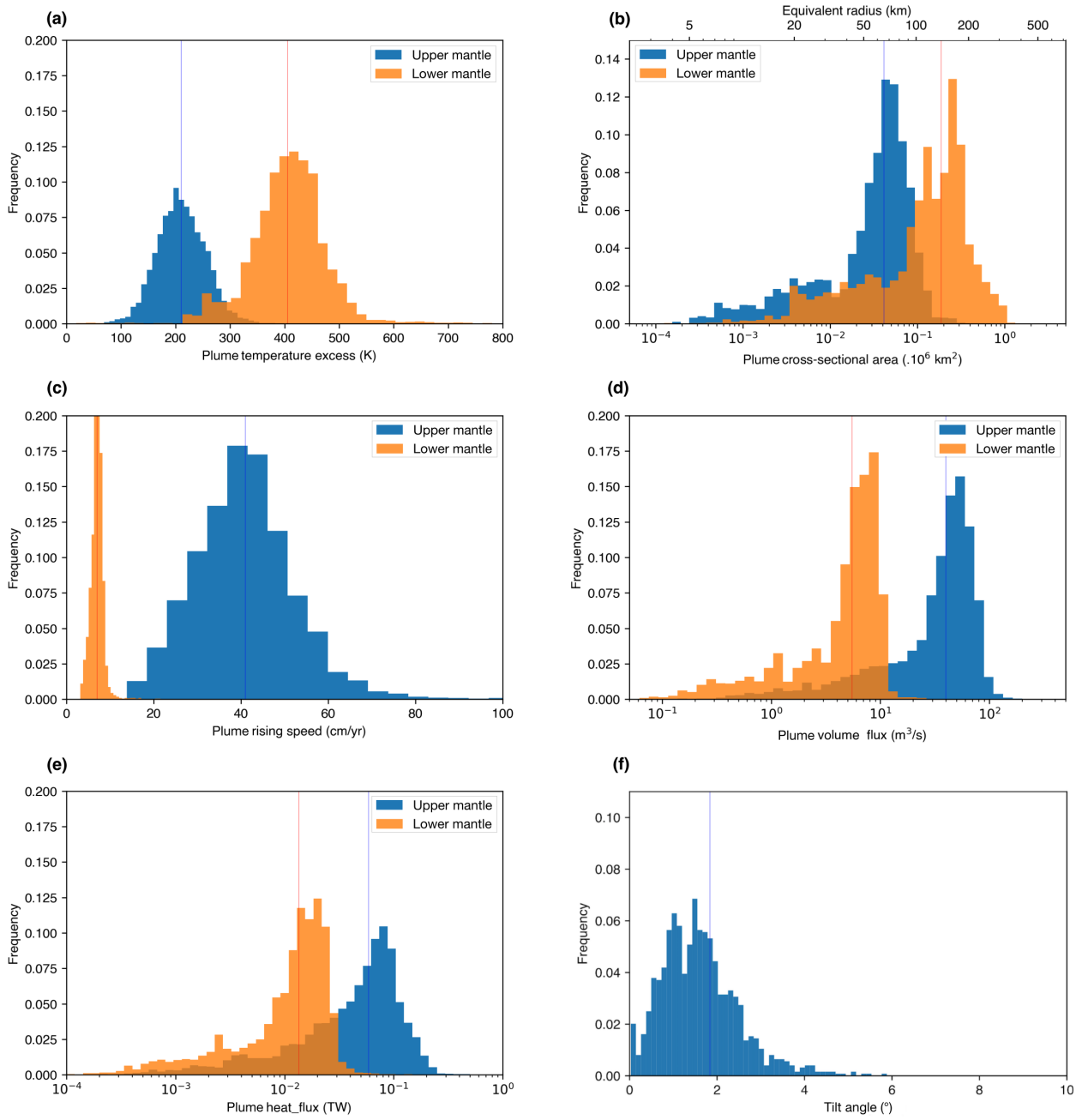


Figure B.9: Characteristics of all modelled plumes detected in the upper (350 km, blue) and the lower (1,000 km, orange) mantle throughout the model time integration. Plume (a) temperature excess, (b) cross-sectional area and equivalent radius (using the approximation of a circular conduit), (c) rising speed, (d) volume flux, (e) heat flux and (f) tilt angle between the lower (1,000 km) and the upper (350 km) mantle.

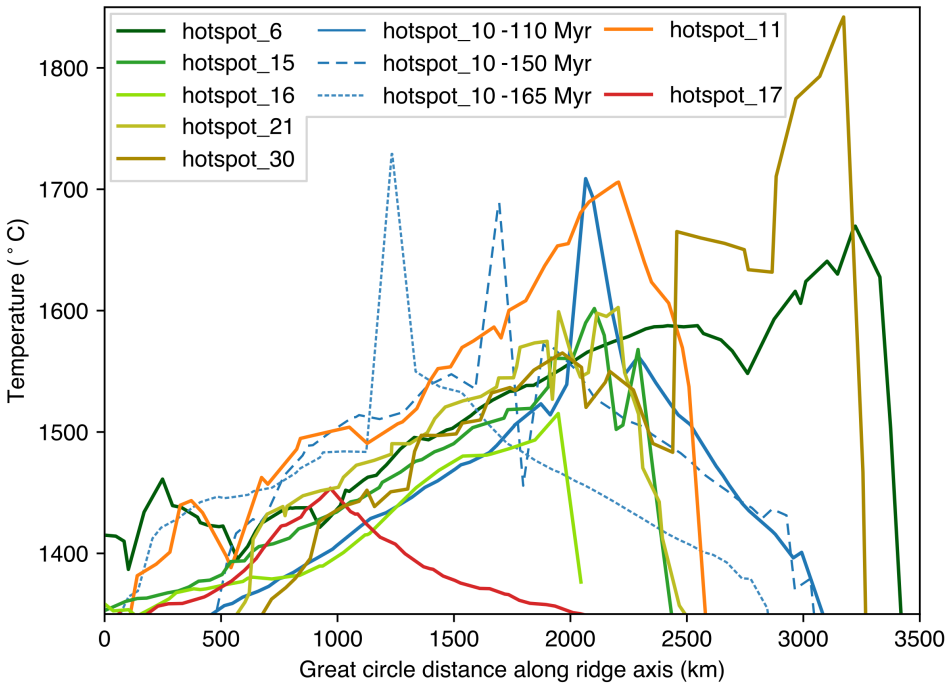


Figure B.10: Temperature profiles at 100 km depth of the modeled plumes interacting with ridges presented on Fig. 4.26f. Hotspots 6, 15, 16, 21 and 30 display a very asymmetric profile and correspond to case 1. Hotspot 10 corresponds to case 2. The temporal evolution of its thermal asymmetry is shown. See Fig. B.11 for details. Hotspot 11's thermal profile is asymmetric and corresponds to case 3 and Hotspot 17 presents a symmetric thermal profile and corresponds to case 4.

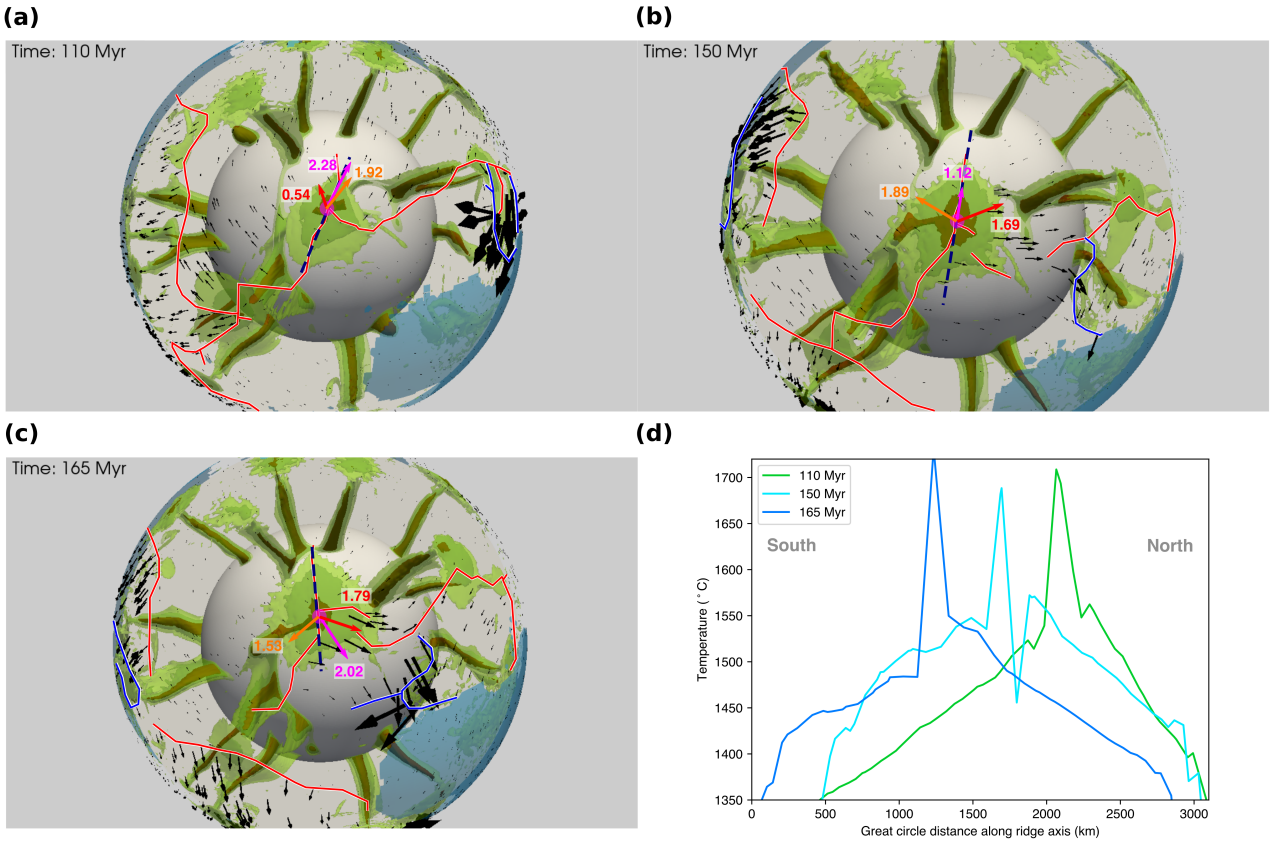


Figure B.11: Effect of changes in the relative motion of plates and hotspot 10 on the asymmetry of the temperature profile. (a), (b) and (c) show the temporal evolution of the ridge system (red lines) and the mantle plume (light green (1,390°C), dark green (1,480°C) and brown (1,700°C) isotherms). Surface plate velocities are shown by the black arrows. Continental material is outlined in transparent blue. The average plate velocity around the considered plume is shown with the red arrow centered on the plume. The plume absolute velocity (pink arrow) is shown in magenta. Between 110 Myr and 150 Myr, the plume moves northward and its speed halves. After 150 Myr, the plume's direction changes and it moves southward at 165 Myr. At the same period of time, a subduction initiates southeast (blue lines) and propagates to the west, which leads to the reorganization of plate velocities in the vicinity of the considered plume. As a consequence, the relative velocity vector between the plume and plates rotates by 180° in 55 Myr. (d) Temporal evolution of the plume temperature profile along the ridge (corresponding to the dark blue dashed line in (a), (b) and (c)) at 100 km depth. Note the change in the symmetry of the profile through time. The corresponding symmetry coefficients are shown on Fig. 4.26f.

B.3 Kinematic analysis of South and Central Atlantic hotspot tracks

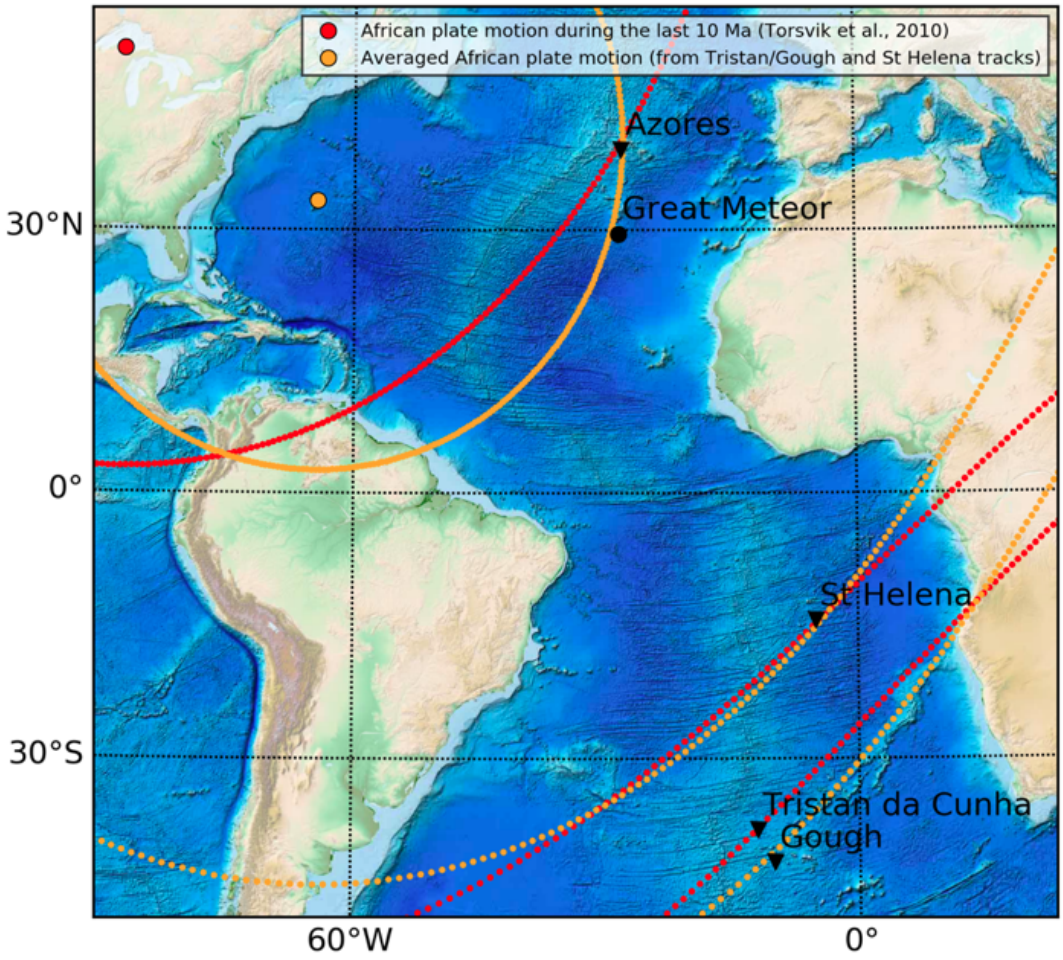


Figure B.12: African plate motion in a reference frame relative to hotspots. The background displays the etopo map (Amante and Eakins, 2009). The African plate motion rotation pole from Torsvik et al. (2010), for the last 10 Ma is indicated by the red filled circle. Tristan da Cunha/Gough and St Helena are considered to remain stationary relative to each other Duncan (1981). The dashed red lines outline small-circles crossing the present-day position of Tristan da Cunha/Gough, St Helena and the Azores (black triangles). The orange rotation pole and small circles represent the average motion of the African plate compared to fixed Tristan da Cunha/Gough and St Helena for the last 80 Ma. The small circles fit Tristan/Gough and St Helena hotspot tracks and indicate a north-eastward rotation of Africa relatively to those hotspots. The corresponding orange small circle for the Azores present-day position superposed to the topographic high linking the Azores to Great Meteor. However, using this potential hotspot track would result in a south-westward motion of the African plate, incompatible with the tracks of Tristan/Gough and St Helena, indicating a north-eastward motion of the African plate.